TOPS
Volume 69

Laser Applications to Chemical and Environmental Analysis

Postconference Digest

Series Editor
Alexander A. Sawchuk

OSA®
Optical Society of America

20030516 065

REPORT DOCUMENTATION PAGE

1. AGENCY USE ONLY (Leave Blank)	2. REPORT DATE 02/28/03	3. REPORT TYPE AND DATES COVERED FINAL 01-01-2002 - 12-31-2002

4. TITLE AND SUBTITLE Organization of the 2002 Photonic Science Topical Meetings	5. FUNDING NUMBERS F49620-02-1-0065

6. AUTHOR(S)
Optical Society of America

7. PERFORMING ORGANIZATION NAME(S) AND ADDRESS(ES) Optical Society of America 2010 Massachusetts Ave., NW Washington, DC 20036	8. PERFORMING ORGANIZATION REPORT NUMBER

9. SPONSORING / MONITORING AGENCY NAME(S) AND ADDRESS(ES) U. S. Air Force Office of Scientific Research 4015 Wilson Blvd. Rm. 713 Arlington, VA 22203	10. SPONSORING / MONITORING AGENCY REPORT NUMBER

11. SUPPLEMENTARY NOTES

The views, opinions and/or findings contained in this report are those of the author(s) and should not be construed as an official US AFOSR position, policy or decision, unless so designated by other documentation.

12 a. DISTRIBUTION / AVAILABILITY STATEMENT Approved for public release; distribution unlimited.	12 b. DISTRIBUTION CODE

13. ABSTRACT (Maximum 200 words)

The OSA topical meetings that received support under this grant provided a forum for researchers in various specialty areas to meet and share ideas and technology in their fields. Following are the meetings that were supported by this grant:

- Advanced Solid State Lasers – This meeting provided a forum for leading edge results in the fields of solid state lasers, laser materials, nonlinear optical materials and high power diode lasers.
- Laser Applications to Chemical and Environmental Analysis – This meeting presented and discussed advances in the use of lasers for chemical analysis and environmental monitoring.
- Biomedical Optics – This meeting was composed of three meetings that offered a unique venue to present and discuss recent research activities and developments in the field of lasers and optics in biomedicine.
- Ultrafast Phenomena - This meeting brought together a multidisciplinary group sharing a common interest in the generation of ultrashort pulses in the picosecond, femtosecond, and attosecond regimes and their application to studies of ultrafast phenomena in physics, chemistry, biology, material sciences and electronics.
- Nonlinear Optics – This meeting provided and international forum for discussion of all aspects of nonlinear optics, including new phenomena, novel devices, advanced materials and applications.
- Nonlinear Guided Waves and their Applications – This meeting emphasized on development of new ideas and novel techniques in the areas of materials, fabrication, devices , applications and nonlinear theory.
- Laser Induced Plasma Spectroscopy and Applications – This Meetings focused on major advances in LIBS fundamentals, instrumentation and applications and featured new commercial laboratory LIBS systems and advanced components, as well as field portable systems.

14. SUBJECT TERMS			15. NUMBER OF PAGES
			16. PRICE CODE

17. SECURITY CLASSIFICATION OR REPORT UNCLASSIFIED	18. SECURITY CLASSIFICATION ON THIS PAGE UNCLASSIFIED	19. SECURITY CLASSIFICATION OF ABSTRACT UNCLASSIFIED	20. LIMITATION OF ABSTRACT UL

NSN 7540-01-280-5500

Standard Form 298 (Rev.2-89)
Prescribed by ANSI Std. 239-18
298-102

Trends in Optics and Photonics Series

Laser Applications to Chemical and Environmental Analysis

Series Editor:
lexander A. Sawchuk

Articles in this publication may be cited in other publications. In order to facilitate access to the original publication source, the following form for the citation is suggested:

Name of Author(s), Title of Paper, *OSA Trends in Optics and Photonics (TOPS) Vol. 69, Laser Applications to Chemical and Environmental Analysis,* OSA, Technical Digest, Postconference Edition (Optical Society of America, Washington, DC 2002), pp. xx-xx.

Technical Digest (meeting edition)

TOPS Vol 69: LACEA Technical Digest Postconference Ed.

Technical Program Committee

David J. Rakestraw, *Eksigent Tech., USA, General Chair*

Markus Sauer, *Physikalisch-Chemisches Inst., Germany, General Chair*

Alan C. Stanton, *Southwest Sciences, Inc., USA, General Chair*

John W. Daily, *Univ. of Colorado, USA, Program Chair*

Andreas Brockhinke, *Univ. Bielefeld, Germany, Program Chair*

John C. Miller, *Oak Ridge Natl. Lab., USA, Program Chair*

*Mark G. Allen, *Physical Sciences, Inc., USA*

Douglas S. Baer, *Los Gatos Res., Inc., USA*

Michael D. Barnes, *Oak Ridge Natl. Lab., USA*

Alfredo E. Bruno, *Novartis Pharma AG, Switzerland*

Jae Won Hahn, *Korea Inst. of Standards, South Korea*

Clemens Kaminski, *Univ. of Cambridge, UK*

Mark A. Linne, *Colorado School of Mines, USA*

Kevin L. McNesby, *U.S. Army Res. Lab., USA*

Juan Carlos Rolon, *Ecole Centrale Paris, France*

Richard M. Williams, *Pacific Northwest Natl. Lab., USA*

Denotes OSA Technical Council Representative

Agenda of Sessions

Wednesday, February 6, 2002

2:00pm–7:00pm	Registration *Flat Iron Room*

Thursday, February 7, 2002

7:00am–5:00pm	Registration/Speaker and Presider Check-In *Flat Iron Room*
8:00am–8:20am	**Opening Remarks** *Century Room*
8:20am–10:00am	**ThA: Biological or Biomedical I** *Century Room*
10:00am–10:40am	Coffee Break *Millenium Room*
10:00am–5:00pm	Exhibits Open *Millenium Room*
10:40am–12:20pm	**ThB: Combustion I** *Century Room*
12:20pm–2:00pm	Lunch Break
2:00pm–3:40pm	**ThC: Biological or Biomedical II** *Century Room*
3:40pm–4:20pm	Coffee Break *Millenium Room*
4:20pm–5:40pm	**ThD: Nonlinear Techniques** *Century Room*

Friday, February 8, 2002

7:00am–5:00pm	Registration/Speaker and Presider Check-In *Flat Iron Room*
8:00am–10:000am	**FA: Laser Induced Breakdown Spectroscopy** *Century Room*
10:00am–10:40am	Coffee Break *Millenium Room*
10:00am–5:00pm	Exhibits Open *Millenium Room*
10:40am–12:20pm	**FB: Combustion II** *Century Room*
12:20pm–2:00pm	Lunch Break

2:00pm–3:00pm	**FC: Combustion III** *Century Room*
3:00pm–4:00pm	**FD: Cavity Ringdown Spectroscopy** *Century Room*
4:00pm–4:40pm	Coffee Break *Millenium Room*
4:40pm–5:40pm	**FE: Plenary Session** *Century Room*

Saturday, February 9, 2002

7:30am–12:30pm	Registration/Speaker and Presider Check-In *Flat Iron Room*
8:00am–10:00am	**SaA: Instrumentation I** *Century Room*
10:00am–10:40am	Coffee Break *Millenium Room*
10:40am–12:20pm	**SaB: Diode Lasers and Applications I** *Century Room*
12:20pm–7:00pm	Lab tour or recreation time
7:00pm–9:00pm	**SaC: Poster Session & Reception** *Millenium Room*

Sunday, February 10, 2002

7:30am–12:00pm	Registration/Speaker and Presider Check-In *Flat Iron Room*
8:00am–10:00am	**SuA: Instrumentation II** *Century Room*
10:00am–10:40am	Coffee Break *Millenium Room*
10:40am–12:20pm	**SuB: Diode Lasers and Applications II** *Century Room*
12:20pm–12:30pm	**Closing Remarks** *Century Room*

Abstracts

Room: *Century*
8:20am–10:00am
ThA ■ Biological or Biomedical I
Michael D. Barnes, Oak Ridge Natl. Lab., USA, Presider

ThA1   8:20am   (Invited)
New advances in optical microscopy of biological systems, *Sunney Xie, Harvard Univ., USA.*
Abstract not available.

ThA2   9:00am
Single molecule fluorescence correlation spectroscopy in an electrophoretic mobility shift assay, *Alan Van Orden, Colorado State Univ., USA; Dale J. LeCaptain, Central Michigan Univ., USA.*
A capillary electrophoresis-based electrophoretic mobility shift assay is described wherein fluorescence correlation spectroscopy is used to resolve the bound and unbound fractions of a DNA-protein complex on the basis of their characteristic electrophoretic flow velocities.

ThA3   9:20am
Probing single ion luminescence in rare-earth doped nanocrystals, *A. Mehta, T. Thundat, M.D. Barnes, Oak Ridge Natl. Lab., USA; R. Bhargava, Nanocrystals Tech., USA; A. Bartko, L. Peyser, R.M. Dickson, Georgia Inst. of Tech., USA.*
We describe experiments probing single europium and terbium ions in isolated nanocrystals (2 –15 nm diam.) using fluorescence microscopy techniques. Emission pattern imaging also shows patterns that are distinctly characteristic of single dipoles.

ThA4   9:40am
Second harmonic generation technique for monitoring of thermo-induced processes in biotissue, *A. Lalayan, Yerevan State Univ., Armenia; E. Janunts, Armenian State Engineering Univ., Armenia.*
Second harmonic generation in collagen contained animal biotissue under picosecond laser irradiation have been studied during conventional and laser heating. Experimental comparison of second harmonic generation and two-photon fluorescence nonlinear optical phenomena has been performed in ordered native tissue.

Room: *Century*
10:40am–12:20pm
ThB ■ Combustion I
Clemens Kaminski, Univ. of Cambridge, UK, Presider

ThB1   10:40am   (Invited)
Multidimensional and multiscalar laser diagnostics in turbulent combusting flows, *Johan Hult, Lund Inst. of Tech., Sweden.*
Measurements in jet flames and engines of time resolved fuel concentration fields, simultaneous OH and velocity fields and three-dimensional soot concentrations, using a high speed laser diagnostic imaging system are presented.

ThB2   11:20am
Raman/Rayleigh/LIF/CRDS measurements in premixed $CH_4/N_2/O_2$ atmospheric pressure flames, *Christopher B. Dreyer, Mark Linne, Colorado School of Mines, USA.*
Measurements of N_2, O_2, CH_4, CO_2, and H_2O have been made by vibrational raman scattering and OH by laser induced fluorescence (LIF) and cavity ringdown spectroscopy (CRDS) as a function of height in a premixed methane/air flame at atmospheric pressure.

ThB3   11:40am
In situ measurement of CO, H_2O, and gas temperature in a lignite-fired power-plant, *H. Teichert, T. Fernholz, V. Ebert, Univ. of Heidelberg, Germany.*
A diode laser based in situ absorption spectrometer is presented for the simultaneous detection of CO (1560nm), water (813nm) and the gas temperature within the combustion chamber of a 600MW lignite-fired power-plant.

ThB4   12:00pm
Nanoscaled particle size distributions and gas temperatures from time-resolved LII measurements, *T. Lehre, B. Jungfleisch, R. Suntz, H. Bockhorn, Univ. Karlsruhe, Germany.*
LII signals are measured in sooting premixed atmospheric and low-pressure flames. Soot particle size distribution P(r) and gas temperature T are measured independently. LII model parameters are validated. P(r) and T are estimated using non-linear regression.

2:00pm–3:40pm
ThC ∎ Biological or Biomedical II
Andreas Brockhinke, Univ. Bielefeld, Germany, Presider

ThC1   2:00pm   (Invited)
Fluorescence correlation spectroscopy and its impact on single molecule biophysics, *Petra Schwille, Unaffiliated, Germany.*
Confocal fluorescence correlation spectroscopy (FCS) combines single molecule sensitivity with high statistical confidence and has proved to be an extremely powerful tool for detection and temporal investigation of biomolecules in solution and living cells.

ThC2   2:40pm
A mid infrared, high power, cw, continuous tunable PPLN OPO for trace gas detection within life science, *M. van Herpen, S. te Lintel Hekkert, F.J.M. Harren, Univ. of Nijmegen, The Netherlands; S.E. Bisson, Sandia Natl. Labs., USA.*
A 2 W continuous wave optical parametric oscillator based on periodically poled lithium niobate and tunable over the 3.0-3.8 micrometer wavelength region is used in combination with photoacoustic spectroscopy to trace small hydrocarbons for applications in medicine and biology.

ThC3   3:00pm
Longitudinal studies of nitric oxide and carbon dioxide in human breath with a single IV-VI mid-IR laser, *Chad Roller, Khosrow Namjou, Jim Jeffers, Ekips Tech., Inc., USA; Adom Mock, Columbia Univ., USA; Patrick J. McCann, Joe Grego, Univ. of Oklahoma, USA.*
NO and CO_2 were measured simultaneously in exhaled breath from seven subjects 10 times over a period of 12 days. Exhaled CO_2 was used to estimate NO values as laser characteristics fluctuate over time.

ThC4   3:20pm
Measurement of $^{13}CO_2/^{12}CO_2$ ratio using tunable diode laser based Raman spectroscopy and an atomic vapor filter, *Philip L. Varghese, Claudia Navarro, Manfred Fink, Univ. of Texas at Austin, USA.*
We describe a novel scheme for detecting the isotopic ratio ($^{13}C/^{12}C$) in gaseous carbon dioxide. Raman scattering is excited with a tunable near-infrared diode laser and isotopic discrimination is obtained with an atomic vapor filter.

4:20pm–5:40pm
ThD ∎ Nonlinear Techniques, etc...
Mark G. Allen, Physical Sciences Inc., USA, Presider

ThD1   4:20pm
Far-infrared semiconductor laser for molecular spectroscopy, *R.E. Peale, A.V. Muravjov, E.W. Nelson, Univ. of Central Florida, USA; S.G. Pavlov, V.N. Shastin, Russian Acad. of Science, Russia; C.J. Fredricksen, Zaubertek, Inc., USA.*
The feasibility of the p-Ge laser for far-infrared laser spectroscopy is enhanced by recent progress in single mode selection and tunable external cavities, allowing continuous tuning from 50-140 cm-1 without mode-hops.

ThD2   4:40pm
Tunable silver and gold substrates for surface enhanced raman spectroscopy, *R. Gupta, W.A. Weimer, Zyvex Corp., USA.*
Use of specific combinations of thermal evaporation parameters allows the deposition of surface plasmon resonance tunable silver and gold island films on glass substrates. The utility of these films for surface enhanced Raman spectroscopy is demonstrated.

ThD3   5:00pm
All-telecom diode laser based mid-IR source for spectroscopic detection of HF, H_2O, and HDO, *Dirk Richter, Alan Fried, Geoffrey S. Tyndall, Natl. Ctr. for Atmospheric Res., USA; Eduardo Oteiza, Coherent, Inc., USA; Miklos Erdelyi, Frank K. Tittel, Rice Univ.,USA.*
A novel difference-frequency mixing architecture for coherent generation of tunable mid-infrared light is reported. Two CW single-frequency diode laser pump sources operating at 1.56 and 0.98 microns were mixed in a periodically poled $LiNbO_3$ crystal and generated 0.25 mW of tunable mid-infrared light at 2.64 microns. The performance of this new source was demonstrated by the spectroscopic detection of HF and water isotopes $H_2^{16,17,18}O$ and $HD^{16}O$ at various reduced pressures. Using direct absorption spectroscopy, a peak-to-peak noise equivalent absorbance of ~1E-4 was observed (0.6 s integration time), corresponding to a HF detection sensitivity of 12 ppb.m at a sampling pressure of 50 Torr.

ThD4   5:20pm
Towards a practical theory of polarisation spectroscopy, *J. Walewski, Lund Inst. of Tech., Sweden; C.F. Kaminski, Univ. of Cambridge, UK; S.F. Hanna, R.P. Lucht, Texas A&M Univ., USA.*
We present a simple phenomenological theory of polarisation spectroscopy and apply it in an assessing fashion to measurements and detailed theoretical calculations. Our model serves also to interpret polarisation spectroscopy measurements of relative OH concentrations.

Room: Century
8:00am–10:00am
FA ■ Laser Induced Breakdown Spectroscopy (LIBS)
Kevin L. McNesby, U.S. Army Res. Lab., USA, Presider

FA1   8:00am   (Invited)
Recent progress in the science and technology of LIBS, *Andrzej W. Miziolek, US Army Res. Lab., USA.*
Abstract not available.

FA2   8:40am
From hot ellipsoid to colder torus: Structure and temperature changes of laser induced plasmas, *K. Hutchison, L. Hüwel, M. Kubitzki, M. Longenecker, K. Rowold, Wesleyan Univ. USA; L. Cadwell, Providence College, USA.*
Using time resolved emission spectroscopy we have recorded changes in both shape and spectral content of the light emitting region of laser generated sparks in argon during the first 100 microseconds after the laser pulse.

FA3   9:00am
Laser induced breakdown spectroscopy of liquid and solid samples in the presence of magnetic field, *Virendra N. Rai, CAT, India; Awadhesha K. Rai, Univ. of Agriculture and Tech., India; Fang Yu Yueh, Jagdish P. Singh, Mississippi State Univ., USA.* The emission properties of laser-produced plasma in the presence of magnetic field from liquid as well as solid samples have been presented. It was found that emission intensity increases by 1.5 - 2 times. This enhancement was due to an increase in the rate of recombination of plasma.

FA4   9:20am
Rapid field screening of soils for heavy metals with spark-induced breakdown spectroscopy (SIBS), *Richard T. Wainner, Amy J.R. Hunter, Physical Sciences Inc., USA.*
Spark-induced breakdown spectroscopy (SIBS) is a new technique that has evolved from the growing field of LIBS. Here we apply portable SIBS technology to the ideally-suited task of detecting small concentrations (10 ppm) of heavy metals in soils.

FA5   9:40am
Laser induced breakdown spectroscopy of nineteenth century daguerreotypes, *John C. Miller, Oak Ridge Natl. Lab., USA; D. Anglos, Foundation for Res. and Tech., Greece.*
Laser-induced breakdown spectroscopy (LIBS) has been applied for the first time to 150-year old daguerreotypes, as a prelude to laser ablation cleaning of tarnished examples.

Room: Century
10:40am–12:20pm
FB ■ Combustion II
Jae Won Hahn, Korea Res. Inst. of Standards, South Korea, Presider

FB1   10:40am   (Invited)
Using picosecond pulses for gas-phase laser diagnostics, *T.B. Settersten, Sandia Natl. Labs., USA.*
This work provides an introduction to picosecond laser diagnostics. The temporal and spectral characteristics of picosecond pulses, modeling of their interactions with molecules, and examples of gas-phase diagnostic applications are described.

FB2   11:20am
Energy transfer in OH, CH, and NO: implications for quantitative LIF measurements, *A. Buelter, U. Lenhard, U. Rahmann, A. Brockhinke, Univ. Bielefeld, Germany.*
Collision-induced processes (quenching, rotational and vibrational energy transfer, polarization scrambling) affect most LIF experiments. For OH, CH and NO, these processes are studied with picosecond resolution. Methods to obtain quench-free data and implications for flame measurements are discussed.

FB3   11:40am
Predictions of chemical species via diode laser spectroscopy, *Shin-Juh Chen, Joel A. Silver, Southwest Sciences, Inc.; Werner J.A. Dahm, Univ. of Michigan; Nancy D. Piltch, NASA Glenn Research Ctr., USA.*
A technique to predict temperature and chemical species in flames from absorbance measurement of one chemical species is presented. Predicted temperature and mole fractions of methane and water agreed well with measured and published results.

FB4   12:00pm
Strategies for NO laser-induced fluorescence in methane/air flames at pressures between 1 and 60 bar, *Wolfgang G. Bessler, Christof Schulz, Univ. Heidelberg, Germany; Dong-Ill Shin, Tonghun Lee, Jay B. Jeffries, Ronald K. Hanson, Stanford Univ., USA.*
Measurements in laminar premixed methane/air flames at pressures between 1 and 60 bar are used here to compare strategies for NO LIF detection exciting selected transitions in the A-X (0,0), (0,1), and (0,2) bands.

FC ■ Combustion III

Jae Won Hahn, Korea Res. Inst. of Standards, South Korea, Presider

FC1 2:00pm
Investigations on laser-Induced Incandescence (LII) for soot diagnostics at high pressure, *Max Hofmann, Wolfgang G. Bessler, Joachim Gronki, Christof Schulz, Heidelberg Univ., Germany; Helga Jander, Göttingen Univ., Germany.*
LII has been investigated in sooting ethylene/air flames at 1 - 15 bar with wavelength-, energy-density- and time-resolved detection. LII decay coefficients increase linearly with pressure. Pressure influence on the LII intensity is limited with prompt detection.

FC2 2:20pm
Temperature-dependent absorption by CO_2: Implications for UV diagnostics in high-temperature flames, *Christof Schulz, Joachim Gronki, Heidelberg Univ., Germany; Jon D. Koch, David F. Davidson, Jay B. Jeffries, Ronald K. Hanson, Stanford Univ., USA.*
Absorption spectra of hot (900 - 3050 K) CO_2 have been measured at 190 - 320 nm. A parameter set allows the calculation of absorption cross sections relevant for laser diagnostic in combustion processes.

FC3 2:40pm
In-situ flame measurements of NO and CO using mid-IR QC lasers, *Shawn D. Wehe, David M. Sonnenfroh, Mark G. Allen, Physical Sciences Inc., USA; Claire Gmachl, Frederico Capasso, Lucent Tech., USA.*
Room-temperature Quantum Cascade Lasers (QCL) allow high-sensitivity measurements of trace gas absorption in the 4.6-11 micron wavelength region. Important combustion generated pollutants such as CO and NO exhibit strong fundamental absorption bands in this region and sub-ppm detection limits are projected. the paper will present initial results for both species obtained in a laboratory flat-flame burner.

FD - Cavity Ringdown Spectroscopy (CRDS)

Mark A. Linne, Colorado School of Mines, USA, Presider

FD1 3:00pm
Development of an enhanced cavity absorption sensor for air monitoring, *A.R. Awtry, M.E. Moses, J.H. Miller, The George Washington Univ., USA.*
The progress on the development of a sensor for the detection of ambient levels of a set of air contaminants is reported. A 1.55 mm external-cavity tunable diode laser is used as a light source that can be incorporated into either Integrated Cavity Output Spectroscopy (ICOS) or cw-Cavity Ringdown Spectroscopy (cw-CRDS). Both techniques exploit the sensitivity enhancements provided by the long effective pathlength from the optical cavity created between two mirrors. Initial experiments of ICOS and cw-CRDS have been performed to determine the sensitivity, selectivity, and reproducibility of this method. In the continuing work, the sensitivity of cw-CRDS will be compared with ICOS to determine which method holds greater promise for a practical sensor.

FD2 3:20pm
Theoretical model analysis of the dynamic saturation in cavity ringdown spectroscopy, *Jae Yong Lee, Jae Won Hahn, Korea Res. Inst. of Standards and Science, Korea.*
Transient saturation in cavity ringdown spectroscopy is theoretically modeled with coupled rate equations accounting for the dynamics of intracavity photons and absorber population, which permits a recipe for retrieving original spectra in the saturation regime.

FD3 3:40pm
Sensitive absorption measurements based on novel cavity enhanced spectroscopy techniques, *Doug Baer, Manish Gupta, Anthony O'Keefe, Joshua Paul, Los Gatos Res., USA.*
A novel absorption diagnostic technique based on off-axis paths in high-finesse optical cavities using near-infrared and mid-infrared lasers provides extremely high sensitivities. Applications to environmental monitoring and industrial process control will be presented.

FE ■ Plenary Session

Mark A. Linne, Colorado School of Mines, USA, Presider

FE1 4:40pm (Plenary)
Cavity ring-down spectroscopy: An overview, *Richard N. Zare, Stanford Univ., USA.*
Cavity ring-down spectroscopy (CRDS) permits absorption measurements to be made with an increase of several orders of magnitude in sensitivity over more traditonal approaches. Novel applications to gases, plasmas, liquids, and solids will be presented.

■ Saturday
■ February 9, 2002

Room: Century
8:00am–10:00am
SaA ■ Instrumentation I
Alfredo E. Bruno, Novartis Pharma AG, Switzerland, Presider

SaA1   8:00am   (Invited)
Microoptics for laser applications, *Hanz Pere Herzig, Univ. of Neuchatel, Switzerland.*
Abstract not available.

SaA2   8:40am
Tunable semiconductor laser spectroscopy in hollow optical waveguides, *G.J. Fetzer, A.S. Pittner, Arete Assoc., USA.*
A spectrometer based on tunable semiconductor lasers and hollow optical waveguides is discussed. Results are presented that characterize the function of the spectrometer in terms of sensitivity, response time, species cross interference and stability.

SaA3   9:00am
Development of a CMOS active-pixel phase-sensitive detector imaging array, *R. Swartzendruber, S. Sedarsky, N. Middleton, M. Linne, Colorado School of Mines, USA.*
We describe the development of a new imaging array that performs phase-sensitive detection signal processing at the chip level, at each pixel. It is predicted to detect 10-5 modulation depth at 1,000 frames/sec.

SaA4   9:20am
Microphotonic laser-based sensors for the rapid detection of approach to lower explosion limit for hydrocarbon vapors, *Kevin L. McNesby, Andrzej W. Miziolek, Army Res. Lab., USA.*
Microphotonic sensors for rapid (10 msec) measurement of vapors from hydrocarbon fuels JP-8, DF-2, and gasoline are discussed. Sensors systems include dual wavelength NIR systems, Fourier transform-based systems, and Mid-IR (interband cascade) systems.

SaA5   9:40am
Fractionation of aerosol particles produced by laser ablation in ICP-MS analysis, *J. Koch, L. Feldmann, N. Jakubowski, K. Niemax, Inst. of Spectrochemistry and Applied Spectroscopy, Germany.*
The element composition of aerosol particles produced by laser ablation of brass and steel in Ar and He and deposited on the wall of the transport tube to an ICP have been measured. Depending on the experimental parameters and the matrix, the element composition of the aerosol particles deviated from the stoichiometric element ratios of the bulk and varied along the tube.

Room: Century
10:40am–12:20pm
SaB ■ Diode Lasers and Applications I
Douglas S. Baer, Los Gatos Res., USA, Presider

SaB1   10:40am
Analysis by diode laser absorption spectroscopy in a linear dielectric barrier discharge, *K. Kunze, M. Miclea, J. Franzke, K. Niemax Inst. of Spectrochemistry and Applied Spectroscopy, Germany; C. Vadla, Inst. of Physics, Croatia.*
The diagnostic as well as the application of a miniaturized dielectric barrier discharge as detector for analytical spectrometry were investigated using diode laser absorption spectrometry of the excited species produced in the plasma.

SaB2   11:00am
Sculpted tone burst modulation spectroscopy, *Chris Hovde, Southwest Sciences, Inc., USA.*
By manipulating the amplitude modulation waveform for tone burst spectroscopy, the response of a tunable diode laser spectrometer can be tailored to avoid the effects of many interference fringes that otherwise limit sensitivity.

SaB3   11:20am
Wavelength agile external cavity diode laser for trace gas detection, *Jeffrey S. Pilgrim, Southwest Sciences, Inc.*
We have developed an external cavity diode laser that is wavelength modulated with injection current. The laser has broad spectral coverage and is inexpensive. We have obtained a minimum detectable absorbance of 5E-05.

SaB4   11:40am
Evanescent-field laser sensor for in-situ monitoring of volcano gas emissions, *Ulrike Willer, Irina Kostjucenko, Christian Bohling, Thomas Zentgraf, Dirk Scheel, Wolfgang Schade, Tech. Univ. Clausthal, Germany.*
A DFB laser diode (1.57 µm) is guided through a pure core fused silica fiber. Tuning the laser frequency across molecular resonances will change the frustrated (FTR) and the attenuated total reflection (ATR). Such an evanescent-field laser sensor is used for in-situ monitoring of H_2S in volcano gases at the site "Solfatara" (Italy).

SaB5   12:00pm
Spectroscopic trace gas detection with pulsed quantum cascade lasers, *Anatoliy A. Kosterev, Frank K. Tittel, Rice Univ., USA; Shawn Wehe, David M. Sonnenfroh, Mark G. Allen, Physical Sciences Inc., USA; Rudeger Kohler, Claire Gmachl, Federico Capasso, Deborah L. Sivco, Alfred Y. Cho, Lucent Tech., USA.*
Pulsed quantum cascade lasers operating at wavelength of 10 and 4.6 microns were used for detection of ammonia and carbon monoxide, respectively. Variations of atmospheric CO concentration were continuously monitored with 12 ppbv precision using a 1 m optical pathlength.

SaC ■ Poster Session

SaC1
Corrections for quantitative NO concentration measurements using time-resolved picosecond laser-induced fluorescence, *J.J. Driscoll, V. Sick, Univ. of Michigan USA; R.L. Farrow, P.E. Schrader, Sandia Natl. Labs, USA.*

The corrections necessary to obtain nitric oxide mole fractions from picosecond laser-induced fluorescence signals are outlined.

SaC2
Optimization of the mode matching in pulsed cavity ringdown spectroscopy, *Dong-Hoon Lee, Youngjee Yoon, Bongsoo Kim, Korea Advanced Inst. of Science and Tech., Korea; Jae Yong Lee, Yong Shim Yoo, Jae Won Hahn, Korea Res. Inst. of Standards and Science, Korea.*

A simple and reliable method is presented for optimizing the mode matching of pulsed cavity-ringdown spectroscopy (CRDS). The method is based on monitoring the non-degenerate transversal mode beating induced by beam clipping and slight cavity misalignment.

SaC3
Spatial-domain cavity ringdown: A potential toward broadband cavity ringdown spectroscopy, *Jae Yong Lee, Yong Shim Yoo, Jae Won Hahn, Korea Res. Inst. of Standards and Science, Korea.*

We propose and demonstrate the idea of spatial-domain cavity ringdown (CRD) technique. The feasibility of the new concept toward broadband CRD implementation is supported by a firm theoretical background and a preliminary experiment.

SaC4
Real-time ground level atmospheric nitric oxide measured by calibrated TDLAS system, *Adam Mock, Columbia Univ., USA; Chad Roller, Jim Jeffers, Khosrow Namjou, Ekips Tech., USA; Patrick J. McCann, Joe Grego, Univ. of Oklahoma, USA.*

A calibrated TDLAS system was used to measure real-time ground level atmospheric NO levels near a busy suburban street. A sample atmospheric NO concentration trend diagram from midday is presented.

SaC5
Maximum-likelihood estimation of model parameters for experiments with pulsed lasers, *Thomas Metz, Joachim Walewski, Lund Inst. of Tech., Sweden; Clemens F. Kaminski, Univ. of Cambridge, UK.*

A fitting method is presented for evaluation of non-linear spectroscopy experiments. Correct treatment of laser intensity fluctuations increases the accuracy and precision and avoids significantly wrong results. The method is compared to common fitting schemes.

SaC6
Detection of conformational changes in proteins with FRET, *R. Plessow, K. Lotte, A. Brockhinke, Univ. Bielefeld, Germany.*

Foerster resonance energy transfer (FRET) is detected using a combination of two techniques: picosecond time-resolved LIF and excitation-emission spectroscopy. This allows the quantitative determination of distances within and in between proteins.

Room: Century
8:00am–10:00am
SuA ■ Instrumentation II
Richard M. Williams, Pacific Northwest Natl. Lab., USA, Presider

SuA1   8:00am   (Invited)
Miniaturized QC and TDL laser spectrometers for biogenic gases and isotope ratios on Mars, Titan, and Venus, *Christopher R. Webster, Jet Propulsion Lab., USA.*
QC lasers have been flown in Earth's stratosphere, making the first atmospheric measurements, and are now incorporated into miniature tunable laser spectrometers for biogenic gases and isotope ratios as biosignatures on Mars and other planets.

SuA2   8:40am
UV laser induced fluorescence portable system for the detection of plastic and organic compounds in water, *Vasanthi Sivaprakasam, Dennis K. Killinger, Univ. of South Florida, USA.*
A 266 nm Laser Induced Fluorescence system that is 1000 times more sensitive than existing in situ fluorescence sensors has been developed and tested for the detection of plastics and organics in water.

SuA3   9:00am
Design of a line-scanned handheld imager for detecting natural gas leaks, *R.P. Bambha, T.A Reichardt, T.J. Kulp, R.L. Schmitt, Sandia Natl. Labs., USA.*
An active infrared imager capable of both single- and differential-frequency detection of methane is being developed for handheld operation. The device will be capable of producing real-time video images of methane plumes.

SuA4   9:20am
Development and evaluation of a portable gas imager using a fiber-amplifier-pumped PPLN OPO illuminator, *Thomas J. Kulp, Karla M. Armstrong, Ricky Sommers, Dahv A.V. Kliner, Uta-Barbara Goers, Sal Birtola, Sandia Natl. Labs.,USA; Lew Goldberg, Jeffrey P. Koplow, Sean Moore, Naval Res. Lab., USA; Thomas G. McRae, Laser Imaging Systems, USA.*
Active imaging allows real-time video imaging of gases through their attenuation of backscattered laser radiation. We describe the development and testing of a portable gas imager that employs a fiber-amplifier-pumped PPLN OPO as its illuminator.

SuA5   9:40am
Ultra-sensitive ammonia detection for industrial applications using photoacoustic spectroscopy, *Michael E. Webber, Michael B. Pushkarsky, Ohan Baghdassarian, L. Ravi Narasimhan, C. Kumar N. Patel, Pranalytica, Inc., USA.*
An industrial trace-ammonia sensor based on photoacoustic spectroscopy and CO_2 lasers has been developed with a minimum detectivity in the parts-per-billion range. This sensor is capable of making simultaneous measurements of up to twenty gas samples with an optically multiplexed arrangement of optoacoustic cells.

Room: Century
10:40am–12:20pm
SuB ■ Diode Lasers and Applications II
Juan-Carlos Rolon, Ecole Centrale Paris, France, Presider

SuB1   10:40am
Rubust external cavity diode laser (ECDL) with implemented antireflection coated blue laserdiodes and their performance in atom absorption spectroscopy, *Lars Hildebrandt, Joachim Sacher, Richard Knispel, Sacher Lasertechnik Group, Germany.*
For the first time we present antireflection coated "blue" laserdiodes and their performance in Littrow and Littman ECDL. The relevance of the achieved progress in ECDL technology for construction of ECDL-based sensor systems for in-situ analysis is discussed.

SuB2   11:00am
Wavelength-agile diode laser sensors for monitoring gas properties in harsh environments, *Scott T. Sanders, Jay B. Jeffries, Jian Wang, Ronald K. Hanson, Stanford Univ., USA.*
Extended wavelength tuning of diode lasers enable the extension of scanned wavelength absorption techniques to transient, high pressure, hostile environments. Examples using frequency agile VCSELs and new wavelength tuning strategies are presented.

SuB3   11:20am
Low cost, low power diode laser sensing: A weather balloon hygrometer, *Mark E. Paige, Southwest Sciences, Inc., USA.*
An inexpensive diode laser hygrometer is described. The engineering advances of this system greatly increase the applicability of diode laser sensors for commercial sensing applications.

SuB4   11:40am
A Near-IR TDL-based sensor for eddy covariance flux measurements of CO_2, *David Sonnenfroh, Mark Allen, Physical Sciences Inc., USA; Gerry Livingston, Univ. of Vermont, USA.*
We describe some of the design considerations for a near-IR TDL-based sensor for eddy covariance flux measurements of CO_2 and H_2O. Initial data from recent field trials will be discussed.

SuB5   12:00pm
External cavity diode laser based on a transmission grating, *Toni Laurila, Timo Joutsenoja, Rolf Hernberg, Tampere Univ. of Tech., Finland; Markku Kuittinen, Univ. of Joensuu, Finland.*
Design and characterization of an external cavity diode laser at 650 nm based on a transmission grating is described. The transmission grating enables compact design and removes the beam direction variation during the wavelength tuning.

Biological or Biomedical I

Thursday, February 7, 2002

Michael Barnes, Oak Ridge Natl. Lab., USA
Presider

ThA
8:20am–10:00am
Flagstaff

Abstract not available

Author: Sunney Xie, Harvard Univ., USA
Title: New advances in optical microscopy of biological systems

Single Molecule Fluorescence Correlation Spectroscopy in an Electrophoretic Mobility Shift Assay

Dale J. LeCaptain[†] and <u>Alan Van Orden</u>[‡]

[†]Department of Chemistry, Central Michigan University, Mt. Pleasant, MI 48859 [‡]Department of [‡]Chemistry, Colorado State University, Ft. Collins, CO 80523

ABSTRACT

A capillary electrophoresis-based electrophoretic mobility shift assay is described wherein fluorescence correlation spectroscopy is used to resolve the bound and unbound fractions of a DNA-protein complex on the basis of their characteristic electrophoretic flow velocities.

INTRODUCTION

Fluorescence correlation spectroscopy (FCS) has recently emerged as a powerful alternative to methods based on immobilization, extraction, separation, etc. for the characterization of ligand-receptor binding in biomolecular systems.[1] In FCS, the fluorescence from a femtoliter sized volume element of an aqueous solution of the analyte, defined by the focal region of a tightly focused excitation laser beam, is monitored as a function of time. Fluctuations in the fluorescence intensity arise due to fluorescence emission from individual molecules passing through the excitation volume one at a time due to Brownian motion and/or uniform flow. Autocorrelation analysis of these intensity fluctuations can yield diffusion coefficients[1] and/or flow velocities[2,3] for the analyte molecules under study. A key advantage to FCS in the study of ligand-receptor binding lies in its ability to determine the binding ratios *in situ* without the need to separate the bound from the unbound complexes or immobilize the receptor molecules on a surface. This greatly enhances the speed and simplicity of the analysis. At nanomolar concentration levels, several hundred analyte molecules pass through the excitation volume per second, such that the autocorrelation analysis can be completed after only a few seconds of data acquisition time. Furthermore, FCS possesses unrivaled sensitivity and is routinely applied to systems in which the analyte molecules are present at picomolar concentration levels, or less. However, a hindrance to the more widespread use of diffusional FCS in ligand-receptor binding studies is that the relative concentrations of bound and unbound complexes can only be determined if their lateral diffusion coefficients, D, differ by at least a factor of ~2.[4] This corresponds to at least an ~8-fold increase in the molecular mass upon binding of the ligand to the receptor, due to the dependence of the molecular mass on the diffusion coefficient of $\sim D^{-3}$.

Recently, it was demonstrated that FCS could be used to determine the electrophoretic flow velocities of charged species flowing through a capillary electrophoresis (CE) system, using a technique referred to as CE/FCS, thus combining the speed and sensitivity of FCS with the selectivity of CE.[5] Since the electrophoretic flow velocity is directly proportional to the charge-to-mass ratio, the autocorrelation times determined by CE/FCS are potentially much more sensitive to molecular mass differences than those obtained by diffusional FCS. The analysis is carried out on analyte solutions continuously flowing through the electrophoresis capillary and does not require sample plug injection or separation of the analytes. This paper describes our efforts to use CE/FCS in an EMSA analysis of a DNA-protein complex. Single-stranded DNA binding protein (SSB) from *Escherichia coli* and fluorescently labeled 39-mer single-stranded DNA (ssDNA) were chosen as the model system.

EXPERIMENTAL SECTION

Figure 1 displays a schematic diagram of the CE/FCS experiment. ssDNA/SSB solutions were flowed continuously through a 20-cm long fused silica capillary (Polymicro Technologies, Phoenix, AZ) by pressurizing the capillary inlet with N_2. +15 kV were applied between the inlet and the outlet of the capillary by means of platinum electrodes connected to a high voltage power supply (Spellman, Model

CZE1000R, Plainview, NY). FCS measurements were performed using a home-built single molecule confocal fluorescence microscope. A 0.5 mW, 514.5 nm cw laser beam generated by an air-cooled Ar-ion laser (Omnichrome/ Melles-Griot, Carlesbad, CA) was used as the excitation source for the rhodamine label attached to the ssDNA. The laser beam was expanded and collimated by a 4× telescope, prefocused by a 150 mm focal length spherical lens, and reflected by a 530 nm long pass dichroic beamsplitter (CVI Laser Corp., Albuquerque, NM) into a 100×, 1.25 NA oil immersion achromatic microscope objective (Edmund Industrial Optics, Barrington, NJ). The objective focused the excitation laser beam into the capillary through an observation window burned into the polyimide coating. Fluorescence, generated by individual analyte molecules

Figure 1. Schematic of the CE/FCS apparatus.

as they flowed through the laser focus region, was collected by the same microscope objective, directed through a 100 μm diameter pinhole positioned at the image plane of the objective, filtered by a 530 nm long pass interference filter (Chroma, Brattleboro, VT), and focused onto a single photon counting silicon avalanche photodiode detector (APD, EG&G Optoelectronics Model SPCM-AQR-14, dark count rate ~50 Hz) by an 11 mm focal length aspheric lens.
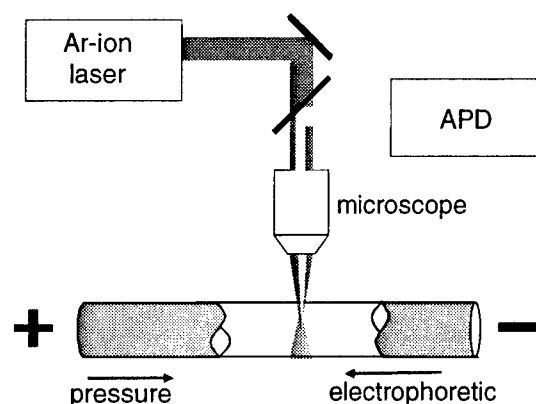
Autocorrelation analysis of the time-dependant fluorescence was performed in real time by feeding the output of the APD detector into a digital correlator card (ALV Model ALV5000/E, Langen, Germany) mounted in a Pentium computer. Photocounts from the detector were accumulated into successive time bins, with multiple sampling times per bin varying from 200 ns to tens of seconds. The normalized autocorrelation functions were calculated in real time by the digital correlator using:

$$G_C(\tau) = \frac{M\sum_{t=1}^{M} n(t)n(t+\tau) - \sum_{t=1}^{M} n(t)\sum_{t=1}^{M} n(t+\tau)}{\sum_{t=1}^{M} n(t)\sum_{t=1}^{M} n(t+\tau)}, \qquad (1)$$

where M is the total number of time bins, $n(t)$ is the number of photocounts accumulated into time bin t, and τ is the lagtime.

RESULTS AND DISCUSSION

Figure 2 displays experimental autocorrelation functions, normalized to an amplitude of one, observed for mixtures of 10 nM ssDNA and 0, 5, 10, and 20 nM SSB. Analysis times of 10-s per sample were used. The width of each curve corresponds to the average transit time of single molecules through the focal region of the excitation laser beam for each sample. The longest transit time corresponds to pure ssDNA. This is the case because the electrophoretic flow velocity of ssDNA, which is directed toward the positive electrode, opposes the pressure driven flow, resulting in a large decrease in the net flow
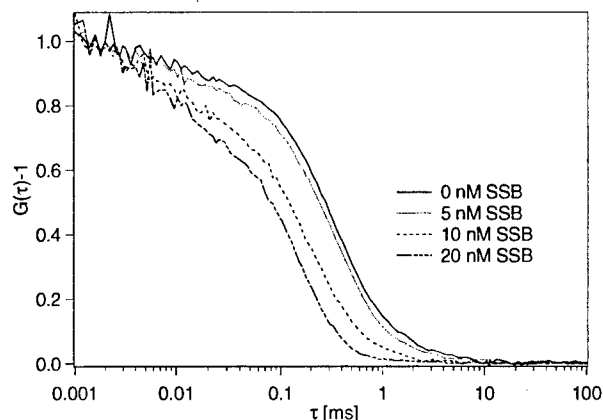

Figure 2. Normalized autocorrelation function for 10 nM ssDNA and varying concentrations of SSB.

velocity relative to the flow velocity at zero field. Binding of ssDNA to SSB reduces the electrophoretic flow velocity, which resulted in a faster net flow velocity for the bound complex. The fastest flow velocity corresponds to the 20 nM SSB sample, for which all of the ssDNA present in the solution is bound in the complex. Intermediate transit times are observed in solutions that contain a mixture of bound and unbound ssDNA. The pure component autocorrelation functions are analyzed by fitting to the equation:[2]

$$G(\tau) = 1 + \frac{1}{N}\left(\frac{1}{1+\tau/\tau_d}\right)\exp\left[-\left(\frac{\tau}{\tau_f}\right)^2\left(\frac{1}{1+\tau/\tau_d}\right)\right],$$

(2)

where N is the average number of molecules occupying the excitation region, and τ_d and τ_f are the average transit times due to diffusion and unidirection flow, respectively. Analysis of the mixtures was accomplished using a linear combination of the pure component autocorrelation functions, given by:[1]

$$G(\tau) = 1 + a[G_{DNA}(\tau) - 1] + b[G_{DNA-SSB}(\tau) - 1]$$
$$a = Q_{DNA}^2(1 - R)$$
$$b = Q_{DNA-SSB}^2 R$$

(3)

where Q_{DNA} and $Q_{DNA-SSB}$ are the fluorescence efficiencies of the free and bound complex, respectively ($Q_{DNA}/Q_{DNA=SSB} = 2.60 \pm 0.01$), R is the binding ratio ($[\text{ssDNA - SSB}]/([\text{ssDNA - SSB}] + [\text{ssDNA}])$), and $G_{DNA}(\tau)$ and $G_{DNA-SSB}(\tau)$ are the pure component autocorrelation functions for the free and bound complexes, respectively. This analysis yielded R-values of $26\pm3\%$ and $82\pm3\%$ for the 5 and 10 nM SSB solutions, respectively. These measurements are consistent with a dissociation constant (K_d) of the complex of $2._4\pm1._3$ nM, determined using $R = 0.5[\text{SSB}]/(K_d + 0.5[\text{SSB}])$.[6] The literature value for K_d of this complex is ~2 nM.[7]

REFERENCES

(1)   Widengren, J.; Rigler, R. *Cell. Mol. Biol.* **1998**, *44*, 857-879.

(2)   Magde, D.; Webb, W. W.; Elson, E. L. *Biopolymers* **1978**, *17*, 361-376.

(3)   Gösch, M.; Blom, H.; Holm, J.; Heino, T.; Rigler, R. *Anal. Chem.* **2000**, *72*, 3260-3265.

(4)   Meseth, U.; Wohland, T.; Rigler, R.; Vogel, H. *Biophys. J.* **1999**, *76*, 1619-1631.

(5)   Van Orden, A.; Keller, R. A. *Anal. Chem.* **1998**, *70*, 4463-4471;LeCaptain, D. J.; Michel, M. A.; Van Orden, A. *Analyst* **2001**, *126*, 1279-1284.

(6)   Foulds, G. J.; Etzkorn, F. A. *J. Chromatogr. A* **1999**, *862*, 231-236.

(7)   Krauss, G.; Sindermann, H.; Schomburg, U.; Maass, G. *Biochem.* **1981**, *20*, 5346-5352.

Probing single ion luminescence in rare-earth doped nanocrystals

A. Mehta, T. Thundat, and M. D. Barnes
Chemical Sciences and Life Sciences Division
Oak Ridge National Laboratory
Oak Ridge, TN 37831
e-mail: barnesmd1@ornl.gov

R. Bhargava
Nanocrystals Technologies
Briarcliff Manor, NY 10510

A. Bartko, L. Peyser, and R. M. Dickson
Georgia Institute of Technolgy
School of Chemistry and Biochemistry
Atlanta, GA 30332-0400

Abstract
We describe experiments probing single europium and terbium ions in isolated nanocrystals (2 – 15 nm diam.) using fluorescence microscopy techniques. Emission pattern imaging also shows patterns that are distinctly characteristic of single dipoles.

Nanoscale doped semiconductor and insulating particles are currently attracting a great deal of interest for both fundamental photophysics, and important applications including display and sensor technologies.[1,2] While the spectroscopy of rare-earth doped inorganic (macroscopic) crystals has been studied extensively since the mid-fifties, new synthetic techniques and effects of nanoscale confinement (for example electron-phonon, and electron-exciton interactions[Error! Bookmark not defined..3]) have motivated significant new interest in these materials. There is, however, relatively little literature on single particle imaging and spectroscopy of these species. In particular, there exists the interesting possibility of using well-known single-molecule (or single quantum dot) spectroscopy[4,5,6,7] techniques to probe single atomic species isolated in room temperature nanoenvironments.[8,9] In contrast with molecular (dye) systems, the optical transitions associated with rare-earth ions are sharp and well defined in terms of atomic eigenstates, thus possibly lending themselves to detailed theoretical analysis. However, the small saturated absorption rates ($\approx$ 1 kHz) – compared to $\approx$ 100 MHz for laser dyes – indicated by bulk or nanoparticle-ensemble fluorescence lifetime measurements for rare-earth ions might seem to preclude single-ion luminescence imaging.

Using ultrasensitive fluorescence microscopy techniques similar to those used to probe single molecules or quantum dots, we have recently been able to image luminescence from single laser-excited europium (and terbium) doped metal-oxide nanoparticles. We observed interesting luminescence dynamics such as on-off blinking, multiple discrete luminescence intensity levels (bright states), and single-step photobleaching that closely resemble familiar fluorescence properties of single molecules or quantum dots. While such behavior, in general, is not expected of multi-chromophoric systems, there are well known examples of blinking and discrete photobleaching in cases where the chromophores may interact in a way that is similar to a single quantum system.[10] Thus, these earlier observations were consistent with, but not necessarily definitive signatures of single quantum system luminescence. In this Summary, we discuss some of the highlights of recent experiments in our laboratory probing the spectroscopy and dynamics of single rare-earth ions in doped nanocrystals.

The well known optical transitions for Eu^{3+} involve spin pairing/unpairing between different 4f(6) configurations with relevant atomic terms for the ground and excited states $^7F_{4,3,2,1,0}$ and $^5D_{0,1,2}$ respectively. For transitions between $^5Dj'$ and $^7Fj''$ states where $j'' \rightarrow j' = 2, 4$, the transitions are electric dipole allowed (**E1**), while for $j'' \rightarrow j' = 0, 1, 3$ the transitions are magnetic-dipole allowed (**M1**) and consequently much weaker. We used a Nikon TE300 inverted microscope in an epi-illumination configuration with a 1.3 N.A. 100x oil immersion objective to simultaneously image the luminescence from several particles within a 15-μm diameter field of view. A long-pass filter with 10% cut-on at 570 nm was used to reject background scattering, and a narrow band laser line filter was used in the beam path to reject plasma emission from the excitation region. A high-speed frame transfer camera was used as a detector operating at a frame rate of 5 – 10 Hz with a 90% quantum efficiency at 600 nm. For size correlated measurements, a modified Digital Instruments Bioscope atomic force microscope was used where the cantilever-laser beam position registration was achieved by centering a 2-μm pinhole on the focused laser beam spot, then scanning the surface with the AFM.

Figure 1 shows a partial linescan (integrated luminescence intensity as a function of time) obtained from a 13.1 nm $Eu^{3+}:Y_2O_3$ particle. Several discrete intensity levels are observed, with a noticeable change in the dynamics between the start and the end of the run. At early times, the emission appears as intense sharp spikes, and at later times, the emission appears more stable. This suggests some structural change in the particle – likely induced by thermal effects – during the observation time. It was suggested in earlier work

Figure 1. Integrated intensity as a function of time (3x3 pixel bin) from a 13.1 nm $Eu^{3+}:Y_2O_3$ nanoparticle.

that the different bright states originated from local symmetry/transition moment orientation fluctuations induced by thermal excitation in the crystal. To test this idea, we used emission pattern imaging techniques developed by Dickson and co-workers[11] to probe the chromophore orientation in the crystal. Figure 2 shows examples of emission patterns taken from different $Eu^{3+}:Y_2O_3$ nanoparticles that show both on-off blinking and dipolar emission patterns. Single chromophores at a dielectric boundary exhibit emission patterns that are uniquely indicative of molecular orientation, differing greatly from that of an isotropic Gaussian source. The measured patterns from a single chromophore derive from a combination of transition moment orientation and coupling to the high-index substrate. Near the coverslip-air dielectric boundary, most of the emitted molecular fluorescence (≈80%) is coupled into the glass at orientation-specific angles, instead of isotropically into the air above the coverslip. This effect is most prominent for dipoles oriented along the optic axis; however, dipoles perpendicular to the optic axis also exhibit enhanced angle-specific coupling into the glass coverslip.[12]

The observation of dipolar emission patterns, combined with other signatures such as blinking and discrete photobleaching, provide strong evidence of single-ion luminescence. These distinct dipolar emission patterns cannot be observed for multichromophoric systems without a high degree of alignment and nanometer proximity. A polarization analysis of emission from particles displaying such dipolar patterns shows that the emission is linearly polarized, again
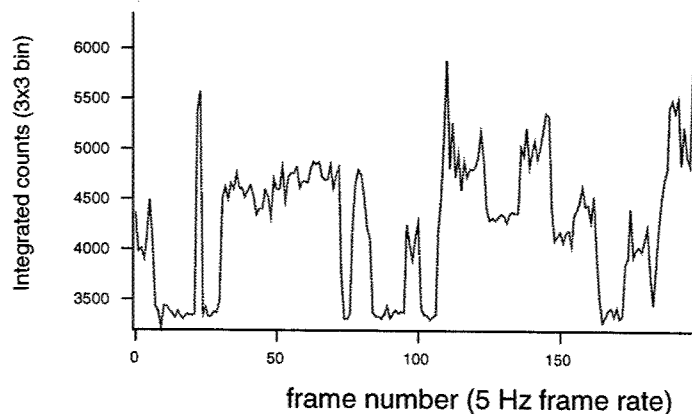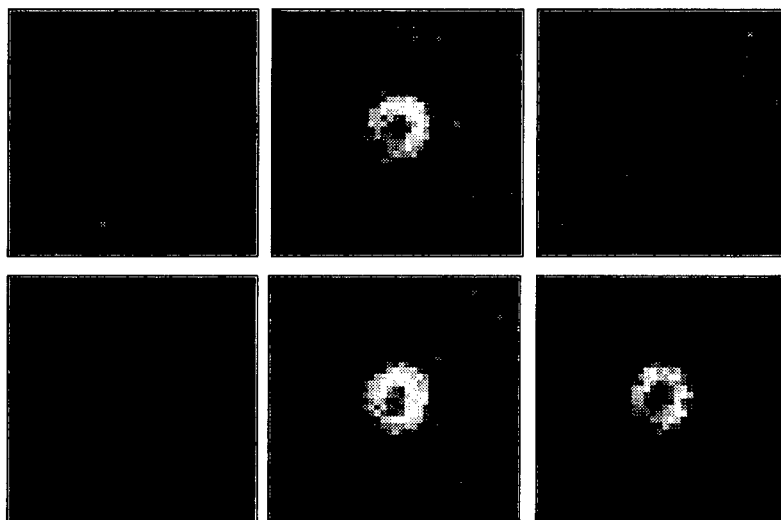
Figure 2. Frame sequence from a single z-oriented ion showing on-off blinking. The integrated luminescence signal in frames 2, 5 and 6 are 1784, 2094, and 2917 counts respectively. Exposure time was 1 second.

consistent with a single-quantum system. Intensity jumps (transitions between different bright states) are not correlated with changes in transition moment orientation as might be expected from a model of local symmetry fluctuations. Current work in our laboratory is designed to understand more fully the nature of the novel luminescence dynamics of doped nanoparticles. Experiments on different dopant ions and excitation wavelengths suggest that the blinking and different bright- states is related to absorption dynamics, consistent with results obtained from emission pattern imaging. If the access and persistence time of the different intensity levels can be controlled, a number of possible applications can be envisioned in nanophotonics, bio-molecular tagging, and optical memory.

REFERENCES
[1] F. Parsapour, D. F. Kelley, and R. S. Williams J. Phys. Chem. B **102**, 7971 (1998).
[2] D. K. Williams, B. Bihari, B. M. Tissue, and J. M. McHale, J. Phys. Chem. B **102**, 916 (1998).
[3] W. Chen, J-O. Malm, V. Zwiller, R. Wallenberg, and J-O. Bovin, J. Appl. Phys. **89**, 2671 (2001).
[4] R. M. Dickson, A. B. Cubitt, R. Y. Tsien, and W. E. Moerner, Nature **388**, 355 (1997).
[5] J. J. Macklin, J. K. Trautman, T. D. Harris, and L. E. Brus, Science **272**, 255 (1996).
[6] X. S. Xie, Acc. Chem. Res. **29**, 598 (1996).
[7] M. Nirmal, B. O. Dabbousi, M. G. Bawendi, J. J. Macklin, J. K. Trautman, T. D. Harris, and L. E. Brus, Nature **383**, 802 (1996).
[8] M. D. Barnes, A. Mehta, T. Thundat, R. N. Bhargava, V. Chhabra, and B. Kulkarni, J. Phys. Chem. B **104**, 6099 (2000).
[9] R. Rodrigues-Herzog, F. trotta, H. Bill, J-M. Segura, B. Hecht, H-J. Guntherodt, Phys. Rev. B 62, 11163 (2000).
[10] D. Hu, J. Yu, B. Bagchi, P. J. Rossky, and P. F. Barbara Nature **405**, 1030 (2000).
[11] A. P. Bartko and R. M. Dickson, J. Phys. Chem. B **103**, 11237 (1999).
[12] E. H. Helen, and D. Axelrod, J. Opt. Soc. Am. B **4**, 337 (1987).

Second harmonic generation technique for monitoring of thermo- induced processes in biotussue

A. Lalayan, E. Janunts

Yerevan State University, Physics Department, A.Manoogian 1,Yerevan, 375025, Armenia
E-mail: alalayan@www.physdep.r.am

Abstract: Second harmonic generation in collagen contained animal biotissue under picosecond laser irradiation have been studied during conventional and laser heating. Experimental comparison of second harmonic generation and two-photon fluorescence nonlinear optical phenomena has been performed in ordered native tissue.
©2001 Optical Society of America
OCIS codes: (170.4580) Optical diagnostics for medicine; (190.4710) Optical nonlinearities in organic materials

1. Introduction

The knowledge of the peculiarities of nonlinear optical phenomena in different types of tissue is important for the development of the new techniques for optical biodiagnostics. The latest researches demonstrated the new unique possibilities for investigations and practitioners in biomedicine by applying the nonlinear optical methods.

R. Alfano et al. [1] and our team [2] demonstrated that frequency doubling (FD) nonlinear optical phenomenon occurs in biotissue irradiated by short duration laser pulses. In work [3] has been shown that magnitude of FD depends on amount of collagen in tissue. Kim et al. [4] reported frequency doubling and tripling of ultrashort –pulse- laser radiation in biological tissues. R. Alfano et al. [5] demonstrated second harmonic tomography technique which was used to evaluate the subsurface layer structure of mucosal tissues using femtosecond laser technology.

2. Results and discussion

In this work FD signal dependence on heating as well as polarization properties have been studied in native tissue under the picosecond laser irradiation (1064nm, 100 MW/cm^2, 30 ps).

The FD signal was registered in the reflection scheme and also for thin samples in the pass scheme. Effectiveness of FD has been correlated with the amount of the collagen molecules, which form the oriented longitudinal birefringence macrostructure in the animal and human tissues. Sizes of these native molecular crystals reach 7x40 microns that are in order of coherence length of FD process and allows to observe effective FD signal. In the different
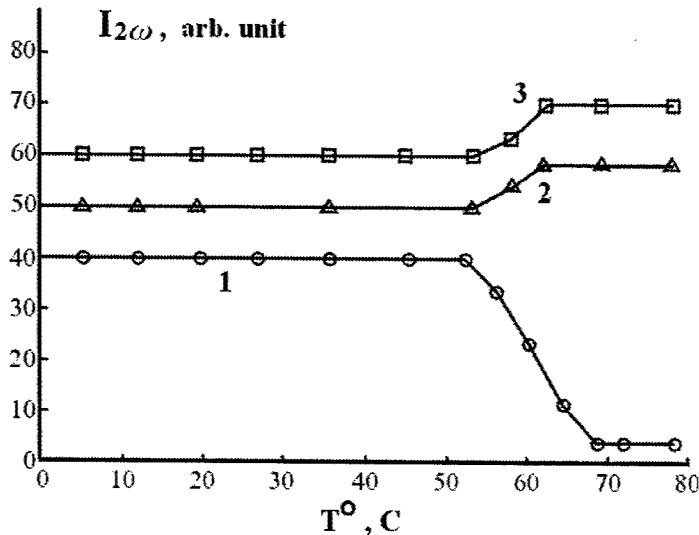

Fig.1. Dependence of intensity of FD signal (curve 1) on heating of tendon sample. Curves 2 and 3 represent changing in amplitude of control beam with wavelengths 1064 and 532 nm correspondingly due to changing of scattering.

investigated samples the FD radiation was more effectively generated in tissue, contained the higher amount of collagen, in particularly, cartilage, tendon, fasciae (about 60-70 %). In the case of nanosecond irradiation, when irradiation intensity is decreased in about three orders but the conditions of registration scheme and energy density are remain the same, FD was not observed. In this case, the effective formation of the plasma with emission spectral lines of the Ca, Na, Ca ions, etc. was registered.

We have investigated influence of heating on intensity of FD signal (see Fig1). The tissue sample was located in water contained thermo-regulated box. The sample was strongly mechanically fixed to avoid the sample distortion under heating process. During heating of collagen contained different types of tissue (excepting bone tissues) the FD radiation was decreased more than 30 times at temperature interval 59-64^{0}C, which is corresponded to spiral - coil transitions of collagen, and not recovered after cooling.

It means, that the method of SHG allow to monitor of the conformational changes of collagen molecules during heating process in real time. The same conformational changes were observed during the laser heating of tissue samples under 200mW microsecond Er: YAG laser irradiation.

Polarization dependence of FD has been studying by comparison with another two-photon process - two-photon fluorescence (TPF) in ordered tissue. Both TPF and FD nonlinear optical phenomena were observed simultaneously in samples of tendon tissue with the thickness of 0.5 mm formed by parallel collagen fibers (see Fig2). For excitation of TFP with signal level in order of FD the samples were colored by Rh6G dye. The colored samples were irradiated by linear polarized beam in the direction, which was perpendicular to biofibers.
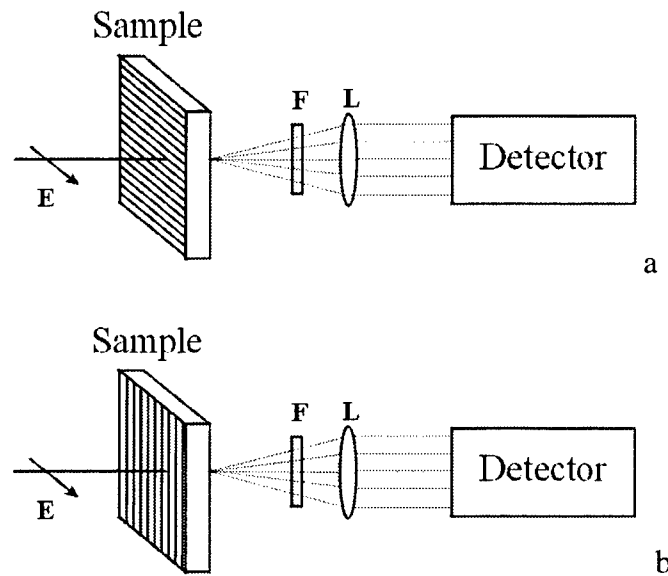
Fig. 2. Experimental scheme to study FD in ordered tissue, here F is spectral filter, L is collimated lens. Two cases have been considered: a) polarization of laser beam was parallel to collagen fibers b) polarization of laser beam was perpendicular to collagen fibers.

FD and TPF exhibit the different polarization dependence. Magnitude of SHG signal was about 2.5 times larger in case when polarization of laser beam was parallel to collagen fibers (Fig. 2a) than in perpendicular case (Fig. 2b). To reveal the dependence of the observed phenomenon on pump laser beam scattering, the attenuation of control weak beam intensity after the passing through the same sample was measured. The study shows that the intensity of the passed beam was 4.9 times larger (low scattering) at parallel polarization than at perpendicular (strong scattering). In contrast to SHG the TPF signal did not show any dependence from the direction of polarization. Since TPF and SHG processes occurs at the same time and both quadratically depend on intensity, the changing of irradiation intensity due to scattering will have the same impact on both these processes. Hence strong polarization dependence of SHG can only be explained by generation of SH in phase matching condition.

3. Conclusions

Obtained results shows, that the SHG nonlinear phenomenon gives unique possibility to monitor the conformational changes of collagen molecules during laser heating process in real time. Especially important, that this technique allows to sense the initial photoinduced changes in biotissue before irreversible photodamage of tissue will be produced. Hence, development of nonlinear optical technologies as diagnostics tool will has a great importance for contemporary laser medicine.

4. References

1. Yici Guo, P. P. Ho, A. Tirksliunas, Feng Liu, R. R. Alfano, "Optical harmonic generation from animal tissues by the use of picosecond and femtosecond laser pulses", Applied Optics-OT **35**, 6810-6813 (1996)
2. Hovanessian V.A., Lalaian A.A., "Investigation of second harmonic generation peculiarities in tissues", Proc. of Int. Conference Lasers -95, 120-124 Ashtarak, (1995)
3. Hovanessian V.A., Lalaian A.A., "Second harmonic generation in biofiber-containing tissues", Proc. of Int. Conference Lasers -96, 107- 109, Portland, OR,USA, (1996)
4. Marion J.E., Kim B.M. "Medical applications of ultrashort-pulse lasers", Proc SPIE **3616**, 42-50 (1999)
5. R. R. Alfano et al., "Subsurface structure of tissues investigated by noninvasive optical second harmonic tomography", Proc SPIE **3597**, 480-482 (1999)

Notes

Combustion I

Thursday, February 7, 2002

Clemens Kaminski, Cambridge Univ., UK
Presider

ThB
10:40am–12:20pm
Flagstaff

Multidimensional and multiscalar laser diagnostics in turbulent combusting flows

Johan Hult

Division of Combustion Physics, Lund Institute of Technology, P.O. Box 118, S-22100 Lund, Sweden
Tel:+46 (0)46 2223733, Fax:+46 (0)46 2224542, E-mail: johan.hult@forbrf.lth.se

Abstract: Measurements in jet flames and engines of time resolved fuel concentration fields, simultaneous OH and velocity fields and three-dimensional soot concentrations, using a high speed laser diagnostic imaging system, are presented.
©2002 Optical Society of America
OCIS codes: (120.1740) Combustion diagnostics; (110.4190) Multiple Imaging

1. Introduction

Laser based diagnostic techniques are powerful tools for the study of turbulent flows and combustion [1]. Two-dimensional (2-d) measurements can be used to characterize a combusting flow at a single time, and by acquiring a large number of images a statistical data set can be created. However, the captured events are independent of each other and no information on the temporal evolution of the flow is gained. Time resolved 2-d measurements can be used to quantitatively reveal the evolution of large scale turbulent structures [2]. Turbulence-chemistry interactions in flames, such as flame extinction and re-ignition, which are a challenge to modern combustion research can be studied as well as the dynamics of ignition and flame propagation. In engines, cycle resolved studies of fuel injection and flame propagation are of great interest. As turbulence is an intrinsically three-dimensional phenomena, three-dimensional (3-d) measurements of scalars are highly desirable. The 3-d information is necessary to reveal the topology of turbulent flames and mixing layers [3]. Three-dimensional information is also needed for the measurement of instantaneous gradients.

For the studies presented here a laser and detector system for high speed imaging of reactive and non-reactive flows has been used [4]. The system can acquire a sequence of up to 8 images with repetition rates ranging from 100 Hz up to 100 MHz. The high performance of the system allows it to be used for a variety of laser diagnostic techniques. The high repetition rate of the system also enables three-dimensional measurements, by rapidly sweeping the laser sheet through a measurement object. In this paper three examples of multidimensional and multiscalar measurements are presented. The first is single cycle resolved fuel concentration measurements in a homogeneous charge compression ignition (HCCI) engine [5]. The second is simultaneous measurements of time resolved OH and velocity fields in a non-premixed jet flame [6], and the third is 3-d imaging of soot volume fractions in a non-premixed flame [7].

2. Experimental set-up

The laser source is a Nd:YAG laser cluster (BMI/CSF-Thomson), consisting of four individual double pulsed Nd:YAG lasers which are combined into one unit. The unit also contains optics to combine the beams from the four lasers into one beam path with minimal energy losses. By firing the individual lasers in series a rapid burst of up to eight laser pulses can be obtained, with a time separation ranging from μs to ms between pulses. The output at 532 nm can be converted to other wavelengths by using a quadrupling crystal, resulting in 266 nm radiation, or by using a dye laser, resulting in a wavelength tunable laser source.

The detector is a modified high speed camera based on eight individual 8 bit intensified CCD cameras (DRS Hadland). The image is collected by a common optical system and is then split into eight identical copies, these are relayed to the individual CCDs. By using very short exposure times and by exposing the eight cameras in series an image sequence can be captured with a separation as short as 10 ns between images.

For the high speed imaging experiments the laser beam is formed into a light sheet using a cylindrical and a spherical lens. In the intersection plane of the laser sheet in the flame the fluorescence or incandescence signals are generated. The signals are detected at right angles by the high speed camera, after appropriate spectral filtering. For fuel tracer planar laser induced fluorescence (PLIF) the frequency quadrupled Nd:YAG output (266 nm) is used, for OH PLIF the doubled output from a dye laser is used (283 nm) and for laser induced incandescence (LII) the doubled Nd:YAG output is used (532 nm).

3. Results and conclusions

High repetition rate (15 kHz) imaging of fuel concentration fields inside an HCCI engine have been performed, in an attempt to gain new understanding of the auto ignition process in this new type of engine [8]. In an HCCI engine a homogeneous mixture of air and fuel is compressed until it auto-ignites. The benefits of the HCCI engine are low emissions of nitrogen oxides and high efficiency, which results in low fuel consumption. The engine was a Scania D12 single cylinder engine, equipped with windows in the piston and in the cylinder liner to gain optical access. Ethanol was used as fuel, with acetone (10%) added as fluorescent tracer.
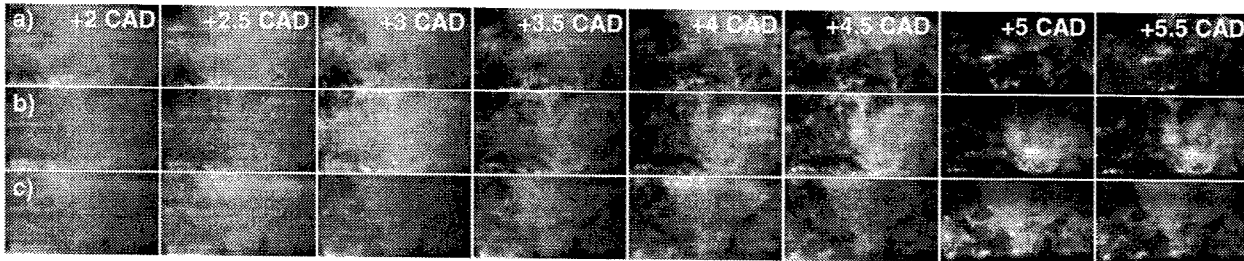

Fig. 1. Three fuel PLIF sequences recorded in an HCCI engine, corresponding to three different engine cycles. The fuel distribution in a plane in the center of the combustion chamber was imaged through the piston, the imaged region corresponds to 95×50 mm^2. The time separation between images is 69 μs.

In Figure 1 three sequences of the fuel concentration during ignition in three different cycles are shown, covering 3.5 engine crank angle degrees (CAD). The fuel tracer PLIF [9] distribution is viewed from below through the piston window. The three sequences were recorded during identical conditions, and thus illustrate the spatial cycle-to-cycle variations in the HCCI combustion process. In the first frame (+2 CAD) a homogeneous fuel distribution is seen. However, several small dark regions can be found, indicating that auto-ignition occurs at several points almost simultaneously, where local conditions are most favorable. The fuel in these regions is then gradually consumed in the following images, some regions also spread and new regions of fuel consumption appear. Cycle-to-cycle variations in the starting location of reactions, the fuel consumption speed, and also in the number of ignition kernels, are observed.
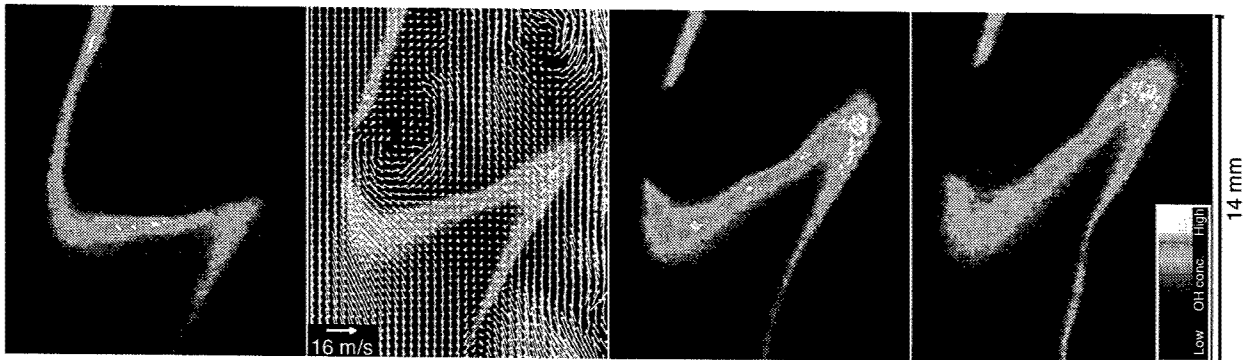
Fig. 2. A local extinction event in a non-premixed jet flame, captured using simultaneous high speed OH PLIF and PIV. The separation between the OH PLIF images corresponds to 125 μs, the velocity measurement is performed simultaneously with the second OH image, and is plotted on top of it. The imaged region corresponds to 14×16 mm, starting 18 nozzle diameters over the burner. In the PIV image a mean vertical velocity of 9 m/s has been subtracted from the velocity vectors.

Local extinction phenomena have a major influence on flame stability and a better understanding of the mechanisms leading to extinction is both of fundamental and practical importance. Simultaneous time resolved measurements of the evolution of the OH radical distribution, using OH PLIF [10], and the instantaneous velocity field, using particle image velocimetry (PIV) [11], were used to study the dynamics of local extinction phenomena in a turbulent non-premixed flame (fuel mixture: $H_2/CH_4/N_2$, Re=20000). From the OH sequences the position, in both space and time, where the local extinction of the flame front begins, could be identified. In the PIV velocity field the flow structures associated with the identified extinction events were captured. Vortices impinging from the fuel side on the flame front were found to be the dominating extinction mechanism in this flame and the time scale of extinction events

was estimated to 100 μs or less. The time development of the OH distribution and the corresponding velocity field near a region of local OH extinction in the upper part of the flame is shown in Figure 2. In the second image a vortex is seen, approaching the flame front and forcing it to bulge out slightly, a decrease in the OH concentration can also be seen at the top of the bulge. In the next frame the flame has just extinguished, as indicated by the sharpness of the two tips of the now separated flame fronts. The large scale wrinkling of the flame front by the flow field is also seen.

Three-dimensional imaging of soot volume fractions in a turbulent non-premixed C_2H_4/air flame have been performed. For the 3-d imaging experiments the set-up shown in Figure 3a) was used. The 532 nm laser beam from the Nd:YAG cluster was deflected by a rotating mirror and formed into a laser sheet by a cylindrical and a spherical lens. By using this configuration eight equally spaced parallel laser sheets were created. The acquisition of the eight planar images was faster than the time scale of the flow, thus providing an instantaneous 3-d image of the measurement object. In Figure 3b) the soot volume fraction in eight planes in the flame are shown, the soot measurements were performed using LII [12]. The imaged regions are 17x12 mm large and the images are separated by 0.4 mm from each other. The maximum intensity in the sequence corresponds to a soot volume fraction of 6 ppm. In Figure 3c) the iso-concentration surfaces for 1 ppm and 2 ppm are shown, viewed from the direction of slice number 8. From the closely stacked 2-d slices it is possible to calculate the full 3-d gradient of the soot volume fraction, in figure 3d) the x, y, and z components of the gradient and the 3-d gradient corresponding to slice number 7 are shown.
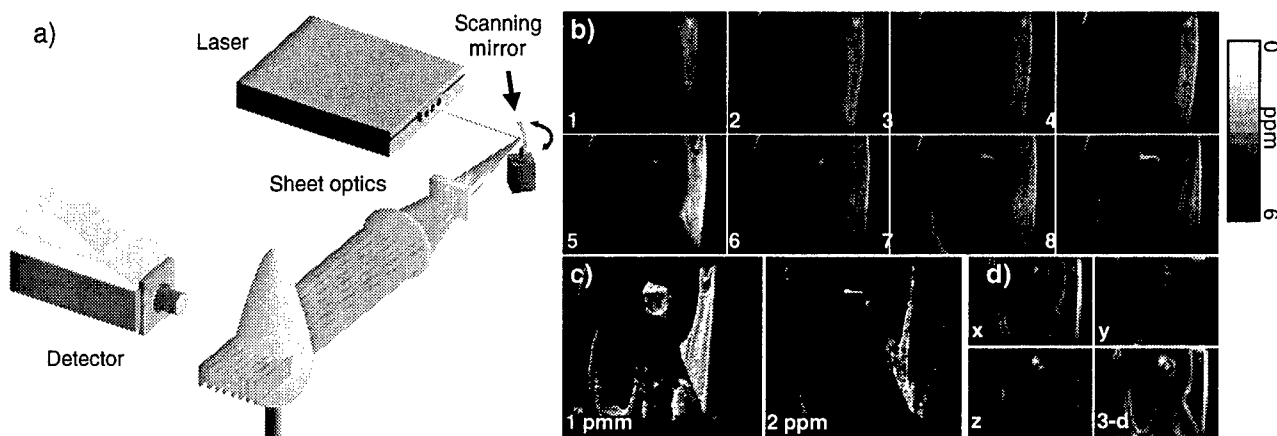

Fig. 3. Three-dimensional imaging of absolute soot volume fractions in a non-premixed flame, a) optical set-up, b) soot volume fraction in eight cuts through the flame, the separation between imaging planes is 0.4 mm, c) 3-d iso concentration surfaces corresponding to 1 ppm and 2 ppm soot volume fraction, d) soot concentration gradients corresponding to image plane number 7.

The work presented here has been performed in collaboration with C.F. Kaminski, M. Aldén, M. Richter, J. Nygren, A. Hultqvist, M. Christensen, B. Johansson, G. Josefsson, A. Omrane, B. Axelsson and R. Collin.

5. References

1. A.C. Eckbreth, *Laser diagnostics for combustion temperature and species, 2nd edition* (Gordon and Breach Publishers, 1996).
2. M. Winter and M.B. Long, "Two-Dimensional Measurements of the Time Development of a Turbulent Premixed Flame," Comb. Sci. Tech. **66**, 181-188 (1989).
3. B. Yip and M.B. Long, "Instantaneous planar measurement of the complete three-dimensional scalar gradient in a turbulent jet," Opt. Lett. **11**, 64-66 (1986).
4. C.F. Kaminski, J. Hult and M. Aldén, "High repetition rate planar laser induced fluorescence of OH in a turbulent non-premixed flame," Appl. Phys. B **68**, 757-760 (1999).
5. A. Hultqvist, M. Christensen, B. Johansson, J. Nygren, M. Richter, J. Hult and M. Aldén, "Characterization of the HCCI Combustion Process in a Heavy Duty Engine by High-Speed Fuel Tracer LIF and Chemiluminescence Imaging," submitted to SAE World Congress 2002.
6. J. Hult, G. Josefsson, M. Aldén and C.F. Kaminski, "Flame front tracking and simultaneous flow field visualisation in turbulent combustion," in Proceedings of the 10th International Symposium on Applications of Laser Techniques to Fluid Mechanics (July 10-13, 2000, Lisbon).
7. J. Hult, B. Axelsson, A. Omrane, R. Collin, J. Nygren P.-E. Bengtsson, M. Aldén and C.F. Kaminski, "Quantitative Three-Dimensional Imaging of Soot Volume Fraction in Turbulent Non-Premixed Flames," submitted to Experiments in fluids.
8. R.H. Thring, "Homogeneous-Charge Compression-Ignition (HCCI) Engines," SAE Technical Paper 892068 (1989).
9. M. Richter, J. Engström, A. Franke, M. Aldén, A. Hultqvist and B. Johansson, "The Influence of Charge Inhomogeneity on the HCCI Combustion Process," SAE Technical Paper 2000-01-2868 (2000).
10. G. Kychakoff, R.D. Howe, R.K. Hanson, M.C. Drake, R.W. Pitz, M. Lapp and C.M. Penney, "Visualization of Turbulent Flame Fronts with Planar Laser-Induced Fluorescence," Science **224**, 382-384 (1984).
11. M. Raffel, C. Willert and J. Kompenhaus, *Particle Image Velocimetry* (Springer Verlag, 1998).
12. L.A. Melton, "Soot diagnostics based on laser heating," Appl. Opt. **23**, 2201-2208 (1984).

Raman/Rayleigh/LIF/CRDS measurements in premixed $CH_4/N_2/O_2$ atmospheric pressure flames.

Christopher B. Dreyer and Mark Linne

Colorado School of Mines

Division of Engineering

Abstract

Measurements of N_2, O_2, CH_4, CO_2, and H_2O have been made by vibrational raman scattering and OH by laser induced fluorescence (LIF) and cavity ringdown spectroscopy (CRDS) as a function of height in a premixed methane/air flame at atmospheric pressure.

Introduction

In order to achieve a better understanding of flame chemistry, laser diagnostics has become an important tool for many combustion researchers. Many "standard flames" are employed to evaluate combustion mechanisms and premixed atmospheric pressure flames of methane and air are among the most common. In this work we have added vibration raman scattering and rayleigh scattering to our existing apparatus for measuring OH concentration in flames.[1] We use vibration raman scattering for measurement of the major species, N_2, O_2, CH_4, CO_2, and H_2O. Temperature is measured using rayleigh scattering, thermocouple, and N_2 raman. The OH radical is measured with LIF and calibrated with CRDS measurements in the post flame region. Measurements are made as a function of height above the burn, from the flame front to the post flame region. Equivalence ratio is varied from lean to rich conditions.

Experimental

The premixed methane–air fames studied in this work were stabilized on a stainless steel honeycomb surface with nitrogen co-flow, consisting of a commercially available mixing chamber and a custom-built Meeker-style burner head. The stainless steel honeycomb surface (23-mm diameter) maintains uniform laminar flow from the mixing chamber and prevents flashback. Copper cooling lines soldered to the circumference of the burner head are used to reject heat from the head. Mass flow controllers (Brooks Instruments, 5850E Series) meter the methane and airflows to the burner. Mass flow meters were calibrated regularly with a sonic nozzle and periodically checked with a bubble flow meter.

The OH $A^2P \leftarrow X^2\Sigma^+$ (0,0) band was probed near 302.5 nm by a frequency doubled pulsed dye laser, PDL-3, pumped by a Spectra Physics GCR-16 Nd:YAG laser. Figure 1 shows the experimental arrangement used in LIF and CRDS. The output telescope of the dye laser was used to focus the beam at the center of the CRDS cavity. The beam focal distance was several meters and the beam diameter was measured to be 400 ± 50 μm at the focus without the CRDS mirrors in place. Fluorescence was collected via a 1:1 optics arrangement with f/3.9. The monochromator, CVI Digikrom 240, had a holographic grating of 1200 grooves/mm and was used in second order with slit width set at 2000 μm, which produced a spectral bandpass of 3.2

nm. The $A^2P \rightarrow X^2\Sigma^+$ (0,1) band of OH was collected, centered on the Q_1 line of the rotational level excited in the LIF measurements. A Burle 1P28 photomultiplier tube (PMT), powered by a SRS PS325 high voltage power supply, was used to collect fluorescence.

Fluorescence signals from the PMT were amplified by a multichannel variable amplifier before arriving at a SRS Model 250 Boxcar Gated Integrator, further amplification was provide by the Boxcar. Fluorescence was integrated over 100 pulses with the gate triggered by the Nd:Yag laser Q-switch sync out and delayed to be coincident with the fluorescence pulse. Boxcar average output was acquired via a Tektronix TDS 540 digital oscilloscope. Oscilloscope acquisitions were communicated to a computer via a general-purpose interface bus (GPIB) by a custom written LabView program. To provide a measure of the noise, background levels and LIF were recorded for every measurement condition for a period of several minutes.

The cavity ringdown mirrors were separated by 21.5 cm and centered on the burner. The cavity was formed by two 4 m radius of curvature high reflectivity mirrors from Research Electro-optics of Boulder, CO, which were set in gimbal mounts. Cavity output was directed through an 800 μm diameter aperture to a Burle 1P28 PMT. The PMT signal was recorded by a Tektronix TDS 540 digital oscilloscope. Ringdown curves were communicated via GPIB to a computer and acquired by a custom written LabView program. A 5 shot average curve was acquired by the LabView program and fit to an exponential decay between 85% and 10% of the peak signal intensity. All CRDS measurements were made by wavelength scanning the laser across a small portion of the spectrum that contained the line to be analyzed. Typically, 20 individual 5 shot average curves were acquired and fit for each wavelength position in a scan. CRDS OH calibration measurements were made by scanning several transitions accessing high-lying states of OH, the P_1 (25) (1,0), P_2 (19) (2,1), and P_2 (12) (3,2) lines.
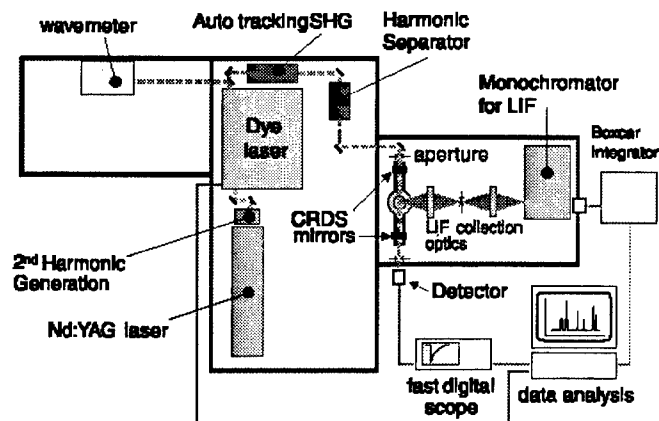
Figure 1: LIF and CRDS experimental arrangement.

The third harmonic (355nm) of a Spectra Physics GCR-16 Nd:YAG laser was used for vibrational raman scattering. The CVI Digikrom 240 monochromator with a 1200 grooves/mm grating blazed at 300 nm was used to collect the scattered light. A long pass filter with 10^{-5} blocking at 355 nm was used to suppress rayleigh scattered light. The beam size was approximately 600 μm, and slit width typically 500 μm, scattered light was collected in a 1:1 optical arrangement. A mirror was used in opposition to the collection optics to double the

collected raman signal. Raman signals were collected by an end-on 9125 photomultiplier tube, a boxcar integrator was used to average pulses, signals were digitized by a scope and acquired by computer via GPIB.

Results

To date, the LIF and CRDS measurements have been made. Results are shown in Figure 2. Raman and rayleigh measurements are proceeding. Preliminary measurements indicate that raman signal-to-noise measurements exceed 150 for room temperature N_2 raman and 30 pulse averaging. These measurements indicate that sufficient vibrational raman signal of major species can be collected at flame temperatures. The flame has been modeled using the using the PREMIX [2] simulation package with GRI-mech 3.0 [3] flame chemistry, thermodynamics, and transport files and a fixed measured temperature profile.
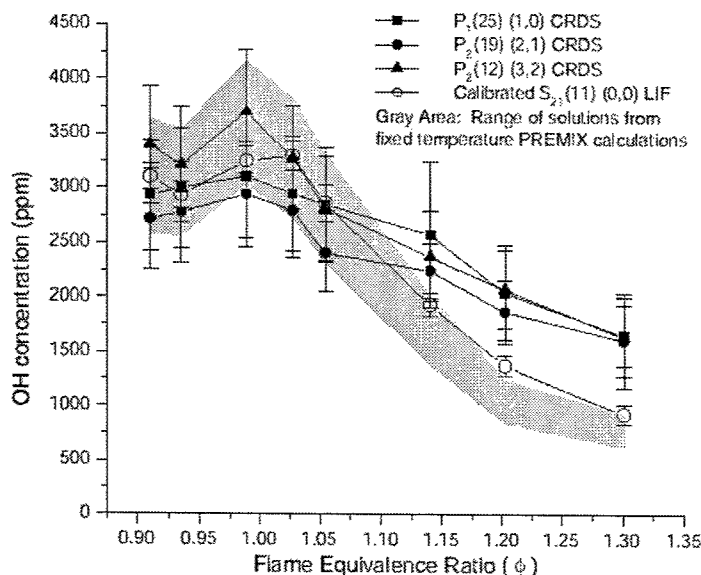
Figure 2: Experimental results of LIF and CRDS measurement of OH.

References

1. C. B. Dreyer, S. M. Spuler, and M. Linne, "Calibration of laser induced fluorescence of the OH radical by cavity ringdown spectroscopy in premixed atmospheric pressure flames", submitted to *Combust. Sci. Tech.*
2. Kee, R. J., Rupley, F. M., Miller, J. A., Coltrin, M. E., Grcar, J. F., Meeks, E., Mo.at, H. K., Lutz, A. E., Dixon-Lewis, G., Smooke, M. D., Warnatz, J., Evans, G. H., Larson, R. S., Mitchell, R. E., Petzold, L. R., Reynolds, W. C., Caracotsios, M., Stewart, W. E., and Glarborg, P. (1999) *CHEMKIN Collection, Release 3.5.* San Diego, CA: Reaction Design, Inc.
3. Smith, G. P., Golden, D. M., Frenklach, M., Moriarty, N. W., Eiteneer, B., Goldenberg, M., Bowman, C. T., Hanson, R. K., Song, S., Gardiner Jr., W. C., Lissianski, V. V., and Qin, Z. (1999) *GRI–MECH 3.0.* http://www.me.berkeley.edu/gri mech/.

In situ Measurement of CO, H₂O and Gas Temperature in a Lignite-Fired Power-Plant

H. Teichert, T. Fernholz, V. Ebert

Institute of Physical Chemistry, University of Heidelberg, Im Neuenheimer Feld 253, 69120 Heidelberg, Germany
Phone: +49-6221-545004, Fax: +49-6221-545050
volker.ebert@urz.uni-heidelberg.de

Abstract:
A diode laser based *in situ* absorption spectrometer is presented for the simultaneous detection of CO (1560nm), water (813nm) and the gas temperature within the combustion chamber of a 600MW lignite-fired power-plant. A fractional absorption resolution better than 10^{-3} equivalent to a few hundred ppmV CO could be demonstrated with a 30 sec time response.

1. Introduction

CO is an important indicator of combustion efficiency. High CO concentrations are responsible for corrosion damages or reduction of the service life of power-plants. We realized an *in situ* CO-spectrometer in a 600 MW lignite fired power-plant by using base band diode laser modulation spectroscopy in the near infrared (NIR). In addition we measured the water vapor concentration to account for possible water interference and to determine the gas temperature by means of two-line thermometry [1,2,5]. Pyrometric temperature data were recorded for comparison with the water vapor temperature. The pyrometric data were used to evaluate the presented results. The spectroscopic data of water vapor absorption are under way.

2. Line selection

Two vibrational overtone bands of CO are relevant for NIR diode laser experiments. The first band can be used with recently developed diode lasers near 2.3 μm [3]. However it is very difficult to obtain suitable single mode lasers due to the limited supply. The line strengths of the second overtone band in the 1.56 μm region are about 100 times weaker. In addition, there is a strong interference from H₂O and CO₂ absorption. However, suitable lasers are commonly available and rather inexpensive. From Hitran'96/Hitemp data [4] we find that the R24 transition at 6412 cm⁻¹ is fairly well isolated from neighboring H₂O and CO₂ absorption lines. Figure 1 shows the calculated spectrum for typical conditions in a lignite combustion.
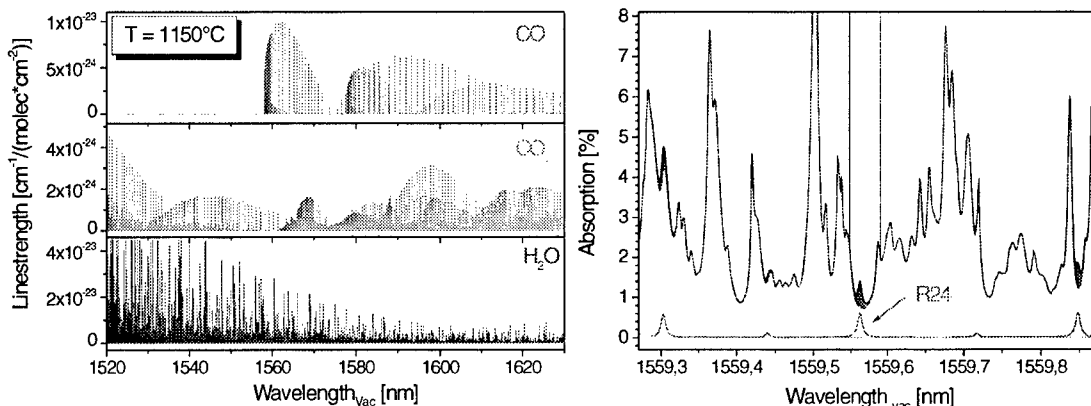

Fig. 1: Left: Line strengths of CO, CO₂ and H₂O in the 1560 nm region at T = 1150 °C (HITRAN'96/HITEMP). right: calculated spectrum for 0.5% CO, 10% H₂O and 10% CO₂ at T = 1150 °C, P = 1 atm, L = 13 m. The R24-transition is most suitable for in situ CO detection. The highlighted region indicates the tuning-depth (by modulating the injection current) of the used diode laser.

2. Experimental details

The experimental setup for the *in situ* measurement within the combustion chamber of the power-plant is relatively simple. The beams of a single mode FP-diode laser at 813 nm and a fiber coupled DFB-diode laser at 1.56 μm were closely overlayed -with a spatial distance below 20 mm- and directed through the combustion chamber via a single 25mm mirror. A small fraction of the laser light was separated by a beam splitter and directed through a reference cell filled with pure 100% CO. The reference signal was used to temperature tune the laser to the desired absorption line. The transmitted laser light was collected with a spherical mirror and separated into the two individual wavelengths by a dichroic beam splitter. Optical narrow band filters in front of the silicon and the InGaAs detectors simultaneously suppressed the strong thermal background radiation and minimized crosstalk between the two wavelength channels. A 12bit/5Msample ADC-board digitized the photo detector signals which were then evaluated with a computer. To align the setup under combustion conditions and to direct the invisible laser beams across the combustion chamber onto the detectors at a distance of 14 m we developed a new automatic alignment and beam stabilization arrangement based on a motorized $\vartheta-\varphi$-mirror. This new device which is based on the setup presented in [5] is able to cope with highly luminous combustion conditions and severe losses in laser power.

3. Data analysis and results

On its way through the combustion chamber the laser light is severely attenuated by broad band absorption and scattering due to coal or ash particles leading to a power loss in the *in situ* path in the order of 99,9% and more. In addition there is -despite the use of narrowband filters- a time dependent background of thermal radiation which is more than two times higher than the detected laser light. Although the transmission fluctuations are much stronger than the specific absorption of the CO molecules we manage to eliminate these disturbances with the help of rapid tuning capabilities of the laser and the direct (base band) detection of the absorption signals.
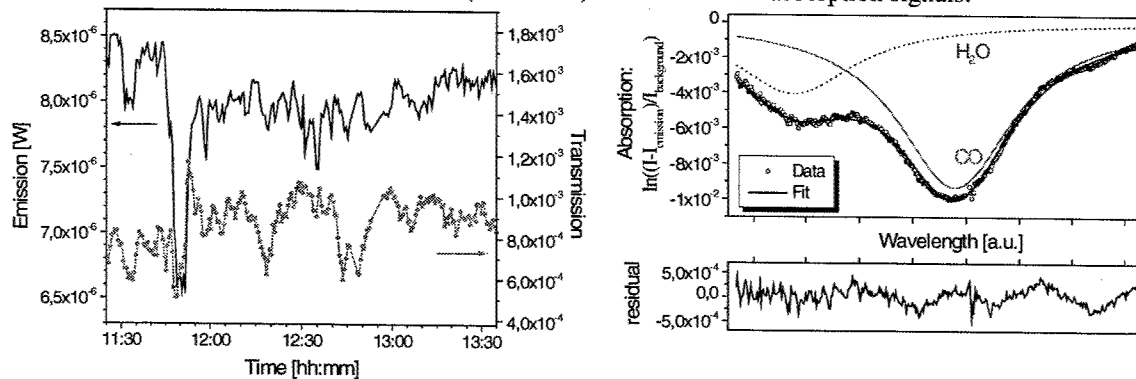

Fig. 2: Left: Time evolution of thermal background emission and transmission of in situ path. Right: In situ absorption signal corrected for thermal radiation and transmission (averaged over 30 seconds). Two lorentzian profiles are fitted to the data to describe the absorption of CO (right) and H$_2$O (left).

The laser wavelength was tuned over the selected absorption lines by a triangular current modulation at 5 kHz. Due to the fast modulation the thermal emission and the transmission of the in situ path is considered to be constant over a modulation period. This assumption is verified by an analysis of the frequency spectrum of the emission and the transmission, which shows a strong decrease of the disturbances at higher frequencies. Hence, the fraction of the detector signal that is due to thermal emission can be derived by evaluating the modulation depth of the laser light, whereas the transmission is determined by fitting the background signal. The noise level on the absorption signal was decreased further by reducing the bandwidth by averaging subsequent scans over 30 seconds. The left graph in figure 2 shows the temporal behaviour of thermal emission and transmission of the *in situ* path over 2 hours.

For transmission correction the averaged raw signal is separated into specific absorption and background. Contributions to the background come from laser intensity modulation, wings of neighboring absorption lines, wavelength dependence of optical filters and transmission perturbations in the order of a few kHz and above. The right graph in figure 2 shows an averaged scan after subtraction of the thermal emission offset and after division by the background. We used a 3rd order polynomial fit to describe the background and two lorentzian profiles to fit the

absorption lines of CO and H_2O. The integrated area of the line profile is proportional to the number density according to Lambert-Beer's law.

Figure 3 shows for the first time the time evolution of the *in situ* CO concentration in such a large power-plant with such severe transmission and emission disturbances. The increase in CO between 12.30 pm and 12.45 pm has been created intentionally by an increase in the fuel to air ratio via a modification in the air supply.
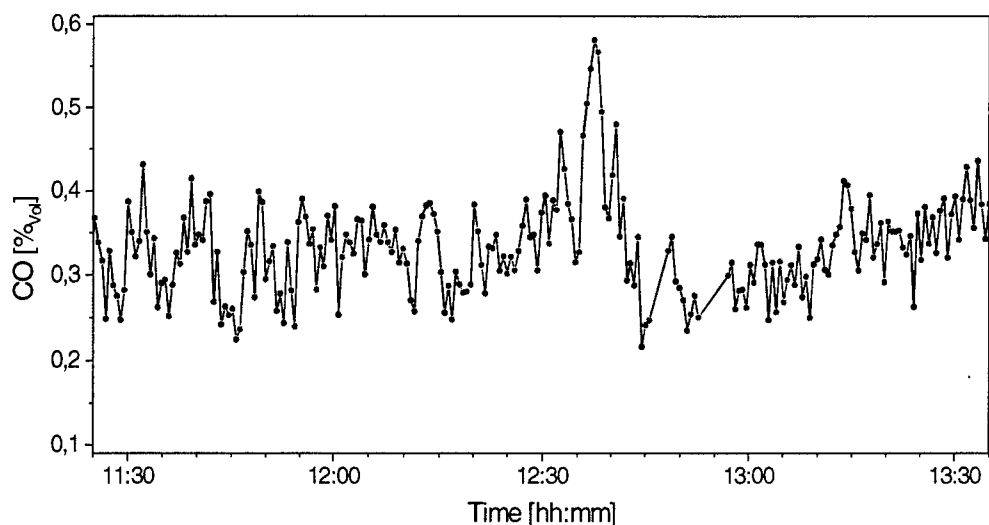

Fig. 3: Time evolution of CO concentration. The time resolution is about 30 seconds. The rise of the CO concentration at t=12:30 to 12:45 is caused by an intentional increase in the fuel to air ratio.

4. Conclusions

In situ measurements of CO and H_2O concentrations and gas temperature could be performed in a 60 hour run in a full scale lignite-fired power-plant. The transmission across the combustion chamber was in the order of 10^{-3} of the initial laser power. Despite the use of narrow band filters we found a strong background radiation which was higher than the collected laser light. Nevertheless we achieved a fractional absorption resolution of better than 10^{-3} with a time resolution of 30 seconds. This is equivalent to a resolution in CO concentration of a few hundred ppm_{Vol}. Especially helpful was a new automatic alignment setup based on a motorized mirror mount, which was able to align laser and detector within a few minutes even at zero visibility along the beam path. The spectrometer is easily extendable to other species like O_2, NH_3, HCl, HF etc. by a simple change of the laser diode and therefore has the capabilities to become a rather universal tool for industrial *in situ* gas analysis in advanced combustion control applications.

5. References

[1]   H. Pitz, T. Fernholz, C. Giesemann, V. Ebert, "Diode-Laser-Based In-situ-CH_4-Detection for the Surveillance of Ignition Processes in Gas-fired Power-Plants", in *Laser Applications to Chemical and Environmental Analysis*, OSA Technical Digest, 111-113 (2000).

[2]   T. Fernholz, H. Pitz, V. Ebert, "In-situ Monitoring of Water Vapor and Gas Temperature in a Coal Fired Power-Plant Using Near-infrared Diode Lasers", in *Laser Applications to Chemical and Environmental Analysis*, OSA Technical Digest, 77-79 (2000).

[3]   J. Wang, M. Maiorov, D. S. Baer, D. Z. Garbuzov, J. C. Connolly and R. K. Hanson, "In situ combustion measurements of CO with diode-laser absorption near 2.3 μm", Appl. Opt. Vol.39, No.30. (2000)

[4]   L. S. Rothman, R. R. Gamache, R. H. Tipping, C.P. Rinsland, M. A. H. Smith, D. C. Benner, V. M. Devi, J.-M. Flaud, C. Camy-Peyret, A. Perrin, A. Goldmann, S. T. Massie, L. R. Brown and R. A. Toth, "The HITRAN molecular database: editions of 1991 and 1992", J. Quant. Spectrosc. Radiat. Transfer **48**, 469-507 (1992)

[5]   V. Ebert, T. Fernholz, C. Giesemann, H. Pitz, H. Teichert, J. Wolfrum and H. Jaritz, "Simultaneous Diode-Laser-Based In-situ-Detection of Multiple Species and Temperature in a Gas-fired Power-Plant", Proc. Comb. Inst. 28, 423-430 (2000)

Nanoscaled Particle Size Distributions and Gas Temperatures from Time-resolved LII Measurements

T. Lehre, B. Jungfleisch, R. Suntz, and H. Bockhorn

Institut für Chemische Technik and Engler-Bunte-Institut / Verbrennungstechnik

Universität Karlsruhe

Abstract

LII signals are measured in sooting premixed atmospheric and low-pressure flames. Soot particle size distribution P(r) and gas temperature T are measured independently. LII model parameters are validated. P(r) and T are estimated using non-linear regression.

THEORETICAL BACKGROUND

By absorbing intense laser light particles are heated up to temperatures far above the ambient gas or flame temperature. Laser-induced incandescent particles emit higher thermal radiation than particles at ambient gas temperature. The subsequent decrease of particle temperature is due to thermal radiation, heat transfer and vaporization (figure 2). The basic equations describing LII signals were first published in detail by Melton (1984). He showed that the laser-induced thermal radiation is approximately linear dependent on the soot volume fraction. This theoretical finding is confirmed by various measurements in premixed and diffusion flames (Tait et al., 1993, Quay et al.,1994, Vander Wal et al. 1994, Bengtsson et al. 1995, Appel et al. 1996, Shaddix et al. 1996). High laser intensities above 30 MW/cm^2 lead to particle temperatures close to the vaporization temperature of carbon ($\approx$4000K) and to significant vaporization of soot particles. At particle temperatures below 3300 K heat transfer is the 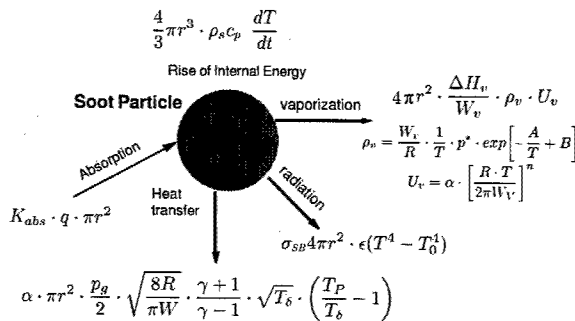dominant cooling process. The rate equations used in the present state of the revised model are summarized in Figure 1. The heat transfer rate equation in figure 1 is valid for the Knudsen regime (Fuchs, 1964), i.e. for particles that are small compared to the mean free path of the gas molecules, which is certainly the case for soot particles under flame conditions. The velocity of vapour molecules U_v evaporating from particles is given by the Hertz-Knudsen equation, including a vaporization coefficient α to account for vaporization kinetics and real gas effects (Knudsen, 1915, Landolt-Börnstein, 1968). For ideal gases, the exponent n can be derived from the kinetic theory of gases as n=0.5. The vapour pressure is approximated by a form of the Antoine equation containing two empirical constants (Landolt-Börnstein, 1968). Knowing all heat and mass transfer rate equations, the particle temperature as a function of time can be obtained by solving the mass and energy balances for one particle. Including this temperature function into Planck's law yields the response function for a monodisperse particle size distribution

Figure 1: Heat and mass transfer rates during LII measurements

$$R\left(t, \lambda_{exc}, \lambda_{em}, \Delta\lambda\right) = \frac{2\pi^2 c^2 h}{\lambda_{em}^5} r(t)^2 K_{abs} \left(\frac{1}{\exp(hc/\lambda_{em}kT_P(t)-1)} - \frac{1}{\exp(hc/\lambda_{em}kT_0-1)} \right) \qquad (3).$$

Considering a particle size distribution results in

$$J\left(t, \lambda_{exc}, \lambda_{em}, \Delta\lambda\right) \propto \int_0^\infty N_v p(r) R\left(t, \lambda_{exc}, \lambda_{em}, \Delta\lambda\right) dr \qquad (4).$$

It is not possible to obtain an analytical solution for the particle size distribution as a function of LII signal intensity. Equation 4 is a Fredholm integral of the first kind and can be solved numerically using a non-linear iterative algorithm (Roth et al.,1996), if the gas temperature is known. This approach yields a particle size distribution starting from an arbitrary initial guess without answering the question wether this solution is unique and independent of the initial guess. Global optimisation can be done using multidimensional non-linear regression. Generally, best fit parameters are obtained by minimizing the quantity

$$\chi^2 \equiv \sum_{i=1}^{N} \left(\frac{y_i - y(x_i, a_1 \ldots\ldots a_M)}{\sigma_i} \right)^2 \tag{5},$$

where σ_i is the standard deviation of the measurement error, y_i are measured values and $y(x_i,a)$ is the model prediction for a parameter vector a. The vector a consists of m fit components, in this work frequencies of particles of a certain size bin $p_i(r_i)$ and the gas temperature T, and n fixed parameters, here e.g. heat of evaporation h_v or the density of solid material ρ_s. Non-linear regression gives a measure of the statistical significance of derived parameters and allows to recognize multiple solutions.
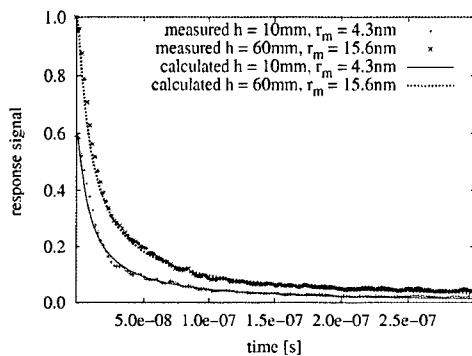

Figure 2: Comparison of measured and calculated response signals in low-pressure flame
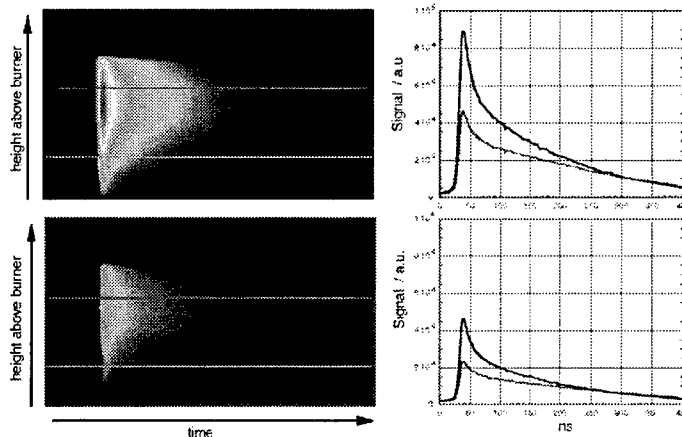
TIME-RESOLVED LII SIGNAL MEASUREMENTS AND MODEL PREDICTIONS

Time resolved LII measurements are performed in a laminar premixed flat flame (acetylene, oxygen, argon) at a pressure of 12kPa. The LII signal decay is detected with a fast photomultiplier (Electron tubes limited, type 9111 WB) and a 500MHz digital oscilloscope (LeCroy, type 9350). The signal is induced by a frequency doubled Nd-YAG laser with a laser energy flux of $5*10^7$ W/cm^2 per pulse. The median particle sizes have been obtained by independent scattering measurements (Schäfer 1994). TEM analysis of soot samples from that flame (Bockhorn et al. 1987) yields a lognormal particle size distribution with a standard deviation of 0.34. Model predictions based on this particle size distribution agree excellently with the measured signal decays as shown in Figure 2. At the present state further measurements of gas temperatures, particle size distributions and 1D LII signals are performed in atmospheric premixed flames using a Streak camera. LII signals are measured at two wavelengths, 633nm and 430nm. From the ratio of the LII intensity at two wavelengths the particle temperature evolution is obtained. This data is used for model validation under atmospheric conditions. The influence of the spatial

Figure 3: 1D LII signals in atmospheric premixed flame at two

distribution of the laser intensity on LII measurements is examined.

ASSESSMENT OF GAS TEMPERATURE AND PARTICLE SIZE DISTRIBUTION USING MULTIDIMENSIONAL NONLINEAR REGRESSION

Time-resolved LII signals from the flame system (figure 2) discussed in the last section have been analysed in order to obtain particle size distributions and gas temperatures. The aim is to get best agreement between modelled and measured LII signal, i.e. minimizing χ^2, by optimising m fit parameters simultaneously.
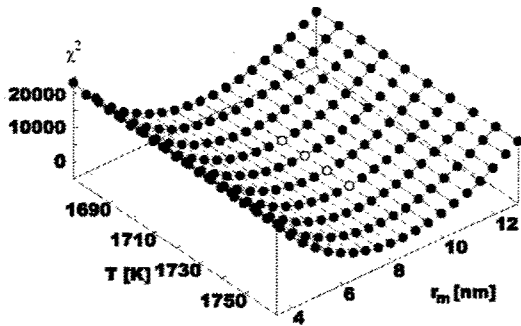
Figure 4: χ^2 as function of gas temperature and mean particle radius
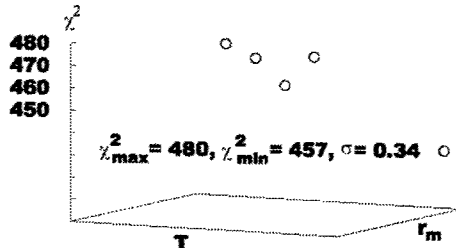
Figure 5: Minimum region of χ^2 for calculation shown in figure 4

Figure 4 shows a 3D plot of χ^2 as a function of two parameters, gas temperature and mean particle radii. In this calculation a lognormal size distribution with $\sigma=0.34$ is input. Figure 5 shows the enlarged minimum region of χ^2 in figure 6. It can be seen that a definite minimum of χ^2 exists. The function minimum stretches along an isoline of the mean particle radius at 8.3 nm. Thus, it can be concluded that the sensitivity of the LII model on mean particle radii is higher than on gas temperatures. In this case, best fit parameters are r_m =8.3nm and T = 1724K, which are in excellent agreement with independent measured values. By statistical means, the uncertainties are less than ±0.1nm and ±5K for r_m and T, respectively, assuming a correct model. These results show the possibility to assess mean particles sizes and gas temperatures simultaneously from time-resolved laser-induced incandescence signals with good accuracy. Standard numerical methods like the Downhill Simplex method or the Marquardt-Levenberg method (Press et al.,1986) are able to solve this multidimensional minimization problem independent of initial parameter guesses within reasonable time. Without assuming a functional form, particle size distributions can be assessed if particle sizes are binned into a moderate number of size bins. Best fit values for number frequencies in each size bins are to be obtained by non-linear regression using adequate minimization methods.

Literature

Appel, J., Jungfleisch, B., Marquardt, M., Suntz, R., Bockhorn, H., 1996. 26[the] Symp. Int. on Combustion, 2387, The Combustion Institute, *Pittsburgh*

Bengtsson, P.-E., and Aldén, M.,1995. *Appl. Phys. B* 60:51-59

Bockhorn, H., Jungfleisch, B., Marquardt, M., Mauß, F., Suntz, R., 1996. 26[the] Symp. Int. on Combustion, 2343-2350, The Combustion Institute, *Pittsburgh*

Bockhorn, H., Fetting, F., Wannemacher, G., Heddrich, A., 1987. Ber. Bunsenges. Phys. Chem. 91:819-825

Fuchs, N.A., 1964. *The Mechanics of Aerosols*, Pergamon Press, Oxford,

Knudsen, M., 1915. Ann. Physik 47:697

Landolt-Börnstein, 1960. 6th Edition, II2a, pp. 1 - 30, Springer Verlag, Berlin-Heidelberg-New York

Landolt-Börnstein, 1968. 6th Edition, II5b, pp. 238 - 246, Springer Verlag, Berlin-Heidelberg-New York

Melton, 1984. L.A., *Appl. Optics* 23:2201-2208

Quay, B., Lee, T.-W., Ni, T., and Santoro, R. J., 1994. *Combust. Flame* 97:384-392

Roth, P., Filipov, A. V., 1996. J. Aerosol Sci., 27:95-104, Pergamon Press

Schäfer, T., 1994. PhD thesis, TH Darmstadt

Smallwood, G.J., Snelling, D.R., Liu, F., Gülder, Ö.L., 2001, J. Heat Transfer, vol 123, pp. 814-818

Shaddix, R.C., Harrington, J.E., Smyth, K.C., 1996, *Combust. Flame* 99, 723

Tait, N. P., and Greenhalgh, D. A., 1993. *Ber. Bunsen-Ges. Phys. Chem.* 97:1619-1625

Press, W.H. , Flannery, B.P. , Teukolsky, S.A. , Vetterling, W.T. 1986. *Numerical Recipes*, Cambridge University Press

Vander Wal, R. L., and Weiland, K. J., 1994. *Appl. Phys. B* 59:445

Will, S., Schraml, S. and Leipertz, A., 1996. 26[the] Symp. Int. on Combustion, 2277-2284, The Combustion Institute, *Pittsburgh*

Biological or Biomedical II

Thursday, February 7, 2002

Andreas Brockhinke, Univ. of Bielefeld, Germany
Presider

ThC
2:00pm–3:40pm
Flagstaff

Introduction

Single protein and nucleic acid molecules are believed to be the smallest functional units in biological systems, their dynamic analysis *in vitro*, but also in living cells and organisms remaining one of the major goals of current biophysical research. Among the most sensitive techniques presently available and frequently employed in biophysical single molecule analysis is fluorescence spectroscopy, due to its non-invasiveness being applicable to a wide variety of biological specimens. Fluorescence correlation spectroscopy (FCS) is one of the many different modes of high-resolution spatial and temporal analysis of single or sparse biomolecules. Its basic principle is the consideration of minute spontaneous deviations of small systems from thermodynamic equilibrium that give rise to fluctuations in the fluorescence emission. Among a multitude of physical parameters which are in principle accessible by FCS, it most conveniently allows to determine local concentrations, mobility coefficients, and characteristic rate constants of inter- and intramolecular reactions of fluorescently labeled biomolecules at very low (nanomolar) concentrations, under equilibrium conditions and without physical separation.

It is obvious that fluctuations can be the better resolved the smaller the system under observation is, i.e. the smaller the measurement volume. Utilizing efficient light sources such as lasers, and ultrasensitive detection devices such as avalanche photodiodes, fluorescence-based detection and analysis of single molecules has lately been accomplished in various ways. A simple and elegant setup is the confocal detection scheme where an extremely small measurement volume is achieved by focussing a laser beam down to the optical resolution limit by an objective with high numerical aperture. Since fluorescence is only excited within the illuminated region, only molecules dwelling in the focal spot contribute to the measured signal. Usually, fluctuations arise from single fluorescent molecules traversing the illuminated region, thereby emitting so-called fluorescence bursts, or by intermittent emission behavior due to internal dynamics of the fluorophores. The recorded signal fluctuations are then quantified by temporally autocorrelating the recorded intensity signal, a mathematical procedure which the technique is named after. Autocorrelation analysis provides a measure for the self-similarity of a time series signal and thereby describes the persistence of information carried by it. The temporal pattern by which fluctuations arise and decay yields invaluable information about the underlying processes governing inter- and intramolecular dynamics.

FCS theory

For a temporal analysis of average fluctuations in the fluorescence signal F(t) recorded from the very sensitive detector (usually an avalanche photodiode), the following normalized fluorescence autocorrelation function G(τ) with lag time τ is considered:

$$G_{ii}(\tau) = \left\langle \delta F_i(t) \delta F_i(t+\tau) \right\rangle / \left\langle F(t) \right\rangle^2$$

G(τ) can in principle be considered as a weighted fluctuation decay function. The amplitude and shape of this function is determined by their relative strength and the underlying processes. The most common fluctuations are just number fluctuations due to the random 3D diffusion of sample molecules through the illuminated volume. In this case, the characteristic decay time of G(τ) reflects the average residence time of

the molecules in the focal spot. Due to the Poissonian nature of the number fluctuations at low concentrations, the amplitude $G(0)$ is inversely proportional to the average number of molecules present in the volume at any time. For freely diffusing molecules of species i with concentration C_i, $G(\tau)$ is given by:

$$G_{diff}(\tau) = V_{eff}^{-1}\langle C_i \rangle^{-1}\left(1 + \tau/\tau_{d,i}\right)^{-1}\left(1 + r_0^2\tau/z_0^2\tau_{d,i}\right)^{-1/2}$$

with V_{eff} the effective volume element and $\tau_{d,i}$ the average residence time of a molecule within V_{eff}. r_0 and z_0 are the $1/e^2$ half axes of the illumination profile in the sample space which is considered to be Gaussian in all three dimensions. The relationship between $\tau_{d,i}$ and the diffusion coefficient D_i is given by $\tau_{d,i} = r_0^2/4D_i$.

If the molecules additionally undergo intramolecular dynamics represented as on/off blinking of the fluorescence on a faster time scale during their residence time in the focal spot, $G(\tau)$ has to be modified as follows:

$$G_{diff+fast} = (1 - F + F \cdot e^{-t/\tau_f}) \cdot G_{diff},$$

if F describes the fraction of particles in the dark state at any time, and τ_f the inverse of the overall characteristic blinking rate: $\tau_f = 1/(k_d+k_d)$ if k_b and k_d are the respective transition rates from the bright to the dark state and vice versa.

Intracellular applications

In spite of their obvious attractiveness, it has not been until recently that an increasing number of intracellular FCS applications were reported. Intracellular applications of fluorescence correlation spectroscopy (FCS) allow to access a large variety of molecular parameters like particle mobility and intramolecular dynamics in the cytosol, membranes, and organelles on the single molecule level. Cellular autofluorescence, reduced signal quality due to light absorption and scattering, but also the danger of cell damage and dye depletion due to irreversible photobleaching, are potential artifacts that can seriously interfere with measurements carried out on a single molecule scale. It can be demonstrated that like in laser scanning microscopy, two-photon excitation yields substantially improved FCS signal quality in turbid preparations like plant cells and deep cell layers in tissue. At comparable signal levels, two-photon excitation minimizes photobleaching in spatially restrictive cellular compartments, thereby preserving long-term signal stability. Applying both one- and two-photon excitation, we give several examples for intracellular diffusion and active transport of single fluorescent particles in mammalian and plant cells as well as association and dissociation reactions. Mobility parameters can be measured over a wide range of characteristic molecular residence times. Deviations from normal diffusion of fluorescent probes are found in various cell compartments and can be explained by interaction with cellular structures.

Dual-color applications

Dual-color cross-correlation extends the standard FCS scheme by introducing two different fluorescent labels which are each excited and detected by independent light

sources and detectors, but share a common focal measurement volume. The cross-correlation function $G_{ij}(\tau)$ is now defined as

$$G_{ij}(\tau) = \left\langle \delta F_i(t) \delta F_j(t + \tau) \right\rangle \Big/ \left\langle \left\langle F_i(t) \right\rangle \cdot \left\langle F_j(t) \right\rangle \right\rangle$$

and reveals underlying mechanisms that relate two measured fluorescence signals F_i and F_j with each other. The instrumental setup and sample design usually gets somewhat more elaborate by this extension, but is compensated by the higher detection specificity and a significant simplification in terms of data analysis, since no changes in diffusion characteristics or molecular mobility are required to follow association or dissociation reactions. The relative amount of double-color particles, inducing coinciding fluctuations $\delta F_i(t)$ and $\delta F_j(t)$, can be easily derived from the amplitudes $G_{ij}(0)$. Thus, by dual-color cross-correlation, all processes can be investigated that lead to conversions between single-color and double-color species and thus establish or prevent coincidences, i.e. correlations in the signal fluctuations recorded by two separate detection channels. The detection specificity is determined by how well the emission spectra of both labels can be separated, favorable are green-red or blue-red dye combinations with ca. 100 nm distance of their respective emission maxima.

In spite of the considerable improvement of detection specificity provided by fluorescence cross-correlation analysis, few applications have so far been reported, presumably due to the practical challenges of properly aligning and controlling the stability of the experimental setup. It is demonstrated that two-photon excitation combined with dual-color FCS can be the key to significantly simplify simultaneous investigations of multiple fluorescent species on a single molecule scale. Two-photon excitation allows to access common fluorophores of largely distinct emission by the same excitation wavelength, because differences in selection rules and vibronic coupling can induce considerable shifts between the one-photon and two-photon excitation spectra. The concept of dual-color, two-photon fluorescence cross-correlation (TPCC) analysis is introduced and experimentally demonstrated with an established assay probing the selective cleavage of dual labeled DNA substrates by restriction endonuclease.

A mid infrared, high power, cw, continuous tunable PPLN OPO for trace gas detection within life science

M. van Herpen
Molecular and Laser Physics, University of Nijmegen, 6525 ED Nijmegen, the Netherlands
S. te Lintel Hekkert
Molecular and Laser Physics, University of Nijmegen, 6525 ED Nijmegen, the Netherlands
S.E. Bisson
Combustion Research Facility, Sandia National Laboratories, Livermore, California, 94550
F.J.M. Harren
Molecular and Laser Physics, University of Nijmegen, 6525 ED Nijmegen, the Netherlands
Tel: +31 24 3652124, Fax: +31-24 3653311, E-mail: fransh@sci.kun.nl, URL: www.sci.kun.nl/tracegasfac

Abstract: A 2 W continuous wave optical parametric oscillator based on periodically poled lithium niobate and tunable over 3.0-3.8μm wavelength region is used in combination with photoacoustic spectroscopy to trace small hydrocarbons for applications in medicine and biology.
© 2001 Optical Society of America
OCIS codes: (190.4970) Parametric oscillators and amplifiers, (300.6390) Spectroscopy, molecular

1. Introduction:

Laser-based photoacoustic spectroscopy offers an elegant and relatively simple way to perform highly sensitive trace gas detection owing in particular to the background free nature of this technique [1]. As the photoacoustic signal is directly proportional to the laser power and to the absorption strength, it is advantageous to use powerful laser sources in the mid-infrared, where most molecules possess strong absorptions due to their fundamental vibrations. These demands have made infrared gas discharge lasers very important, in particular CO- and CO_2-lasers. A wide variety of applications in biological [2-5], medical [6,7] and environmental [8] research have been developed from these lasers. Detection limits around a part per billion ($1:10^9$) are accomplished using the strong intra-cavity fields of these lasers. A severe drawback of these systems, however, lies in the fact that they cannot be tuned continuously. Therefore, one must rely on coincidences between laser emission frequencies and molecular absorption lines. Nowadays, solid-state cw, tunable infrared laser sources are being developed. For some applications quantum cascade lasers are an ideal source as monitor instrument because of their small size and their moderate high power [9,10]. However as analytical instrument optical parametric oscillators (OPO's) have a wide field of applications because of their wide tunability and their high out put power [11,12].

2 Experimental:

Here we present a cw OPO for the mid infrared wavelength region of 3.0-3.8 micrometer with an idler output power of more than 2 Watt. The OPO is pumped with a 10 Watt, cw, single frequency Nd:YAG Laser (Lightwave M6000). This YAG laser has a master oscillator power amplifier system. The master oscillator can be continuously tuned over 8 GHz, mode hop free; its total tunability is over 24 GHz including two mode hops, but covering the entire 24 GHz range. The power amplifier enhances the laser power from 100mW (laser bandwidth 5 kHz over 1 ms) to 10-15 W. To vary the laser power onto the ring OPO a combination of a half wave plate, polarizing beam splitter is used. A 10 cm lens focuses the YAG beam into the periodically poled lithium niobate (PPLN) crystal in the resonator cavity (Fig. 1). It was found that a beam waist of 100 µm in the PPLN crystal is optimal for generating the signal and idler beam. Narrow focusing resulted in 50% lower idler beam intensities with the same configuration.
The ring cavity itself is a four-mirror ring cavity in which the signal beam at 1.5-1.7 µm is resonating (Free Spectral Range cavity 320 MHz). In this cavity the two curved mirrors (radius of curvature 10 cm) and the two flat mirrors have high reflectivity for the signal wave at 1.5-1.7 µm (R>99.9%), but a high transmission for the pump at 1064 nm (T>90%) and idler waves T>80% at 3.0-3.8 µm. The pump beam is focused into the PPLN plate, which is 5 cm long and 0.5 mm thick and has a fan-out grating design as described earlier [13]. Due to the fan-out design of the PPLN crystal used in this study, the periodicity of the crystal could be chosen anywhere between 29.3 and 30.1 µm, by changing the vertical position of the crystal in the laser beam. This resulted in tuning of both signal and idler

wavelength. Additionally, the wavelength can be tuned by changing the temperature of the oven containing the crystal.

In this way an OPO signal and idler wavelength could be covered from 1.5–1.65 µm and 3.0 - 3.8 µm, respectively. To prevent photo-refractive damage, the crystal is kept at 180 °C within a commercially available oven and is temperature stabilized at 0.1 °C. The input and output faces of the PPLN are anti-reflection coated for 1.064 µm, 1.5-1.7 µm and 3.0-3.8 µm.
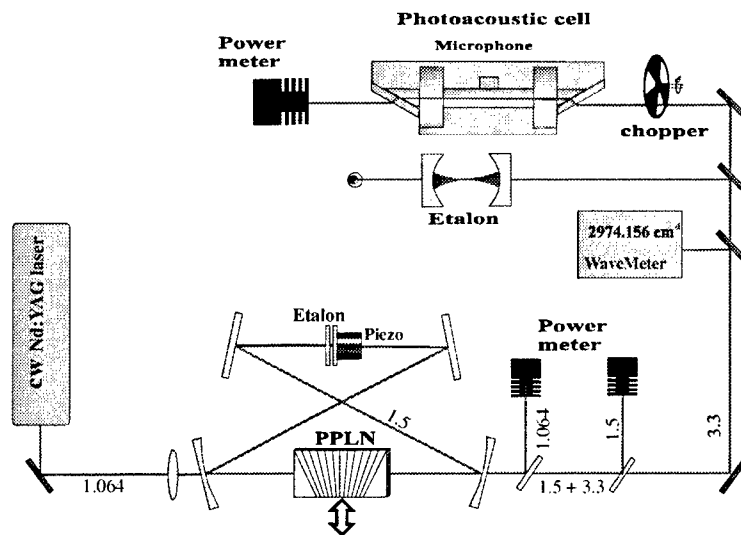

Fig. 1: Experimental set-up showing the pump laser, the OPO ring cavity containing the fan-out PPLN crystal and etalon, additional diagnostic equipment and photoacoustic cell.

3 Results:

The single resonant OPO has a threshold pump power of 3 Watt, after that the idler power increases linear with the pump power to 2.2 W at a pump power of 10.4 W. The pump depletion at this point maximizes at value of 86%, which is very close pump depletion records reported elsewhere [12].

Without any intracavity etalon or air spaced Fabry-Perot the OPO is operating single mode although mode hops occur frequently during operation. By inserting a low finesse etalon in the cavity a better frequency stability is achieved. For this we decided to insert 30% reflectivity air-spaced Fabry Perot (air space 1 mm, FSR 150 GHz). Even though this Fabry Perot introduces additional losses, the advantage of better OPO stability and the possibility for mode-hope-tuning [13] by changing the length of the Fabry Perot was found to be more important. Walk-off losses are minimized by placing the air-spaced etalon between the two flat mirrors in the second focal point of the cavity. Inserting the air-spaced etalon caused the output power to go down from 2.2 W to about 700 mW.

We demonstrated single frequency continuous pump-tuning by recording the one atmosphere pressure-broadened v_7 vibrational mode, $v=1\leftarrow0$, Q branch transition (J=4-39) of ethane, using photoacoustic spectroscopy [14]. Recently, work has been focused on using mode-hop tuning next to pump-tuning to increase the total OPO tuning range. Fig. 2 shows an absorption line of 10 parts per million of ethane in nitrogen at 3229 nm (3097 cm^{-1}) measured with photoacoustic spectroscopy while mode-hop tuning the OPO. The idler wavelength was monitored by means of an infrared wavemeter (Burleigh WA1000 IR, NY, USA) and a 7.5 GHz Fabry Perot, which showed that a total tuning of 100 GHz has been achieved using this tuning method.

The strength of the photoacoustic signal, compared to the noise level shows that at this absorption line an estimated detection limit can be calculated of 0.03 part per billion (S/N ratio =1).
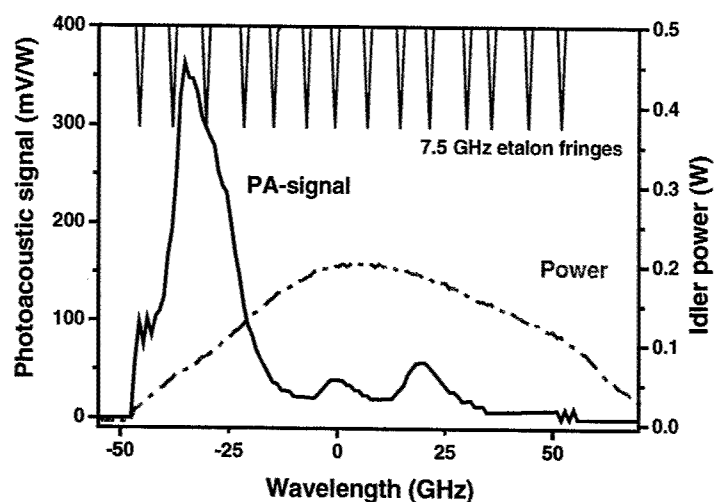
Fig. 2: A 100 GHz 5 seconds scan over three absorption lines of ethane at 3097 cm-1. The scan was made, by changing the length of the intracavity Fabry Perot. Every FSR (320 MHz) of the cavity the OPO made a mode hop which gave a somewhat irregular, although reproducible, spectrum.

4 Future:

Present research focuses on optimizing the total OPO tuning range, output power and long term stability. With these improvements this OPO will certainly be a very good source for most spectroscopic applications. We will use this OPO system in Life Science by combining it with photoacoustic spectroscopy in order to develop a highly sensitive trace gas detector.

5 References:

1. MW Sigrist, "Air Monitoring by Spectroscopic Techniques", John Wiley and Sons, New York NY, pp. 163-227 (1994).
2. FGC Bijnen, FJM Harren, JHP Hackstein, J Reuss, "Intracavity CO laser photoacoustic trace gas detection; cyclic CH_4, H_2O and CO_2 emission by cockroaches and scarab beetles", Appl. Opt. **35** 5357-5368 (1996).
3. H. Zuckermann, F.J.M. Harren, J. Reuss and D.H. Parker, "Dynamics of acetaldehyde production during anoxia and post-anoxia in Red Bell pepper studied by photoacoustic techniques", Plant Physiology **113** 925-932 (1997).
4. J Oomens, H Zuckermann, S Persijn, DH Parker, FJM Harren, "CO laser based photoacoustic trace gas detection; Applications in postharvest physiology" Appl. Phys. B **67** 459-466 (1998)
5. S.T. Persijn, R.H. Veltman, J. Oomens, F.J.M. Harren, and D.H. Parker, "CO laser absorption coefficients of biological relevance: H_2O, CO_2, ethanol, acetaldehyde and ethylene", Appl. Spectroscopy **54**, 62-71 (2000).
6. F.J.M. Harren, R. Berkelmans, K. Kuiper, S. te Lintel Hekkert, P. Scheepers, P. Hollander, R. Dekhuijzen and D. H. Parker, "On-line laser photoacoustic detection of ethene in exhaled air as biomarker of ultraviolet radiation damage of the human skin", Appl. Phys. Lett. 74 1761-1763 (1999).
7. S. Stolik, E. Ramon-Gallegos, M. Pacheco, SA Tomas, A. Cruz-Orea, A.J. Perez-Zapata R. Gaebler, F. Sanchez-Sinencio, "Photoacoustic measurement of ethylene as a real time biomarker of lipid peroxidation processes in mice", Anal. Sci. **17** S365-S367 (2001)
8. M.A. Moeckli, MA, M. Fierz M, M.W. Sigrist, "Emission factors for ethene and ammonia from a tunnel study with a photoacoustic trace gas detection system", Environ. Sci. Technol. **30** 2864-2867 (1996)
9. B.A. Paldus, T.G. Spence, R.N. Zare, J. Oomens, F.J.M. Harren, D.H. Parker, C. Gmachl, F. Capasso, D.L. Sivco, J.N. Baillargeon, A.L. Hutchinson, A.Y. Cho, "Photoacoustic spectroscopy using quantum cascade lasers", Opt. Lett. **24** (1999) 178-180
10. D. Hofstetter, M. Beck M, J. Faist, M. Nagele, MW Sigrist, "Photoacoustic spectroscopy with quantum cascade distributed-feedback lasers", Opt. Lett. **26** 887-889 (2001).
11. LE Myers, RC Eckardt, MM Fejer, RL Byer, WR Bosenberg, JW Pierce, "Quasi-phase-matched optical parametric oscillators in bulk periodically poled $LiNbO_3$", J. Opt. Soc. Am. B **12** 2102-2116 (1995)
12. W.R. Bosenberg, A. Drobshoff, and J.I. Alexander, "93% pump depletion, 3.5W continuous-wave, singly resonant optical parametric oscillator", Opt. Lett. **21** 1336-1338 (1996)
13. P.E. Powers, T.J. Kulp, and S.E. Bisson, "Continuous tuning of a continuous-wave periodically poled lithium niobate optical parametric oscillator by use of a fan-ut grating design", Opt. Lett. **23** 159-161 (1998)
14. M. van Herpen, S. te Lintel Hekkert, S.E. Bisson, F.J.M. Harren, "Wide single mode tuning of a 3.0-3.8 micrometer, 1.5 W, continuous wave Nd:YAG-pumped optical parametric oscillator based on periodically poled lithium niobate", Opt. Lett. in press

Longitudinal studies of nitric oxide and carbon dioxide in human breath with a single IV-VI mid-IR laser.

Chad Roller, Khosrow Namjou, Jim Jeffers
Ekips Technologies, Inc., 6002 Flaming Oaks Circle. Norman. OK 73026
(405) 325-5419, croller@ekipstech.com

Adom Mock
Columbia University. N.Y., N.Y.
apm30@columbia.edu

Patrick J. McCann, Joe Grego
University of Oklahoma, Dept. of Electrical and Computer Engineering. 202 W. Boyd St. Room 219, Norman, OK 73019
(405) 325-4288, pmccann@ou.edu

Abstract: NO and CO_2 were measured simultaneously in exhaled breath from seven subjects 10 times over a period of 12 days. Exhaled CO_2 was used to estimate NO values as laser characteristics fluctuate over time.
©2000 Optical Society of America
OCIS codes: (300.6260) Spectroscopy, diode lasers; (000.1430) General. medicine and biology

1. Introduction

Recent medical literature has identified exhaled nitric oxide (eNO) as a biomarker for assessing the severity of airway inflammation [1,2]. Chronic airway inflammation is a symptom of asthma and can be reliably assessed by measuring eNO levels [3]. Chemiluminescence detection, the most utilized method for eNO analysis, requires frequent calibrations using expensive gases not readily available in most medical offices [4].

TDLAS systems using IV-VI semiconductor mid-IR lasers have the unique ability to measure eNO and CO_2 simultaneously with a single laser. Typical human exhalations contain 3% to 5% CO_2 consistently over time [5], eNO/CO_2 ratios can be used to calculate eNO concentrations. This technique eliminates the need for expensive calibration gases and corrects for laser power fluctuations over time. Dedicated user-friendly software for analysis and instrument control allows medical technicians to operate the TDLAS system with less than one day of training. The TDLAS system is equipped with a closed-cycle cryogenic refrigerator to cool the laser and detector eliminating the need for liquid nitrogen, another expensive consumable not available in many clinics.

This presentation summarizes the results from a 10-day study of measured eNO from 2 steroid naïve asthmatics and 5 non-asthmatics. Fluctuations of laser characteristics over time due to temperature cycling and slow dark current drifts were corrected for by using the peak CO_2 absorption magnitudes. Results show eNO can be monitored over time using TLDAS without the need for calibration gases. The TDLAS system presented in this report has many of the required attributes for becoming the next generation breath diagnostic tool for aiding asthma diagnosis.

2. Experimental Design and Results

A schematic of the breath collection apparatus (Quintron, Inc., Milwaukee, WI) and TDLAS system is shown in Fig. 1. A double heterostructure IV-VI tunable diode laser was mounted on a temperature controlled stage located inside a sealed cryostat. The beam emitted from the laser exited a ZnSe window where an OAPM reflected the beam onto two field mirrors, which directed the beam into a 107-meter optical path length White Cell (16 Liters). Upon exiting the White cell, the beam was focused with a ZnSe lens before striking a photodetector also located on the cold finger inside the cryostat.

A temperature controller and integrated heater maintained constant laser operating temperature at 102 K. A laser current controller supplied injection currents between 800 mA and 900 mA. Two function generators provided the control waveforms for modulating the laser using a technique known as sweep integration coupled with frequency modulation. A sawtooth ramp (40Hz, $0.11V_{PP}$) tuned the laser across NO, CO_2, and H_2O absorption features near 5.2 μm. A triangle waveform (22kHz, $0.01V_{PP}$) was superimposed on the sawtooth waveform to tune repetitively across individual absorption features. A commercial lock-in amplifier sampled the pre-amplified photo

detector output at twice the modulation frequency ($2f$). A personal computer with an analog-to-digital (A/D) converter card collected 500 data points per scan and performed a running co-average of 75 scans.
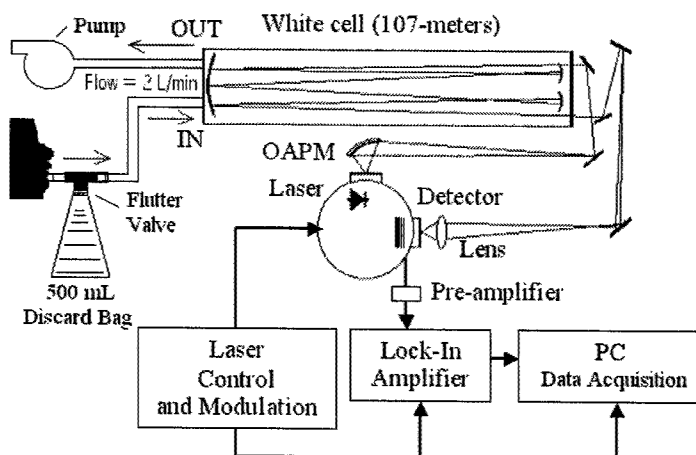

Fig. 1. Breath collection apparatus (BCA) and TDLAS system diagram.

A collected absorption spectrum of human breath matched to HITRAN 96 line intensities is shown in Fig. 2. Measured absorption features of interest for NO and CO_2 were at 1912.79 cm^{-1} and 1912.96 cm^{-1}, respectively. The unambiguous H_2O absorption peak at 1912.57 cm^{-1} was used to align spectra before averaging, eliminating the need for a separate reference cell and detector. Institutional Review Board approval from the University of Oklahoma (Norman campus) was granted for performing studies using human subjects. Each volunteer signed an Informed Consent Form prior to donating breath.
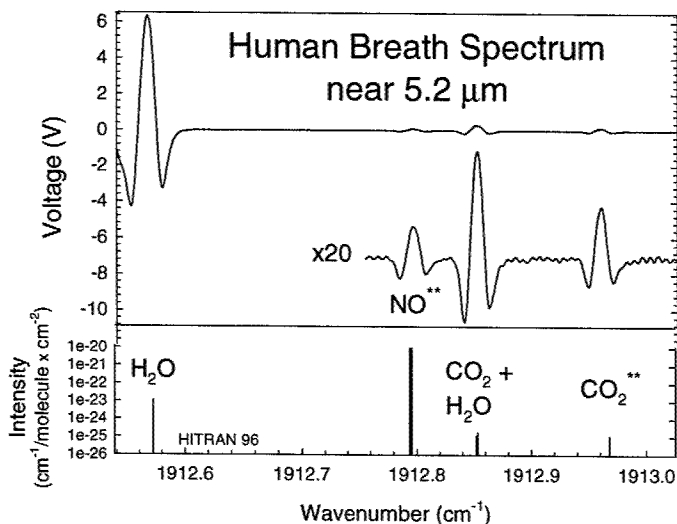

Fig. 2. Absorption spectrum taken from human breath. The lines of interest were NO at 1912.79 cm^{-1} and CO_2 at 1912.85 cm^{-1}. The H_2O line at 1912.57 cm^{-1} was used as a spectral reference to align each spectrum prior to coaveraging. (** measured lines).

Volunteers were asked to exhale for 20 seconds into the breath collection apparatus shown in Fig. 1 to obtain breath samples. Flow controllers maintained a constant sampling flow of 2 L/min (not shown in schematic). A roughing pump induced flow and reduced the White cell pressure to 14 Torr eliminating molecular species interference. A custom designed T-piece with flutter valve was used to connect a disposable mouthpiece, 500 mL discard bad, and Teflon tubing. The first 500 mL of breath, mainly deadspace, flowed through a one-way flutter valve into a 500 mL discard breath collection bag at little to no breathing reistance. The second half of the breath,

enriched alveolar breath, was sampled at a constant breathing resistance limiting the contribution of nasal NO by helping to close the vellum [6].

Both the NO line at 1921.79 cm-1 and CO_2 line at 1912.96 cm-1 were compared to a common reference spectrum (Fig. 2) using a linear least squares fitting routine. The linear slope evaluated for each was multiplied by the peak voltage values for NO and CO_2 at the same respective lines in the reference spectrum to compute overall absorption intensities (A) for eNO and CO_2. Equation (1) was used to calculated eNO values,

$$C_{ENO} = \left(\frac{A_{NO}}{A_{CO_2}}\right)\left(\frac{g_{NO}}{g_{CO_2}}\right)\left(\frac{S(v)_{CO_2}}{S(v)_{NO}}\right) \times C_{CO_2} \qquad (1)$$

where (A) is the measured absorption magnitudes, (g) is the pressure-broadening coefficients, and (S) and cross sectional line strengths found in the HITRAN 96 database. The exhaled CO_2 concentration is assumed to be 4 %.

The results for 10 consecutive weekdays of eNO/CO_2 measurements from breath donated by 2 mild-asthmatic volunteers and 5 non-asthmatic volunteers are shown in Fig. 3. Two abnormally high eNO concentrations were recorded for two non-asthmatic volunteers during the study, but both volunteers reported developing an airway inflammatory related illness. However, results from non-calibrated measurements were able to differentiate between healthy non-asthmatics and those with airway inflammatory related conditions. Future investigations should cover the deviations of CO_2 from 4% to assess relative error when using equation (1). In conclusion, TLDAS is a likely next generation breath measurement technique for sensitive detection of eNO.
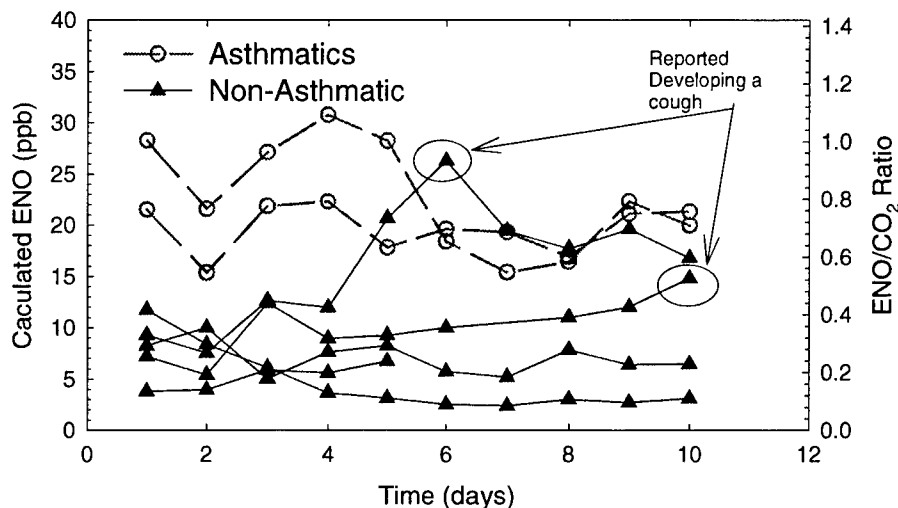

Fig. 3. Results of ENO/CO2 ratios measured for 5 consecutive days from 2 asthmatic volunteers and 5 non-asthmatic volunteers.

3. References

[1] K. Alving, E. Weitzberg, and J. M. Lundberg, "Increased amount of nitric oxide in exhaled air of asthmatics", *Eur. Respir. J.*, **6**, 1368-1370 (1993).

[2] S. A. Kharitonov, D. Yates, R. A. Robbins, R. Logan-Sinclair, E. A. Shinebourne, and P. J. Barnes, "Increased nitric oxide in exhaled air of asthmatics", *Lancet*, **343**, 133-135 (1994).

[3] I. Tsujino, M. Nishimura, A. Kamachi, H. Makita, M. Munakata, K. Miyamoto, and Y. Kawakami, "Exhaled nitric oxide–Is it really a good marker of airway inflammation in bronchial asthma?", Respiration, **67**, 645-651 (2000).

[4] M. Bernareggi, G. Cremona, "Measurement of exhaled nitric oxide in humans and animals", Pulmonary Pharmacology and Therapeutics, **12**, 331-352 (1999).

[5] J. J. Carr, and J. M. Brown, "Chapter 10 – The human respiratory system and its measurement", Introduction to Biomedical Equipment Technology, 3rd Edition, ed. C. E. Stewart, Prentice-Hall, Upper Saddle River, N.J. (1998).

[6] P. E. Silkoff, "Recommendations for standardized procedures for the online and offline measurement of exhaled lower respiratory nitric oxide and nasal nitric oxide in adults and children – 1999", Am. J. Respir. Crit. Care Med., **160**, 2104-2117 (1999).

Title: Measurement of $^{13}CO_2/^{12}CO_2$ ratio using tunable diode laser based Raman
spectroscopy and an atomic vapor filter

Authors: Claudia Navarro, Philip L. Varghese, and Manfred Fink

Submitting author: Philip L. Varghese

Address: ASE-EM Department, UT Austin, Austin, TX 78712

Phone: (1) 512-343-2460

e-mail: varghese@mail.utexas.edu

Abstract:

We describe a novel scheme for detecting the isotopic ratio ($^{13}C/^{12}C$) in gaseous carbon dioxide. Raman scattering is excited with a tunable near-infrared diode laser and isotopic discrimination is obtained with an atomic vapor filter.

Measurement of $^{13}CO_2/^{12}CO_2$ ratio using tunable diode laser based Raman spectroscopy and an atomic vapor filter

Claudia Navarro and Philip L. Varghese
Department of Aerospace Engineering and Engineering Mechanics
Manfred Fink
Department of Physics
The University of Texas at Austin
Austin, Texas 78712

Abstract

We describe a novel scheme for detecting the isotopic ratio ($^{13}C/^{12}C$) in gaseous carbon dioxide. Raman scattering is excited with a tunable near-infrared diode laser and isotopic discrimination is obtained with an atomic vapor filter.

Description

Warren and Marshall implicated *Helicobacter pylori* in the genesis of peptic ulcer disease changing the diagnosis and treatment of ulcers in the last 20 years [1]. *H. pylori* is a spiral-shaped, microaerophilic bacterium that colonizes the human stomach and duodenum. It has been identified as the cause of chronic gastritis, ulcers, and gastric cancer [2]. The bacterium protects itself from the gastric juices by hydrolyzing urea into bicarbonate (containing the radical HCO_3), ammonia (NH_3), and carbon dioxide (CO_2), to neutralize the acids.

One of the diagnostic tests for *H. pylori* is the carbon urea breath test [3]. The carbon urea breath test (C-UBT) exploits the urea hydrolyzing property of H. pylori to measure urease activity through isotopically labeled CO_2 expired in breath. Air is in equilibrium with blood across the alveoli in the lungs, allowing breath to be a good indication of blood composition and bodily chemical processes [4]. The detection of isotopically labeled carbon dioxide in the breath samples indicates *H. pylori* infection since no other urease-producing bacteria colonize the stomach.

There are two carbon isotopes used in C-UBT: ^{13}C, and the radioactive isotope ^{14}C. In either case the patient is fed a meal containing isotopically labeled (^{13}C or ^{14}C) urea. The administered dose of ^{14}C-urea is equivalent to 55 hours of exposure to radiation from the natural environment [5] and it is advisable that pregnant women and children avoid exposure [3]. Alternatively, patients are given ^{13}C-urea and the amount ^{13}C in exhaled breath is measured spectroscopically. An increase of 5-6 parts per thousand of ^{13}C indicates presence of *H. pylori* [6]. Conventionally the $^{13}CO_2/^{12}CO_2$ in the exhaled breath is measured via mass spectrometry or spectroscopically [6,7], and both techniques are time consuming and require processing of collected samples in a central laboratory.

We are developing a novel technique for $^{13}CO_2$ detection that is fast, local, and inexpensive. We use a near infrared tunable diode laser as a source for Raman scattering and obtain the $^{13}C/^{12}C$ ratio *without* a spectrometer using atomic vapor absorption cells. The detectability of the isotopomer ratio is called the δ-value, defined in terms of the ratio of intensities of the isotopomers in the breath measured before and after the administration of the labeled urea:

$$\delta(\%_0) \equiv \frac{R_a - R_b}{R_b} \times 1000,$$

where R is the ratio of the $^{13}CO_2/^{12}CO_2$ intensities before (b) and after (a) the urea exposure [8].

Figure 1 shows a Raman spectrum of pure CO_2 at 50 Torr measured using our present apparatus without any modifications, in the wavelength range relevant for the analysis of breath. The goal of this work is to isolate the lines labeled 1370 cm^{-1} and 1388 cm^{-1} and to determine their ratio as precisely as possible. Figure 2 shows the experimental arrangement needed to achieve this objective. Most elements are already used in the present set-up.
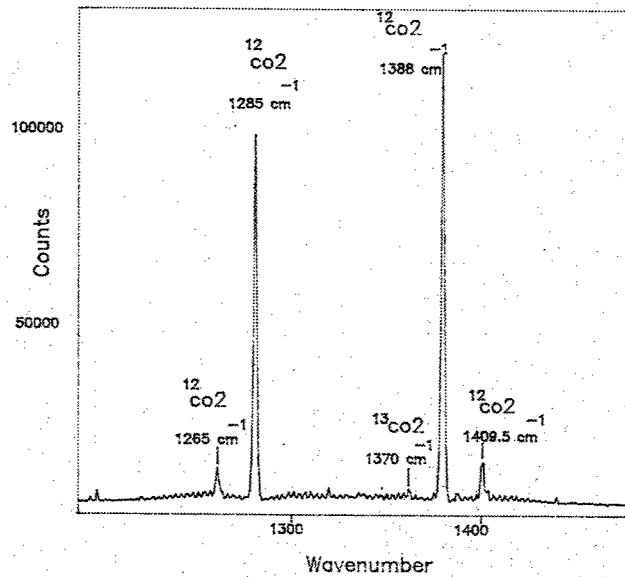
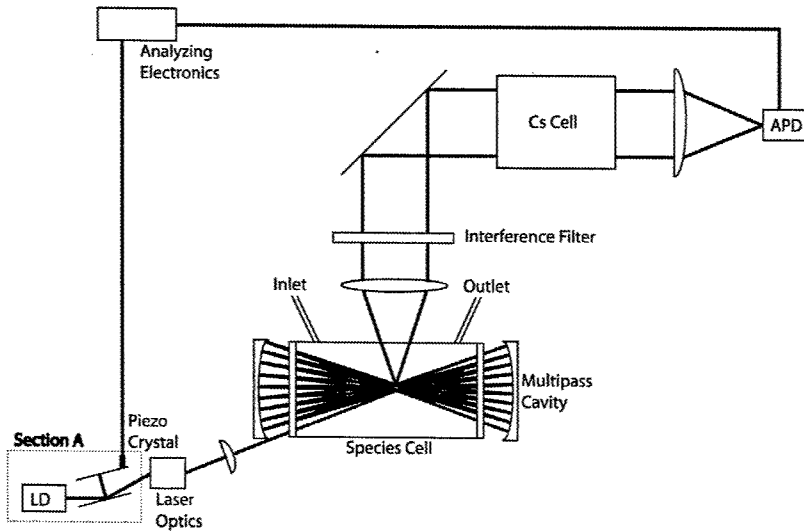Figure 1: Raman spectrum of pure CO_2 at 50 Torr.

Figure 2 Optical elements of the experiment.

The optical components in Section A produce an intense monochromatic laser beam emitted from a laser diode (LD). Its frequency stability is better than 400 MHz. The laser optics include a chopper and polarization rotator ($\lambda/2$ plate) that are installed to record two spectra with orthogonal polarization. The difference of these measurements will isolate the Q-branches of the spectrum, removing the anisotropic O- and S-branches [9] seen on the baseline of Figure 1. The laser beam is focused into the species cell with double-sided anti-reflection coated windows to allow multi-pass operation. This cell will contain the sample gas in our experiment and will receive the patient breath sample in real time in a medical diagnostic application. It will be irradiated by the diode laser beam and the light scattered at the focal point in the cell is collected at 90° with an f/1 by an achromat that illuminates a narrow band pass filter (2 ± 0.4 nm), centered at the ^{13}C line of the $^{13}CO_2$ dyad that is shifted down 1370.08 cm^{-1}, from the laser excitation frequency of 12569 cm^{-1} (corresponding to an excitation wavelength of 795.6 nm). The scattered light passed by the filter now contains only the 2 spectral lines of the CO_2 isotopomers. Crossing through a Cesium (Cs) vapor cell, light that is inelastically scattered by the Q-branch of $^{12}CO_2$ is shifted down by 1388 cm^{-1} and will be absorbed very efficiently (60db) by the Cs D_1 transition at 894.35 nm. Only the $^{13}CO_2$ Q-branch lines will reach the avalanche photodiode detector (APD). The rotating half-wave plate polarizer alternately blocks and transmits the polarized (isotropic) pure vibrational (Q-branch) contribution. The depolarized (anisotropic) O- and S-rotational branches are transmitted with equal intensity in either orientation. Hence, the difference between the two recordings gives the Q-branch contribution. Next, the laser diode frequency is shifted by a small amount with the piezo-crystal. The light scattered inelastically by $^{12}CO_2$ is no longer in resonance with the Cs filter and both $^{12}CO_2$ and $^{13}CO_2$ transitions reach the detector. The polarization analysis is repeated to determine the sum of the intensities of the Q-branches of $^{12}CO_2$ and $^{13}CO_2$. The ratio of isotopes in the sample (R) is easily calculated from these two measurements, and measurements of R in samples before and after administration of urea gives δ. With a 100 mW laser diode and 50 passes through the cell, we estimate that the ratio of the CO_2 isotopomers will be determined to a δ-value of 0.005 % or better with a recording period of 1 minute. Experiments are currently in progress to verify system performance.

<u>References</u>

1. BJ Marshall and JR Warren. Lancet, 1:1311-1315, 1984.
2. CD Mansfield and HN Rutt. Physics in Medicine and Biology, 43:1225-1239, 1998.
3. KE Brown and DA Peura. Gastroenterology Clinics of North America, 22:105-115, 1993.
4. S Eriksen. New Scientist, 381:608-611, 1964.
5. JB Stubbs and BJ Marshall. Journal of Nuclear Medicine, 34:821-825, 1993.
6. PD Klein, et al. The American Journal of Gastroenterology, 91(4):690-694, 1996.
7. AF Cutler and P Toskes. The American Journal of Gastroenterology, 94(4):959-961, 1999.
8. S Koletzko, et al. The Lancet, 345:961-962, 1995.
9. HW Klöckner, et al. Applied Spectroscopy, 32(4): 401-402, 1978.

Nonlinear Techniques

Thursday, February 7, 2002

Mark Allen, Physical Sciences Inc., USA
Presider

ThD
4:20pm–5:40pm
Flagstaff

Far-infrared semiconductor laser for molecular spectroscopy

R. E. Peale, A. V. Muravjov, E. W. Nelson, *Physics, University of Central Florida, Orlando FL 32816,*
S. G. Pavlov and V. N. Shastin, *Inst. Physics of Microstructures, Russian Academy of Science, GSP-105 Nizhny Novgorod, Russia*
C. J. Fredricksen, *Zaubertek, Inc. 12656 Research Parkway Suite 300, Orlando FL 32826,* info@zaubertek.com

Abstract
The feasibility of the p-Ge laser for far-infrared laser spectroscopy is enhanced by recent progress in single mode selection and tunable external cavities, allowing continuous tuning from 50-140 cm^{-1} without mode-hops.

The far-infrared p-Ge laser operates on intervalence band transitions of holes in crossed electric and magnetic fields when the crystal is cooled to cryogenic temperatures[1]. It has potential for molecular laser spectroscopy in the 1-4 THz range of the electromagnetic spectrum, which is rich in characteristic molecular absorption bands from rotations and low frequency vibrations. Though lasers have become indispensable tools of modern UV-vis-IR spectroscopy, the availability of convenient laser sources has restricted activity in the far-IR (1-10 THz). The only commercial far-IR laser is based on fixed-frequency transitions of molecules in a gas, so that tuning is restricted to a number of discrete wavelengths depending on the choice of gas. Far-IR free electron lasers are so bulky and expensive that only a few facilities exist in the world. By comparison, the p-Ge laser is compact and low cost.
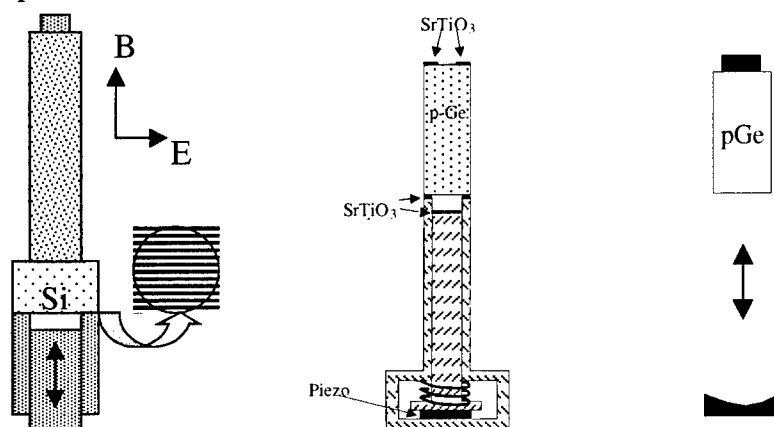

Fig. 1. (*Left*) Piezo controlled tunable p-Ge laser of Refs. [2,3]. The evaporated aluminum stripes on the bottom of the insulating silicon spacer serve as a partially reflecting mirror. The output coupler is a polished copper mirror, smaller than the active crystal cross section, and insulated by teflon film. (*Center*) Improved design of piezo controlled tunable p-Ge laser. The silicon spacer is eliminated and the partially reflecting metal pattern is deposited directly on the active crystal. Electrical insulation from the brass selector apparatus is achieved using $SrTiO_3$ far-infrared mirrors. The copper output coupler is replaced by a $SrTiO_3$ mirror with a ~1 mm hole. (*Right*) External semiconfocal resonator design for a p-Ge laser. The gold-coated silicon curved mirror is separated from the end of the active crystal by a variable space of 1 to 4 cm. The flat output coupler is $SrTiO_3$. The entire cavity resides within a superconducting magnet immersed in liquid helium at 4 K.

The first commercial p-Ge laser was announced in July 2001[4] by Zaubertek. The purpose of this presentation is to report ongoing development of tunable wavelength selectors and cavity design that will directly impact application of the commercial p-Ge laser to chemical spectroscopy.

Fabry-Perot type intracavity wavelength tuners (Fig. 1) can select single longitudinal modes (Fig. 2) from an otherwise broad p-Ge laser spectrum consisting of several hundred modes[2]. The linewidth of single modes is on the order of MHz [5], which is defined by the ~µs duration of the laser pulse.
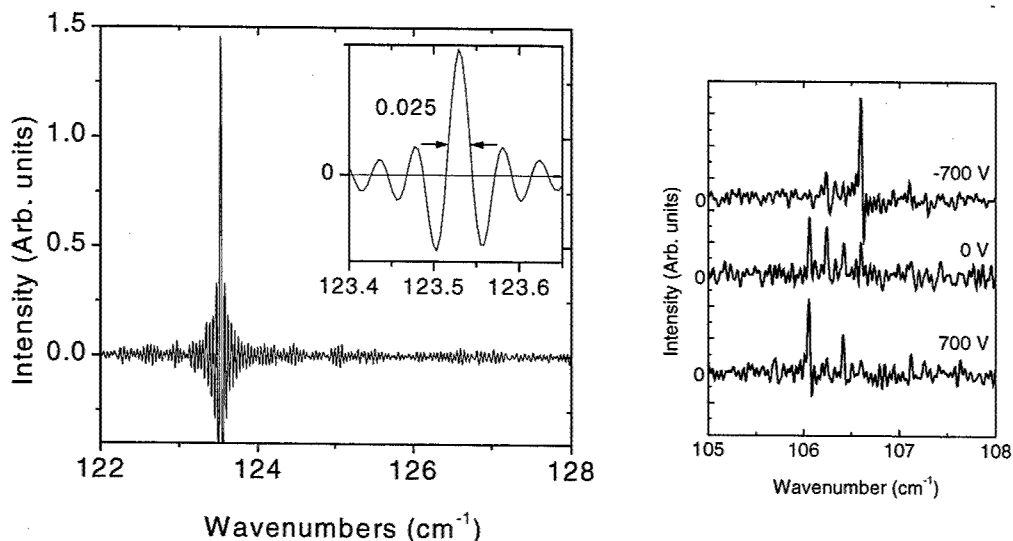

Fig. 2. (*Left*) Emission spectrum of p-Ge laser with selective cavity. Inset: Close-up of peak. The measured FWHM (in cm^{-1}) equals the instrumental line width. The resolution and 40 - 140 cm^{-1} range of the complete spectrum are sufficient to show that only a single longitudinal mode is present. (*Right*) Fine control of the tuning element by a piezo electric actuator for the Fig. 1(left) design shows that single mode emission occurs only for special selector positions and that only every 5th longitudinal laser mode is strong. The text describes a design change that can eliminate these problems.

The wavelength selector can be controlled by piezo-electric actuators (Fig. 1)[3]. The fine control achieved with piezo actuators revealed an additional unwanted selection, which appears as discontinuous tuning between every 5th longitudinal mode (Fig. 2)[3,6]. This effect is caused by resonance in the silicon spacer, which has been used to support a partially reflecting mirror of aluminum evaporated on a face of the spacer and to isolate the brass selector mirrors from the crystal's high voltage contacts (Fig. 1) [6]. The effect can be eliminated by removing the spacer, applying the partially reflecting metal pattern directly to the active laser crystal face, and replacing the brass mirrors in the tunable selector with dielectric SrTiO$_3$ mirrors. Such mirrors have comparable reflectivity to copper, yet do not tarnish or require isolation from the active sample by teflon film. SrTiO$_3$ is harder and more easily polished than metal mirrors, and commercial polished substrate material is usable *as is*.

Next is described cavity developments for the p-Ge laser. Cavity mirrors for p-Ge lasers are traditionally applied directly to the flat polished end faces of high-index media (Fig. 1). In such constructions, the cavity length and longitudinal mode frequencies are

fixed. Tuning can occur only discontinuously between these fixed frequencies, which are separated by a few hundredths of wavenumbers (cm^{-1}) for typical cavity lengths of a few cm. This characteristic is disadvantageous for spectroscopy of sharp molecular absorption lines. A solution is to shift the mode frequencies by controlling the cavity length, which can be achieved if one of the mirrors is separated from the solid medium.

We report here the first demonstration of a p-Ge laser operation with an external semiconfocal resonator of variable length. A 13 mm diameter gold-coated silicon spherical mirror with 15 cm radius of curvature was separated from the end of the active crystal by a several cm(Fig. 1). The output mirror was flat $SrTiO_3$ mirror attached directly to the active sample surface. Stable laser operation was observed over a 1 to 4 cm range of separation between the mirror and the active sample. The combination of a tunable cavity length and an improved tunable selector (Fig. 1 center) would permit broad continuous tuning without mode hops.

A coupled cavity configuration was also explored. An active p-Ge laser cavity using a $SrTiO_3$ mirror with a 2.5 mm centered hole for radiation output was found to be strongly influenced by feedback from an external plane copper mirror. Laser operation could be controllably manipulated when the external mirror was located up to 15 cm away from the laser crystal. This suggests the possibility of controlling the laser operation by such a mirror located outside the cryostat, which would allow use of room temperature frequency selectors or modulators. It also suggests use of an external high-Q passive cavity for ringdown spectroscopy or for ultra-sensitive intracavity laser absorption spectroscopy.

References
1. Special Issue on Far-infrared Semiconductor Lasers, Opt. Quantum Electron., E. Gornik and A. A. Andronov, eds., (Chapman and Hall, London, 1991), Vol. 23.
2. "Single axial-mode selection in a far-infrared p-Ge laser," A. V. Muravjov, S. H. Withers, H. Weidner, R. C. Strijbos, S. G. Pavlov, V. N. Shastin, and R. E. Peale, Appl. Phys. Lett. 76 1996-1998 (2000).
3. "Piezo controlled intracavity wavelength selector for the far-infrared p-Ge laser," E. W. Nelson, A. V. Muravjov, S. G. Pavlov, V. N. Shastin, R. E. Peale, Infrared Phys. Tech., 42 107-110 (2001).
4. "Far-infrared laser," Zaubertek, Inc. new product release, Laser Focus World July 2001, p174.
5. "Mode fine structure of the p-Ge intervalenceband laser measured by heterodyne mixing spectroscopy with an optically pumped ring gas laser," E. Bruendermann, H. P. Roser, A. V. Muravjov, S. G. Pavlov and V. N. Shastin, Infrared Phys. Technol. 36, 59 (1995).
6. "High-resolution study of composite cavity effects for p-Ge lasers," E. W. Nelson, S. H. Withers, A. V. Muravjov, R. C. Strijbos, R. E. Peale, S. G. Pavlov, V. N. Shastin, C. J. Fredricksen, to appear IEEE J. Quantum Electronics, vol. 37, no. 12, Dec. 2001.

Tunable Silver and Gold Substrates for Surface Enhanced Raman Spectroscopy

R. Gupta and W.A. Weimer

Zyvex Corporation. 1321 North Plano Road, Richardson, Texas, 75081
Tel: (972) 235-7881, Fax (972) 235-7882, wweimer@zyvex.com

Abstract: Use of specific combinations of thermal evaporation parameters allows the deposition of surface plasmon resonance tunable silver and gold island films on glass substrates. The utility of these films for surface enhanced Raman spectroscopy is demonstrated.

1. Introduction

Surface enhanced Raman spectroscopy has been used to achieve single molecule detection. To detect single molecules, a significantly large enhancement is needed. Nie and Emory[1], and Kniepp et. al.[2] have independently demonstrated enhancement on the order of 10^{14}, thus achieving single molecule detection. One condition necessary to achieve enhancement is that the incident radiation frequency must overlap the surface plasmon resonance of the substrate[3-5]. Traditionally, this has been done by varying the laser frequency. However, another method is to tune the surface plasmon wavelength of the substrate. By doing so, the surface plasmon resonance can overlap the set frequencies of more economical lasers. When employing a tunable laser, more precise overlap can be achieve, matching the plasmon resonance and the laser line to the absorption maxima of the analyte molecule. This letter describes a method for growing silver and gold island films whereby the surface plasmon resonance can be tuned to frequencies spanning the visible region of the electromagnetic spectrum.

2. Silver Island Films

The process involves adjusting the deposition parameters of a thermal evaporator with respect to substrate temperature, deposition rate, and film thickness. Given an input parameter range, the combinations are optimized using a three-factor, three-level Box-Behnken experimental design. We first attempted this process with silver films, since this has been the material of choice for SERS. The input parameter ranges for temperature, deposition rate, and film thickness were 100-300 °C, 0.3-1.2 Å/s, and 30-120 Å, respectively. The Box-Behnken design of experiments required fifteen runs at specific combinations, including three replicate runs at the parameter midpoints. Transmission spectra were taken on the fifteen samples, and extinction curves were plotted to find the plasmon resonance wavelength. It was evident by the extinction curves that we had indeed achieved plasmon resonance tunability[6].

Upon proceeding with the SERS, we found that our enhancement was due to carbonaceous deposits on the silver surface[7-8]. When we investigated this, we found that silver was highly susceptible to carbon contamination due to it's reactive surface. We then chose to attempt the deposition process with gold. Figure 1 shows the Raman spectra of the source metals. It can be seen that silver exhibits large features due to nanocrystaline carbon, whereas gold is feature-free.

3. Gold Island Films

Our initial deposition parameters for gold were the midpoints of the silver deposition. The results of which showed us that the surface plasmon resonance of gold existed at a much higher wavelength than silver when the deposition parameters were identical. We gauged the effectiveness of each parameter using results received in the design of experiments. From this, we decided to increase the overall substrate temperature range (100-400 °C), decrease the film thickness (10-50 Å), and keep the deposition rate as is (0.3-1.2 Å/s). Once again, the Box-Behnken design of experiments came up with a set of 15 combinations with three replicate runs taken at the midpoint.

We took optical transmission spectra on each of the fifteen samples (in the same manner as the silver substrates), and plotted the extinction curves. We found that the substrate surface plasmon resonance could be tuned through the visible region of the electromagnetic spectrum. Figure 2 shows the optical

transmission spectra of all 15 samples. After determining the surface plasmon resonance wavelength of each sample, we used the design of experiments to come up with an equation relating the plasmon wavelength to the deposition parameters. The equation is as follows:

$$SPRW = (477.284-0.0537037*T) + (140.062*R) + (7.62083*F) + (0.000268519*T^2) - (0.0518519*T*R) - (0.011*T*F) - (67.6955*R^2) - (0.694444*R*F) - (0.0230208*F^2), \quad (1)$$

where SPRW is the surface plasmon resonance wavelength (nm), T is the substrate temperature (°C), R is the deposition rate (Å/s), and F is the film thickness (Å).

4. Further Research

Further studies include a mapping of the surface morphology of the gold films. It has already been shown that there is a relationship between the plasmon resonance and the morphology of the film for both gold and silver[9-10]. The next step would be to precisely link the deposition parameters to a resulting film morphology. Utilizing a TM AMF, we have seen how the plasmon resonance increases with particle size (as seen in Figure 3). However, the plasmon resonance may be further affected by factors such as particle shape and height.

We also intend on performing Raman spectroscopy on the gold island films. We will use a 10^{-6} molar Rhodamine 6G dye in methanol as our analyte, and a 514.5 nm Ar$^+$ laser to excite the sample. We hope to see large enhancement with substrates whose surface plasmon resonance wavelength match both the absorption maxima of the R6G and the laser line.
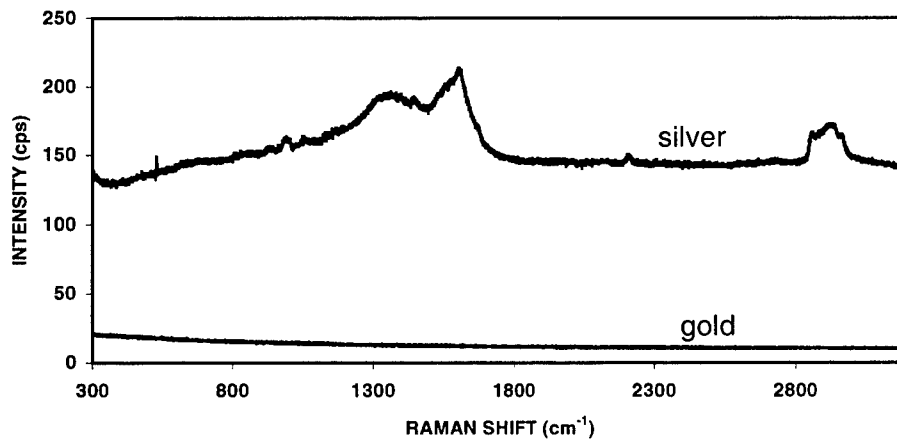

Fig 1. Raman spectra of silver and gold shot used as source materials for thermal evaporation of metal island films.
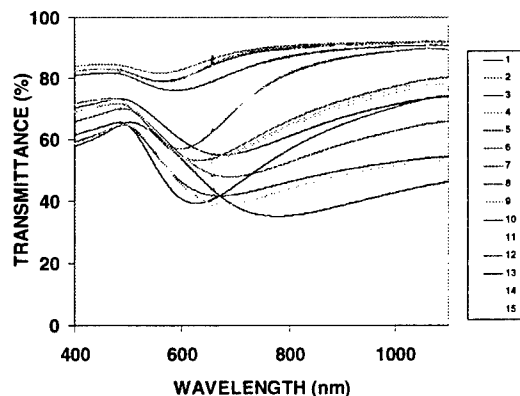

Fig 2. Optical transmittance spectra of gold films.
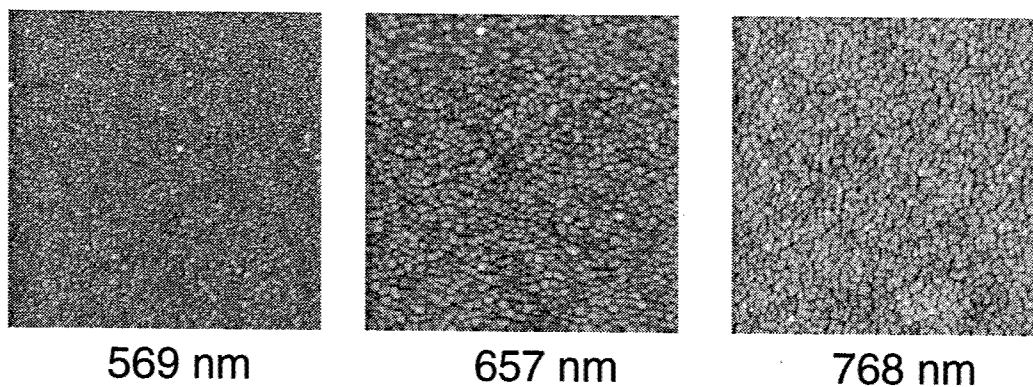
| 569 nm | 657 nm | 768 nm |

Fig 3. Representative atomic force micrographs of gold films, listed with measured surface plasmon resonance wavelengths.

5. References

1. S. Nie and S.R. Emory, Science **275**, 1102-1106 (1997).
2. K. Kneipp, Y. Wang, H. Kneipp, L.T. Perelman, I. Itzkan, R.R. Dasari, and M.S. Field, Phys. Rev. Lett. **78**, 1667-1670 (1997).
3. A. Campion and P. Kambhampati, Chem. Soc. Rev. **27**, 241-250 (1998).
4. M. Moskovits, Rev. Mod. Phys. **57**, 783-826 (1985).
5. A. Otto, I. Mrozek, H. Grabhorn, and W. Akemann, J. Phys. Condens. Matter **4**, 1143-1212 (1992).
6. W.A. Weimer and M.J. Dyer, Applied Phys. Lett. (in press).
7. P.J. Moyer, J. Schmidt, L.M. eng, and A.J. Meixner, J. Am. Chem. Soc. **122**, 5409-5410 (2000).
8. C.E. Taylor, S.D. Garvey, and J.E. Pemberton, Anal. Chem **68**, 2401-2408 (1996).
9. S.R. Emory, W.E. Haskins, and S. Nie, J. Am Chem. Soc. **120**, 8009-8010 (1998).
10. L. Link and M.A. El-Sayad, J. Phys. Chem. **B 103**, 4212-4217 (1999).

All-telecom diode laser based mid-IR source for spectroscopic detection of HF, H₂O and HDO

Dirk Richter, Alan Fried, and Geoffrey S. Tyndall
National Center for Atmospheric Research. Boulder. CO 80305
dr@ucar.edu

Eduardo Oteiza
Coherent, Inc., Santa Clara, CA 95054

Miklos Erdelyi and Frank K. Tittel
Rice Quantum Institute, Rice University, Houston, TX 77005

Abstract: A novel difference-frequency mixing architecture for coherent generation of tunable mid-infrared light is reported. Two CW single-frequency diode laser pump sources operating at 1.56 and 0.98 μm were mixed in a periodically poled $LiNbO_3$ crystal and generated 0.25 mW of tunable mid-infrared light at 2.64 μm. The performance of this new source was demonstrated by the spectroscopic detection of HF and water isotopes $H_2^{16,17,18}O$ and $HD^{16}O$ at various reduced pressures. Using direct absorption spectroscopy, a peak-to-peak noise equivalent absorbance of ~1E-4 was observed (0.6 s integration time), corresponding to a HF detection sensitivity of 12 ppb·m at a sampling pressure of 50 Torr.

1. Introduction

Tunable mid-infrared laser sources are increasingly utilized for rapid precision gas sensing in environmental, industrial, and research applications. For this purpose, advanced compact solid-state laser sources, including quantum-cascade-, lead-salt- and difference-frequency generation (DFG) -lasers have been developed. Primarily, the developments of these sources were aimed at wavelengths covering the 3-5 μm and 6-16 μm region, overlapping with strong fundamental rotational-vibrational bands of many trace gas species [1]. Access to another prime spectroscopic window ranging from 2 –3 μm has been limited due to the difficulty of producing tunable laser sources in this wavelength region. This spectral region offers access to unique absorption bands of HF (S=1E-18 cm molecule^{-1}), H_2O with respective isotopes, NH_3 (free of any water interference), and CO (2.3 μm)[2,3]. This paper describes the design and evaluation of an all telecom diode laser based mid-IR source at 2.64 μm, which can also be configured to operate in the 2.3 – 2.7 μm wavelength range. This source was then used to measure HF and H_2O in a closed cell as means of demonstrating the narrow laser linewidth, and superior amplitude and frequency stability.

2. Experimental

The use of standard telecom diode lasers as DFG pump sources offers robust fiber optic coupling while providing the best possible pump beam quality (i.e. Gaussian), and a wide wavelength coverage by selecting and multiplexing off-the-shelf near-IR diode laser channels. In addition, telecom diode lasers based on InGaAsP/InGaAs/GaAs typically possess similar temperature tuning coefficients as one another (~0.4 cm^{-1}K^{-1}). This offers predictable spectral performance and leads to a self-compensation of wavelength drifts in a DFG-based mid-IR architecture and minimizes the effect of electronic driver temperature instabilities induced by environmental changes. This property can significantly increase the spectroscopic stability and hence the accuracy of gas concentration measurements. In particular, if such a mid-IR source is applied to operate in industrial applications where considerable changes of temperature, pressure and vibrations can be encountered.

Fig.1 shows the optical architecture used in this experiment. A 1562 nm single-mode fiber pigtailed DFB diode laser serves as the DFG pump source and provides an optical fiber output power of 15 mW, with <2 MHz linewidth and a 46 dB sidemode suppression ratio. The output fiber is fusion spliced to an Er/Yb optical fiber amplifier and produces a maximum output power of 575 mW. The long-term power stability of the seeded amplifier was measured to be less than 0.2 % h^{-1}.
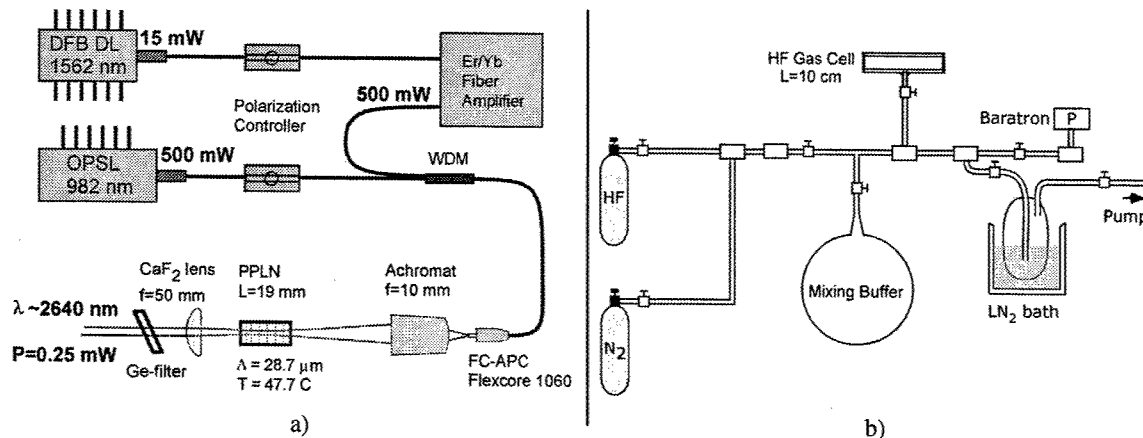

a)   b)

Fig.1: a) Schematic of difference frequency generation laser source at 2.64 μm. OPSL, optically pumped semiconductor laser; DFB DL, distributed feedback diode laser; WDM, wavelength division multiplexer; FC-APC, fiber coupler – angled polished connector; b) Schematic of HF gas filling line. LN$_2$, liquid nitrogen.

The DFG signal source is an optically pumped semiconductor laser (OPSL^{TM}) and has recently become commercially available (Coherent OPSL^{TM} 980-500) [4,5]. The OPSL^{TM} was designed for use as a telecom pump source in Er^{3+} doped fiber amplifiers. Unlike other high-power 980 nm telecom pump diode laser sources, this laser provides excellent spectroscopic characteristics of >500mW single-frequency laser radiation from a single mode fiber (Corning 1060 PureMode^{TM}, Mode field diameter = 5.9 μm @ 980 nm). Both fibered laser sources were fusion spliced to a WDM. The output fiber of the WDM was terminated by a Flexcore 1060 single-mode FC-APC fiber (8° fiber polished end). Respective insertion losses of 11% (OPSL) and 5 % (Er/Yb fiber amplifier) were introduced by fiber fusion splices to the WDM, and inherent WDM coupling losses. The two DFG pump beams were imaged (M~12) into a 19 mm long / 0.5 mm thick PPLN crystal with a 28.7 μm quasi-phasematching period. The PPLN crystal was AR coated with a single SiO$_2$ layer and optical transmissions at 982 nm and 1562 nm were measured to be 0.84 and 0.98, respectively. A plano-convex CaF$_2$ lens (f=50mm) was used to collect and collimate the DFG radiation. Residual pump beams were blocked by a Ge-filter.

For spectroscopic measurements, the DFG beam was directed through a 10 cm long gas-probing cell and the absorption signals detected with an InSb detector. For safety reasons associated with handling HF gas-mixtures, the cell was made from Teflon material (O.D.=1 in. I.D.=0.5 in.), and end-fitted with sapphire windows sealed with Viton o-rings. We employed the filling line depicted in Fig.1b for filling the gas cell with HF dry N$_2$ mixtures at various pressures (1 – 300 Torr). All tubing was made of ¼" O.D. stainless steel or glassware. For safety reasons, the gas filling line was operated under a venting hood and the exhaust gas pumped through a liquid-nitrogen trap to avoid HF contamination of the vacuum pump.

3. Optical characterization and spectroscopic measurements

Before splicing the OPSL^{TM} device to the WDM, the output power as a function of pump current was measured. At a device temperature of 25 °C, a maximum optical fiber output power of 611 mW was observed with a pump current of 2.2 A. With various fiber and achromatic lens insertion losses a pump power of 492 mW (20% total insertion power loss) was available at the input facet of the PPLN crystal. Likewise, insertions losses in the 1562 mm channel resulted in a maximum effective pump power of 440mW (15% total insertion power loss) at the PPLN input facet. A maximum DFG power of 250 μW was measured, which corresponds to a conversion efficiency of 650 ± 25 μW·W^{-2}·cm^{-1}. The conversion efficiency was determined by measuring the slope of DFG power (past the Ge-filter) at different input

power levels. Both pump and DFG power levels were measured with a NIST traceable calibrated thermopile detector.

The mid-infrared radiation could be varied over 7.59 cm^{-1} (6404.98-6397.39 cm^{-1}) by means of temperature tuning the 1562 nm DFB DL from 19.31 °C- 38.65 °C. Within this tuning range the Hitran database [1] lists molecular absorptions of $H_2^{16}O$, $H_2^{17}O$, $H_2^{18}O$ and $HD^{16}O$, HF and NO. For the detection of HF and HDO at 2.64 μm, the DFB-DL was temperature tuned to 6398.599 cm^{-1} (T_{DFB-DL}=35.56 °C) and current modulated by applying a 160 Hz triangular waveform. Fig.2a shows the respective direct absorption spectra averaged over 313 s. The mid-IR scan was frequency calibrated using a Ge-etalon (FSR=0.01601cm^{-1}). An analysis of the Ge-etalon fringe spacing showed a continuous frequency tuning (~1E-3 cm^{-1} pt^{-1}), superimposed by a small 1st order nonlinearity of 8E-6 cm^{-1}/pt (500 pt/scan). This nonlinearity was found to be constant over the DFB DL temperature tuning range, whereas the tuning rate showed a temperature dependence of 8.57E-6 cm^{-1} pt^{-1} °C^{-1}.
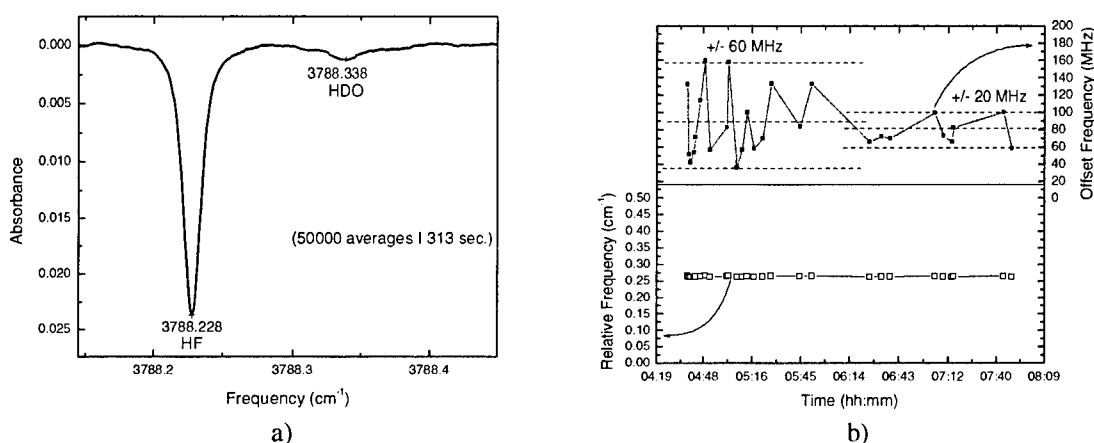

Fig.2: a) Direct absorption spectra of HF and HDO at 2.64 μm (p<10 Torr). The residual peak-to-peak baseline noise is <0.01%. b) Spectroscopic stability in units of cm^{-1} and MHz over a 200-minute time period. The peak fit precisions were better than ±4 MHz and are represented as solid squares in the upper graph 2.b).

To evaluate the long-term spectroscopic stability, HF absorption spectra at 2.64 μm were periodically measured over a 200-minute time period. Fig. 2b depicts the frequency drift shown both as relative frequency within the scanning width and offset frequency. Upon enabling laser operation, a maximum DFG-frequency drift of ±60 MHz was initially observed and this gradually decreased to ±20 MHz over a 2 hour period. At a later time, the drift was less than a 5 MHz over 10 minute time periods. Occasional mode-hopping of the OPSL™ was observed when the laser was operated from a cold start. No mode-hopping was observed after the OPSL™ was continuously operated for 2-3 hours and fully temperature stabilized. In summary, a novel tunable DFG based mid-infrared spectroscopic source at 2.64 μm and its application for the detection of HF and H_2O was demonstrated. Replacing the Er/Yb fiber amplifier with an Er^{3+} doped fiber, inline with the OPSL™ and DFB-DL at 1.5 μm, will result in an ultra compact low cost design [6].

References:

1. L. S. Rothmann, et.al.,"The HITRAN molecular spectroscopic database and HAWKS (HITRAN atmospheric workstation): 1996 edition", J. Quant. Spectrosc. Radiat. Transfer 60, 665-710 (1998)
2. Daniel B. Oh, Alan C. Stanton, "Measurement of nitric oxide with an antimonide diode laser," Appl. Opt. 36, 3294-3297 (1997)
3. Michael E. Webber, Douglas S. Baer, Ronald K. Hanson. "Ammonia Monitoring Near 1.5 μm with Diode-Laser Absorption Sensors," Appl. Opt. 40, 2031-2042 (2001)
4. Mark Kuznetsov, Farhad Hakimi, Robert Sprague, and A. Mooradian, "Design and Characteristics of High-Power (>0.5-W CW) Diode-Pumped Vertical-External-Cavity Surface-Emitting Semiconductor Laser with Circular TEM$_{00}$ Beams," IEEE J. Select. Topics Quantum Electron. 5, 561-573 (1999)
5. Coherent Telecom Group, Santa Clara, CA 95054 USA; URL: http://www.coherentinc.com/cohrtelecom/
6. D. Richter, PhD-thesis, Rice University (2001)

Towards a practical theory of polarisation spectroscopy

J. Walewski[1,], C. F. Kaminski[2], S. F. Hanna[3], and
R. P. Lucht[3]

[1] *Division of Combustion Physics, Lund Institute of Technology, P.O. Box 116,*
SE-221 00 Lund, Sweden
[2] *Department of Chemical Engineering, University of Cambridge, Pembroke*
Street, Cambridge CB2 3RA, U.K.
[3] *Department of Mechanical Engineering, Texas A&M University, College*
Station, TX 77843-3123, USA
+46-46-2220354, +46-46-2224542, joachim.walewski@forbrf.lth.se

Abstract: We present a simple phenomenological theory of polarisation spectroscopy and apply it in an assessing fashion to measurements and detailed theoretical calculations. Our model serves also to interpret polarisation spectroscopy measurements of relative OH concentrations.
© 2001 Optical Society of America
OCIS codes: (300.6290) Spectroscopy, four-wave mixing; (300.6460) Spectroscopy, saturation

1 Introduction

Polarisation spectroscopy (PS) is a resonant four-wave mixing technique dating back to the mid 1970s [1]. In this technique birefringence and dichroism is induced into a sample upon resonant excitation with an intense polarised pump laser. A linearly polarised probe beam is crossed with the pump beam within the sample, and the change in the probe beam's polarisation state due to resonant interaction with the sample is monitored with aid of crossed polarisers on opposite sides of the sample. Although PS features a number of beneficial properties for trace species detection and although it has been demonstrated for several species in flames and cold flows (see section 8.4 in [2] and references therein), it has not yet reached the state of a fully quantitative technique. The main reason for this is the lack of a general and practical PS theory. Teets *et al.* were the first to present a PS theory [3]. Their theory is limited to stationary absorbers and negligible excited state collisions and has not been extendable to realistic measurement conditions, *e.g.* those in a flame, and later approaches offered only little improvement in this respect (see the extensive discussion in [4]). The recent presentation of a general PS theory, based on direct-numerical integration (DNI) of the quantum-mechanical Liouville equation, was the first real breakthrough in this respect [5, 6]. The DNI approach covers, in contrast to former theories, all aspects of a realistic PS theory, *i.e.* it puts no restrictions on collision rates and quenching rates, nor on pump intensity, and it is extendable to combined homogeneous and Doppler broadening, and it may even include a stochastic multi-axial-mode laser model. Despite these favourable attributes DNI suffers from drawbacks due to its numerical nature. First, all input parameters to the DNI code must be known in advance, which impedes the derivation of unknown parameters from measurement data. Second, the DNI code provides no simple models or generic functions describing the PS signal generation process. Such generic models may be highly beneficial for an intuitive understanding of PS and for turning it into a quantitative tool.

In this work we present a practical generic model for PS with which we try to overcome the drawbacks of the otherwise powerful DNI approach. Such a practical model has to fulfil the following demands: 1) Providing simple algebraic relations between measured signal levels and parameters like number density and temperature. 2) Putting no restrictions on collision and quenching rates, nor on the pump intensity, the latter including the saturated regime. The latter is important for trace species detection, where one compensates for low signal levels by increasing the pump intensity. 3) Including both homogeneous and Doppler broadening. The model presented here copes successfully with the first two demands and it is also in excellent agreement with DNI calculations [4], while it in its present form only is valid for homogeneous broadening. Anyhow, comparisons of the presented model with both DNI calculations and measurements for dominating Doppler broadening indicate that the model provides a good description for pump intensities in the unsaturated and partially saturated regime. To demonstrate its potential for practical situations we apply our generic model to PS measurements of relative OH concentrations in a low pressure flame. With the model's aid we are able to explain the observed weak dependence of the PS signal on changes in collision and quenching rates.

2 Theory

In contrast to the algebraically and numerically demanding DNI approach our generic model is algebraically rather simple. Here we assume that the interaction of non-stationary absorbers with the pump field can be described by a two-level system instead of considering all Zeeman sublevels for the rotational levels coupled by the laser, and instead of considering population transfer from and to other rotational levels, as it is done in the DNI approach (see [4] for a thorough discussion). The first level of our model comprises constituents with isotropically distributed orientation and the second level aligned constituents. The latter are the cause of birefringence and dichroism in the sample. The constituents are transfered forth and back between level one and two upon interaction with the pump field. The population in the second level is also transfered to the first level due to collisions and quenching. As the PS signal generation can be described as coherent forward scattering of the probe beam at the aligned constituents [7] one can easily show that the above model results in the following generic equations [4]:

$$I_{PS} = r_{\text{PS}} \times I_{\text{probe}} \quad \text{with} \tag{1}$$

$$r_{\text{PS}} = a \left(\frac{n}{1 + I_{\text{sat}}^{\text{PS}}/I_{\text{pump}}} \right)^2 \tag{2}$$

$$a \sim C_{\text{al}}, \quad \text{and} \quad I_{\text{sat}}^{\text{PS}} = \frac{c\,\Gamma}{2\,B_{\text{PS}}\,C_{\text{al}}}, \tag{3}$$

where I_{PS} is the PS signal, r_{PS} is the so-called PS reflectivity, I_{probe} is the probe intensity, a a is scaling factor, n is the constituent's number density, $I_{\text{sat}}^{\text{PS}}$ is the so-called PS saturation intensity, c is the vacuum velocity of light, Γ is the collision rate, B_{PS} is proportional to the Einstein B coefficient for the pumped transition, and C_{al} is the overlap integral of laser and absorption line profile.

3 Experiment

The proposed generic model and DNI calculations were compared with experiment for a large variation of parameters in Equations 2 and 3. This was done by recording PS power dependence scans from OH in a low-pressure burner for different pressure settings [4]. In this way I_{pump}, Γ, and C_{al} could be varied. We excited the $Q_2(8)$ line in the $A^2\Sigma^+ - X^2\Pi(0,0)$ band of OH in a co-propagating beam geometry. A detailed description of the setup and the conducted measurements is found in [4]. We also conducted PS measurements of relative OH concentrations, see Section **4.2.**

4 Results and Discussion

4.1 *Comparison of DNI Calculations, Generic Model, and Experimental Results*

Because of the rather large bandwidth of our excitation source ($\Delta\nu = 0.3\,\text{cm}^{-1} \approx$ Doppler width), sub-Doppler excitation was not possible. Therfore only DNI calculations could be compared with our generic model for the case of homogeneous line broadening. Figure 1a shows the fit of our generic model to a power dependence scan for a homogeneous linewidth of $0.14\,\text{cm}^{-1}$. The residuals shown in Figure 1b confirm that our generic model provides an excellent description of the PS saturation behaviour over a large span of pump intensities. The same was found for a wide variation of homogeneous and laser linewidths. Also the proposed dependence of the fit parameters a and $I_{\text{sat}}^{\text{PS}}$ on physical quantities (*cf.* Expression 3) was found to agree excellently with DNI calculations [4].

For the case of dominating Doppler broadening the power dependence curve does not level out for large pump intensities. This behaviour is caused by inhomogeneous line broadening of the excited transition. However, DNI calculations and measurements resulted in similar saturation curves and our generic model describes the curve shape well for non-saturating and partially saturating pump intensities. The generic model was fitted to partially saturated power dependence curves for a large range of the pressure (30–900 mbar), and hence for a large range of collision rates and absorption linewidths. Saturation intensities from experiment and DNI calculations were found to be in good agreement [4].
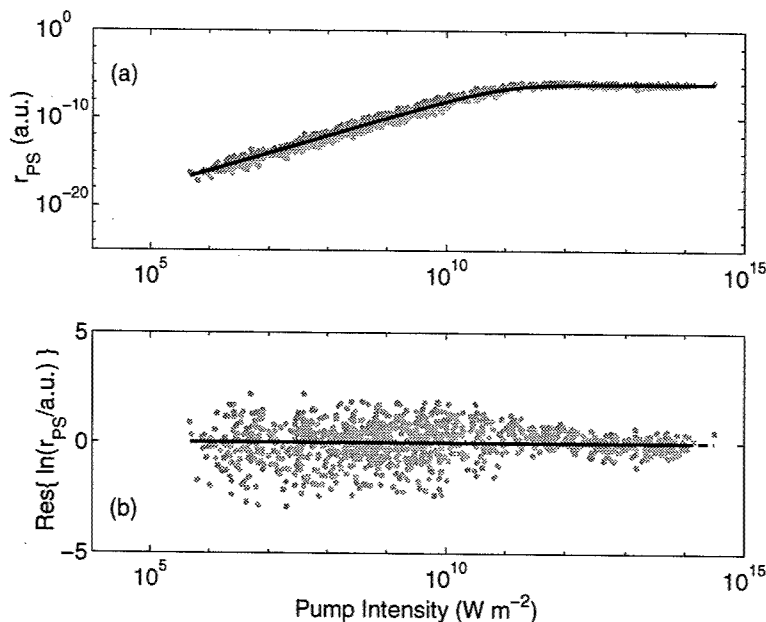
Fig. 1. a) Power dependence scan resulting from DNI calculations (dots) for the $Q_2(8)$ line in the $A^2\Sigma^+ - X^2\Pi(0,0)$ band of OH and a pure homogeneous linewidth of $0.14\,\mathrm{cm}^{-1}$. A stochastic multi-mode laser model is included in the code and a dot represents the signal from a single laser pulse. The solid line is our generic model fitted to the logarithm of the DNI data. b) Residuals of the fit.

4.2 Measurement of relative OH concentrations

PS signals and absorption along the burner's centreline were measured for constant pulse energy for a large range of the pressure ($p = 30$–$900\,\mathrm{mbar}$). When dividing the PS signal with the measured absorbance ($\sim$ number density of OH), the yielded values are only weakly dependent on the pressure. This indicates that saturated PS provides the number density directly without the necessity of correcting for collisions and quenching. This promising result can be readily interpreted with our generic model. Since we measured with partially saturating pump intensities Equation 2 yields $r_{\mathrm{PS}} \approx an^2$, and with $I_{\mathrm{probe}} = const.$ one gets $I_{\mathrm{PS}}/n^2 \approx a \sim C_{\mathrm{al}}$ (Equation 1 and Expression 3), i.e. the scaled PS signal is proportional to the overlap integral of laser and absorption line. For the conditions in the low pressure flame in our experiment the absorption line is dominated by Doppler broadening. Furthermore, from temperatures calculated with a detailed kinetic model of the flame, we judge that the temperature and hence the Doppler broadening in our probe volume is nearly independent of the pressure [4]. The overlap integral and the scaling factor a are thus constant and we derive $I_{\mathrm{PS}}/n^2 \approx const.$, which agrees excellently with our experimental findings.

This example demonstrates the great potential of our model, how it can serve to interpret PS measurements, and how an intuitive understanding of the underlying physical process is readily attained.

References

1. C. Wieman and T. W. Hänsch. Doppler-free laser polarization spectroscopy. *Phys. Rev. Lett.*, 36(20):1170–1173, 1976.
2. A. C. Eckbreth. *Laser Diagnostics for combustion temperature and species.* Overseas Publishers Association, Amsterdam, 1996.
3. R. E. Teets, F. V. Kowalski, W. T. Hill, N. Carlson, and T. W. Hänsch. Laser polarization spectroscopy. In *Proc. Soc. Photo-Opt. Instrum. Eng.*, **113**, pages 80–87, Bellingham, Washington, 1977. Soc. Photo-Opt. Instru. Eng.
4. J. Walewski, C. F. Kaminski, S. F. Hanna, and R. P. Lucht. Dependence of partially saturated polarization spectroscopy signals on pump intensity and collision rate. *Accepted for publication in Phys. Rev. A*, 2001.
5. T. A. Reichardt and R. P. Lucht. Theoretical calculation of line shapes and saturation effects in polarization spectroscopy. *J. Chem. Phys.*, 109(14):5830–5843, 1998.
6. W. C. Giancola, T. A. Reichardt, and R. P. Lucht. Multi-axial-mode laser effects in polarization spectroscopy. *J. Opt. Soc. Am. B*, 17(10):1781–1793, 2000.
7. S. Nakayama. Optical pumping theory in polarization spectroscopy of Na. *Journal of the Phys. Soc. of Japan*, 50(2):609–614, 1981.

Notes

Laser Induced Breakdown Spectroscopy (LIBS)

Friday, February 8, 2002

Kevin McNesby, US Army Res. Labs., USA
Presider

FA
8:00am–10:00am
Flagstaff

Abstract not available

Author: Andrzej Miziolek, Army Res. Lab., USA
Title: Recent progress in the science and technology of LIBS

From Hot Ellipsoid to Colder Torus: Structure and Temperature Changes of Laser Induced Plasmas

K. Rowold, M. Kubitzki, M. Longenecker, K. Hutchison and L. Hüwel
Wesleyan University, Physics Department, Middletown CT 06459-0155
phone: (860) 685-2052; FAX: (860) 685-2031; e-mail: lhuwel@wesleyan.edu

L. Cadwell
Providence College, Department of Engineering-Physics-Systems, Providence, RI 02918

Abstract: Using time resolved emission spectroscopy we have recorded changes in both shape and spectral content of the light emitting region of laser generated sparks in argon during the first 100 microseconds after the laser pulse.
©2000 Optical Society of America
OCIS Codes: (020.0020) Atomic and molecular physics; (020.3690) Line shapes and shifts; (300.0300) Spectroscopy; (300.6210) Spectroscopy, atomic

1. Introduction

A large number of both theoretical and experimental studies[1-3] have revealed details of how laser produced sparks in gases come into existence and how they spread out into the surrounding environment. Somewhat less well investigated is the late time evolution of such plasma plumes. However, it is generally found that visible light emission occurs during the first 100 µs or so after the spark is produced. While detailed values depend on parameters such as gas pressure and laser power density, such emission data indicate that the order of magnitude of the plasma temperature ranges from a few 10,000 K at about 1 µs[4] to several 1000 K at around 100 µs[5,6] after "ignition". We have measured more systematically both the apparent shape of the hot plasma as well as its excitation temperature up to delay times of more than 100 µs. We find that over a period of about 40 µs the plasma is transformed by complex dynamics from an initially roughly ellipsoidal shape into an expanding toroid. There is evidence that at least during the late phase, the laser spark deviates from local thermodynamic equilibrium (LTE) by an overpopulation of ground and lower lying electronic states. Single bubble sonoluminescence studies show that at vastly higher particle densities argon plasmas at similar temperatures are more nearly in complete LTE with even the emission being thermalized to a black body distribution[7]. Under the conditions of our experiment, the characteristic temperature of an argon plasma at atmospheric pressure, initiated by a focussed laser pulse with an estimated power density of 10^{11} W/cm^2 leads to temperatures of about 10,000 to 5,000 K for delay times of 60 and 140 µs, respectively. At that time the plasma kernel has already taken the distinct form of a torus with a core diameter that increases from about 3 to 5 mm during this time span. Apart from the morphology of the plasma which we obtain by time resolved emission imaging of the plasma, we also have measured details of spectrally resolved argon emission in the wavelength range from 675 to 750 nm. Careful analysis of the relative intensities and lineshapes of almost 20 different neutral argon lines leads us to the above quoted temperature ranges and electron densities between 2.0 and 0.7×10^{16} cm^{-3} for the same time interval.

2. Experimental Details

A Q-switched, Neodymium:Yttrium-Aluminum-Garnet (Nd:YAG) laser with wavelength of 1064 nm, pulse energy of about 250 mJ and pulse duration of approximately 20 ns is focused along the vertical direction (z-axis) through a 10 cm focal length lens into a small stainless steel chamber containing high purity argon gas. Two lenses image emission from the plasma onto the slit of a Czerny-Turner 0.6m monochromator which is mounted on its side so that the entrance slit has its long dimension of about 18 mm along the horizontal direction (x-axis). Data were taken with the entrance slit width set to 50 µm. A flat mirror inside of the monochromator in front of the exit slit directs the dispersed light onto a gated, linear diode array (LDA). The array detector consists effectively of 750 diodes, 25 µm x 2.5mm, which are actively intensified by a gated image intensifier. The gate width was adjusted to a duration of 50 ns for delay times up to and including 1 µs and of 1 µs after that. Typically, 100 laser pulses are integrated on the detector and the resulting data file is then stored for further analysis.

3. Spatially resolved Measurements

When the diodes of array are aligned parallel to the entrance slit height (x-axis), each one of them detects the same band of wavelength of about 2.5 nm because of the diode geometry and a monochromator linear dispersion in this spectral range of about 1 nm/mm. The images shown in figure 1 are obtained by interpolation of a set of such horizontal slices through the plasma taken with the plasma laser focussing lens repositioned along the z-axis in steps of 0.25 mm. The gate of the image intensifier was set to a delay time indicated to the right of each panel in figure 1. Since the overall intensity decreases rapidly, emission at the latest delay time were recorded with an amplification of about x100 relative to the maximum emission at 215 ns delay. For all panels, the laser enters from the top and scale and origin of the vertical axis are kept the same. As can be seen, there is only a slight vertical motion of the plasma center of about 1 mm over the period of our observation.
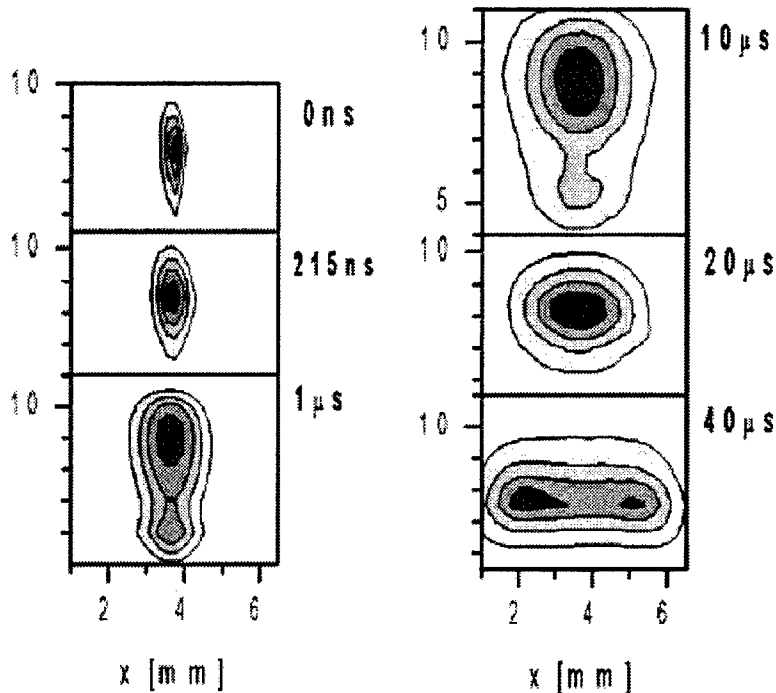

Figure 1: For six different delay times, indicated to the right of each panel, contour plots of the normalized emission intensity at $\lambda = 753$ nm are shown. The relative peak intensity of the last panel is about a factor 100 lower than that at the maximum at 215 ns delay. The graphs represent planes through the plasma center; the 3D shape of the plasma is cylindrically symmetric about a vertical axis through the center.

4. Spectroscopic Measurements

For a specified delay time and at vertical z-position of maximum plasma emission, we have measured the spectral content of the plasma light in the range from about 675 to 750 nm with a resolution of about 0.1 nm. After correcting for instrument collection-detection efficiencies, the emission spectra are fitted by Lorentzian lineshapes. The non-linear least square fit procedure results in three parameters for each emission line: total intensity, center wavelength and thus shift and line width. Using the appropriate spectroscopic constants and a standard Boltzmann analysis, the relative intensities of the emission lines yield an excitation temperature of the plasma. As shown in figure 2, temperatures are found to be between around 5,000 and 10,000 K for delay times of 140 and 60 μs, respectively.

The extremely good fit of the observed lines by Lorentzian lineshape signifies a dominance of Stark broadening. Indeed, for the above quoted temperatures the Doppler contribution to the measure total line width is found to be negligible. Therefore, we use the Griem's theoretical expression for Stark broadened lines[8] in conjunction with the known Stark broadening parameters for argon emission lines at 703.0 and 720.7 nm to obtain the electron density values at the various delay times shown in figure 2.
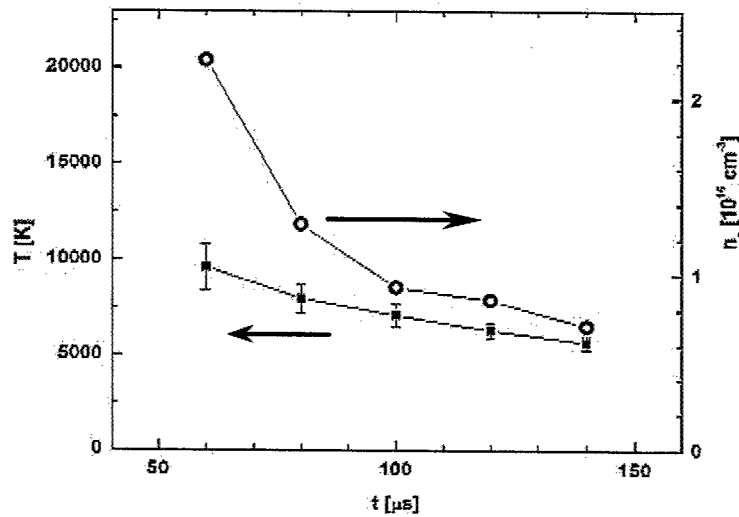
Figure 2: Excitation temperature in K (left scale) and electron density in units of 10^{16} cm^{-3} (right scale) of a laser induced argon plasma at atmospheric pressure as a function of delay time after the laser pulse.

If LTE would prevail under the present conditions, the Saha equation could be used to calculate from the observed temperatures a corresponding equilibrium electron density. However, at a delay time of 60 μs when we find an excitation temperature of about 10,000 K this method would predict an electron density of only 0.7×10^{16} cm^{-3}. Since it plummets near exponentially with temperature, already at about 8500 K the equilibrium electron density would be below 0.1×10^{16} cm^{-3}. Clearly, our data indicate that the electron density in the decaying plasma is not in equilibrium with the excitation temperature obtained for argon states with excitation energies between about 13.3 and 14.8 eV.

5. References:

[1] Y.-L. Chen, J. W. L. Lewis, and C. Parigger, "Spatial and temporal profiles of pulsed laser-induced air plasma emissions," J. Quant. Spectrosc. Rad. Trans. **67**, 91-103 (2000).

[2] T. P. Hughes, "Plasmas and Laser Light", (John Wiley & Sons, New York, 1983), pp. 145-272.

[3] G. Bekefi, "Principles of Laser Plasmas", (John Wiley & Sons, New York, 1976), pp. 457-507.

[4] S. Yalcin, D.R et al., "Influence of Ambient Conditions on the Laser Air Spark", Appl. Phys. B **68**, 121-130 (1999).

[5] R.C. Alam et al., "Time Resolved Emission Spectroscopy in Laser Generated Nitrogen Plasmas," Phys. Rev. A**42**, 383-390 (1990).

[6] D. Nassif and L. Hüwel, "Appearance of toroidal structure in dissipating laser-generated sparks," J. Appl. Phys. **87**, 2127 (2000).

[7] D. Hammer and L. Frommhold, "Sonoluminescence: how bubbles glow," J. Mod. Opt. **48**, 239-277 (2001).

[8] H. R. Griem, "Spectral Line Broadening by Plasmas", (Academic Press, New York, 1974)

LASER INDUCED BREAKDOWN SPECTROSCOPY OF LIQUID AND SOLID SAMPLES IN THE PRESENCE OF MAGNETIC FIELD

Virendra N. Rai,[*] Awadhesha K. Rai,[**] Fang Yu Yueh and Jagdish P. Singh

Diagnostic Instrumentation and Analysis Laboratory, Mississippi State University

205 Research Boulevard, Starkville, MS 39759

Tel: 662-325-7375, e-mail:singh@dial.msstate.edu

SUMMARY

Investigation of optical emission from laser-produced plasma expanding across an external magnetic field is the subject of current interest and has its application in various field of research[1-2]. It is well known that various external parameters such as energy and wavelength of the laser, electric and magnetic field, and ambient condition, affects the plasma parameters and emission properties. The effects of magnetic field on the emission properties of laser-produced plasma have been studied earlier [1-2]. During the process of plasma expansion (deceleration in the presence of magnetic field), the kinetic energy of the plasma is totally transformed into thermal energy of the plasma as well as in the energy of the magnetic field. In this situation, the plasmas emission as well as its various other physical properties change. Effect of magnetic field on the emission from the laser-produced plasma has been studied by many authors from X-ray to visible wavelength range at different experimental conditions. Laser Induced Breakdown Spectroscopy (LIBS) is a laser based diagnostics technique, which has been used to study the atomic emission from various samples such as solid, liquid or gas [3]. In the light of the above discussion, it will be interesting to study the effect of a low intensity steady magnetic field on the LIBS signal from liquid as well as solid samples, which will be important for trace element analysis. In the present experiment we have studied the emission properties of the laser-produced plasma from the metal seeded liquid samples as well as aluminum alloy in the presence of magnetic field.

The details of the LIBS setup for the liquid jet experiment were given in Reference 4. In the solid sample experiment, a Q-switched frequency doubled Nd:YAG laser that delivers a maximum laser energy ~150mJ in 8 ns time duration at 532 nm was used. The laser was operated at 10 Hz. The laser beam was focused on the target of aluminum alloy using an ultra violet (UV) grade quartz lens of 20 cm focal length. The

same focusing lens was used to collect the optical emission from the laser-induced plasma. One UV grade quartz lenses of focal length 100 mm was used to couple the LIBS signal to an optical spectrograph equipped with 1800 l/mm diffraction grating through an optical fiber bundle. Two rare earth (neodymium and samarium cobalt) permanent magnets of size $0.5 \times 0.5 \times 0.125$ inches were used for generating the 5 KG steady magnetic field during this experiment. Finally, data acquisition and analysis were performed using a personal computer.

Fig-1 shows the LIBS spectra of 10ppm aqueous solution of chromium in the absence and in the presence of magnetic field. All the three emission peaks of chromium show enhancement in its intensity in the presence of magnetic field. LIBS spectra of aluminum alloy were recorded at different experimental conditions. The spectra of aluminum alloy contain many emission lines which are from the elements such as Fe, Cr, Cu, Mn and Ti. The effects of laser energy on the LIBS signal of Cr and Fe were studied. The presence of magnetic field shows that line emission intensity remains nearly same up to ~10mJ and then increases up to the laser energy of 20mJ. Further increase in laser energy shows decrease in the line emission intensity. This decrease may be due to self-absorption or due to the generation of instability in the plasma. The temporal evolution of Cr (Fig.-2) and Fe line emission shows that emission intensity increases in the presence of magnetic field. The enhancement in the emission intensity was found to be due to the increase in the density of emitting elements in the plasma plume due to magnetic confinement. The signal enhancement in the presence of magnetic field will depend on the elements and the type of transition. In this study, we found a 1.5 to 2 times signal enhancement in both liquid and solid samples. The detail of the experimental results from the liquid and solid samples will be presented.

LIBS is a promising technique for detecting the trace elements in solid and liquid samples. Since LIBS signal can be enhanced with an external magnetic field, it might be applied to improve LIBS sensitivity for trace analysis.

* Visiting Scientist from CAT, Indore-452013, India

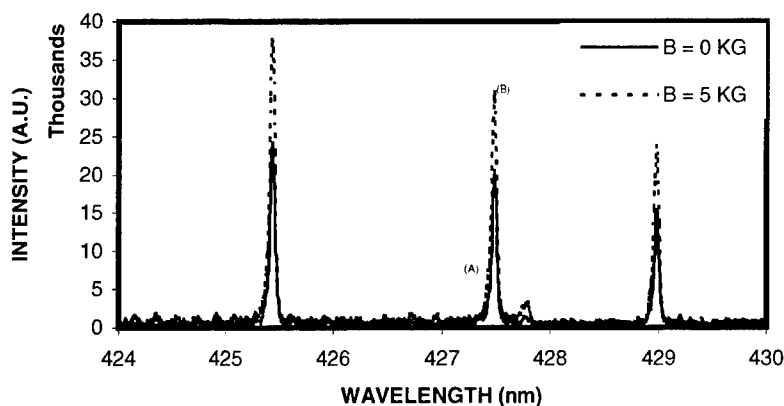** Visiting Scientist from G.B. Pant, University of Ag. & Technology, Pantnagar, India

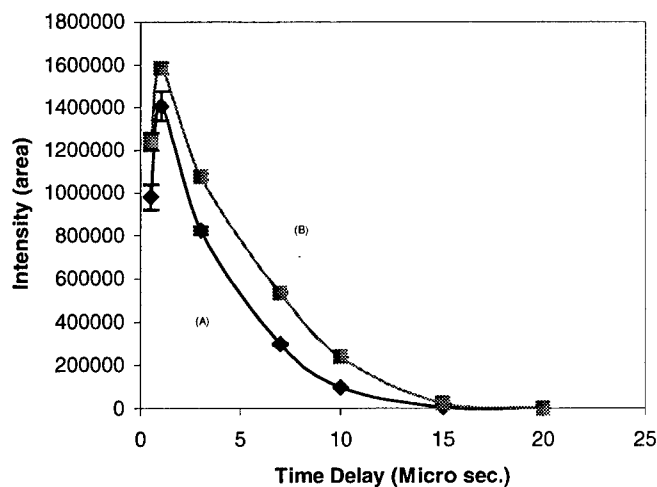Fig.-1 LIBS spectra of 10ppm chromium in the absence and presence of magnetic field

Fig.-2 Variation of LIBS signal with gate delay (A) B=0 KG, (B) B=5 KG

References

[1] K.J.Mason and J.M. Goldberg, Appl. Spectrosc.**45**, 370 (1991).

[2] V.N.Rai, M. Shukla and H.C.Pant, Laser and Particle Beam **16**, 431(1998).

[3] F.Y.Yueh, J.P.Singh and H.Zhang, "Encyclopedia of Analytical Chemistry", John Wiley and Sons Ltd (2000) p.2066.

[4] V.N. Rai, J.P. Singh, F.Y. Yueh, and R.L. Cook, 32nd AIAA Plasmadynamics and Laser Conference, AIAA-2001-2812 (2001).

Rapid Field Screening of Soils for Heavy Metals with Spark-Induced Breakdown Spectroscopy (SIBS)

Richard T. Wainner and Amy J. R. Hunter
Physical Sciences Inc., 20 New England Business Center, Andover, MA 01810
Tel.: 978-738-8142, fax: 978-689-3232, email: wainner@psicorp.com

Abstract: Spark-induced breakdown spectroscopy (SIBS) is a new technique that has evolved from the growing field of LIBS. Here we apply portable SIBS technology to the ideally-suited task of detecting small concentrations (10 ppm) of heavy metals in soils.
©2002 Optical Society of America
OCIS codes: (300.6210) Spectroscopy, atomic; (140.3440) Laser-induced breakdown; (350.5400) Plasmas

1. Introduction

Spark-induced breakdown spectroscopy (SIBS) is a relatively new analytical technique that has emerged from the rapidly-growing field of laser-induced breakdown spectroscopy (LIBS). In general, advances in one field are shared by the other. Both methods generate a high-energy dielectric breakdown, and ensuing high-temperature plasma, in the probe volume and monitor the presence and abundance of particular elements via atomic fluorescence spectroscopy. In each case the material within the thermal plasma is vaporized, atomized (perhaps ionized) and electronically excited. Elemental components of the analyte material within the spark are identified by the unique fingerprint of the spectral emission lines generated by the relaxing excited atoms. The concentration of the species of interest in the sample (spark) volume is proportional to the number of (excited) atoms and to the intensity of the emission of the atomic transition. A number of schemes have been devised recently in the LIBS community for calculating absolute elemental concentrations and the same benefits and challenges of these strategies apply to SIBS.

The significant difference between the two techniques is that while LIBS employs a focused high-intensity laser pulse to generate the spark, the SIBS spark is generated between two rugged electrodes that are subjected to a high-voltage pulse. This eliminates SIBS as a standoff analysis tool and from some solid material analysis, but several important analytical arenas remain available to SIBS interrogation. These include, at the least, fluids, aerosols, grains, and powders. The consistency of soil is a mixture of these last two categories and this report is an investigation of the application of SIBS to the analysis of soils for metal elements of interest (typically heavy metals).

As with LIBS, most often signal detection is delayed a significant amount of time after the spark onset to allow the plasma to cool and the broadband bremsstrahlung (free electron) emission to disappear. However, the SIBS spark is typically much stronger and long-lived and this delay can be up to many tens of microseconds. Spark energies used in this work were usually on the order of 5 Joules, much larger (albeit slower) and more efficiently-generated than the 10-100 mJ typically delivered by pulsed lasers.

SIBS was first developed at PSI to monitor lead (Pb) in particulate aerosols [1-3]. Specific examples where such a tool might be well-utilized are indoor firing ranges and lead paint removal, as on bridges. Further development has lead to new sampling geometries for analyzing soils and powders and for process control. The focus of this research has been to develop the speed, accuracy, sensitivity, efficiency, and portability of this analytical tool for measuring toxic metal (e.g., Hg and Pb) concentrations in soils.

2. Experimental Setup

This research involved two stages of the SIBS soil-analyzing device; the first (phase 1), and earliest, a lab-scale, research-grade setup by which preferred operating parameters were established; the second a miniaturized prototype designed for portability and cost efficiency.

2.1 Spark generator

In both cases the spark generation is the same. This spark is driven by a large capacitor bank (<2000 V, 100 J/s). After these are charged, a transformer provides a high voltage (15-40 kV), low current trigger pulse that initiates the creation of an ion channel between the electrodes. This creates a low resistance path for the prompt discharge of the capacitor bank. The spark can be run from single pulse mode to about 10 Hz, as limited by the power supply. The

discharge heats the air between the electrodes to extremely high temperatures (we have observed Boltzmann temperatures near 20,000 K).

2.2 Sampling apparatus

In both the lab-scale and miniaturized versions, the sampling apparatus is a mobile head entailing a hollow acrylic chamber in which the electrodes are contained, mounted to the housing via ceramic standoffs (see Figure 1). Two high-power electrical leads connect this assembly to the spark-generating unit. The electrodes point downward at an angle to form the spark gap near the open bottom end of the sampling head. This head, and thus the electrode gap, is placed directly over (and near) a small soil sample on a nonconductive plate. The spark gap is typically 4 to 6 mm. The electrodes are composed of proprietary materials which have been chosen for high corrosion resistance, high melting temperature and low ablation propensity. Additionally, it is not common to analyze the emission spectra for these materials as, in most cases, the electrode material emission does not add significantly to the analyte signals. Also, in each case a fiber or light guide is housed in the sampling head and aimed at the spark region.
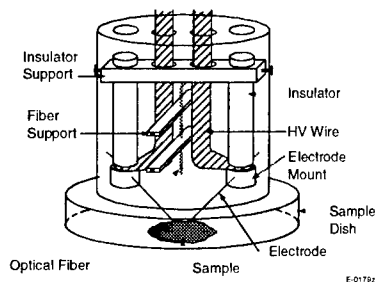

Fig. 1. Diagram of the lab-scale SIBS sampling apparatus.

2.3 Signal detection

The fiber or light guide delivers the light it collects from the spark to a spectrometer. In the phase 1 setup, this device is a 1/3 m Czerny-Turner with a 2400 gr/mm grating and a high resolution (0.025 nm/pixel), 'gate'-able intensified photodiode array at the exit slit. The portable spectrometer is palm-sized and is one of a number of different resolutions (grating/detector) and fixed wavelength ranges. The detection delay is variable for this unit, but the detection gate is fixed and long (ms scale). For wavelengths longer than 450 nm, a 420 nm long-pass filter was employed to reject second order spectral contributions.

3. Results

An initial extensive set of results for Pb, Cr, Hg, and Ba have been acquired with the research-grade setup. SIBS measurements have been performed in metal-doped (and dried) aliquots of a sample of local, loamy Andover soil as well as in the two NIST reference materials San Joaquin soil and Montana soil. As a secondary reference to metal concentrations (and to quantify the doped samples independently), many soil samples were also sent to an outside analytical laboratory for atomic absorption or ICP analysis following sample digestion with aqua-regia. With many concentrations of these exported samples well-known, this also served as a test of the accuracy of one of the standard analytical methods used today for metals concentration analysis. It became clear that metals contributed via doping were easily acid digested in the laboratory, but some naturally occurring constituents are difficult to extract. In this research barium and iron, to a lesser degree, was problematic in this way. Mercury, barium and iron concentrations in Montana soil, for example, were 32.6, 707, and 33800 μg/g. The independent laboratory measured levels of 36, 320, and 26000 μg/g.

SIBS spectra were recorded at many spectral regions, looking at a number of potential emission lines for the elements of interest. However, analytical measurements for the metals mentioned above were performed at 405.78 nm for Pb, 425.43 nm for Chromium, 546.07 nm for Hg, and 553.55 nm or 551.91 nm for Ba. An example of such an emission spectrum and line of interest is illustrated in Figure 2 for Andover soil and Andover soil doped with 200 μg/g added Pb. Line intensities are calculated as peak heights from a local baseline (average of local minima to either side). This approach is especially important when there is partial overlap with bright adjacent interfering lines or when the background continuum radiation is not uniform.
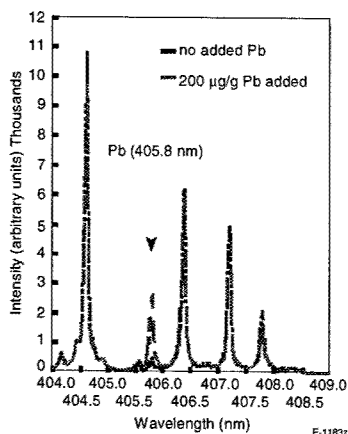
Fig. 2. Excited SIBS emission spectrum between 404 and 409 nm of Andover soil in the absence of added lead and with lead added at a level of 200 µg Pb/g soil. The lead emission is at 405.78 nm. The signal was acquired with a 35 µs delay and 20 µs gate.

The method of standard additions was performed to determine unknown metal concentrations. This well-established technique involves spiking a number of portions of a given soil sample with increasing amounts of the contaminant of interest. This doping has been performed using both a dry additive or a metal salt solution (with subsequent sample drying). A linear fit is made to the signals (normalized by a reference line) generated by each sample plotted against the known added metal concentration. The ratio of the signal at zero added contaminant to the slope of this linear fit indicates the contaminant concentration in the unspiked sample. This is illustrated in Figure 3, where an "unknown" concentration of chromium is determined in a sample of San Joaquin soil. This concentration is actually known and in this case is 111 ± 24 µg Cr/g soil. The prediction from this plot is 130 ± 20 µg Cr/g soil.
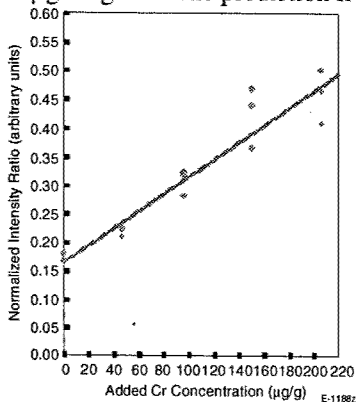

Fig. 3. Ratio of the intensity of the Cr (I) line at 425.43 nm normalized by the Fe (I) line at 427.15 nm as a function of added Cr concentration in San Joaquin soil (111 ± 24 µg Cr/g soil). Signals are acquired with a 40 µs delay and 20 µs gate.

Initial results with the more portable SIBS system are proceeding and are also quite promising. Timing issues and required spectral resolution are being determined. This paper will focus on the development of this physical sytem, optimization of sample handling and preparation (or lack thereof), metal monitoring accuracy, speed, signal normalization, and data processing automation.

4. References

1. Hunter, A.J.R., Morency, J.R., Senior, C.L., Davis, S.J., and Fraser, M.E., "Continuous Emissions Monitoring Using Spark-Induced Breakdown Spectroscopy (SIBS)," J. Air &Waste Management **50**, 111 (2000).

2. Fraser, M.E., Panagiotou, T., Hunter, A.J.R., Anderson, E.B., Davis, S.J., Braybrooke, G., and Hay, K.J., "Fugitive Emission Measurements Above a Hard Chromium Plating Tank Using Spark-Induced Breakdown Spectroscopy (SIBS)," *Plating and Surface Finishing* **87**, No. 1, 80-87 (2000).

3. Hunter, A.J.R., Davis, S.J., Piper, L.G., Holtzclaw, K.W., and Fraser, M.E., "Spark-Induced Breakdown Spectroscopy (SIBS) - A New Technique for Monitoring Heavy Metals," *Appl. Spectr.* **54**, 575 (2000).

Laser Induced Breakdown Spectroscopy of Nineteenth Century Daguerreotypes

John C. Miller
Oak Ridge National Laboratory, Oak Ridge, TN, USA, 37831-6125
millerjc@ornl.gov

D. Anglos
Foundation for Research and Technology-Hellas, Institute of Electronic Structure and
Laser, Heraklion, Greece

Abstract: Laser-induced breakdown spectroscopy (LIBS) has been applied for the first time to 150-year old daguerreotypes, as a prelude to laser ablation cleaning of tarnished examples.

1. Introduction

Millions of daguerreotypes were produced around the world during the two decades between about 1839 and 1860. These delicate, first photographs provided a short-term bridge between the portrait and "miniatures" painters whose artistic images mimicked reality, and modern photographers using paper-based film to capture starkly accurate images of the world.

The chemistry and physics of the daguerreian process are equally fascinating. A comprehensive book by Barger and White gives an overview of the science as well as a rich description of the history and esthetics of daguerreotypes [1]. In the peer-reviewed scientific literature a limited number of papers describe the physical properties of daguerreotypes [2 and references therein]. Likewise, the art conservation literature contains technical details concerning the characterization and restoration of daguerreotypes [1,3 and references therein].

Briefly, daguerreotypes were made by the following process. A highly polished, silver-coated copper plate was exposed to iodine along with bromine or chlorine to form the light-sensitive, silver halide surface. The sensitized plate was then placed in the focal plane of a camera and exposed to light reflected from the subject to be photographed. Exposure to light formed the latent image that is composed of small silver clusters. After removal from the camera, the image was "developed" with mercury vapor, which led to the growth of 0.1 to 100 micron sized particles of silver-mercury amalgam. The image was "fixed' with sodium thiosulfate and "gilded" with a warm solution of gold chloride.

Unfortunately, with the passing of time, most daguerreotypes were plagued by the growth of silver sulfide tarnish. At best, the image was degraded; at worst, it was totally obscured. In general, the presence of tarnish diminishes the esthetic and monetary value of daguerreotypes. The central problem in the storage and conservation of daguerreotypes is the avoidance or the removal of the tarnish. The motivation for the

present work is to understand and characterize daguerreotypes using laser-based techniques as an adjunct to attempts to clean them by laser ablation.

2. Laser induced breakdown spectroscopy – LIBS

Laser-Induced Breakdown Spectroscopy, or **LIBS**, is a semi-quantitative, analytical technique which uses the spectrally resolved emission from a laser- produced spark to provide the elemental composition of a substance. It was the first such technique demonstrated shortly after the invention of the laser in 1960. Initially called (at least for solid samples) laser microprobe analysis, it was first reported in 1962 and formed the basis for a commercial instrument by the mid-sixties. The underlying physics of the laser-matter interaction can be quite complex and several recent books on laser ablation [4,5] provide an entry into the voluminous literature.

Of relevance to the present work, LIBS has recently been used for the characterization of objects of artistic or historic interest. Studies of marble, limestone, stained glass and painted artworks have recently appeared [6]. In addition to the initial characterization of the object, LIBS can provide a real-time, in situ snapshot of the surface layers being ablated, thus allowing the conservator a guide to the progress of the restoration and a quantitative indication of when the cleaning is complete (Gobernado-Mitre, 1997).

The major elements observed by LIBS in the analysis of daguerreotypes are, as expected, silver, copper and gold. The relative peak heights of these elements were not dependent on the position of the laser spot on the daguerreotype. Silver, of course, is always the major peak. The copper can have a variety of sources. Most likely, the silver available and routinely used at the time was simply not the highest grade and contained a fraction of copper in the alloy. The gold arises from the gilding process and it has previously been shown that it appears in all areas of the daguerreotype. The gold is seen only on the surface, however. The spectrum following the second laser shot shows a reduced relative intensity of gold and by the third shot the gold peak can no longer be seen. Several other elements are seen in the spectra at considerably lower intensity. Peaks due to Mg, Ca, Al and Si are observed and may be attributed to glass accretion, household dust and /or remnants of polishing material imbedded in the surface.

Two elements, S and Hg, obviously expected from the daguerreian process or the subsequent tarnishing, were not observed by LIBS, although for different reasons. For the former, the strongest lines are in the vacuum ultraviolet. The absence of mercury may indicate that only a small amount remains from the initial processing. Studies of pigmented daguerreotypes and depth profiling studies were also performed. In many cases, the identity of the pigment can be uniquely determined by its LIBS spectrum. More details may be found elsewhere [7].

3. Laser ablation cleaning

The characterization of the surface structure and composition of daguerreotypes described above served as a prelude to attempts to clean tarnished samples by laser ablation. A proof-of-principle laser cleaning has been demonstrated by the present authors and, independently, by another research group [3, 8].

In order to optimize the experimental conditions for the efficient laser cleaning of daguerreotypes, it was first necessary to determine the best choices of laser power, wavelength and pulse length. Beam quality and spot size (i.e. focussed or not focussed) are also important for the best and most efficient cleaning. We have compared laser cleaning results using the fundamental (1064 nm), second harmonic (532 nm), and third harmonic (355 nm) of Nd:YAG lasers. Both nanosecond (Quanta Ray, 10ns) and picosecond (Continuum, 25ps) versions of the YAG laser were tried. To achieve uniform cleaning, the daguerreotype was moved in a zigzag trajectory in front of the laser beam with displacement increments of 0.2 mm between two laser shots. A computer controlled X-Y translation stage was used to move the sample. When possible, an unfocused laser beam was used in order to avoid focussing "hot spots" from a poor quality beam that could lead to streaking.

So far, the best cleaning results have been obtained using the second harmonic (532 nm) of the 25-psec Nd:YAG laser. Nanosecond pulses usually caused more difficulty with peeling of the silver layer and produced less uniform cleaning when the daguerreotype was exposed to large numbers of laser shots. We also observed a distinct difference in the cleaning depending on the wavelength for the case of the 25-ps laser. For the same energy fluence of 50 mJ/cm^2 and same laser exposure, the second harmonics (532 nm) produced a much better cleaning compared with the fundamental wavelength (1064 nm). We believe the difference can be attributed to the higher optical absorption of tarnish at 532 nm as compared with 1064 nm. However, a more systematic investigation of the wavelength effect for different types of surface contamination is necessary. More details may be found elsewhere [3].

4. References

1. M. S. Barger and W. B. White, The Daguerreotype – Nineteenth Century Technology and Modern Science, Smithsonian Institution Press, Washington DC (1991).
2. D. L. Hogan, V. V. Golovlev, M. J. Gresalfi, J. A. Chaney, C. S. Feigerle, J. C. Miller, G. Romer, and P. Messier, "Laser ablation mass spectroscopy of nineteenth century daguerreotypes", Appl. Spectrosc. **53**, 1161-1168 (1999).
3. V. V. Golovlev, M. J. Gresalfi, J. C. Miller, G. Romer and P. Messier, "Laser characterization and cleaning of nineteenth century daguerreotypes", J. Cult. Heritage, **1**, S139-S144 (2000).
4. J. C. Miller, ed, Laser Ablation: Principles and Applications, Springer Series in Material Sciences Vol. 28, Springer-Verlag, Berlin (1994).
5. J. C. Miller and R. F. Haglund, Jr., eds, Laser Ablation and Desorption, Experimental Methods in the Physical Sciences Vol. 30, Academic Press, New York (1998).
6. D. Anglos, "Laser-induced breakdown spectroscopy in art and archeology", Appl. Spectrosc. **55**, 186A (2001).
7. D. Anglos, K. Melesanaki, V. Zafiropulos and J. C. Miller, "Laser-induced breakdown spectroscopy for the analysis of 150-year old daguerreotypes", Appl. Spectrosc. submitted (2001).
8. I. Turovets, M. Maggen and A. Lewis, "Cleaning of daguerreotypes with an excimer laser", Stud. Conserv. **43**, 89-100 (1998).

Combustion II

Friday, February 8, 2002

Jae Won Hahn, Korea Res. Inst. of Standards, Korea
Presider

FB
10:40am–12:20pm
Flagstaff

Using picosecond pulses for gas-phase laser diagnostics

T. B. Settersten

Combustion Research Facility, Sandia National Labs, Livermore, CA 94551-0969
925-294-4701, tbsette@sandia.gov

Abstract: This work provides an introduction to picosecond laser diagnostics. The temporal and spectral characteristics of picosecond pulses, modeling of their interactions with molecules, and examples of gas-phase diagnostic applications are described.

1 Introduction

The use of picosecond lasers for diagnostic implementations in gas-phase systems is gaining popularity. These lasers provide the diagnostician with unique characteristics that are otherwise unavailable with conventional dye lasers (multimode, nanosecond lasers). First, picosecond lasers can produce pulses that have well-behaved temporal and spectral profiles, have excellent noise properties, and are amenable to modeling. Secondly, the short pulse duration permits adequate time resolution for investigation of dynamic processes and the high peak power necessary for efficient nonlinear processes. Finally, the spectral bandwidth of picosecond pulses is well-matched to the molecular line widths typical in atmospheric-pressure gas-phase systems, producing efficient coupling to the probed species.

Characteristics of picosecond laser pulses are described in "Picosecond Laser Characteristics." An introduction to the subject of modeling of picosecond laser-molecule interactions is given in "Modeling." Finally, examples of applied gas-phase laser diagnostics are given in "Applications."

2 Picosecond Laser Characteristics

The picosecond laser sources considered here produce laser pulses that are nearly transform limited, meaning that the spectral envelope of the laser pulse is the Fourier transform of the temporal envelope. Examples include mode-locked lasers [1, 2], synchronously-pumped dye lasers [3], and distributed-feedback dye lasers [4]. Depending on the laser, the temporal envelope is often modeled as a Gaussian or hyperbolic secant function.

The time-bandwidth product is defined as the product of the intensity full-widths at half-maximum of the laser temporal and spectral profiles, Δt_o and $\Delta\nu_\mathrm{o}$, respectively. The transform-limited time-bandwidth products for Gaussian and hyperbolic-secant pulses are

$$(\Delta t_\mathrm{o}\Delta\nu_\mathrm{o})_\mathrm{G} = 2\ln 2/\pi = 0.441 \tag{1}$$

$$(\Delta t_\mathrm{o}\Delta\nu_\mathrm{o})_\mathrm{S} = \left[2\ln(\sqrt{2}+1)/\pi\right]^2 = 0.315 \tag{2}$$

For example, a transform-limited hyperbolic-secant pulse with a pulse width of 50 ps has a spectral width of 6.3 GHz ($0.21\ \mathrm{cm}^{-1}$). Such a pulse provides the time resolution required to study sub-nanosecond dynamics while efficiently coupling to a typical molecular line width in an atmospheric-pressure system. Furthermore, the peak power of a 100-μJ, 50-ps pulse is on the order of 2 MW. A conventional pulsed dye laser, on the other hand, requires close to 20 mJ per pulse to produce the same peak power.

Compared to typical nanosecond dye laser pulses from a multimode oscillator, picosecond laser pulses are well-behaved and have excellent noise characteristics. Simple analytical functions can be used to faithfully represent transform-limited laser pulses. As a result, comprehensive models describing the laser-molecule interaction are much simpler to implement for transform-limited picosecond pulses than for multimode dye laser pulses. The latter case requires significantly increased computational complexity to accurately model the molecular interactions with the fluctuating laser field [5].

3   Modeling

Quantification of laser diagnostic measurements requires the development of models that describe the physics of the laser-molecule interaction. Both rate equations (RE) [6] and density matrix equations (DME) [7] have been used to describe laser-molecule interactions. The RE relate the temporal derivatives of the population occupying particular quantum levels of an atom or molecule to rates, such as stimulated absorption and emission rates, spontaneous emission rates, quenching rates, etc. On the other hand, the DME are derived from a quantum-mechanical description of the molecular system with the laser field entering the Hamiltonian through a dipole interaction term. In the steady-state limit, coherences in the wavefunction describing the molecule are rapidly damped during the laser pulse, and the DME and the RE are equivalent.

Typically laser diagnosticians rely on the RE to describe the excitation process. Unfortunately, for picosecond excitation in gas-phase atmospheric-pressure systems, the steady-state approximation is not strictly valid, and the DME must be used to properly model laser-molecule interactions [8].

The DME are not as intuitive as the RE and are certainly not as familiar to many laser diagnosticians. Therefore, Settersten and Linne [9] investigated the discrepancies between predictions based on these two formalisms for a wide range of conditions. Their results showed that for linear excitation (less than 20% of the population from the ground state being promoted to an excited state) a linearized RE was in good agreement with the DME. The agreement was good even for "collision-free" systems typical of vacuum cells, where the steady-state limit is clearly violated. On the other hand, the transient details of the excitation process were not estimated well by the RE, as demonstrated in Figure 1. Here, the excited-state population fraction ρ_{22} is shown as a function of time during a 50-ps sech pulse. The RE and DME predictions are shown as dotted and solid lines, respectively. The laser pulse is shown in the bottom panel for reference. The results in the top panel were obtained by setting the homogeneous line width to 3.2 GHz and the excited-state lifetime to 500 ps. For the results in the bottom panel, Doppler broadening is included (the Doppler width has been set to 8 GHz, typical for a light diatomic intermediate in a combustion environment).
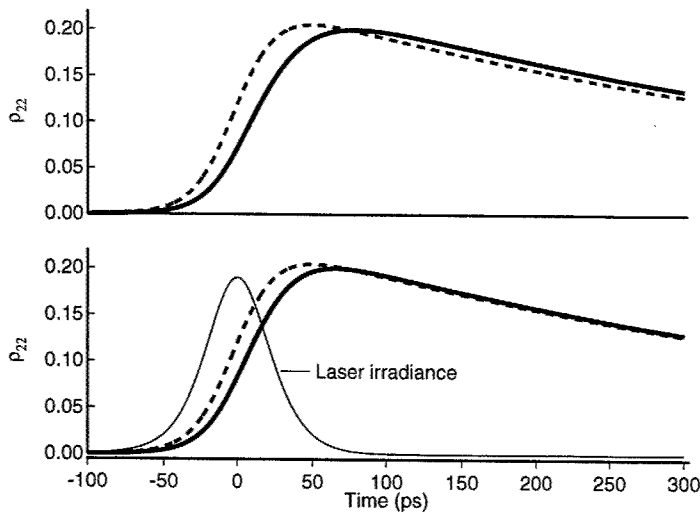

Fig. 1. Excited-state population fraction for a 3.2-GHz homogeneous line width as a function of time during a 50-ps sech pulse. RE results are shown as dotted lines, and the DME results are shown as solid lines. Top panel: no Doppler broadening. Bottom panel: Doppler width is 8 GHz.

Agreement between the RE and DME improves as dephasing of the coherences during the laser pulse increases. Increased dephasing results when either the laser pulse width increases or the elastic collision rate increases. Doppler broadening can also cause dephasing because the coherences for molecules with different velocities oscillate at slightly different frequencies, effectively washing-out the coherent response of the ensemble population. This effect is seen in the bottom panel of Fig. 1.

4 Applications

The time resolution afforded by picosecond laser pulses is ideally suited for dynamics studies in gas-phase systems. Additionally, the high peak power attainable with these lasers is desirable for nonlinear techniques. In this section, some examples of picosecond laser diagnostics are described.

4.1 *Time-resolved LIF*

Conventional LIF diagnostics use nanosecond dye lasers to excite target molecules. When fluorescence lifetimes are shorter than or on the order of the laser pulse width, one must have knowledge of the quenching rate to infer an absolute concentration measurement from an unsaturated LIF signal. Picosecond excitation, however, provides impulsive excitation of the target population, and the excitation and relaxation processes can be effectively isolated. In this case, the fluorescence lifetime can be directly measured either with a streak camera [10, 11] or a microchannel plate photomultiplier tube [12, 13]. Photon counting has also been used to determined the lifetime from multiple picosecond laser shots [14].

The time resolution and the efficient two-photon excitation scheme afforded by picosecond pulses were employed to characterize quenching of the $B\,^1\Sigma^+(v'{=}0)$ state of CO [13]. In these experiments, the CO $B\,^1\Sigma^+(v'{=}0)$ state was populated via two-photon excitation using the frequency-tripled output of a pulse-amplified distributed-feedback dye laser with a pulse width of 55 ps. The $B\,^1\Sigma^+ \to A\,^1\Pi$ fluorescence was collected, spectrally filtered, and detected with a microchannel-plate photomultiplier tube. Quenching cross sections were determined from the dependence of the fluorescence-decay rate on quencher-gas pressure.

4.2 *Picosecond pump-probe techniques*

Pump-probe techniques perturb a sample and then probe the perturbation after some delay. By varying the pump-probe delay, the system response to the perturbation can be determined. Using picosecond lasers, it is possible to study sub-nanosecond dynamics such as molecular energy transfer.

As a variation on this theme, picosecond pump-probe absorption spectroscopy (PPAS) can be used to measure spatially-resolved, absolute species concentrations with reduced sensitivity to collisions [15, 16]. For this technique, the laser beam is split into a pump beam and a probe beam. The two beams are focused and crossed to form the sample volume. When the pump pulse crosses the sample volume, it excites some fraction of the atoms originally in the lower resonant state into the upper resonant state. On the timescale of a weak pump pulse, only stimulated absorption is significant. Several pulse widths later, the probe pulse passes through the sample volume and experiences a modified attenuation due to the pump-perturbed population. The pump beam is modulated, and lock-in amplification is used to measure the differential absorption of the probe beam. Because the pump-probe interaction can occur on a timescale shorter than collisional times, the resulting signal is insensitive to collisional effects.

RE-based and DME-based models can be used to relate the differential absorption of the probe beam to the species number density. By comparing RE and DME models, it was demonstrated that simple RE-based models can be used to accurately describe PPAS provided the excitation is in the linear regime. Furthermore, experimental verification demonstrated quantitative agreement between experimental data and a RE-based model, without the use of any calibrations or corrections [16, 15].

4.3 *Nonlinear Spectroscopy*

Nonlinear diagnostics can benefit from the very high peak power attainable with picosecond pulses. Examples of such techniques include multiphoton processes, such as resonance-enhanced multiphoton ionization and multiphoton LIF, as well as wave-mixing experiments such as polarization spectroscopy [17] and degenerate four-wave mixing [18]. Furthermore, when compared to nanosecond excitation, a picosecond technique may reduce sensitivity limitations imposed by single-photon photolytic interferences because lower pulse energies can be used.

References

1. P. M. W. French, "The generation of ultrashort laser pulses," Rep. Prog. Phys. **58**, 169–261 (1995).
2. A. E. Siegman, *Lasers*, (University Science Books, Mill Valley, CA, 1986), Ch. 27–28.
3. G. J. Blanchard and M. J. Wirth, "Transform-limited Behavior from a Synchronously Pumped CW Dye Laser," Opt. Commun. **53**, 394–400 (1985).
4. P. P. Yaney, D. A. V. Kliner, P. E. Schrader, and R. L. Farrow, "Distributed-feedback dye laser for picosecond ultraviolet and visible spectroscopy," Rev. Sci. Instrum. **71**, 1296–1305 (2000).
5. W. C. Giancola, T. A. Reichardt, and R. P. Lucht, "Multi-axial-mode laser effects in polarization spectroscopy," J. Opt. Soc. Am. B **17**, 1781–1794 (2000).
6. see, for example, J. W. Daily, "Laser induced fluorescence spectroscopy in flames," Prog. Energy Combust. Sci. **23**, 133–199 (1997); R. Kienle, M.P. Lee, and K. Kohse-Höinghaus, "A detailed rate equation model for the simulation of energy transfer in OH laser-induced fluorescence," Appl. Phys. B **62**, 583–599 (1996).
7. see, for example, R.P. Feynman, F.L. Vernon, Jr., and R.W. Hellwarth "Geometrical representation of the Schrödinger equation for solving laser problems," J. Appl. Phys. **28**, 49–52 (1957); M. Sargent III, M.O. Scully, and W.E. Lamb, Jr., *Laser Physics*, (Addison-Wesley, London, 1974); L. Allen and J.H. Eberly, *Optical Resonance and Two-Level Atoms*, (Wiley, N.Y., 1975); B.W. Shore, *The Theory of Coherent Atomic Excitation*, (Wiley, N.Y., 1990), Vol. 1 and 2; R. W. Boyd, *Nonlinear Optics*, (Academic Press, San Diego, CA, 1992), 116–123, 192–199.
8. J. W. Daily, "Use of rate equations to describe laser excitation in flames," Appl. Opt. **16**, 2322–2327 (1977).
9. T. B. Settersten and M. A. Linne, "Modeling pulsed excitation for gas-phase laser diagnostics," J. Opt. Soc. Am. B (submitted).
10. F. Ossler and M. Aldén, "Measurements of picosecond laser induced fluorescence from gas phase 3-pentanone and acetone: Implications to combustion diagnostics," Appl. Phys. B **64**, 493–502 (1997).
11. A. Brockhinke, W. Kreutner, U. Rahmann, K. Kohse-Höinghaus, T. B. Settersten, and M. A. Linne, "Time-, wavelength-, and polarization-resolved measurements of OH ($A\,^2\Sigma^+$) picosecond laser-induced fluorescence in atmospheric-pressure flames," Appl. Phys. B **69** 477–485 (1999).
12. F. Di Teodoro and J. E. Rehm and R. L. Farrow and P. H. Paul, "Collisional quenching of CO $B\,^1\Sigma^+(v'=0)$ probed by two-photon laser-induced fluorescence using a picosecond laser," J. Chem. Phys. **113**, 3046–3054 (2000).
13. T. B. Settersten, A. Dreizler, F. Di Teodoro, and R. L. Farrow, "Temperature- and species-dependent quenching of CO $B\,^1\Sigma^+(v'=0)$ probed by two-photon laser-induced fluorescence using a picosecond laser," in preparation.
14. M.W. Renfro, S.D. Pack, G.B. King, and N.M. Laurendeau, "A pulse-pileup correction procedure for rapid measurements of hydroxyl concentrations using picosecond time-resolved laser-induced fluorescence," Appl. Phys. B **69**, 137–146, (1999).
15. T. B. Settersten, "Picosecond pump/probe diagnostics for combustion," Ph.D. Dissertation (Colorado School of Mines, Golden, CO, 1999).
16. T. B. Settersten and M. A. Linne, "Picosecond pump-probe absorption spectroscopy in gases: models and experimental validation," Appl. Opt. (submitted).
17. T. A. Reichardt and R. P. Lucht, "Degenerate four-wave mixing spectroscopy with short-pulse lasers: Theoretical analysis," J. Opt. Soc. Am. B **13**, 2807–2816 (1996).
18. T. A. Reichardt, F. Di Teodoro, R. L. Farrow, S. Roy, and R. P. Lucht, "Collisional dependence of polarization spectroscopy with a picosecond laser," J. Chem. Phys. **113**, 2263–2269 (2000).

Energy transfer in OH, CH and NO: Implications for quantitative LIF measurements

A. Bülter, U. Lenhard, U. Rahmann and A. Brockhinke
Physikalische Chemie I, Universität Bielefeld, Universitätsstr. 25, D-33615 Bielefeld, Germany
Fax: +49-521-106-6027, e-mail: brockhinke@pc1.uni-bielefeld.de

Abstract: Collision-induced processes (quenching, rotational and vibrational energy transfer, polarization scrambling) affect most LIF experiments. For OH, CH and NO, these processes are studied with picosecond resolution. Methods to obtain quench-free data and implications for flame measurements are discussed.

1. Introduction

Laser-induced Fluorescence (LIF) is one of the most frequently used methods for quantitative minor-species detection. In most cases, atoms or molecules are excited with an appropriate narrow-band laser, and the frequency-shifted fluorescence radiation is detected at right angles. LIF has several advantages such as being non-intrusive, flexible (several dozen combustion intermediates may be detected), offering a high selectivity, high sensitivity (down to the ppb range), spatial resolution and the possibility for time-resolved, single-pulse measurements [1]. In fact, in the major part of the papers published in the most recent issue of *Proceedings of the Combustion Institute* [2], LIF is the method of choice if small radicals are to be detected in high-temperature environments.

However, in most cases the natural lifetime of the excited state is much longer than typical collision times (~100 ps in atmospheric pressure flames). Collisions might thus remove a part of the population ('quenching'), decreasing the total fluorescence yield. Moreover, collisions frequently induce other energy transfer processes and populate different states, further complicating the spectrum. These processes depend on the quantum numbers of the state probed, temperature, pressure and the collision partners (i.e. the chemical composition of the flame) and have to be taken into account for quantitative measurements – usually by either measurements in calibration flames or by measuring the gas composition and computing the quenching correction from literature values.

Short-pulse spectroscopy offers an attractive alternative to this rather complicated procedure: If LIF is excited with a laser pulse with a duration of less than typical collision times and an appropriate detection system is used, quenching effects can be minimized. Observing the temporal decay of the signal even allows completely 'quench-free' measurements and it allows one to create a database that quantifies these effects.

2. Experimental

A laser system based on a regeneratively amplified Ti:sapphire laser which produces tunable, Fourier-limited pulses of 80 ps duration is used as light source. The output is converted to the UV by a combination of KDP crystals for frequency doubling and tripling and a Raman shifter (10 bar H_2). Pulse energies of up to 3 mJ are obtained for the third harmonic radiation with wavelengths between 250 and 300 nm. LIF signals are collected by a spherical mirror in the usual 90 degrees excitation-detection geometry. After passing a Glan-Thompson polarizer, they are spectrally dispersed by a 275 mm focal length monochromator and then detected by a streak camera. The overall temporal resolution of the complete system (including trigger jitter and broadening effects in the detection optics) is about 120 ps and thus is very well matched to the typical time between collisions in atmospheric pressure flames ($\tau_c \approx 100$ ps). This setup is described in detail elsewhere [3, 4].

3. Energy transfer measurements in OH

For these measurements, only moderate pulse energies (in the order of 100 μJ) and mild focussing of the radiation are employed to avoid saturation effects. Several rotational lines in the OH A-X (2-0) transition are probed. Entrance slits of spectrograph and streak camera are oriented perpendicular to each other. This detection geometry yields two-dimensional spectra; temporal resolution corresponds to the vertical axis and the spectral dispersion corresponds to the horizontal axis.
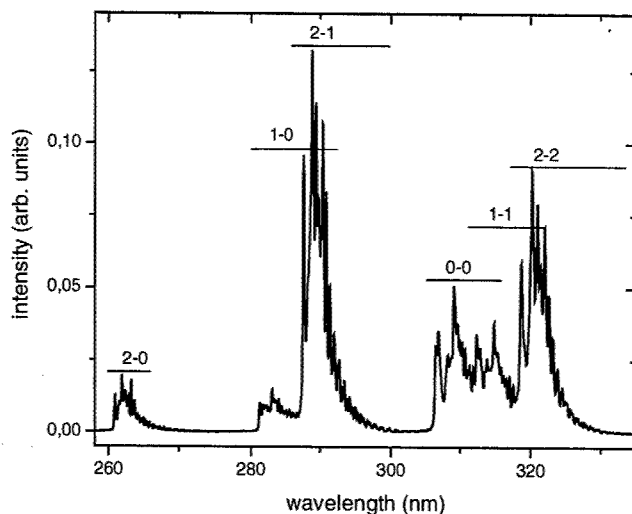
Fig. 1. Time-integrated LIF spectrum after excitation in the OH A-X (2-0) band. Contributions of bands populated by vibrational energy transfer are marked.

Figure 1 shows a time-integrated LIF-spectrum after excitation in the OH (2-0) band. Some fluorescence from the directly populated level is visible in the bands 2-0, 2-1 and 2-2. However, rotational energy transfer (RET) has already taken place, and a multitude of additional rotational lines is visible. Moreover, due to vibrational energy transfer (VET), several additional bands can be observed; their positions are marked in Fig. 1. Since Einstein A-coefficients are usually significantly different for bands populated by VET (for OH, the averaged A-coefficient in the $v'=0$ level is 50% larger in the $v'=1$ level), this has a significant impact on the detected LIF signals. Thus, quenching is not the only process that affects signal strength in this case [6].
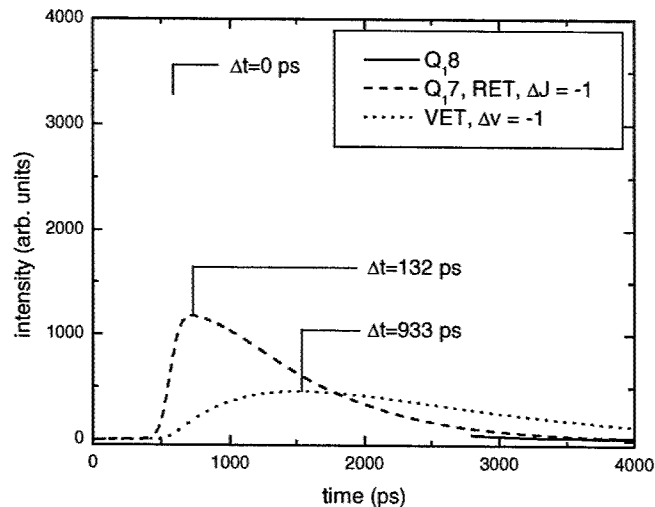
Fig. 2. Temporally dispersed LIF traces for several fluorescence lines after OH A-X (1-0) $R_1(7)$ excitation.

With the simultaneous temporal and spectral resolution of the system used in our investigations, it was possible to study the temporal development of LIF signals. At the time of the exciting laser pulse, LIF signals are dominated by fluorescence from the directly populated level; at later times, the major part of the signal stems from levels populated by RET and VET (Fig. 2).

Furthermore the influence of energy transfer on polarization effects in LIF spectra are studied [4] for both narrow-band and broadband detection. This is important to take into account for quantitative measurements, since most lasers are polarized and efficiencies of many detectors depend on the polarization. Comparisons with energy

transfer models [5, 7] are performed and show a reasonably good agreement. Additional investigations focussed on the role of energy transfer in higher vibrational levels (that is, with $\Delta v = +1$) and on VET steps with $\Delta \leq -2$.

4. Energy transfer measurements in CH

Similar measurements have been performed for CH. Here, the B-X transition has been probed in the (0-0) band. As shown in Fig. 3, this leads to an overlap between the LIF signals (detected in the 0-0 band as well) and Rayleigh-scattered light. However, this can be easily corrected in our time-resolved images. The time-integrated spectrum shows, that most intensity originates from levels populated by RET.
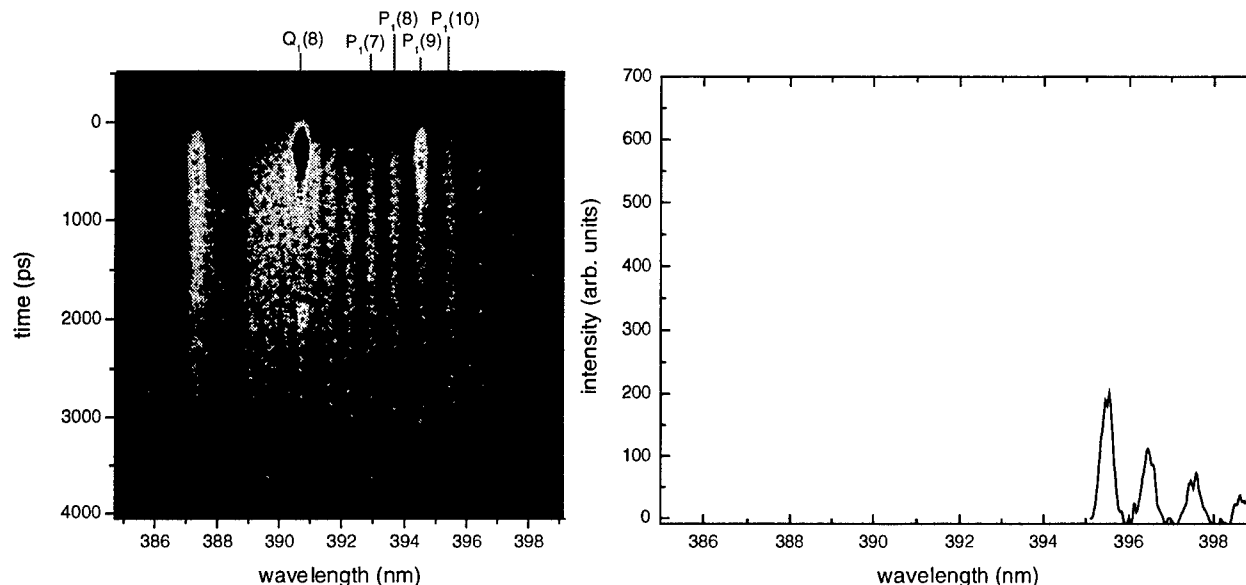
Fig. 3. CH$_4$/O$_2$ flame, excitation CH B-X (0-0) Q$_1$(8).

5. Summary

In this contribution, we discussed LIF experiments with a regeneratively amplified Ti:sapphire laser (80 ps duration, pulse energies of up to 3 mJ in the UV). Signals have been spectrally dispersed by a spectrograph and detected by a streak camera. Energy transfer processes for several molecules (OH, CH and NO) are studied for several excitation lines. Effects of polarization and different detection strategies are investigated. Comparisons with model calculations show a reasonably good agreement. From the time-resolved fluorescence spectra, quench-free results can be obtained by extrapolating the observed decay curves backwards to the time of the laser excitation.

6. References

[1] K. Kohse-Höinghaus, "Laser techniques for the quantitative detection of reactive intermediates in combustion systems", Prog. Energy Combust. Sci., **20**, 203-279, (1994)

[2] Proceedings of the Combustion Institute, vol. **28**, (2001)

[3] A. Brockhinke, A. Bülter, J.C. Rolon, K. Kohse-Höinghaus, "ps-LIF measurements of minor species concentration in a counterflow diffusion flame interacting with a vortex", Appl. Phys. B **72**, 491-496, (2001)

[4] A. Brockhinke, W. Kreutner, U. Rahmann, K. Kohse-Höinghaus, T.B. Settersten, M.A. Linne, "Time-, wavelength-, and polarization-resolved measurements of OH (A$^2\Sigma^+$) picosecond laser-induced fluorescence in atmospheric-pressure flames", Appl. Phys. B **69**, 477-485 (1999)

[5] U. Rahmann, W. Kreutner, K. Kohse-Höinghaus, "Rate-equation modeling of single- and multiple-quantum vibrational energy transfer of OH (A$^2\Sigma^+$, v'=0 to 3)," Appl. Phys. B **69**, 61-70 (1999)

[6] A. Brockhinke, K. Kohse-Höinghaus, "Energy transfer in combustion diagnostics: experiment and modeling", Proc. Royal Soc. (Faraday Discussion 119), in press, 2001

[7] R. Kienle, M. P. Lee, K. Kohse-Höinghaus, "A detailed rate equation model for the simulation of energy transfer in OH laser-induced fluorescence," Appl. Phys. B **62**, 583-599 (1996)

Predictions of chemical species via diode laser spectroscopy

Shin-Juh Chen, Joel A. Silver
Southwest Sciences, Inc., 1570 Pacheco Street, Suite E-11, Santa Fe, New Mexico 87505
Tel. (505) 984-1322, Fax. (505) 988-9230

Werner J. A. Dahm
The University of Michigan, 1320 Beal Avenue, Ann Arbor, Michigan 48109-2140

Nancy D. Piltch
NASA Glenn Research Center, MS 110-3, 21000 Brookpark Road, Cleveland, Ohio 44135

Abstract: A technique to predict temperature and chemical species in flames from absorbance measurement of one chemical species is presented. Predicted temperature and mole fractions of methane and water agreed well with measured and published results.
©2001 Optical Society of America
OCIS codes: (120.1740) Combustion diagnostics; (300.6260) Spectroscopy, diode lasers

1. Introduction

For combustion flows, the determination of temperature is extremely important for quantifying species concentrations from diode laser measurements. Such needs could be circumvented through the use of a novel prediction techniques coupled with combustion models. In non-combusting flows without temperature variations, species concentrations measured using diode laser spectroscopy (DLS) are trivially quantified using simply prepared calibration standards. However, in combusting flows, line shape variations and density corrections become large over the wide range of temperatures experienced. For real-time measurements in time-varying flows, wavelength modulation spectroscopy (WMS) provides the high sensitivity to achieve quantitative detection. But calibration issues in determining the temperature-dependence of spectroscopic parameters and response of the system to varying line-shapes become critically dependent on accurate knowledge of the temperature. While fitting absorption lineshapes or making ratio measurements of line intensities can provide an estimate of local temperature, this is extremely difficult for high bandwith systems.

A generalized approach, referred herein as *Iterative Temperature with Assumed Chemistry* (ITAC), is suggested. From DLS measurements of a single major or minor species absorbance, ITAC can be utilized to quantify the measured species and to predict the other chemical species with the appropriate choice of combustion models. The approach of a conserved scalar (e.g. mixture fraction) is taken here to model the interaction between combustion and fluid dynamics in reacting flows. Chen et al. [1] have already applied ITAC to flame-vortex interactions under microgravity conditions. In this paper, the technique is used to probe chemical species in a methane/air diffusion flame generated by a Wolfhard-Parker burner under atmospheric conditions. Methane concentration is measured and other chemical species and temperature are predicted and compared to published results.

2. Experimental setup

The diode laser spectroscopy system includes the laser system, digital signal processor (DSP) board, controller, data acquisition system and pre-amplifier [1]. The laser beam is collimated by an anti-reflection coated aspheric lens and is pointed onto a raster scanner mirror. As the mirror is rotated over an angle of about 30 degrees, the reflected laser beam hits an off-axis paraboloid reflector (OAP). The scanner mirror is positioned at the focus of this OAP so that all rays reflected by the OAP are parallel. As the beam is swept by the scanner, it tracks in parallel lines across the flame. After traversing the flame, a second OAP collects the beam and refocuses it onto a single photodetector. This optical system can scan a range of up to 4 cm. The result of this process is that data acquired sequentially in time are used to obtain spatially-resolved line-of-sight measurements across a diffusion flame. A diode laser is used to detect the nearly degenerate rotational triplet R3 A2 in the $2v_3$ vibrational band of methane at 1652.9 nm. The HITRAN [2] database is used to analyze the spectra. Wavelength modulation spectroscopy detection is accomplished by digitally modulating (using a modified square wave) the laser wavelength at 25 kHz and detecting the $2f$ (50 kHz) component of the photocurrent. Each spectrum of 65 points, spanning a 1.18 cm^{-1} wavelength range, are recorded in 3.0 msec. A total number of 31 positions are measured across the flame with spatial resolution of 1 mm. The DSP board controls all laser

and scanner ramps, and acquires the raw data from the photodiode. These data are then $2f$ demodulated at the correct phase, normalized to the incident laser intensity and stored for subsequent download and analysis.

The flame is generated from a Wolfhard-Parker burner [7] using methane and air. The burner consists of three sections of rectangular nozzles. The center nozzle is 8 mm × 40 mm with a cold fuel exit velocity of 11 cm/s, and the side nozzles are 16 mm × 40 mm each with a cold oxidizer exit velocity of 22 cm/s. The laser beam is scanned across the width of the nozzle. Methane measurements were conducted at heights of 7, 9 and 11 mm above the nozzle. In this paper, only measurements at 9 mm above the nozzle are presented.

3. Combustion Models

The process of converting measured absorbances to mole fractions is trivial for chemical species in non-combusting flows. However, the process becomes complicated when measurements are conducted in combusting flows. In order to convert measured absorbances to mole fractions, the local temperature needs to be known accurately. Combustion models can be utilized to predict the temperature at the measurement locations. As the Damkohler number (the ratio of characteristic flow time and characteristic chemical time) approaches infinity, equilibrium chemistry dominates the reactions for which the chemical species and temperature are only a function of mixture fraction [3]. The mixture fraction is defined as the ratio of the mass originating from the fuel stream and the mass of the mixture. For finite Damkohler number, non-equilibrium chemistry dominates the reactions for which the chemical species and temperature are functions of mixture fraction and scalar dissipation rate. The scalar dissipation rate sets the molecular mixing rate between the fuel and oxidizer, and it is the instantaneous dissipation rate of the scalar energy per unit mass due to molecular diffusion in the flow.

The state relationships for the equilibrium chemistry suggest that by just knowing the mixture fraction, all the chemical species concentrations and temperature in the flame can be readily determined. On the other hand, the mixture fraction and scalar dissipation rate need to be known for non-equilibrium chemistry in order to accurately determine the chemical species concentrations and temperature. ITAC was implemented and compared using two models.

The first combustion model uses CETPC [4] to generate the equilibrium chemistry database for methane-air reaction. The peak temperature is 2225 K and the stoichiometric mixture fraction is 0.055. The second combustion model uses OPPDIF [5] and includes differential diffusion effects and chemical kinetics to generate near-equilibrium chemistry results. In the computations, the strain rate was set to as low as 2.5 s $^{-1}$. Simplified or full chemical kinetics can also be incorporated into the code. In this case, GRI-Mech 3.0 was used for the chemical kinetics [6]. These databases store the chemical species and temperature as a function of mixture fraction

4. ITAC

At each spatial location, absorbance measurements of the methane mole fraction is provided and analyzed asuuming (arbitrary) T= 300 K at all points. In order to quantify the measurements, temperature needs to be known. The following procedures are used to correct the DLS measurements by determining the temperature iteratively: (1) Guess the mixture fraction. The corresponding mixture fraction for the initial mole fraction as determined from the data can be used as the initial guess; (2) Obtain theoretical mole fraction of methane and temperature for the guessed mixture fraction from the database; (3) Correct mole fraction of methane from DLS using the temperature obtained from the second step. The mole fraction of methane changes with temperature due to the decrease in number density, change in absorption cross section, and from line-shape effects on the WMS response; (4) Compare the methane mole fraction obtained from the database and the temperature-corrected methane mole fraction from DLS measurements. If the two values are comparable, then the correct local temperature was obtained. If not, then the the above procedures are repeated by guessing a new mole fraction and iterating.

5. Results & Conclusions

Figure 1 shows the comparison between published [7], experimental, and predicted results of methane, water, and temperature for the Wolfhard-Parker burner at 9 mm above the nozzle. Note that only measurements of methane absorbances were used with ITAC for predicting methane and water concentrations, and temperature profiles. The iterative process of ITAC guesses and refines the mixture fraction by comparing the resulting mole fraction of methane with the guessed mixture fraction and the mole fraction of methane computed from the methane absorbances with the resulting temperature for the guessed mixture fraction. The discrepancy between the measured concentration of methane (using

Fig. 1. Comparisons between measured, predicted, and published results of methane concentrations (top), temperature (middle), and water concentrations (bottom) in a methane/air diffusion flame of a Wolfhard-Parker burner at 9 mm above the nozzle.
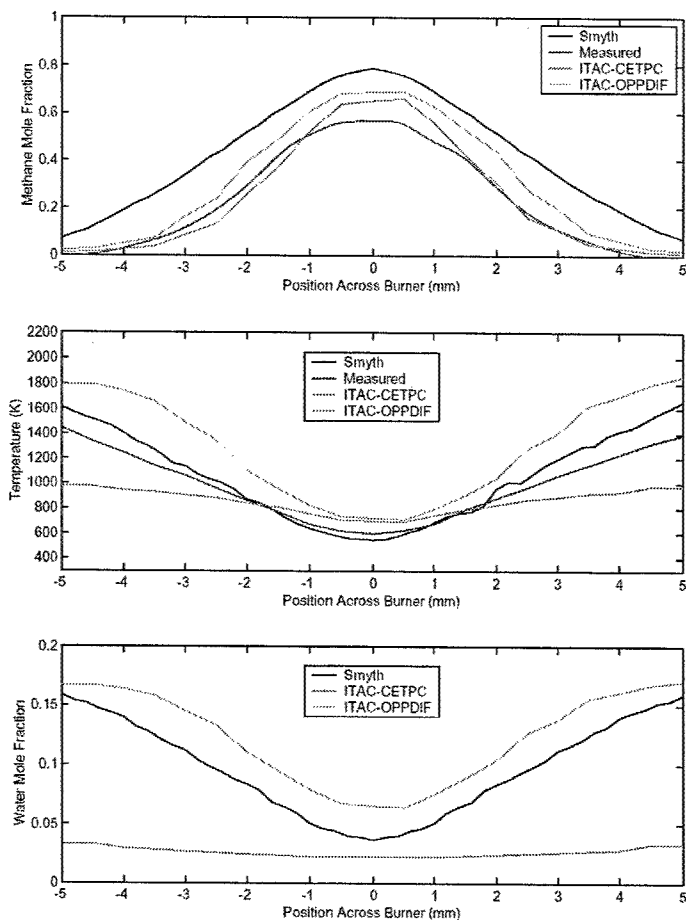
measured temperature for quantifying the absorbances) and the published results of Smyth et al. [7] is possibly due to the incomplete response of the laser to a modified square wave modulation. Concentrations of methane are well predicted by the two combustion models. However, the temperature distribution and water concentrations are not well predicted by CETPC. Better agreement between predictions and measurements is seen with the near-equilibrium model of OPPDIF. The comparisons further suggest that non-equilibrium chemistry models will need to be implemented to improve predictions of the major species and temperature profile, especially the minor species; this will entail the measurement of a radical species (e.g. OH).

The method of ITAC provides a way to predict combustion reactants, products and temperature from the absorbance measurements of one (e.g. CH_4, H_2O, or CO_2) or two species (e.g. CH_4 and OH). ITAC eliminates the need to directly measure temperature in order to quantify DLS measurements, and may prove to be a very powerful tool in monitoring combustion by improving efficiency and reducing the emissions of pollutants.

6. References

1. S. J. Chen, W. J. A. Dahm, J. A. Silver, N. D. Piltch, "Microgravity diode laser spectroscopy measurements in a reacting vortex ring," 39th AIAA Aerospace Sciences Meeting & Exhibit, AIAA Paper 2001-0187 (2001).
2. L. S. Rothman et al., J. Quant. Spectrosc. Radiat. Transfer **48**, 469 (1992); updates in 1998 and 2001.
3. R. W. Bilger, "Reaction rates in diffusion flames," Comb. Flame **30**, 277-284 (1977).
4. B. J. McBride, M. A. Reno, and S. Gordon, "CET93 and CETPC: An interim updated version of the NASA Lewis Computer program for calculating complex chemical equilibria with applications," NASA Tech. Mem. 4557 (1994).
5. R. J. Kee et al., CHEMKIN Collection, Release 3.6, Reaction Design, Inc., San Diego, CA (2000).
6. GRI-Mech 3.0, http://www.me.berkeley.edu/gri_mech/version30.
7. K. C. Smyth, J. H. Miller, R. C. Dorfman, W. G. Mallard, and R. J. Santoro, " Soot inception in a methane/air diffusion flame as characterized by detailed species profiles," Comb. Flame **62**, 157-181 (1985).

Strategies for NO Laser-Induced Fluorescence in Methane/Air Flames at Pressures between 1 and 60 bar

Wolfgang G. Bessler,* Christof Schulz,* Dong-Ill Shin, Tonghun Lee,
Jay B. Jeffries, and Ronald K. Hanson

High Temperature Gasdynamics Laboratory, Mechanical Engineering Department, Stanford University, Stanford, CA, 94305-3032
*Physikalisch-Chemisches Institut, Universität Heidelberg , Im Neuenheimer Feld 253, 69120 Heidelberg, Germany
Jeffries@Navier.Stanford.edu

Abstract: Measurements in laminar premixed methane/air flames at pressures between 1 and 60 bar are used here to compare strategies for NO LIF detection exciting selected transitions in the A-X (0,0), (0,1), and (0,2) bands.

OCIS Codes: (280.1740) combustion diagnostics; (300.2530) laser-induced fluorescence

1. Introduction

Detection of nitric oxide during combustion is of particular interest as NO is one of the most important combustion-generated pollutants. Engine effluent is a major source of NO, and this species influences atmospheric ozone depletion and smog formation. In the future drastic regulatory restrictions on NO release are expected. Laser-based diagnostics techniques are widely used to develop the understanding needed to engineer improvements in practical combustion emissions[1]. Laser-induced fluorescence (LIF) can provide instantaneous two-dimensional images of absolute concentration fields without influencing the combustion process[2]. The NO A-X(0,0) system at 225 nm has been successfully used for measurements in high-pressure methane/air flames[3] and in engines fueled with propane under conditions up to 20 atmospheres[4]. Variations of spectra with pressure and temperature have been studied[5,6]. Measurements in Diesel engines with special geometric arrangements are also reported[7].

LIF of hot molecular oxygen is the main interference that is excited in lean and stoichiometric flames in the respective wavelength range. At pressures of a few bar, the quantum yield of this O_2 LIF is dominated by predissociation, and the NO quantum yield decreases due to collisional quenching whilst the O_2 quantum yields remains constant. As the pressure increases the O_2 LIF quantum yield eventually becomes quenching dominated and the ratio of NO and O_2 LIF becomes constant. In addition, as the pressure increases the collisional broadening of the transitions also increases the spectral overlap. This is further complicated by the predissociation lifetime broadened O_2 excitations. The predissociation lifetime of the excited O_2 varies significantly with the specific vibrational level; thus, careful experiments and spectral simulation are required to quantify this interference. To correct for the interference of O_2 LIF a two-color detection strategy was suggested for lean combustion environments[8].

In this paper we present spectroscopic measurements exciting the NO A-X (0,0), (0,1), and (0,2) bands in a high-pressure burner covering the pressure range 1 to 60 bar[9,10]. Each of the vibrational bands offers a choice of specific rotational transitions with minimum O_2 LIF interference. Based on previous work, we choose the A-X(0,0) P_1(23.5), Q_1+P_{21}(14.5), Q_2+R_{12}(20.5) excitation feature at 226.03 nm[9], the A-X(0,1) Q_1+P_{21}(17.5), R_1+Q_{21}(11.5), P_1(25.5) transition at 235.88 nm[11], and the A-X(0,2) O_{12} bandhead at 247.94 nm[12] providing the best NO LIF/background ratio in the respective vibrational bands. These choices are compared for different equivalence ratios and different detection schemes. Excitation of multiple rotational lines is not a major problem for NO because excited state energy transfer processes are known to be independent of rotational level[13,14].

2. Experimental

Laminar, premixed methane/air flat-flames at pressures between 1 and 60 bar are stabilized on a porous, sintered-bronze plate[15]; the burner housing is pressure stabilized ± 0.1 bar. The fuel/air equivalence ratio ranges between $0.8 \le \phi \le 1.3$, which results in native NO concentrations between 10 and a few hundred ppm[16]. Additional NO is seeded into the feedstock gases to mimic engine-like conditions. The beam of a Nd:YAG-pumped frequency-doubled dye laser is aligned parallel to the burner surface and passed through the center of the flame through quartz windows (fig. 1). Fluorescence signals were collected at right angles to the laser beam, dispersed with a 250 mm imaging spectrometer, and detected on an intensified CCD. The signal is spatially averaged over the uniform flat flame and a fluorescence spectrum is collected for each laser excitation wavelength. This allows us to construct detection filters with arbitrary bandpass to explore the various detection strategies. Alternatively, the spectrometer is replaced by filters to isolate detection of light from the NO (0,1), (0,0), or (0,2) bands for high-pressure LIF 2-D images.
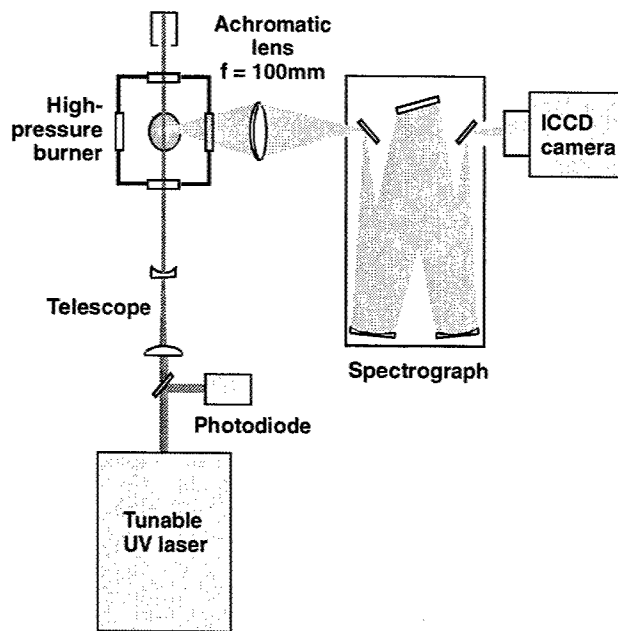
FB4-2

Fig. 1. Experimental Arrangement

3. Results and Discussion

We have examined and compared the A-X(0,0), (0,1), and (0,2) candidate excitations in terms of signal strength, temperature dependence, detection scheme and attenuation of laser and signal light.

LIF diagnostics of practical systems are greatly simplified if the signal is relatively insensitive to the local gas temperature. The Boltzmann population of each of the vibrational manifolds produces quite different temperature sensitivity. In the temperature range relevant in post-flame gases (1500 – 2500 K) the signal intensity after excitation in the (0,0) band decreases with increasing temperature whereas in the (0,1) and (0,2) bands signals are strongly increasing. Minimal variation of the rovibrational population with temperature is found for the intermediate rotational levels in the (0,0) band. The (0,1) band has minimal pressure dependence since the chosen excitation line is within a very dense part of the spectrum where at elevated pressures neighboring lines contribute significantly to the overall signal. The simulated temperature dependence of the NO LIF signal is shown in fig. 2 for $p = 10$ bar. The data in Fig. 2 include the temperature dependence of Boltzmann population, spectral overlap of laser and NO transition, and collisional quenching. Note this temperature dependence can be mitigated with the judicious choice of rotational level and the choice of measuring either number density or mole fraction. Excitation in the (0,0) band has weak temperature dependence of number density; however, excitation of the (0,1) or (0,2) bands can provide mole fraction measurements that are weakly temperature dependent.

The absorption of ultraviolet light by CO_2 becomes quite important in combustion gases at high pressure[17]. There is more than twice the CO_2 absorption at the 226 nm wavelength for NO (0,0) than at the 248 nm excitation for NO(0,2).

4. Conclusions

There are three practical schemes for NO A-X LIF, which involve exciting transitions in the (0,0), (0,1) and (0,2) bands. Although A-X(0,1) excitation with (0,0) detection provides the largest signal strength, least variation of signal with gas temperature, and optimal suppression of O_2 LIF interference, any scheme exciting or detecting (0,0) in high-pressure hydrocarbon combustion is plagued by optical absorption of the excitation or fluorescence light. Excitation of A-X(0,1) with (0,2) detection provides significantly stronger signals with less temperature variation than strategies using (0,2) excitation, and the interference from O_2 LIF is comparable for (0,1) and (0,2) excitation. However, practical engine diagnostics have hydrocarbon fluorescence interference red of the excitation light. The strategy of exciting NO A-X(0,2) and detection of (0,1) provides LIF signal blue shifted compared to the excitation light. This advantage[18] may outweigh the lower signal and greater temperature sensitivity for practical diagnostics applications.

Evaluation of number density

Evaluation of mole fraction

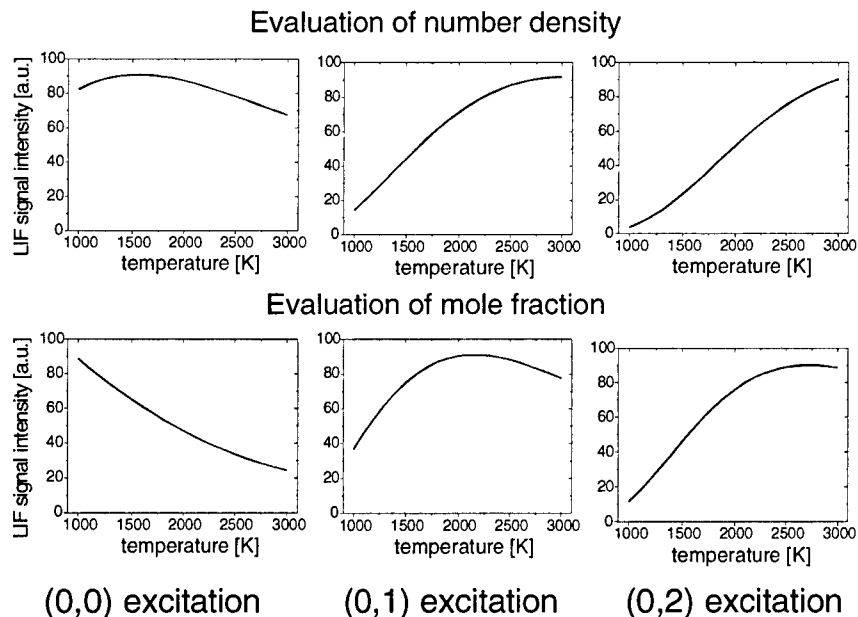(0,0) excitation   (0,1) excitation   (0,2) excitation

Fig. 2. Simulated variation of NO LIF signal with temperature for three excitation strategies. Rotational transitions with minimal O_2 LIF interference have been chosen.

5. Acknowledgement

1   A.C. Eckbreth, Laser Diagnostics for Combustion, Temperature, and Species, 2nd ed., Gordon and Breach, Amsterdam, 1996.
2   K. Kohse-Höinghaus, Prog. Energy Combust. Sci. 20, 203-279 (1994).
3   A.O.Vyrodow, J. Heinze, M. Dillmann, U.E. Meier, W. Stricker, Appl. Phys. B 61, 409-414 (1995).
4   A. Bräumer, V. Sick, J. Wolfrum, V. Drewes, R.R. Maly, M. Zahn, SAE Paper No. 952462 (1995).
5   M.D. Di Rosa, R.K. Hanson, J. Mol. Spectrosc. 164, 97-117 (1994); M.D. Di Rosa, R.K. Hanson, J. Quant. Spectrosc. Radiat. Transfer 52, 515-529 (1994).
6   W.P. Partridge, Jr. M.S. Klassen, D.D. Thomsen, N.M. Laurendeau, Appl. Opt. 35, 4890-4904 (1996).
7   J.E. Dec, R.E. Canaan, SAE paper No. 980147 (1998).
8   M.D. DiRosa, K.G. Klavuhn and R.K. Hanson, Comb. Sci. & Tech. 118, 257-283 (1996).
9   W. Bessler, C. Schulz, T. Lee, J.B. Jeffries, R.K. Hanson, Appl. Opt., submitted 2001.
10 C. Schulz, B. Yip, V. Sick, J. Wolfrum, Chem. Phys. Lett. 242, 259-264 (1995).
11 W.G. Bessler, C. Schulz, T. Lee, J.B. Jeffries, R.K. Hanson, Western States Section / The Combustion Institute, 2001 Spring Meeting, Oakland, CA (2001)
12 C. Schulz, V. Sick, J. Heinze, W. Stricker, Appl. Opt. 36, 3227-3232 (1997)
13 F. Fernandez-Allonse, G.A. Raiche, D.R. Crosley, Spring meeting, Western States Section, The Combustion Institute, paper 94-047 (Sandia National Laboratories, Livermore, CA) (1994).
14 P.H. Paul, J.A. Gray, J.L. Durant Jr., J.W. Thoman Jr., AIAA Journal 32, 1670-1675 (1994).
15 H. Eberius, T. Just, T. Kick, G. Höfner, W. Lutz, Proc. Joint Meeting German/Italian Section Comb. Inst., Ravello (Italy), 3.3 (1989).
16 C. Schulz, V. Sick, U. Meier, J. Heinze, W. Stricker, Appl. Opt., 38, 1434-1443 (1999).
17 C. Schulz, J. Koch, D.F. Davidson, J.B. Jeffries, R.K. Hanson, Chem. Phys. Lett., submitted 2001.
18 F. Hildenbrand, C. Schulz, A. Hartmann, F. Puchner, G. Wawrschin, SAE paper No. 1999-01-3545 (1999)

Combustion III

Friday, February 8, 2002

Jae Won Hahn, Korea Res. Inst. of Standards, Korea
Presider

FC
2:00pm–3:00pm
Flagstaff

Investigations on laser-induced incandescence (LII) for soot diagnostics at high pressure

Max Hofmann, Wolfgang G. Bessler, Joachim Gronki, Christof Schulz, Helga Jander*

Physikalisch-Chemisches Institut, Universität Heidelberg, Im Neuenheimer Feld 253, 69120 Heidelberg, Germany
*Institut für Physikalische Chemie, Universität Göttingen. Tammannstr. 6, 37077 Göttingen, Germany

Abstract: LII has been investigated in sooting ethylene/air flames at 1 – 15 bar with wavelength-, energy-density- and time-resolved detection. LII decay coefficients increase linearly with pressure. Pressure influence on the LII intensity is limited with prompt detection.

OCIS codes: (120.1740) combustion diagnostics; (300.6280) fluorescence, luminescence

1. Introduction:

Laser-induced incandescence (LII) has proved to be a powerful tool for soot diagnostics. It has been used successfully for measuring volume fractions of soot in flames[1] and exhaust gases[2] as well as non-carbon particulates[3]. Particle sizes have been deduced from the temporal behavior of the LII signal[4].

Nevertheless, many aspects of the microscopic processes during irradiation of soot particles with intense laser light still remain unknown. The influence of particle morphology and chemical composition is barely known and not yet included in LII models. While applications in high-pressure environments (namely IC engines) are frequently performed, systematic investigations of LII at elevated pressures are lacking.

One issue is of main interest when evaluating LII measurements obtained at high and potentially variable pressure: Is the LII yield systematically changing with pressure; i.e. is a correction of pressure influence necessary when comparing LII intensities obtained at various pressures, and is it possible to use calibration flames operated at atmospheric pressure for quantifying LII signals obtained under elevated pressures?

We measure LII intensities at 1 – 15 bar in laminar sooting ethylene/air flames with wavelength, excitation-energy-density- and time-resolved detection. Additionally, soot volume fractions were obtained from modulated HeNe-laser absorption measurements[5].

2. Background:

The LII signal intensity is governed by numerous competing processes[6]. While the absorption of laser light heats up the soot particles, energy loss occurs due to evaporation, heat conduction and radiation. In the low laser energy-density regime LII intensities rise monotonically with laser intensity. At high laser energies soot evaporates during the laser pulse duration which decreases the LII signal intensity. In the intermediate plateau region the variation of LII with laser energy density is minimized. LII models have shown[6] that for this condition of maximum particle temperature the LII signal is nearly proportional to soot volume fraction.

In practical applications, usually laser profiles with energy gradients (i.e. Gauss profiles) are employed which yield LII signal from an increasing cross section with increasing laser energy. With spatially integrated detection, the LII signal eventually becomes constant with increasing laser energy[1], minimizing the influence of laser attenuation. For fundamental investigations, however, the use of spatially invariant laser energy densities (tophat) are preferred.

3. Experimental:

Laminar premixed ethylene/air flames (C/O ratio: 0.65 – 1.05, p = 1 – 15 bar) were stabilized on a flat flame burner. The central sooting flame (20.5 x 37.5 mm^2) is surrounded by a lean flame (81 mm dia.). The burner consists of a stack of vertically oriented 15 µm thick aluminum foils. Every second foil has a corrugated profile resulting in parallel vertical channels 30 µm in diameter[7]. The burner housing is equipped with three quartz windows. A section of a doughnut-shaped beam of a frequency doubled Nd:YAG laser (10 mJ/pulse) was separated with slit apertures and one-dimensionally focused into the sooting flame (local laser power densities up to 100 MW/cm^2). Signals were collected at right angle and focused (*Halle*, f = 100 mm, $f_\#$ = 2) on the entrance slit of an imaging spectrometer (*Oriel*). The resulting images were detected with an intensified camera (*LaVision*, flamestar 2). The modulated beam of a HeNe laser was combined with the beam of the doubled Nd:YAG via a dichroic mirror from the opposite direction, detected with a photodiode and analyzed with a lock-in amplifier.

To investigate the influence of laser energy on the LII signal while at the same time being able to reliably identify the plateau region, we use a laser profile with a tophat energy profile in one dimension and Gauss in the

second dimension. Whereas the tophat-dimension is spatially averaged, the axis with varying laser energy densities is imaged onto the entrance slit of the spectrometer. With a single laser shot measurements at various energy densities are therefore carried out simultaneously. During data reduction, the area where the plateau assumption holds was extracted. This ensures comparable local conditions in the volume under investigation independent of laser attenuation. Fig. 1 demonstrates this technique. While the laser energy density increases towards the middle of the frame, the resulting LII signal (color coded in the right image) is maximum at intermediate laser energies. The maximum represents the plateau region and can easily be extracted.

The images were corrected for signal attenuation by soot using the soot volume fraction obtained by the extinction technique using soot optical property data from[8].
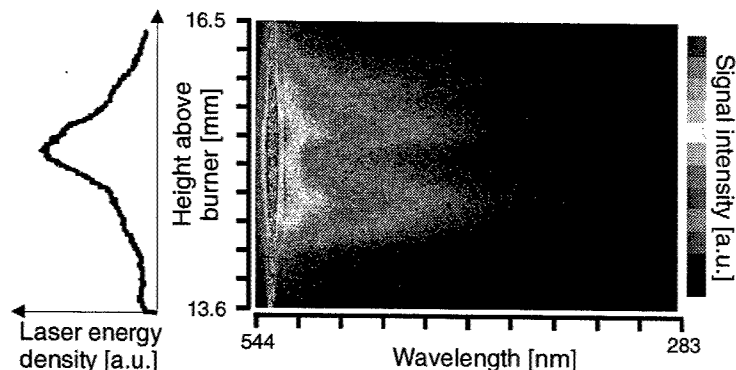
Fig. 1. Wavelength- and laser-energy density-resolved detection of LII signal. The bright line at 532 nm is scattered light. The laser intensity distribution (determined from the Rayleigh signal at a total laser energy below vaporization threshold) is shown on the left.

4. Results:

A. Spectral purity: Wavelength-dependent detection of LII-emission spectra enabled us to detect the presence of interference. Mainly laser-induced fluorescence of small molecules (C_2) has frequently been discussed to interfere with the LII signal at high laser power densities[9]. This can easily be distinguished from LII by its narrow-band emission. In the present experiments, no evidence of C_2 signals was found in the emission spectra in the complete investigated range of laser energies, pressures, and equivalence ratios (cf. fig. 1). Although being above the soot vaporization threshold, we believe that laser power density was too low to produce excited C_2 molecules.
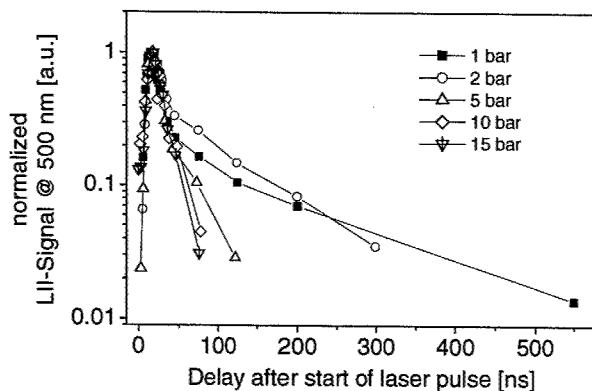
Fig. 2. Time-dependence of the LII signal at various pressures (normalized).
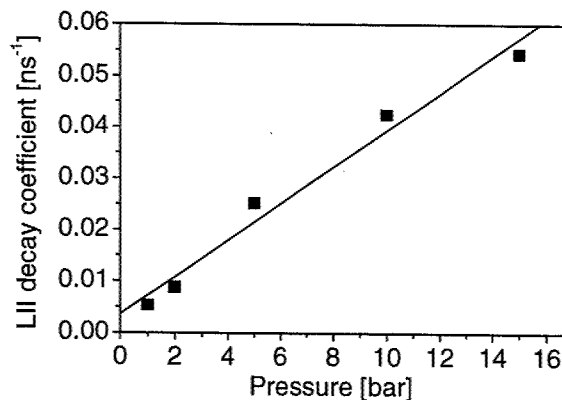
Fig. 3. LII-decay coefficient for various pressures.

B. Temporal development of the LII signal: We investigated the signal decay as a function of pressure using gated detection (5 ns) at various delays after the beginning of the laser pulse. The temporal development of the LII signal for the investigated pressures is shown in fig. 2. The decay curves are normalized to their maximum. During the first 50 ns after onset of the laser pulse, the LII signals are self-similar and the temporal development does not depend on pressure. Models show that this is the regime where vaporization is the dominant heat loss mechanism[4]. Later, the decay rate increases strongly with pressure, with the signal decay being exponential. Here, heat conduction is the dominant cooling mechanism. The exponential decay coefficient was determined from the LII signals 50 ns after the

onset of the laser pulse. It is plotted vs. pressure in fig. 3. The results show that the decay coefficient is linearly proportional to pressure which has been predicted earlier for soot particle sizes in the Knudsen regime[10].

For soot volume fraction measurements, the LII signal is usually temporally integrated. Figs. 2 and 3 show that the pressure influence on such measurements will be severe when integrating over times longer than 50 ns after onset of the laser pulse or when using delayed detection[11]. For the comparison of the LII technique with extinction measurements we therefore chose a prompt detection gate of 50 ns.

C. Comparison to soot volume fraction extinction measurements: From images as shown in fig. 1 the LII signal was integrated over a 400 ± 15 nm band pass at the plateau region. C/O ratio, gas velocity and detection height above burner were varied for any given pressure to yield a wide range of soot volume fractions. Fig. 4 shows the LII signal plotted versus the soot volume fraction as obtained by the extinction technique. The LII error bars are due the correction of signal attenuation using the extinction data (which themselves have uncertainties in extinction, path length, and soot refractive index) and due to minor flame fluctuations.
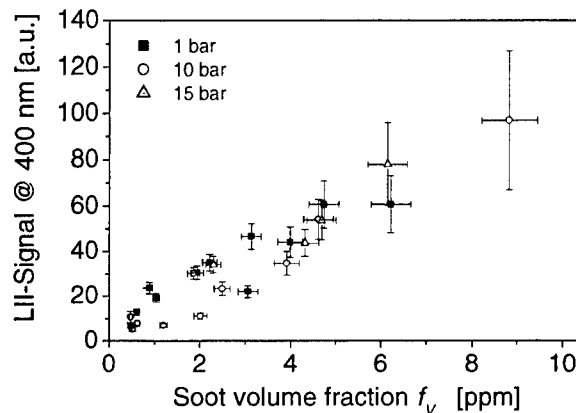
Fig. 4. LII signal intensity vs. soot volume fraction measured by laser attenuation for 1, 10 and 15 bar.

Significant differences in LII vs. soot volume fraction are observed when varying flame conditions (in terms of C/O ratios and gas velocities). We believe that the scattering of the data points is at least partly due to changes in soot particle diameter and -morphology when changing flame conditions. Within the range of LII intensities, no systematic effect of pressure on the proportionality of LII signal vs. soot volume fraction can be found. Since the scatter of the data points at fixed pressure is of the same magnitude as the scatter between different pressures, the results indicate that there is only a minor influence of pressure on the LII intensity with prompt (50 ns) detection. This, however, indicates that further influences on LII signal intensities must be investigated which might complicate the transfer of calibration information obtained from standard flames.

5. Summary:

Systematic investigations of the LII process at 1 – 15 bar were performed. The time-resolved measurements show that the LII decay rate in the heat conduction regime is linearly proportional to pressure. Comparison with soot volume fractions obtained by extinction measurements do not show a significant influence of pressure. When using prompt detection, calibration of the LII signal at atmospheric pressure should be feasible for high-pressure applications. However, the influence of varying flame conditions on LII must be addressed.

1   T. Ni, J. A. Pinson, S. Gupta, R. J. Santoro, Appl. Opt. 34, 7083 (1995)
2   D.R. Snelling, G.J. Smallwood, R.A. Sawchuk, W.S. Neill, D. Gareau, D.J. Clavel, W.L. Chippior, F. Liu, ".L. Gülder, SAE Paper No. 2000-01-1994 (2000)
3   R.L. Vander Wal, T.M. Ticish, J.R. West, Jr., Appl. Opt. 38, 5867 (1999)
4   S. Will, S. Schraml, K. Bader, A. Leipertz, Appl. Opt. 37, 5647 (1998)
5   T. Pape, PhD-thesis, University of Göttingen (1997)
6   L. A. Melton, Appl. Opt. 23, 2201 (1984).
7   S. Hanisch, H. Jander, T. Pape, H.Gg. Wagner, Proc. Comb. Inst. 25, 577 (1994)
8   H. Chang, T.T. Charalampopoulos, Proc. R. Soc. Lond. A 430, 577 (1990)
9   P.E. Bengtsson, M. Aldén, Appl. Phys. B 60, 51 (1995)
10 P. Roth, A. V. Filippov, J. Aerosol Sci. 27, 95 (1996)
11 F. Cignoli, S. Benecchi, G. Zizak, Appl. Opt. 33, 5776 (1994)

Temperature-dependent absorption by CO_2: Implications for UV diagnostics in high-temperature flames

Christof Schulz,* Joachim Gronki,* Jon D. Koch, David F. Davidson,
Jay B. Jeffries, and Ronald K. Hanson

High Temperature Gasdynamics Laboratory, Department of Mechanical Engineering, Stanford University, Stanford CA 94305
*Physikalisch-Chemisches Institut, Universität Heidelberg , Im Neuenheimer Feld 253, 69120 Heidelberg, Germany
Jeffries@Navier.Stanford.edu

Abstract: Absorption spectra of hot (900 – 3050 K) CO_2 have been measured at 190 – 320 nm. A parameter set allows the calculation of absorption cross sections relevant for laser diagnostic in combustion processes.

OCIS codes: (120.1740) combustion diagnostics; (300.1030) absorption

1. Introduction

Laser-based diagnostics have been frequently used to study combustion processes within the past several years[1]. Many of the species of interest are probed in the ultraviolet spectral range. In many practical applications, absorption of laser and signal light limits the accuracy of measurements[2] or even prevents the observation of specific spatial locations or detection times within the process under investigation[3]. This problem increases in high-pressure processes like internal combustion engines and gas turbines due to high number densities of potential absorbers.

Different effects can contribute to UV attenuation. For laser-induced fluorescence (LIF) detection species with large absorption cross sections are resonantly excited. At high concentrations the laser beam might then be significantly attenuated by the species under investigation. As long as this species is the only absorber present, its absorption in concert with detection of the spatial distribution of fluorescence intensity can be used for correcting for laser attenuation[4] and for quantifying the species concentrations using bi-directional LIF[5]. At the same time, trapping of fluorescence light by the species under investigation might occur especially if signal light is detected from transitions to low-lying vibrational states in the electronic ground state.

In addition to absorption by small molecules with rotational and vibrational line spectra, broad-band absorption is observed in several combustion systems that attenuates laser and signal intensities independent of the presence of the probed species[2,6]. In addition to intermediate combustion products like polycyclic aromatic hydrocarbons (PAH) and partially oxidized fuel compounds, highly vibrationally excited CO_2 and H_2O are known to exhibit broad-band absorption behavior in the UV. Absorption spectra measured in the 220 – 270 nm range in hot post-flame gases in internal combustion engines show excellent agreement with simulation calculations based on the assumption that hot CO_2 is the only relevant absorber[7]. Knowledge about broad-band UV absorption is crucial when conducting laser-based concentration and temperature measurements in such environments.

The data for CO_2 absorption at elevated temperature is sparse; however there are studies at 193 nm[8,9] and 238 nm[10], and limited data in the 190 – 300 nm range[11-13]. All studies report a strong increase of absorption cross-sections with temperature and a red-shift of absorption features extending up to 350 nm. These measurements were conducted either in combustion systems[12], electrically heated flow cells[8,11] or shock tubes[10,13]. Whereas flame measurements yield over-all absorption data of all species present, electric furnaces give access to a limited temperature range only.

We performed temporally and spectrally resolved absorption measurements in shock-heated CO_2 diluted in Ar. In shock-heated gases the initial gas composition is well controlled; however, the post-shock composition is subject to shock-induced reactions and dissociation at high temperatures. These effects have been neglected in earlier publications[13]. The data presented here are corrected for CO_2 decomposition and CO and O_2 formation using chemical modeling using GRI-Mech version 3.0[14] and additional measurements of temperature-dependent absorption by CO and O_2.

We present here a set of empirical parameters to calculate the CO_2 absorption cross section as a function of temperature and wavelength in the 900 – 3050 K and 190 – 320 nm ranges.

2. Experimental

Absorption measurements are made behind reflected shock waves with a kinetic spectrograph (fig. 1). Reflected shocks are generated in a high-purity turbo-pumped stainless steel shock tube 15.24 cm in diameter[15]. Reflected shock conditions are calculated from measured incident shock velocities using a standard ideal-gas chemically-frozen shock code[16]. First order corrections to the highest temperature shocks are made from the kinetic modeling.

1

Mixtures were made manometrically using research grade CO_2 mixed into Ar. Absorption measurements are made 20 mm from the shock tube end wall. Shock tube loading pressures P_1, were 6 – 80 mbar, and reflected shock pressures P_5, of 0.7 – 1.5 bar result.
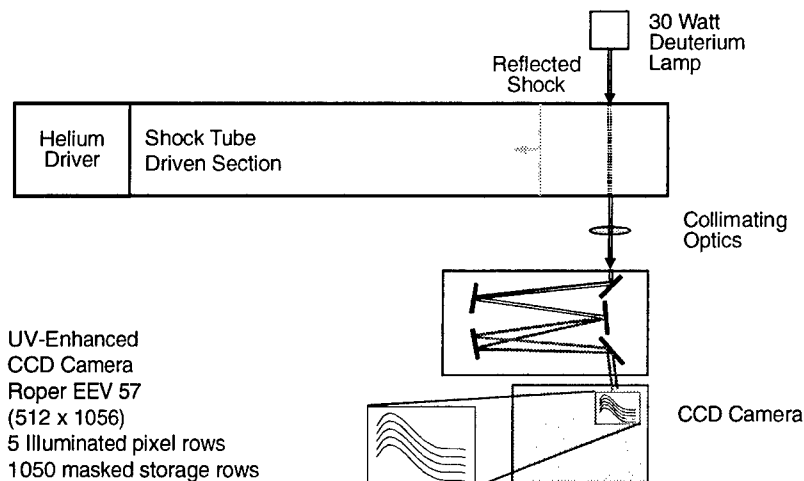

Fig. 1. Experimental setup

The kinetic spectrograph provides absorption spectra with a 10 μs time resolution. A deuterium lamp (Oriel, 30W), collimating optics, and monochromator (Acton, 150 mm, f/4) are combined with an un-intensified lumogen-coated EEV 57 CCD camera (Roper Scientific). A mechanical mask covering all but the first 5 rows of pixels is installed to convert the fast-framing EEV 57 chip to a kinetics format. Every 2 μs the pixels are displaced one row and the five row window produces a 10 μs exposure time. The 2.9 nm (fwhm) spectral resolution is limited by the 150 μm monochromator slit width. The optical setup was completely purged with N_2 to avoid the contribution of O_2 absorption.

3. Results and Discussion

The CO_2 absorption cross-sections between 190 – 320 nm for gas temperatures of 900 – 3050 K are reported in ref. 14[17] along with details of the data reduction procedure. The data are corrected for contribution of absorption by CO and O_2 formed at high temperatures by thermal decomposition of CO_2.

The largest uncertainties to be found in this transmission experiment are those associated with measurements of the smallest cross-section values. These are derived from very small measured absorbance and are adversely influenced by temporal variations in the lamp intensity. Replicate measurements of the lamp intensity indicate the precision of I_0 to be ±0.1%. The 2-σ uncertainties in the present study vary from ± 6% at the largest cross-sections to ± 50% at the smallest cross-sections.

Corrected concentrations, pressures, and temperatures for the CO_2 and H_2O mixtures were derived from constant U, V chemical kinetics calculations. Corrections to the initial mole fraction of CO_2 of order of 20% were made at the highest temperatures.

CO_2 absorption cross-sections are in good agreement with the studies of Jensen et al.[11] and Hartinger et al.[8]. There is fair agreement (within 50%) with the values given by Joutsenoja et al.[8] and the Generalov et al.[10] results as analyzed by Jensen. We are not in agreement with the study by Koshi et al.[9]. The Russian work reviewed in ref. 13 agrees quite well with the present results (a clear typographical error is present in eqn. 9 in ref. 13).

The measured absorption cross sections were parameterized in Fig 2, according to a suggestion by Lyman[18] interpolating (least square fit) between the measured cross sections ($\sigma_a(\lambda,T)$ in 10^{-19} cm^2) throughout the temperature (T in 1000 K) and wavelength (λ in 100 nm) range of interest (eqs. 1-3). Two wavelength regions (190 – 210 nm and 200 – 320 nm resp.) were fitted independently to get optimum fit quality (error < 3% at T > 1400 K and error < 10 % at 900 K < T < 1400 K).

$$\ln \sigma_a(\lambda,T) = a + b\,\lambda \qquad (1)$$

$$a = c_1 + c_2\,T + c_3/T \qquad (2)$$

$$b = d_1 + d_2\,T + d_3/T \qquad (3)$$

Laser Applications to Chemical and Environmental Analysis, OSA Topical Meeting, February, 2002
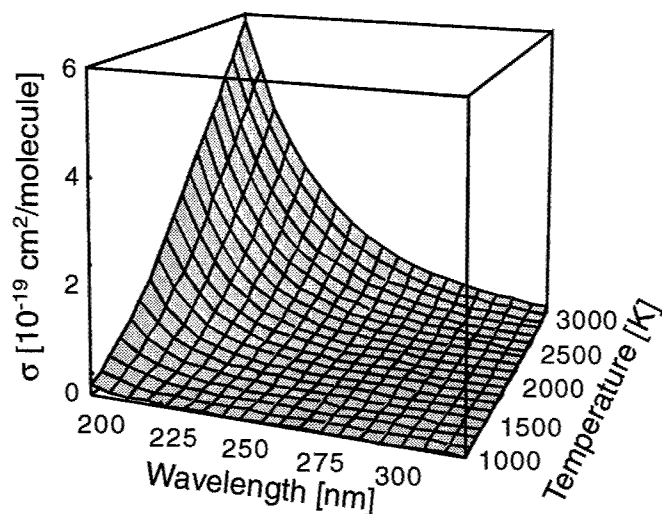

Fig. 2. Variation of CO_2 absorption cross-sections with temperature and wavelength. Calculated from the interpolated parameters shown in table 1.

Range	190 – 210 nm	200 – 320 nm
c_1	–0.3258	17.2456
c_2	–0.3250	–3.1813
c_3	21.9718	0.8836
d_1	1.6783	–7.0094
d_2	0.1948	1.6142
d_3	–13.5828	–3.1777

Table 1. Parameters of the CO_2 absorption function (eq. 1 – 3). The valid temperature and wavelength range is 900 – 3050 K. The wavelength range is split to improve fit quality. With T in 1000 K, λ in 100 nm, σ in 10^{-19} cm^2/molecule.

4. Conclusions

UV absorption cross sections of CO_2 190 – 300 nm were measured at combustion relevant temperatures from 900 – 3050 K. Absorption cross sections of $\sigma > 10^{-19}$ cm^2/molecule were found showing that absorption by CO_2 is highly relevant for UV combustion diagnostics.

The resulting data was interpolated yielding a parameter set enabling the calculation of over-all absorption i.e. in post-flame gases in near-stoichiometric and lean combustion systems. Earlier investigations have shown that these data are crucial for correcting quantitative laser diagnostics techniques for laser and signal attenuation effects.

5. Acknowledgements:

1 A.C. Eckbreth, Laser Diagnostics for Combustion, Temperature and Species, (Gordon and Breach Publishers, Amsterdam, 1996); K. Kohse-Höinghaus, Prog. Energy Combust. Sci. 20, 203 (1994); J. Wolfrum, Proc. Combust. Inst. 27, 1 (1998)
2 M. Knapp, A. Luczak, H. Schlüter, V. Beushausen, W. Hentschel, P. Andresen, Appl.Opt. 35, 4009 (1996)
3 C. Schulz, V. Sick, J. Wolfrum, V. Drewes, M. Zahn, R. Maly, Proc. Combust. Inst. 26, 2597 (1996)
4 H.M. Hertz, M. Aldén, Appl. Phys. B 42, 97 (1987)
5 M. Versluis, N. Georgiev, L. Martinsson, M. Aldén, S. Kröll, Appl. Phys. B 42, 97 (1997)
6 F. Hildenbrand, C. Schulz, V. Sick, E. Wagner, Appl. Opt. 38, 1452 (1999)
7 F. Hildenbrand, C. Schulz, Appl. Phys. B73, 165 (2001)
8 K.T. Hartinger, S. Nord, and P.B. Monkhouse, Appl. Phys. B 70, 133 (2000)
9 M. Koshi, M. Yoshimura, H. Matsui, Chem. Phys. Lett. 176, 519 (1991)
10 N.A. Generalov, S.A. Losev, V.A. Maksimenko, Opt. Spectrosc. 15, 12 (1963)
11 J.R. Jensen, R.D. Guettler, J.L. Lyman, Chem. Phys. Lett. 277, 356 (1997)
12 T. Joutsenoja, A. D'Anna, A. D'Alessio, and M.I. Nazzaro, Appl. Spect. 55, 130 (2001)
13 A.P. Zuev and A.Yu. Starikovskii, J. Appl. Spectrosc. 52, 304 (1990)
14 G.P. Smith, D.M. Golden, M. Frenklach, N.W. Moriarty, B. Eiteneer, M. Goldenberg, C.T. Bowman, R.K. Hanson, S. Song, W.C. Gardiner, V. Lissianski, Z. Qin: GRI-Mech 3.0 web site, http://www.me.berkeley.edu/gri_mech/ (1999)
15 D. F. Davidson, J. T. Herbon, D. C. Horning, and R. K. Hanson, Int. J. Chem. Kinetics, in press (2001).
16 G. Ben-Dor, O. Igra, T. Elperin eds., Handbook of Shock Waves Vols. 1-3, Academic Press San Diego 2001.
17 C. Schulz, J.D. Koch, D.F. Davidson, J.B. Jeffries, and R.K. Hanson, Chem Phys. Lett. Submitted, 2001.
18 J.L. Lyman, Los Alamos National Laboratory, personal communication (2000)

3

In-situ flame measurements of NO and CO using Mid-IR QC lasers

Shawn D. Wehe, David M. Sonnenfroh and Mark G. Allen
Physical Sciences Inc., 20 New England Business Center, Andover, MA 01810-1077
Ph:(978) 738-8175; fax: (978) 689-3232; e-mail: wehe@psicorp.com

Claire Gmachl and Federico Capasso
Bell Laboratories, Lucent Technologies, 600 Mountain Ave., Murray Hill, NJ

Abstract: Room-temperature Quantum Cascade Lasers (QCL) allow high-sensitivity measurements of trace gas absorption in the 4.6 to 11 micron wavelength region. Important combustion-generated pollutants such as CO and NO exhibit strong fundamental absorption bands in this region and sub-ppm detection limits are projected. The paper will present initial results for both species obtained in a laboratory flat flame burner.
©2000 Optical Society of America
OCIS codes: (300.6260) Spectroscopy; diode lasers; (120.1740) Combustion diagnostics

1. Introduction

Advances in gas turbine combustor technology for aeroengine applications are driving combustor designs toward high pressure, ultra-lean operating points. High-pressure operation, up to 50 atm, is desired for improved thrust-to-weight ratio (i.e., a higher energy density heat release) and ultra-lean operation is desired to ameliorate the increase in NO_x and particulate emissions associated with higher-pressure operation. The emissions reduction is also being driven by increasing regulatory pressure to limit NO_x and particulate emissions during all flight phases, not just cruise conditions.

Ultra-lean conditions can move the gas turbine toward stability margin boundaries, resulting in deleterious or potentially destructive combustion instabilities or flame blow-off. Combustor re-light at altitude is also more difficult at ultra-lean conditions, thereby substantially increasing the penalty associated with blow-off. Also, operating at optimum ultra-lean conditions throughout the power envelope places severe demands on a fixed geometry combustor concept and suggests that adaptive operating modes involving fuel or air distribution may be required to ensure safe and low-emission performance.

For these reasons, there are emerging requirements for sensors, actuators, and control technology suitable in advanced gas turbine combustors. A basic sensor requirement that may become important in advanced actuator/control schemes is for continuous and real-time measurements of exhaust gas emission of CO and NO at bandwidths of a few Hz. The NO measurement provides for continuous optimization of the engine NO_x emissions while the CO measurement provides for on-line determination of combustion efficiency and serves as a global health monitor diagnostics for fouled fuel and/or injectors.

The recent emergence of quantum cascade (QC) lasers enables the next major advancement in trace species detection: access to the strong, mid-infrared fundamental vibration-rotation transitions with a room temperature, single-mode, tunable laser. QC lasers achieve gain via the transitions of electrons between two subbands in the conduction band of a coupled quantum well structure [1,2].

Our work focuses on quasi-CW, room temperature operation of the laser source with high sensitivity detection achieved using the balanced ratiometric technique. We have demonstrated the operation of a breadboard QC laser system to detect N_2O and NO near 5.4 μm [3] and are currently developing a number of related sensors. While QC lasers can be operated CW at cryogenic conditions, we take the approach of pulsed operation at thermoelectrically cooled conditions near room temperature. The noise reduction techniques include (1) reduction of thermal noise through use of liquid-nitrogen-cooled field of view, and (2) dual-beam, balanced ratiometric detection (BRD) [4,5].

2. Mid-IR spectroscopy of CO and NO

Although strong fundamental transitions are available for both CO and NO in the mid-IR, strong water vapor interferences are also present. This interference is the primary issue that our work is presently addressing. We use the HITRAN and HITEMP databases to predict the absorption spectra of typical engine exhaust conditions (800 K). This allows identification of target spectral lines for laser selection and experimental study. Because the HITEMP database for water vapor is not based on complete experimental data, we must verify the predicted spectra in laboratory burners.

Predictions using HITEMP for NO absorption in the presence of water vapor show that the $R_{(6.5)}$ transition may be well isolated. Preliminary results for water vapor and NO absorption near 1900 cm^{-1} in an 1100-K flame are shown below.

3. Flat flame burner measurements

The pulse generating scheme used to fine tune a laser is by way of joule heating through desired absorption transitions and is shown in Fig. 1. Two current waveforms are added together to provide the laser with high amplitude current pulse for lasing and a sub-threshold current for tuning via joule heating. In the experiment the sub-threshold current is modulated at 10 Hz.

Fig. 2 depicts the experimental schematic for the room-temperature absorption measurements. The IR output of a QC laser is nearly collimated into an average beam diameter of approximately 3 mm. A CaF_2 beam splitter sends approximately 60% of the power to a multipass pass cell (MPC) while the remainder is collected on an LN_2-cooled InSb reference detector (with a cold field of view) using an off-axis-parabolic mirror (OAP). The MPC is constructed of two 5-cm diameter, 10-cm focal length, gold spherical mirrors approximately 15 cm apart with holes permitting the beam to pass. Additionally the HeNe laser is co-aligned with the IR beam and is used for alignment with the MPC. The burner region between the mirrors is 2.5 cm square and nine passes yields a 23 cm absorption pathlength.
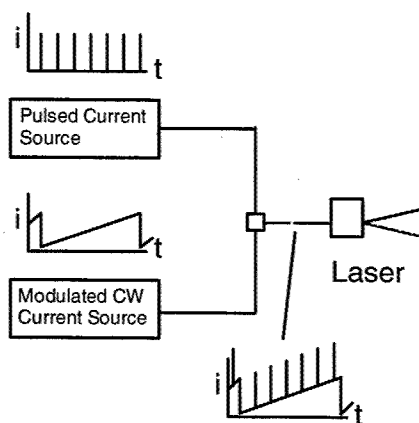
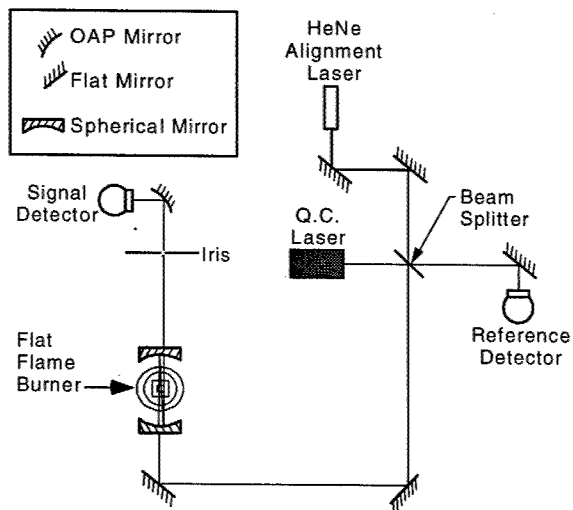Fig. 1. Pulsed current supply scheme used to tune QC-DFB lasers.

Fig. 2. Experimental schematic of the flat-flame burner measurements.

Fig. 3 shows some preliminary results of NO detection in a flat-flame burner. The spectral scan range is approximately 1 cm^{-1}, and the curves are 100-sweep averages. The top shows the stronger portion of the $R_{(6.5)}$ doublet near 1900 cm^{-1}, and illustrates that the laser is centered over the transition of interest. Figure 3B illustrates the spectra in a flame with and without seeded NO. These results are promising because they illustrate that this spectral region is smoother than predicted by HITEMP. More importantly, the NO absorbance clearly stands out. Figure 3C uses the flame without NO to provide a means for background subtraction. A polynomial fit is used in Figure 3D to illustrate NO signal. Currently we are able to achieve a signal to noise ratio of approximately 30 in the 200 ppbv seeded flame.
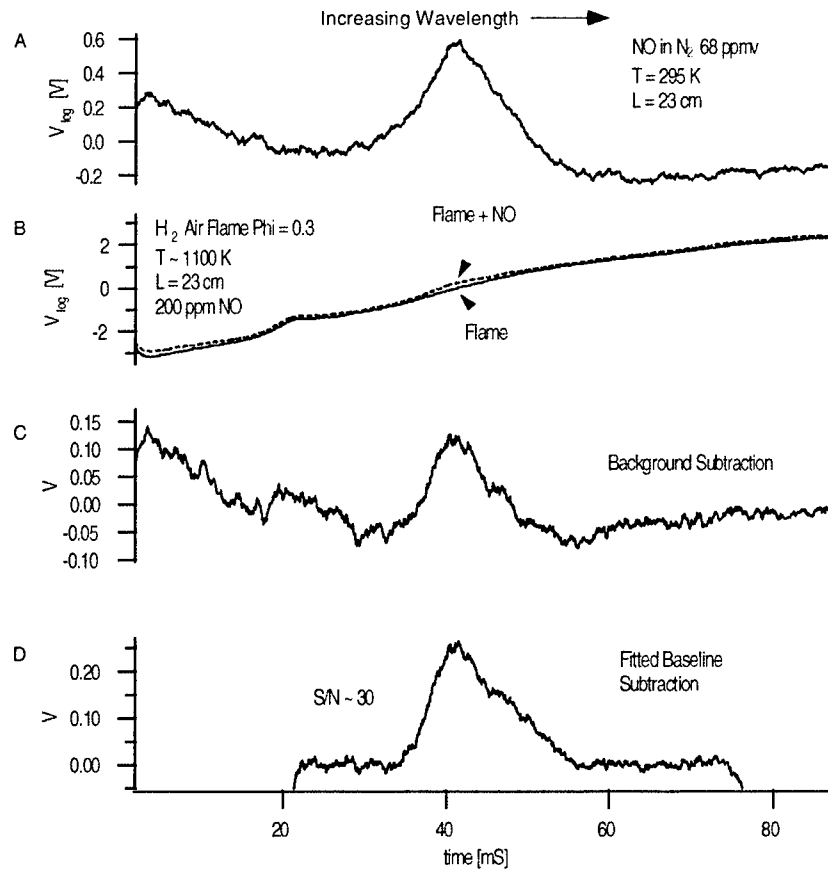
Fig. 3. (A) Measurement of a portion of the $R_{(65)}$. NO doublet in air. (B) Absorbable measurement of NO in a Phi=0.3 H_2-air flame. (C) Flame with NO - flame background subtraction. (D) Polynomial baseline subtraction.

4. References

1. J. Faist, F. Capasso, D.L. Sivco, C. Sirtori, A.L. Hutchinson, and A.Y. Cho, *Science* **264**, p. 553, 1994.

2. C. Gmachl, J. Faist, J.N. Baillargeon, F. Capasso, C. Sartori, D.L. Sivco, S.N.G. Chu, and A.Y. Cho, "Complex-Coupled Quantum Cascade Distributed-Feedback Laser," *IEEE Photonics Tech. Letts.* **9**, p. 1090, 1997.

3. D.M. Sonnenfroh, E.W. Wetjen, M.F. Miller, M.G. Allen, C. Gmachl, F. Capasso, A.L. Hutchinson, D.L. Sivco, J.N. Baillargeon, and A.Y. Cho, "Application of Balanced Detection to Absorption Measurements of Trace Gases with Room-Temperature, Quasi-CW QC Lasers", *App. Opt.* **40**(6), pp. 812- 820, 2001.

4. J. Faist, F. Capasso, D.L. Sivco, C. Sirtori, A.L. Hutchinson, and A.Y. Cho, Science **264**, 553 (1994).

5. C. Gmachl, J. Faist, J.N. Baillargeon, F. Capasso, C. Sartori, D.L. Sivco, S.N.G. Chu, and A.Y. Cho, "Complex-Coupled Quantum Cascade Distributed-Feedback Laser," *IEEE Photonics Tech. Letts.* **9**, 1090 (1997).

Cavity Ringdown Spectroscopy (CRDS)

Friday, February 8, 2002

Mark Linne, Colorado School of Mines, USA
Presider

FD
3:00pm–4:00pm
Flagstaff

Development of an Enhanced Cavity Absorption Sensor for Air Monitoring

A.R. Awtry, M.E. Moses, and J.H. Miller
The George Washington University, Washington, DC 20052

Abstract

The progress on the development of a sensor for the detection of ambient levels of a set of air contaminants is reported. A 1.55 μm external-cavity tunable diode laser is used as a light source that can be incorporated into either Integrated Cavity Output Spectroscopy (ICOS) or cw-Cavity Ringdown Spectroscopy (cw-CRDS). Both techniques exploit the sensitivity enhancements provided by the long effective pathlength from the optical cavity created between two mirrors. Initial experiments of ICOS and cw-CRDS have been performed to determine the sensitivity, selectivity, and reproducibility of this method. In the continuing work, the sensitivity of cw-CRDS will be compared with ICOS to determine which method holds greater promise for a practical sensor.

Introduction

Absorption spectroscopy using tunable diode laser absorption spectroscopy (TDLAS) with wavelength or frequency modulation signal detection provides reasonably selective and sensitive detection of many air components. However, they are generally orders of magnitude less sensitive than techniques such as GC/MS, laser induced fluorescence (LIF), resonant ionization methods (REMPI), and photoacoustic spectroscopy (PA). Cavity ringdown spectroscopy (CRDS) is a sensitive absorption technique that is capable of monitoring a wide range of species.[1,2] Although most often performed using pulsed lasers, a number of groups are now exploring the use of cw, solid state lasers which are smaller, more efficient, and relatively inexpensive. In cw-CRDS, a beam from the diode laser is injected into an optical cavity formed between two highly reflective mirrors. Only light with a frequency that matches a cavity transmission mode is coupled into the cavity due to constructive interferences.[3] The energy of light at these resonant frequencies builds up in the cavity over time. When the energy reaches a set threshold, the input beam is shut off and a ringdown is recorded.[4] The CRDS technique, while very sensitive, depends on fast electronics both for shuttering and for the data acquisition card needed to capture and store the ringdown waveform that is on the order of microseconds.

Integrated Cavity Output Spectroscopy (ICOS, or cw-ICOS) provides enhanced cavity sensitivity using a less complex setup than CRDS.[5,6] With this method, the transmitted output of the cavity is time-integrated to provide an absorption spectrum as the wavelength is scanned through the region of interest. The spectrum is then converted to absorbance through the Bougert-Lambert equation.

In this paper we report the use of ICOS and CRDS to the measurement of acetylene, ammonia, carbon dioxide, and carbon monoxide. In measurements performed at the time of this submission, measurements at concentration levels in the sub-ppm range have been accomplished. We will also discuss how this technology could be packaged in a portable sensor.

Theory

Both ICOS and cw-CRDS use a light signal that is transmitted through, and amplified by an optical cavity constructed of two highly reflective mirrors (R>99.95%). Light in the cavity undergoes constructive interference when the wavelength matches the transmission modes. At each mirror surface, the ratio of transmitted light (I_t) to incident light (I_i) is defined by the Airy function (A):

$$\delta = (FSR - \lambda) \times \left(\frac{360}{FSR} \right) \times \left(\frac{1}{180} \right)$$

$$\frac{I_t}{I_i} = \frac{1}{A} = \frac{1}{1 + F \times \sin^2 \left(\frac{\delta}{2} \right)}$$

The frequency spacing between transmission peaks is the free spectral range (FSR) of the cavity:

$$FSR = 1/L_{rt}$$

where L_{rt} is the round trip pathlength of the cavity in centimeters. The width of the transmission peaks is a function of the cavity finesse (F):

$$F = \left(\frac{2\,r}{1 - r^2} \right)^2$$

where r is the mirror reflectivity.[7] High finesse cavities have very narrow transmission modes. In ICOS no care is taken to continually match the laser wavelength to the cavity transmission modes. Instead, the cavity length (and therefore the transmission mode) is randomized by modulating a piezo-electric transducer (PZT) on the second mirror. Modulating the PZT continuously changes the cavity length and "smears" the transmission modes as well as allowing the transmission of higher order cavity modes. To further increase the random matching of cavity modes the laser wavelength is also modulated at a high frequency. The result is that the laser light builds up in the cavity at every frequency allowing a continuous spectrum. A single sweep across the wavelength range of interest produces a noisy spectrum with spikes and valleys due to the random matching of the laser frequency with cavity modes. Sweep-averaging of these individual scans produces a spectrum with a relatively high signal to noise ratio.

In contrast, only the TEM_{00} mode of the laser is coupled to the cavity in CRDS. By a varying the cavity length with using PZT actuators, mode matching can be achieved at every laser frequency and a spectrum can be collected.

In both techniques, signal enhancement can be traced to the long effective pathlength of the cavity, which is a function of mirror reflectivity. In our laboratory, we use both a pair of Newport Supermirrors that have a reflectivity greater than 0.9995 and a pair of mirrors from Los Gatos Research that were listed at an order of magnitude greater reflectivity.

Experimental

The light source used in both the ICOS and CRDS experiment is an external cavity diode laser (ECDL) by New Focus (Velocity 6328).

The ECDL has a continuous wavelength range from 1510-1580 nm with a maximum power of 8mW (typical 6mW) and a bandwidth of 5 MHz. Tuning the laser is accomplished by changing the distance between the end mirror and the grating (in the laser housing). A DC motor is used to course tune, while a PZT attached to the mirror is used to fine-tune the laser. A Burleigh wavemeter was used to determine the wavelength of light emitted by the laser throughout the scan. In ICOS experiments a Stanford Research Systems function generator (SRS345) applied a 10 Hz ramp to the ECDL to scan the wavelength. A LeCroy oscilloscope (9304A) averaged 500 scans captured the spectrum, which was then transferred to the computer.

For CRDS a desktop computer equipped with a Gage Compuscope 1250 PCI card was used to control the experiment. Detector signal levels were monitored looking for cavity energy buildup. When a threshold detector voltage is observed, the computer de-energized the first order beam exiting from an Isomet Acousto-Optic Modulator (thus shutting off the light into the cavity). The Gage card then captured the ringdown signal and stored it to a file. For each step in the CRD spectrum, 100 ringdowns were captured on the compuscope card and saved to the computer. The ringdowns were then fit to a single exponential decay to determine their decay constant. A Box and Whisker analysis was preformed on the 100 decay constants to determine an average decay.

Results

Figure 1 shows an ICOS spectrum of ammonia in the cavity. The ammonia was injected into the empty cavity and was then diluted several times sufficient to bring the concentration in the cell to below ppm levels. However, signal levels observed indicate residual levels of ammonia were above the calculated concentration values. Without independent determination of the NH_3 concentrations we are unable to produce an accurate calibration curve. Fortunately, acetylene has similar linestrengths as ammonia in this region and provides more reliable sensitivity determination. The acetylene P4 line at 1527.44[8] was chosen because its calculated linestrength of 2.37×10^{-21} cm/molecule closely matches the largest NH_3 line in Figure 1 that has a reported strength of 2.33×10^{-21} cm/molecule.[9] The calibration curve for this acetylene line with
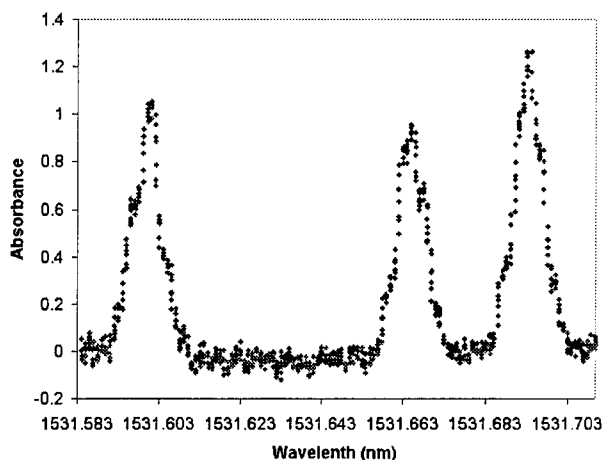
Figure 1 - **ICOS spectrum of ammonia.**

Figure 3 - CRDS spectrum of ammonia.

the CRDS setup resulted in a linear slope ranging from 53 ppm down to 5 ppm (figure 2). The dynamic range of CRDS is hampered by the fact that at high concentrations the absorption in the cavity inhibits the buildup of light. In order to detect high concentrations of a particular molecule a weak line should be used.

With the calibration of acetylene it is possible to determine the residual concentration of ammonia that is detected in ambient air samples. Figure 3 shows a CRDS spectrum of air at 10 torr where the ammonia peaks are clearly visible. The peak maximum absorbance of NH_3 corresponds to a concentration of 36.5 ppm. Since NH_3 was injected into the cavity at the beginning of these experiments, its residual effects have not allowed us to attempt an accurate measurement NH_3 in ambient air.

Conclusions and Acknowledgements

We have demonstrated that enhanced cavity techniques can be used in the development of an air-monitoring sensor. We plan to continue to improve the signal to noise in both CRDS and ICOS experiments hopefully leading to lower detection limits for each technique.

y = 0.0041x
R2 = 0.9911

Figure 2 –Calibration curve of acetylene P4.

References

[1] J.Xie, B.A. Paldus, E. H. Wahl, J. Martin, T.G. Owano, C.H. Kruger, J.S. Harris, R. N.Zare, Chem. Phys. Lett., 284 (1998) 387-395.
[2] J. J. Scherer, D.J. Rakestraw, Chem. Phys. 102 (1995) 5269.
[3] B. A. Paldas, C. C. Harb, T. G. Spence, B. Wilke, J. Xie, J. S. Harris, J. of Appl. Phys. 83(8) (1998) 3991-3997.
[iv] K. J. Schulz, W. R. Simpson, Chem. Phys. Lett. (1998) .
[5] A. O'Keefe, Chem Phys. Lett. 293 (1998) 331.
[6] A. O'Keefe, J. J. Scherer, J. B. Paul, Chem. Phys. Lett. 307 (1999) 343-349.
[7] Optics book
[8] NIST SRM 2517a, http://ois.nist.gov/srmcatalog/datafiles
[9] M.Webber, D.S. Baer, R. Hanson, Appl. Opt. (1999).

Theoretical model analysis of the dynamic saturation in cavity ringdown spectroscopy

Jae Yong Lee and Jae Won Hahn

Laser Metrology Group, Korea Research Institute of Standards and Science,
P.O. Box 102, Yusong, Taejon 305-600, Korea
Phone: +82-42-868-5221, Fax: +82-42-868-5188, E-mail: jwhahn@kriss.re.kr

Abstract: Transient saturation in cavity ringdown spectroscopy is theoretically modeled with coupled rate equations accounting for the dynamics of intracavity photons and absorber population, which permits a recipe for retrieving original spectra in the saturation regime.
© 2001 Optical Society of America
OCIS codes: (300.6460) Spectroscopy, saturation; (999.9999) Cavity ringdown

Cavity ringdown spectroscopy (CRDS) is a direct absorption measurement technique permitting ultra-sensitive trace species detection. [1] In order for the CRDS to warrant absolute quantification of a sample loss, a cavity ringdown (CRD) signal is presumed to be in a single exponential decay waveform to yield a definite decay constant which we referred to as ringdown time; the requirement is stringent for CRDS since the CRD technique is only valid for the case of linear absorption obeying the Beer's law. [2] Saturation of an absorbing sample, one of the well-known nonlinear effects in spectroscopy, is thus quite detrimental to CRDS that the effect will lead to a serious failure in CRD signal analysis, while it has paved the easy way to realize a Doppler-free high resolution technique indeed. [3-6]

We present here an initiating theoretical formulation for the dynamic saturation of CRDS based on coupled rate equations that exactly describe the transient behaviors of both the intracavity light intensity and the absorbing species population. Our approach could offer a pertinent way to deal with saturated CRD signals, making it possible to extract the correct spectral information even in the saturation regime and to define a reliable CRDS measurement regime characterized in terms of a proper saturation parameter.

The ambiguity arising from the non-exponential decay caused by saturation can be resolved only through a complete modeling of the saturated CRD signal. The attenuation of a probe light I propagating in an absorber is described by the Beer's law given by

$$dI/dt = -c\,\alpha I \,, \tag{1}$$

where $\alpha = n\sigma$ is the absorption coefficient with the absorbing species density n and the cross-section σ. The saturated absorption coefficient is characterized by $\alpha = [n_0/(1+S)]\,\sigma$, or equivalently $\alpha = \alpha_0/(1+S)$, in terms of the saturation parameter S with α_0 and n_0 denoting unsaturated absorption coefficient and absorbing population density, respectively. The saturation parameter S, for steady-state condition, is given by $S = 2\tilde{T}\int d\nu\, c\rho(\nu)\sigma(\nu)/h\nu$, taking the form of $2\tilde{T}\sigma I_\nu/h\nu$ for monochromatic probe light. Here, $\rho(\nu)$ is the spectral energy density of the light, $\sigma(\nu)$, cross-section of the absorbing medium, $\tilde{T} = 1/\tilde{R}$, the relaxation time of the excited level, I_ν, the light intensity at the frequency ν, and $I_s = h\nu/2\sigma\tilde{T}$, the saturation intensity. Considering a homogeneously broadened two-level absorber in a closed system, a saturated CRD signal in a ringdown cavity is described by a simple rate equations:

$$\frac{dn}{dt} = (A + A_{\text{ind}})(N_0 - n) - 2B_\nu\rho_\nu n \,, \tag{2}$$

$$\frac{d\rho_\nu}{dt} = -\gamma_m\rho_\nu - B_\nu\rho_\nu nh\nu + \eta_p I_p/L \,, \tag{3}$$

for the time evolution of absorbing population density $n = N_1 - N_2$ and the intracavity photon density ρ_ν. The absorbing sample is assumed to have total number density $N_0 = N_1 + N_2$ and the overall relaxation rate of $\tilde{R} = 1/\tilde{T} = A + A_{\text{ind}}$ which is the sum of contributions from the Einstein's A coefficient $A = 1/T_{\text{sp}}$ and the indirect relaxation rate $A_{\text{ind}} = 1/T_{\text{ind}}$. In terms of Einstein's B coefficient $B = \int d\nu B_\nu$, one gets $B_\nu = Bg(\nu) = \sigma(\nu)c/h\nu$ for a lineshape function $g(\nu)$ specified. The time rate of cavity loss $\gamma_m = -\rho^{-1}(d\rho/dt)$ is $2(1-R)/t_r$ for a ringdown cavity having the mirror reflectivity R and the round-trip time t_r. and the intensity of light coupled out through the cavity mirrors can be obtained with the relation $I_{\text{out}} = (1-R)\rho_\nu c$.

The cavity excitation is specified by incident laser beam with intensity $I_p(t)$ and the effective coupling coefficient η_p.

Using the rate equations with given cavity excitation parameters, the saturation in either cw CRDS or pulsed CRDS can be investigated in principle. The initial status of cavity excitation in cw CRDS, however, is somewhat difficult to specify and quite different among the realization schemes. Hence we present the saturation dynamics for the case of frequency-tuned pulsed CRDS system.
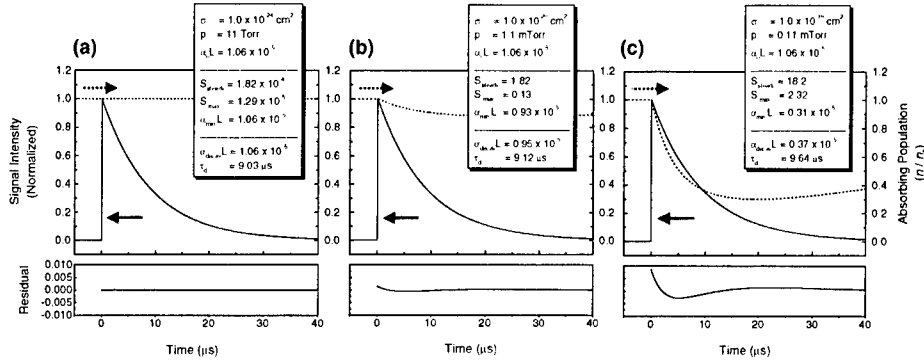
Fig. 1. Non-exponential CRD signals and depleted absorbing population in a pulsed CRDS system. Lower panels show the fit residuals of the non-exponential CRD signals. Parameters used in the simulation are shown in each inset: Samples are with the same single-pass absorbance $\alpha_0 L$ of 1.0×10^{-5} the indirect relaxation time T_{ind} set to be ~ 100 μs, but in different combinations of the cross-section and the pressure. The ringdown cavity with 99.99%-reflectivity mirrors in the separation of 30 cm, is excited by a laser pulse at 570-nm wavelength, delivering 5-mJ energy in the pulse duration of 5 ns and the beam diameter of 1 mm.

By the numerical calculation on the time evolution of the intracavity photon density and the absorbing population density, the CRD signal deviated from a single exponential decay and the time-dependent absorption saturation are examined. As displayed in Fig. 1, the saturation of the sample absorption begins to develop after the injection of a pulsed excitation, and increases as the time evolves. If the relaxation process is appreciable, the sample absorption is recovered with the decrease of intracavity light in the tail part of CRD. It is remarkable that the absorption saturation in pulsed CRDS is suppressed even for the intense laser injection, because of the drastic attenuation upon cavity entrance as well as the transient decrease of intracavity light intensity. Moreover, a fast indirect relaxation process, such as the diffusion or the transit of a sample gas from the probing beam area, may be introduced in the experimental setup to prevent the buildup of the saturation. Since the saturation parameter S evolves in time, characterization of saturation in a single parameter is doomed to fail; Although the maximum saturation parameter S_{max} defined at the minimum absorption coefficient α_{min} is available, such a representative parameter S_{max} cannot predict exactly the resultant absorption coefficient α_{decay} that is obtained from the erroneous exponential fit of a saturated CRD signal. The conventional procedure of CRD signal analysis is no more reliable in the saturation regime.

To avoid from the saturation regime of CRDS, one should examine the constraints on absorbing samples, the probe light intensity, and the cavity finesse. As shown in Fig. 2, a valid dynamic range of CRD measurement can be obtained by the numerical calculation estimating the effective saturation. The saturation-free absorption regimes are illustrated as white areas for several set of system parameters indicated in the figure.

In the course of a spectral scan in CRDS, a certain range of sample cross-section $\sigma(\nu)$ must be covered where the sample saturation might occur. Exploiting the complete formulation for saturation dynamics we developed, we can extract the information regarding both the absorption and the saturation from the saturated CRD signal, since a non-exponential decay carries the dynamics involved with sample saturation; a saturated CRD signals is fit to the synthesized signal transients, one can have access to the unsaturated absorption as well as the saturation-related parameters by finding the best fit,.

Figure 3(a) displays the saturation of CRD spectra predicted in the saturation regime, where attempts of fitting the saturated CRD signals to exponential decays are applied. In contrast, an exact fit to a simulated CRD transient permits the unsaturated absorption that makes it possible to retrieve the original spectrum, as indicated by the results given in Fig. 3(b).
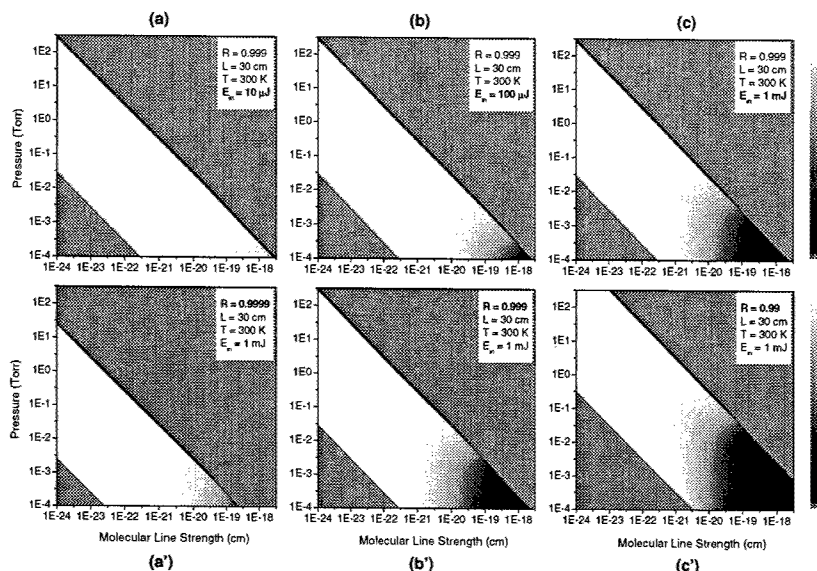
Fig. 2. Saturation-free dynamic range of the CRDS measurement depending on (a-c)the excitation pulse energy and (a'-c')cavity finesse. Dynamic ranges are determined over 2-D space of $(n, S_{\mathrm{mol}} = \int \sigma d\nu)$, by estimating the sample depletion parameter $D = (n/n_0)_{\mathrm{avg}}$ at the line center of a given homogenously broadened line. The shaded regions represent the parameter space beyond the CRDS dynamic range.
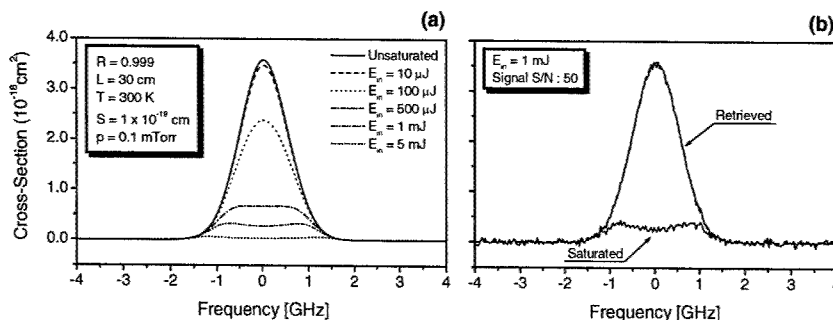

Fig. 3. Saturation of absorption spectra in the conventional in CRDS and the retrieval to the unsaturated spectra from the saturated ringdown signals. (a) Saturated spectra are obtained for different probe laser intensities indicated in the figure, and (b) the retrieval of unsaturated absorption spectrum from the saturated ringdown signals is demonstrated with a synthesized saturation signals having the random statistical noises in the S/N level of 50.

To conclude, it has been found be feasible that the saturated CRD signals can be analyzed reasonably on the basis of a theoretical formulation accounting for dynamical saturation, allowing the retrieval of an original spectrum. Extension of our work to be applicable for the dynamic saturation with inhomogeneous broadening is expected to find many practical applications.

References

1. K. W. Busch and M. A. Busch, "Introduction to cavity-ringdown spectroscopy," in *Cavity-ringdown Spectroscopy: an ultratrace-absorption measurement technique*, K. W. Busch and M. A. Busch, eds. (Oxford U. Press, New York, 1999), pp. 7 - 19.
2. P. Zalicki and R. N. Zare, "Cavity ring-down spectroscopy for quantitative absorption measurements," J. Chem. Phys. **102**, 2708 - 2717 (1995).
3. L. Lehr and P. Hering, "Quantitative nonlinear specroscopy: a direct comparison of degenerate four-wave mixing with cavity ring-down spectroscopy applied to NaH," IEEE J. Quantum Electron. **33**, 1465 - 1473 (1997).
4. P. Zalicki, Y. Ma, R. N. Zare, E. H. Wahl, J. R. Dadamio, T. G. Owano, and C. H. Kruger, "Methyl radical measurement by cavity ring-down spectroscopy," Chem. Phys. Lett. **234**, 269 - 274 (1995).
5. D. Romanini, P. Dupré, and R. Jost, "Non-linear effects by continous wave cavity ringdown spectroscopy in jet-cooled NO$_2$," Vib. Spectrosc. **19**, 93 - 106 (1999).
6. C. R. Bucher, K. K. Lehmann, D. F. Plusquellic, and G. T. Fraser, "Doppler-free nonlinear absorption in ethylene by use of continuous-wave cavity ringdown spectroscopy," Appl. Opt. **39**, 3154 - 3164 (2000).

Sensitive absorption measurements based on novel cavity enhanced spectroscopy techniques

Doug Baer, Manish Gupta, Anthony O'Keefe, Joshua Paul
Los Gatos Research, 67 East Evelyn Ave, Suite 3, Mountain View, CA 94041
Tel: (650) 965-7772, Fax: (650) 965-7074, dsblgr@earthlink.net

Abstract: A novel laser-based absorption diagnostic technique based on off-axis paths in high-finesse optical cavities provides high measurement sensitivities ($\sim 2 \times 10^{-10}$ cm^{-1}). Applications to environmental monitoring and industrial process control using near-IR semiconductor diode lasers and mid-IR quantum cascade lasers will be presented.
OCIS codes: spectroscopy, diode lasers (300.6260), spectrometers and spectroscopic instruments (120.6200)

1. Introduction

Absorption measurements based on cavity enhanced techniques (including cavity ringdown spectroscopy, integrated cavity output spectroscopy, cavity enhanced absorption spectroscopy) offer the potential for very high sensitivity due to the long effective optical path lengths (typically thousands of meters) inside high finesse cavities. For CRDS measurements using continuous-wave lasers, optimum sensitivity and precision generally requires careful optical alignment of the laser TEM$_{00}$ mode with a single cavity resonance. This approach typically requires very stable systems and can be complex and expensive to implement. For pulsed-laser CRDS, the coherence length of the laser is typically short compared with the cavity length so that the laser bandwidth spans several longitudinal cavity modes. As a result, the transmission is determined by the wavelength-integrated cavity transmission spectrum (e.g., integrated over the cavity free spectral range). This allows a constant fraction of the incident laser power to be coupled through the cavity for each laser shot. For this case, the cavity remains passive thereby reducing the expense and complexity compared with continuous-wave methods. To date, the sensitivity of pulsed-laser CRDS methods has not approached that of resonant coupling (cw) methods.

Integrated cavity output spectroscopy (ICOS) and cavity enhanced absorption spectroscopy techniques rely on broadband cavity transmission characteristics like pulsed-CRDS, but employ narrowband CW-lasers. These methods monitor the cavity transmission while effectively averaging the cavity-mode structure either by intentionally dithering the cavity length or by anti-mode-matching the laser with the cavity such that the laser couples to a large number of transverse cavity modes. These methods have yielded sensitivities comparable to those obtained using pulsed-CRDS, as expected. The limiting noise source in these cases was related to the ability to effectively average the cavity transmission function, which directly translates to noise in the resulting absorption spectrum.

The present work employs an optical alignment strategy in which the incident beam is aligned in an off-axis configuration with respect to optical cavity, instead of using the conventional on-axis alignment. The alignment patterns, commonly used in multi-pass

absorption cells, were first explored in conjunction with optical cavities and result in a dramatic decrease the effective free spectral range (FSR) of the cavity for certain alignment geometries. This property can be used to obtain more effective averaging of the cavity transmission spectrum, resulting in an order of magnitude improvement in measurement sensitivity over previous ICOS results.

2. Experimental

Figure 1 illustrates the experimental setup used for off-axis ICOS measurements. Individual distributed feedback diode lasers were used to record absorption measurements of C_2H_2 (1532 nm), CO_2 (1600 nm), CO (1564 nm), and CH_4 (1650 nm) to demonstrate the potential for industrial process control and environmental monitoring applications. The optical cavity consisted of two 1-meter radius of curvature, 1-inch diameter mirrors spaced 85-cm apart. The cavity mirrors (Los Gatos Research) had a nominal reflectivity of 99.99% over the range 1550-1650-nm. A single aspheric lens and a steering mirror were used to direct the beams into the cavity at an acute angle with respect to the cavity axis so that a Lissajous spot pattern was generated on the cavity mirrors. Light exiting the cavity was focused by a (2-inch diameter, F/1) lens, filtered by a narrow band-pass interference filter and onto an InGaAs detector (0.3-mm diameter, 200-kHz bandwidth). The DFB lasers were wavelength tuned by supplying a current ramp to the laser current source while holding the diode-laser case temperature constant. The detected transmission signal was sent to a digital A/D board on-board a personal computer for analysis.

To illustrate the potential for process measurements of acetylene in ethylene flows, figure 2 (left) shows a measurement of C_2H_2 absorption (50-ppbV in N_2 at 50-torr total pressure) obtained by wavelength tuning a DFB diode laser across the P(11) line (v_1+v_3 band) near 1532 nm at a 200 Hz rate in a 2-second measurement interval. The signal to noise ratio obtained (~30) translates to a C_2H_2 minimum detection limit of less than 2 ppbV. Figure 2 (right) presents measurements of C_2H_2 absorption for various mixture fractions in N_2.

Figure 3 presents measurements of CH_4 absorption ($2v_3$ band) near 1651 nm in ambient air (total pressure ~100 torr). The measured multi-line absorption feature was fit to several overlapping Voigt profiles. The methane concentration (~1950 ppbV) was determined from the measured absorbance). The signal to noise ratio obtained translates to a CH_4 minimum detection limit of less than ~3 ppbV. In addition, measurements of other species using mid-IR quantum cascade lasers will be presented at the meeting.

3. Summary

Sensitive measurements of several gases have been recorded using continuous-wave diode lasers operating in the near-infrared spectral region using off-axis integrated cavity output spectroscopy. The reasonably high measurement sensitivity (typically ~2×10^{-10} cm^{-1}) and low-cost components of the system suggest that this technique can be effectively employed for industrial process control, environmental monitoring and other applications that require ultra-sensitive real-time measurements of trace gases.
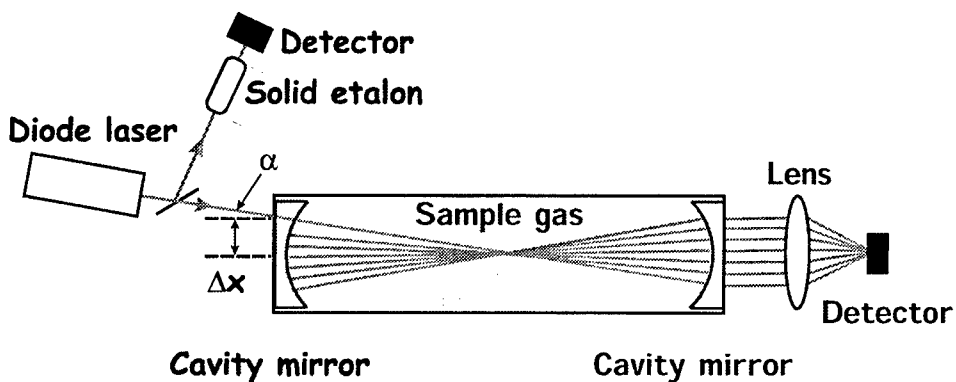
Figure 1. Experimental setup used to record absorption measurements using off-axis integrated cavity output spectroscopy.
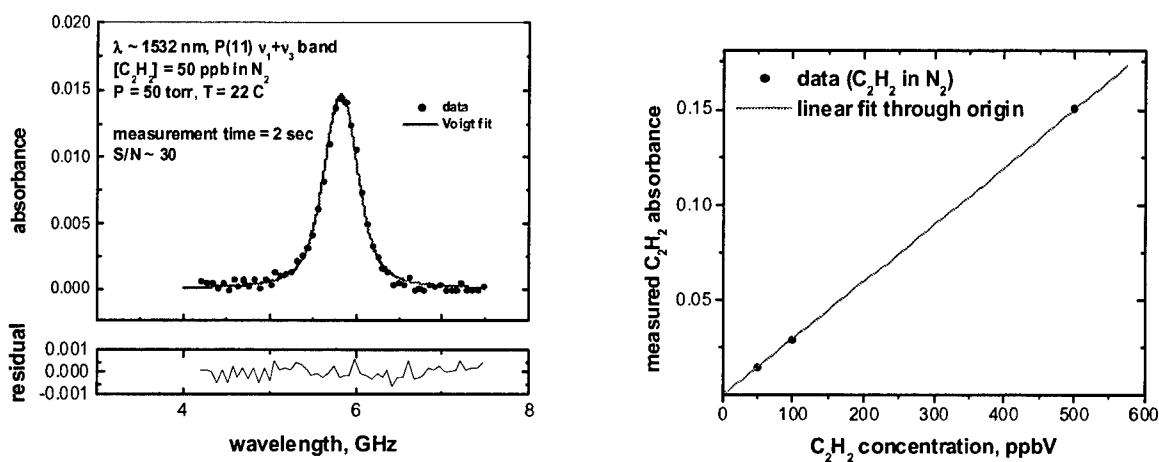

Figure 2. (Left) Measurements of C_2H_2 absorption [P(11) line, $\nu_1+\nu_3$ band)] near 1532 nm obtained using off-axis ICOS. (right) Comparison of measured C_2H_2 absorption with various mixture fractions of C_2H_2 in N_2.
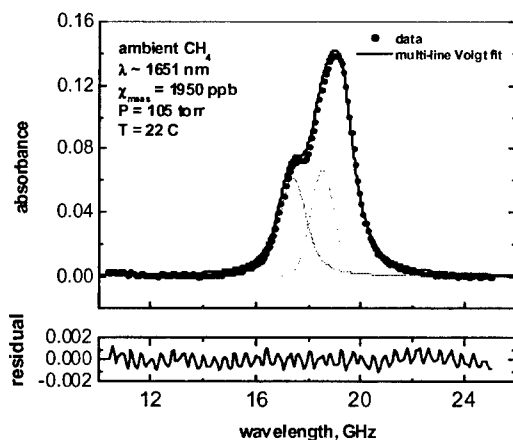

Figure 3. Spectrally resolved measurement of CH_4 absorption [$2\nu_3$ band)] near 1651 nm in ambient air obtained using off-axis ICOS.

Plenary Session

Friday, February 8, 2002

Mark Linne, Colorado School of Mines, USA
Presider

FE
4:40pm–5:40pm
Flagstaff

Cavity Ring-Down Spectroscopy: An Overview

Richard N. Zare
Department of Chemistry
Stanford University
Stanford, CA 94305-5080 USA

Cavity ring-down spectroscopy (CRDS) is a new technique for carrying out absorption measurements with increased sensitivity. Briefly, a pulse of radiation is injected into an optical cavity where it bounces back and forth between high-reflectivity mirrors. Some radiation leaks out an end mirror on each bounce, and the stored radiant energy inside the optical cavity decays exponentially (rings down) with time. When absorber molecules are present inside the optical cavity, the ring-down lifetime is shortened. A plot of the reciprocal of the ring-down lifetime (the ring-down rate) versus frequency gives the absorption spectrum.

The real advantage of CRDS is a combination of the multipass character of the multiply reflected radiation inside the optical cavity with the insensitivity of the ring-down lifetime to the pulse amplitude. This last feature means that the pulse intensity does not need to be stabilized or even made reproducible. By this means, the sensitivity of absorption measurements, which is traditionally no better than about one part in 10^4 per cm, is extended to one part in 10^7 or one part in 10^8 per cm, depending on the quality of the mirrors and the nature of the detector noise.

Recently, several groups have made a breakthrough in sensitivity by achieving one part in 10^{10} or one part in 10^{11} per cm by an optical heterodyne technique. One way this feat is accomplished is by actively locking together a cw laser source and an optical cavity using two beams of orthogonally polarized light, one that produces the feedback signal for locking, the other that is modulated and used to record the CRDS signal. Further advances have allowed us to

achieve a sensitivity of one part in 10^{12} per cm, which is within a factor of ten of the shot-noise limit.

Cavity ring-down spectroscopy can be applied to any sample that is not too opaque. Many applications will be reviewed. These include rarefied gas samples, those at high pressure, and those that have highly luminous backgrounds, such as flames and plasmas. CRDS can also be applied with good success to examine interfaces and to probe liquid samples.

It is also possible to use CRDS to observe rapid changes in the sample composition, limited by the time it takes for the light to traverse the sample enclosed by the optical cavity. In this manner we have examined the electron density in dc plasmas following pulsed excitation on the submicrosecond time scale. We have also examined the nature of dye solutions under irradiation at the subpicosecond time scale.

Some prospects for commercializing CRDS will also be discussed.

Notes

Instrumentation I

Saturday, February 9, 2002

Alfredo Bruno, Novartis Pharma AG, Switzerland
Presider

SaA
8:00am–10:00am
Flagstaff

Abstract not available

Author: Hans Peter Herzig, Univ. of Neuchatel, Switzerland
Title: Microoptics for laser applications

Tunable semiconductor laser spectroscopy in hollow optical waveguides

G. J. Fetzer and A. S. Pittner
Arete Associates
333 N. Wilmot Road
Suite 450
Tucson AZ 85711
520-571-8660 (O)
520-571-8232 (F)
gfetzer@arete-az.com

Abstract:
A spectrometer based on tunable semiconductor lasers and hollow optical waveguides is discussed. Results are presented that characterize the function of the spectrometer in terms of sensitivity, response time, species cross interference and stability.
©2001 Optical Society of America
OCIS codes 120.6200 Spectrometers and spectroscopic instrumentation 300.6380 Spectroscopy, modulation

1. Introduction

Tunable semiconductor laser absorption spectroscopy has been applied to many gases and applications in the past 30 years[1-3]. While many sensitive and difficult measurements have been achieved, the technology has not reached commercial maturity. A number of factors have been responsible: One problem is the need for relatively expensive long path absorption cells. These cells are usually comprised of a set of reflective optics that folds the optical path, allowing long absorption lengths in modest volumes. The response time of a sensor based on these cells is often limited by the time required to completely exchange the gas in the cell. A second problem has been the lack of adequate coverage for much of the optical spectrum by compact lasers that can be operated at room temperature. Finally, the signal processing equipment that has been used for these types of sensors has been bulky and expensive analog electronics. We present a spectrometer design that exploits the marriage of emerging technologies in the fields of hollow optical waveguides, room temperature semiconductor lasers, and modern digital signal processing technology. The spectrometer has been applied to the acquisition of high-resolution spectra in the near- and mid-infrared (NIR/MIR) regions of the optical spectrum. In addition, a number of gases have been measured as trace quantities in air and in other mixtures. Both distributed feedback laser diodes and quantum cascade lasers have been used in the system. The system exhibits high sensitivity, with rapid response to changes in trace gas concentrations.

2. System Description

Measurements are performed using the setup depicted in Figure 1. The system has been used with a DFB laser operating near 1.5μm and with a QC laser operating at 5.2μm. When operating in the NIR the detectors used are PIN InGaAs photodiodes. When operating in the MIR either cryogenically or thermoelectrically cooled HgCdTe detectors are used. Traditional wavelength modulation (harmonic) spectroscopy techniques are used in the system.

Two perforated optical waveguides serve as gas cells. The waveguides are constructed of fused silica capillary tubing, internally coated with silver followed by deposition of an AgI dielectric coating. The waveguides used in this experiment are commercially available and were optimized for transmission at 2.94μm. The waveguides are 1000μm inside diameter and approximately 3m and 1m in length for the sample and reference cell, respectively. The waveguide is coiled on the inside edge of a metal ring. The inlet and exhaust ports are mounted on opposing sides of the ring. Once an unperforated guide is mounted, individual coils, located within the exhaust and inlet ports are drilled using a CO_2 laser. The drilling system is set up to perforate one wall of the waveguide in a single exposure. In this manner clean, circular holes approximately 50μm diameter, are created in the waveguide wall.

A pressure differential between the inlet and exhaust cells fills the waveguide with sample and complete exchange occurs when the gas travels one half of a bend circumference from inlet to exhaust. The arrows in Figure 1 indicate the direction of the gas flow in the system. For the work discussed here, there are two perforations in each coil at both the inlet and exhaust providing a total flow of approximately 60ml/min at a pressure differential of a few Torr. Because the holes are small and few in number, the drilling process or the presence of the perforations does not measurably change the optical transmission of the waveguide. Pneumatic seals at the waveguide ends are accomplished using O-rings and either a window or the face of a lens.

Data acquisition, signal processing, and control were performed using custom built electronics that include a dedicated DSP processor interfaced to a PC. A calibrated gas delivery system allows blends of a variety of gases to be produced for various experiments.

3. Measurements

A typical CO_2 second harmonic spectrum collected while ramping the diode laser temperature is shown in Figure 2a. The peak absorbance of CO_2 in this spectral region is approximately 2×10^{-2}. The gas pressure in the cell is near atmospheric and the sample cell length is 3m. The laser current modulation amplitude is 5mA, corresponding to a wavelength modulation of $0.21 cm^{-1}$. For comparison, a theoretical second-harmonic absorption spectrum, computed using HITRAN [4] data is included. To generate the figure, the peaks near $6521 cm^{-1}$ from each spectrum were aligned. A laser temperature-tuning factor of $0.08 nm/°C$ is assumed. The theoretical data is generated assuming a Lorentzian line shape with a $0.09 cm^{-1}$ linewidth (HWHM) [4]. The agreement between the data is good. A small non-linearity in laser diode wavelength dependence on temperature is the reason for the slight shift of the measured lines relative to the theoretical lines on the extreme right and left hand sides of the plot. The spectral resolution of the sensor is estimated at better than $0.02 cm^{-1}$ based on the data shown here. A plot, illustrating the line center locations and line strengths predicted by HITRAN for CO_2 are shown for comparison in Figure 2b. Trace concentrations of CO_2 have also been measured using the spectrometer. Lower detectable absorbance of 1×10^{-5} in a 3m length of waveguide has been demonstrated. This corresponds to approximately 0.05% by volume concentration of CO_2.

Extended results including measurements of NO and H_2O near 5.2 and 5.4mm will be presented in detail at the conference.

4. Summary

A novel laser absorption spectrometer that employs hollow optical waveguides as sample cells has been described. The system has been operated with DFB and QC lasers at 1.5µm and 5.2µm respectively. High-resolution absorption spectra have been measured as well as trace gas detection and measurement. Lower detectable absorbance of 1×10^{-5} in 3m lengths of waveguide have been achieved. Measurements of CO_2 and NO are presented.

5. References

1. "Air Monitoring by Spectroscopic Techniques", M.W. Sigrist, Wiley and Sons, Chemical Analysis,Volume 127, 1994.
2. Reid and D. Labrie, "Second-harmonic detection with tunable diode lasers-comparison of experiment and theory," *Appl. Phys. B.*, **26**, 203, 1981.
3. R. M. Mihalcea, D. S. Baer, and R. K. Hanson, "Diode laser sensor for measurements of CO, CO_2, and CH_4 in combustion flows", Appl. Opt., 36, 8745-8752, 1997.
4. L. S. Rothman, C. P. Rinsland, A. Goldman, S. T. Massie, D. P. Edwards, Y. Y. Mandin, J. Schroeder, A. McCann,R. R. Gamache, R. B. Wattsin, K. Yoshino, K. V. Chance, K. W. Juck, L. R. Brown, V. Nemtchechin, and P Varanasi, J. Quant. Spectros. Radiat. Transfer, **60**, 665-710, 1998.
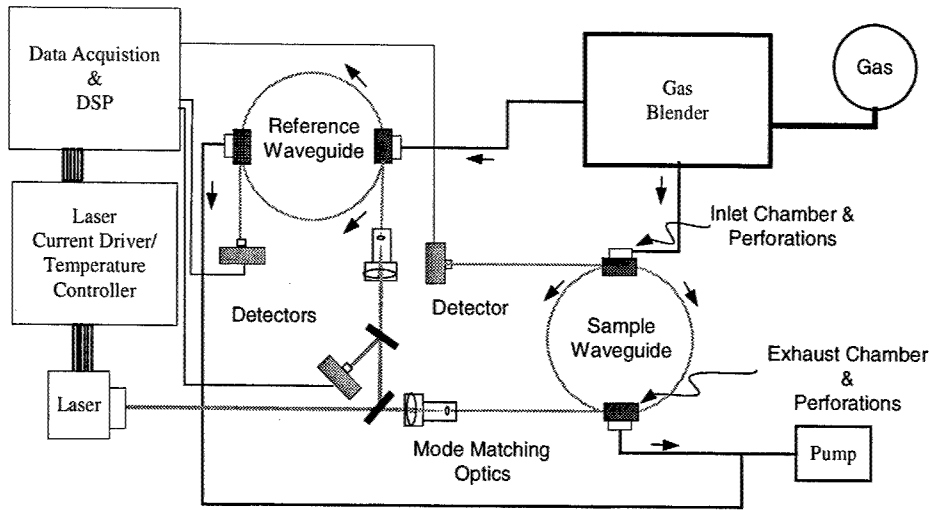
Fig. 1 System schematic block diagram. The small arrows in the figure indicate the direction of gas flow in the pneumatic system.
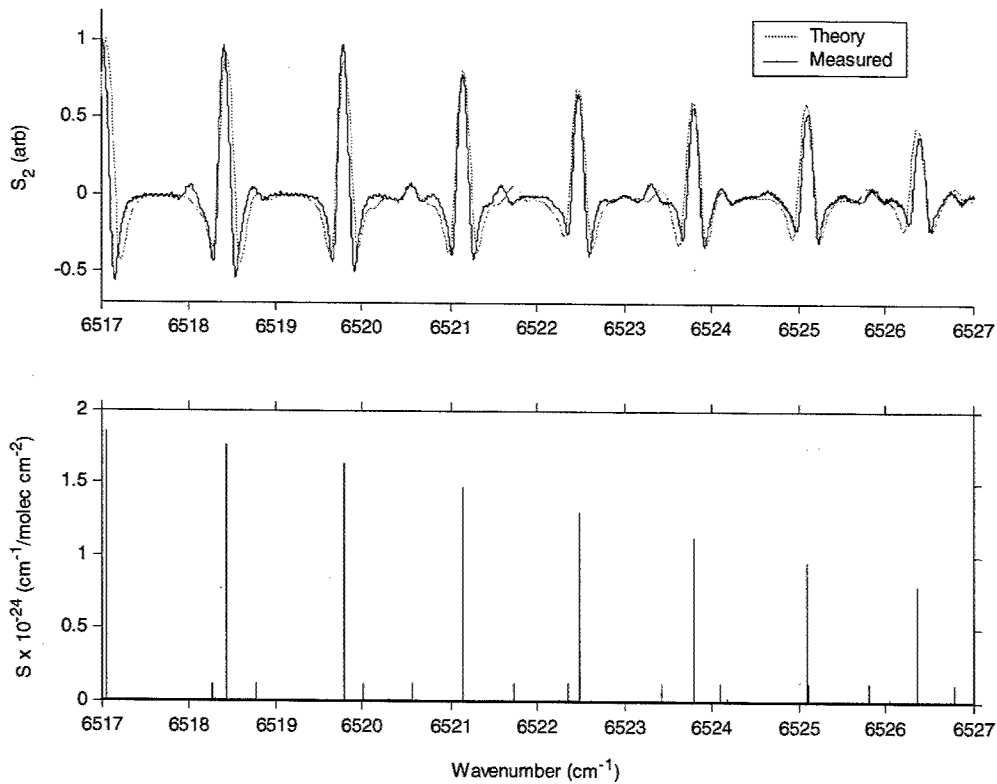

Fig. 2 CO_2 spectrums near 1.5μm. (a) Second harmonic spectrum (S_2) captured using the hollow waveguide system in comparison with a spectrum calculated using HITRAN data. (b) Line strength and location data as predicted by the HITRAN model.

Development of a CMOS active-pixel phase-sensitive detector imaging array

R. Swartzendruber, S. Sedarsky, N. Middleton and M. Linne
Division of Engineering
Colorado School of Mines
Golden, CO 80401

Introduction

Single-point laser diagnostics use various electronic signal-processing techniques to improve signal-to-noise ratios (SNR). These include simple signal averaging, gated integration (boxcar averaging) for pulsed systems, and phase sensitive detection (lock-in amplification) for modulated cw systems. An ongoing program at the Colorado School of Mines (CSM) has evaluated methods for implementation of electronic signal processing in imaging arrays (see e.g. Fisher[1] for a gated-integrator array). Here we describe the development of a new imaging array that performs phase-sensitive detection signal processing at the chip level, at each pixel.

CMOS array description

This array is based upon discrete element mock-ups that were evaluated at CSM, but the VLSI design was developed by Black Forest Engineering in Colorado Springs, CO. Forty percent of the 40 μm x 40 μm pixel area (27.75 μm x 20.1 μm) is used for optical sensing, with the remainder devoted to signal processing. The sensor has a substrate that is red sensitive (estimated quantum efficiency = 70% at 600 nm) while a snake-like overlay is blue sensitive (estimated quantum efficiency = 25% at 284 nm), for a broad optical response curve. The array has 80 x 80 pixels, chosen in order to evaluate the signal-processing ideas with good chance of success in manufacture. This design can be easily scaled to 256 x 256, while a modified VLSI design (smaller features) can generate a 512 x 512 array. The current design is predicted to detect modulation depths of 10^{-5} at 1 kHz frame rates. Lower modulation depths can be sensed by averaging in software. The camera must frame at 1 kHz or faster because the device uses passive capacitance, and this can drift slowly. The demodulation frequency can be as high as 400 kHz.

Phase sensitive detection

In order to describe the operation of the camera, basic phase sensitive detection will be described first. In the simplest experiment, the optical signal has been amplitude modulated. Because the experimentalist imposes the amplitude modulation, the modulation frequency (the "reference" modulation frequency, f_m) is known. The reference frequency is then used by the lock-in amplifier to extract the signal of interest. A lock-in amplifier in its simplest configuration is simply a mixer and a filter, as shown in Figure 1. The input signal to the lock-in from the photodetector consists of a dc offset (dc_i), the modulated signal at frequency f_m, and noise that spans a broad range of frequencies f_i (note that the range of f_i's will contain f_m; there is both noise and signal at f_m). The mixer then multiplies the input signal and the relatively clean reference signal (often a sinusoid). In the frequency domain, the fact that the reference has a zero at dc causes the term dc_i to be removed past the mixer.

The mixer output is then $s_i \otimes s_m$, without the dc_i term. The product of the two sine functions (s_i and s_m) is decomposed by trigonometric identity into difference frequency and sum frequency terms:

[1] "Synchronous Focal Plane Detection of Weakly Modulated Images with the Interline Transfer CCD", C. Fisher, Ph.D. Thesis, Colorado School of Mines, (2000).

$$s_i \otimes s_m = 0.5 \sum_i (S_i S_m)\left[\cos\left(2\pi f_i - 2\pi f_m\right)t - \cos\left(2\pi f_i + 2\pi f_m\right)t \right]$$

For the portion of s_i that is at f_m, the difference term becomes zero. The signal of interest has thus been "mixed down to dc". The output of the mixer then passes through an adjustable filter that removes the sum term and other noise elements that are located beyond the filter cutoff frequency. If the optical source is modulated at a frequency above the point where the $1/f$ noise reaches the noise floor, this technique moves the signal outside of the $1/f$ noise range, removing this source of signal corruption. This is one major reason for using phase-sensitive detection.

Figure 1. Schematic of the phase sensitive detection process.
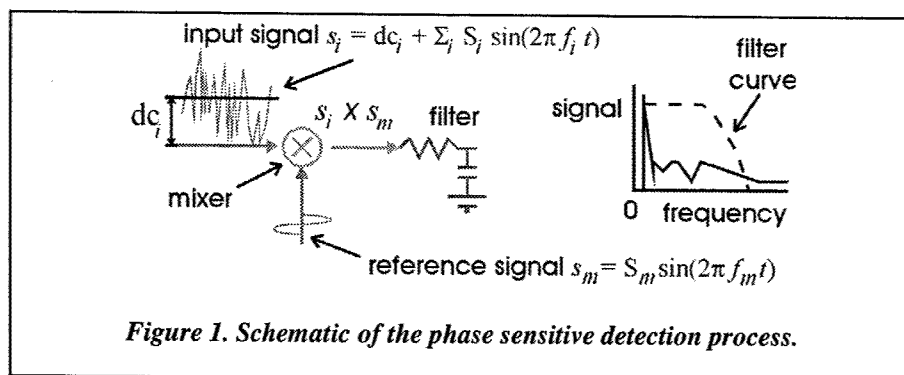
A system that uses an analog mixer produces best results when both the optical amplitude modulation and the reference are a pure sinusoid. A square wave, for example, has many frequency components that will be rejected by the filter, and this reduces signal power. The time to acquire the signal varies inversely with the filter cutoff frequency. As the cutoff frequency is reduced, SNR is improved but more averaging takes more time. The system described is phase sensitive in the sense that the phase between the input and reference signals can be adjusted, allowing simultaneous access to both the "in phase" and "quadrature" terms.

Demodulation on-chip

The new CMOS device performs functions that are analogous to phase-sensitive detection as just described, but it has been designed to optimize performance using typical imaging CMOS structures. The system-level model for the operation of one unit cell (one active pixel) is shown in Figure 2. The device has been designed to demodulate square waves because it is a digital device. It therefore samples in the odd harmonics characteristic of a square wave, but those are the same harmonics in a square-wave-modulated optical signal. Thus, the square-wave/sinusoid mismatch at the mixer and filter described above does not occur here. This theoretically infinite spectrum is ultimately band limited, however, by other devices throughout the system.

The optical signal is represented at the left in Figure 2 by a cartoon depicting an amplitude-modulated square wave with a large optical offset (also called "dc$_i$" here). The optical signal is then converted into an electrical signal at the photodetector. One "off" period is sampled at the start of each camera frame, suitably clocked in phase with the modulation signal. This signal is held in a sample and hold device, and that dc signal level is used to control a current amplifier that subtracts this sensed dc level from the photodetector current (this function is represented by the first summing junction in the figure). This removes most of the dc offset before signal processing commences. The signal-processing path in Figure 2 then splits into an upper and lower section. The upper section depicts signal processing during the in-phase ("on" in the cartoon) portion of each cycle and the lower section denotes the out-of-phase (or quadrature, "off" in the cartoon) portion. The actual chip doesn't have two identical lines, most of the functions are accomplished with one set of devices by control of clocking, but that is difficult to depict in a diagram.

Figure 3. Schematic of demodulation for the active-pixel CMOS array.
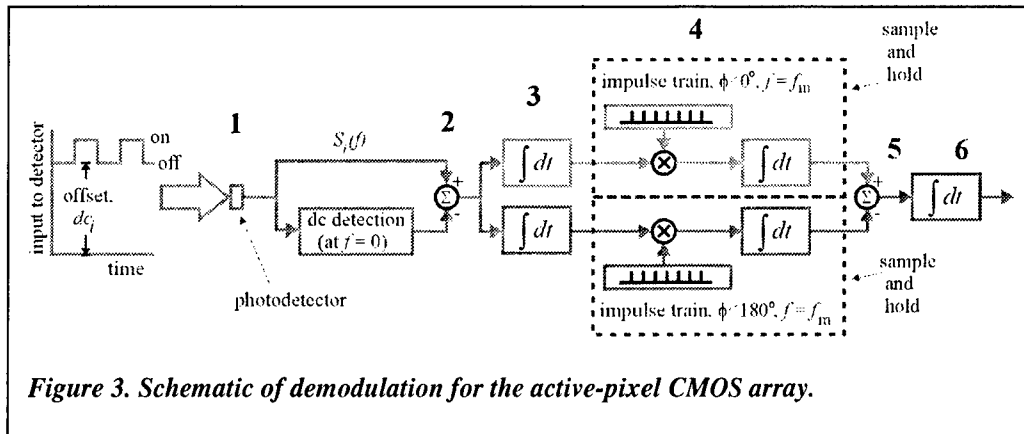
The integrator that follows dc rejection sums up the "on" or "off" portions of the individual modulation curves. The impulse train inside the upper sample and hold section then samples the average from the "on" (or in-phase) cycle once every cycle. The lower section shows that the same function occurs for the quadrature portion ("off") of each cycle. The sampling output then goes to another integrator that collects these samples, and averages over multiple cycles. There actually are two of these fed by one switched input. It will be possible to shift the phase of the demodulation process relative to the trigger input.

A lock-in amplifier modulates gain by the mixing process. Here, we modulate gain by switching into integrators every half cycle for the in-phase signal and every half cycle for the quadrature signal. Functionally, it is a square-wave, gated-integrator *pair* that modulates gain (i.e. collected photoelectrons) in a phase-sensitive way. Next these two are differenced in order to produce a signal that represents the modulation itself. Note also that residual dc offset is removed here. The final integrator in Figure 2 is the camera frame rate. The functions just described allow this CMOS device to perform square-wave phase sensitive detection on-chip, at the pixel level.

Figure 3. Mounted CMOS chip.
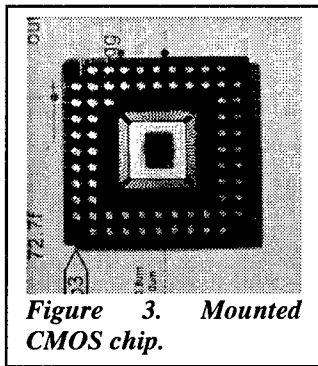
At the time of this writing, 10 chips (see Figure 3) have been delivered to CSM. Working with Black Forest Engineering, we have designed electronics for imaging chip control, including a flexible system that uses programmable driver chips. Prototype PC boards for camera control have been tested and commercial-grade PC boards have been purchased. Initial output tests have been completed. Pixel yield is clearly very high; there are no failed pixels on any of the chips tested. The chip is very sensitive to modulated optical input and insensitive to un-modulated input. It has not been possible to saturate the chip at dc, even with direct laser illumination. Analog processing on-chip is working well. We are currently integrating the system with a Bitflow® frame grabber.

Concluding remarks

Planned initial experiments will test the camera by using it as the sensor in an imaging spectrometer (CVI ¼ M device in our lab). The spectrometer will then be used to demonstrate two-photon Frequency Resolved Optical Gating (FROG). This experiment provides a good test of the camera, because the two-photon absorption signal will be modulated but it will reside on a large background. Following that, our plan is to apply this chip to imaging using pump/probe absorption spectroscopy.

Microphotonic laser-based sensors for the rapid detection of approach to lower explosion limit for hydrocarbon vapors

Kevin L. McNesby and Andrzej W. Miziolek
U.S. Army Research Laboratory
Aberdeen Proving Ground, MD 21005-5066
Tel/Fax: 410-306-0715/1909 Email:mcnesby@arl.army.mil

Abstract:
Microphotonic sensors for rapid (10 msec) measurement of vapors from hydrocarbon fuels JP-8, DF-2, and gasoline are discussed. Sensors systems include dual wavelength NIR systems, Fourier transform-based systems, and Mid-IR (interband cascade) systems.
OCIS codes: (280.3420) Laser sensors; (300.6260) Diode lasers

1. Introduction

This paper describes U.S. Army efforts of development of a microphotonic sensor for detection of fuel vapors. Several approaches are being investigated. For the first generation sensor, we provide results of quantitative measurements of room temperature vapor from the hydrocarbon-based fuels JP-8, DF-2, and gasoline. The first generation sensor is based upon near-infrared tunable diode laser absorption spectroscopy [1]. Second generation sensors, under development, use arrays of lasers (near and mid-infrared) to cover a wider spectral range. The fuel vapors of interest typically are mixtures of several hundred hydrocarbons, with an average molecular weight near 110 grams/mole (vapor), 150 grams/mole (liquid), and boiling points near 440K [2]. The fuels are liquids near room temperature and have flash points (often depending on age, storage conditions, etc.) in the vicinity of 315K.

2. Background

Using modulation techniques and phase sensitive detection methods for gas sensing, temporal resolution routinely exceeds 1 ms per measurement. Detection methods employed (typically wavelength modulation spectroscopy (WMS) and balanced ratiometric detection (BRD) techniques) [3,4] give good results for gas phase concentration measurements of small molecules with well resolved ro-vibrational absorption lines, such as hydrogen fluoride, methane, carbon monoxide, water, etc [5]. However, large and/or heavy molecules may not exhibit well resolved ro-vibrational absorption bands because of overlap between fundamental, combination, and/or overtone vibrations, and because of rotational constants which may be less than typical gas phase linewidths [6]. For mixtures of heavy molecules, e.g., the middle distillate fuels, the spectra may be even less structured. Figure 1 shows the near-infrared gas phase absorption spectrum of dry air saturated at 294K by the hydrocarbon fuels JP-8, DF-2, and gasoline (0.75 meter optical path), measured using a Fourier transform spectrometer. Both WMS and BRD, as usually employed, are not suitable for gases that have broad, unstructured absorption spectra [3,4,5]. For both techniques, the main limitation for fuel sensing is the narrow tuning range of the diode laser.

3. Measuring broad band absorbers with narrow band lasers

The method used in the first generation sensor takes advantage of the residual amplitude modulation (RAM) which occurs when a distributed feedback (DFB) diode laser is driven by a time varying injection current. This RAM occurs when the wavelength of a semiconductor tunable diode laser is varied by modulating the laser injection current. For the first generation sensor, two different DFB lasers are driven using a sinusoidally varying injection current. Each laser injection current is modulated at the same frequency but out of phase by 180 degrees [7]. These two lasers are combined to produce the probe beam used for the line-of-sight measurement. When the mixed, modulated probe beam is passed through a gas which preferentially absorbs the laser radiation from only one of the lasers, the signal at the detector is

modulated at the injection current modulation frequency and, for small absorptions, has an amplitude whose magnitude is proportional to the concentration of absorbing gas.

4. Results – first generation sensor

Figure 2 shows the gasoline vapor concentration (measured using the first generation sensor) as dry air saturated by gasoline vapor slowly displaces (several hundred cm^3/minute) the dry air in a 13.7 liter volume optical cell (4 meter path length). Also shown in this figure is the change in oxygen concentration that occurs during the displacement (oxygen sensor courtesy of Oxigraf, Inc., Mountain View, CA). This figure shows the sensor response as the vapor concentration approaches and exceeds the lower explosive limit (LEL) for most hydrocarbon vapors (e.g., for JP-8 the LEL is approximately 9500 ppm [2]). Each data point is the average of the lock-in amplifier output measured over 10 ms. All measurements were made at atmospheric pressure. We estimate the current limit of detection for each of these fuel vapors, using the first generation sensor, to be approximately 100 ppm-meter.

5. Discussion

An implication of the results presented here is that the device may be used to measure hydrocarbon vapor concentration for any middle distillate fuel. However, careful examination of the C-H overtone bands for each of the fuels shows that the contours of the absorption features, when normalized to each other, are not truly superimposable. Additionally, changes in temperature and changes in fuel composition make it necessary to measure the full C-H absorption envelope to get a truly accurate measure of approach to LEL.

6. Second generation sensor development

The second generation of our microphotonic-based fuel vapor sensor uses an addressable array of diode lasers, each emitting light at a slightly different wavelength, and power modulated at slightly different acoustic frequencies, to simulate the output of a Michelson interferometer. For this sensor system, several microphotonic lasers are used to span the spectral region from a wavelength of 1.55 to 1.75 micrometers (corresponding to the first overtone of C-H vibrations in hydrocarbons). The output from each laser is combined onto a single optical fiber. Each laser is power modulated (each at a different frequency) using standard tel-com drivers. This modulated light beam [8] is passed into free space, through a gas, liquid, or solid, and the transmitted light focused onto a detector. The output of the detector is then processed using a Fast Fourier Transform (FFT), in a manner identical to that of commercially available instruments. Time for each measurement is user controlled by varying the frequency of power modulation. Resolution is user controlled by varying the number of periods of power modulation measured per "scan", allowing spectral resolution on the order of natural linewidths in gases, with no hardware changes. Optical fiber coupling allows measurement in remote or dangerous locations.

References

[1] . K.L. McNesby, R.T. Wainner, R.G. Daniel, R.R. Skaggs, J.B. Morris, A.W. Miziolek, W.M. Jackson, and I.A. McLaren, "Detection and measurement of middle distillate fuel vapors using tunable diode lasers", Applied Optics, Vol. 40, pp. 840-845 (2001).
[2] D.W. Naegeli and K.H. Childress, "Lower Explosion Limits and Compositions of Middle Distillate Fuel Vapors", Proceedings of the Fall Meeting of the Society of Automotive Engineers, SAE paper # 982485, (1998), pp. 1-7.
[3] D.S. Bomse, A.C. Stanton, and J.A. Silver,"Frequency modulation and wavelength modulation spectroscopies: comparison of experimental methods using a lead-salt diode laser", Appl. Optics, Vol. 31, 718-731 (1992).
[4] P.C.D. Hobbs, "Ultrasensitive laser measurements without tears", Appl. Optics, Vol. 36, pp. 903-21, (1997).
[5] P. Werle, "A review of recent advances in semiconductor laser based gas monitors", Spectrochimica Acta Part A, Vol. 54, pp.197-236 (1998);
[6] G. Hertzberg, *Infrared and Raman Spectra*, Van Nostrand Rheinhold Co., New York, 1945.
[7] personal communication. 1 April 1999, Mark Allen, Physical Sciences, Inc., 20 New England Business Center, Andover, MA 01810.
[8] I. Linnerud, P. Kaspersen, and T. Jaeger, "Gas monitoring in the process industry using diode laser spectroscopy", Applied Physics B, Vol. 67, pp. 297-305, (1998).
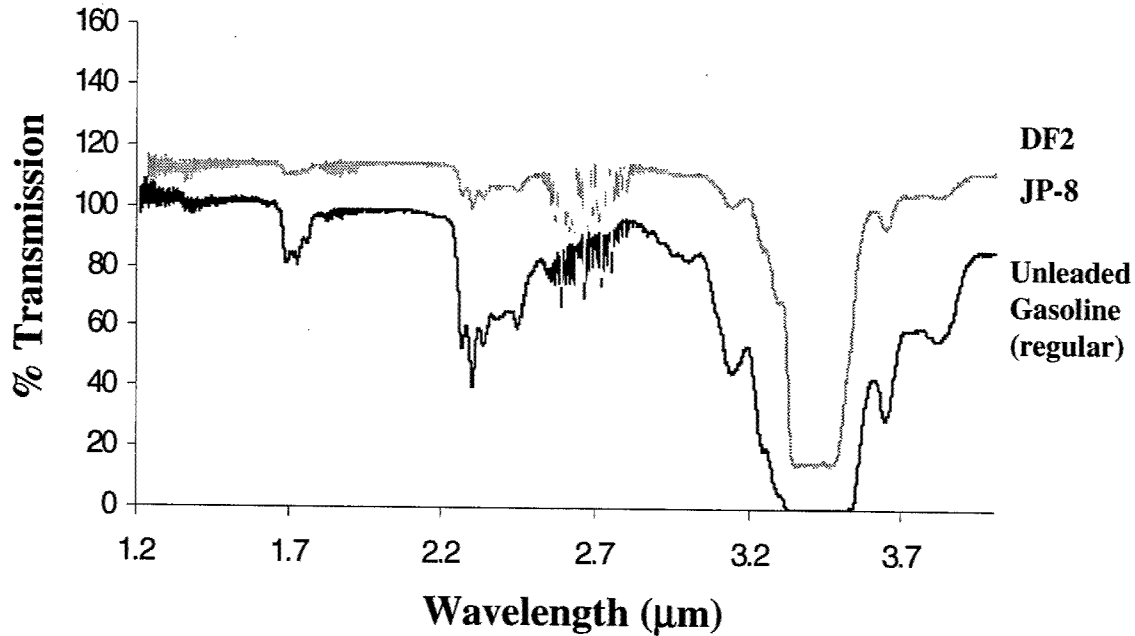
Figure 1: The infrared transmission spectrum of room temperature vapor from JP-8, DF2, and gasoline. The fundamental C-H absorption in each of these fuels is near a wavelength of 3.3 μm. The first overtone of the C-H stretch is near a wavelength of 1.71 μm. Spectra are offset for clarity
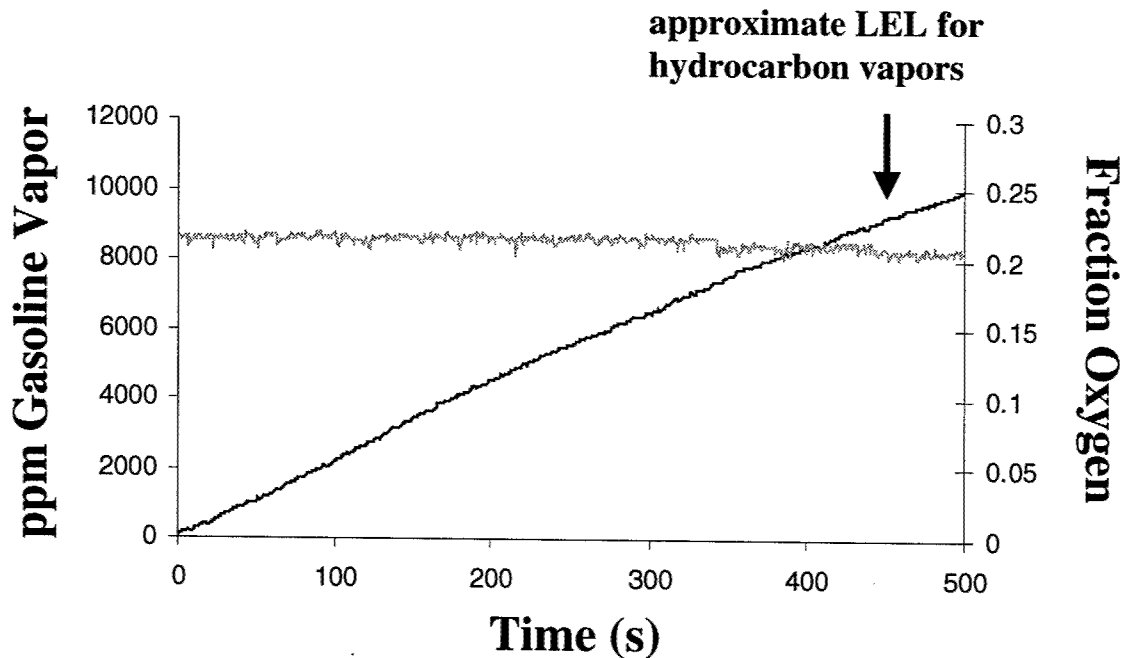

Figure 2: The approach to the lower explosion limit for hydrocarbon vapor, measured with the first generation sensor, as the dry air in a 13 liter optical cell is slowly displaced by air saturated with gasoline vapor at 1 atmosphere and 294K. Also shown is the change in oxygen concentration during the displacement (oxygen sensor courtesy of Oxigraf, Inc.).

Fractionation of aerosol particles produced by laser ablation in ICP-MS analysis

J. Koch, L. Feldmann, N. Jakubowski, K. Niemax
Institute of Spectrochemistry and Applied Spectroscopy, Bunsen-Kirchhoff-Strasse 11, 44139 Dortmund, Germany
Phone: +49-231-1392-101, Fax: +49-231-1392-310, e-mail: niemax@isas-dortmund.de

Abstract: The element composition of aerosol particles produced by laser ablation (laser wavelength: 266 nm; laser pulse length: 5 ns) of brass and steel in Ar and He and deposited on different segments of the transport tube to an Ar ICP have been measured by ICP-MS. Depending on the experimental parameters and the matrix, the element composition of the aerosol particles deposited on different parts of the tube deviated from the stoichiometric element ratios of the bulk and varied along the tube.
©2000 Optical Society of America
OCIS codes: (140.3440) Laser-induced breakdown; (999.9999) Solid-state analysis, Laser ablation ICP-MS

1. Introduction

In recent years laser ablation (LA) has become a popular technique of solid sampling, in particular, in ICP-MS analysis. Almost all companies producing ICP-MS instruments offer pulsed lasers, sample cells and appropriate tubes for the aerosol particles. However, the laser ablation process is very complex. It depends on many experimental parameters, such as the laser intensity, laser pulse length and wavelength, the buffer gas and its pressure in the ablation cell, and the morphology and composition of the matrix [1]. The problem is that all mentioned parameters are more and less dependent on each other. Therefore, optimization of the analytical figures of merit is difficult and problems with accuracy of the analytical results may occur. In particular, it is not obvious whether or not the element composition of aerosol particles transported into the ICP is the same as in the bulk.

The present paper investigates fractionation effects on the aerosol transport by studying the element composition of the aerosol particles deposited on the walls of the transport tube. Furthermore, it has been investigated whether or not the dry aerosol particles produced in the ablation process and transported into the ICP can be calibrated using aqueous standards which are nebulized and transported into the ICP as wet aerosols.

2. Experiment

Laser ablation is performed in a cylindrical cell of 12.5 cm^2 volume with the focussed beam of the fourth harmonic of a Nd:YAG laser (Spectron SL801, pulse width: 5 ns, pulse rate: 10 Hz). Argon and helium are applied as buffer gases in the ablation cell. The aerosol produced in the ablation process is transported by a gas flow of 2.5 L/min through a polyethylene tube (length: 3 m, inner diameter: 4 mm) into a quadrupole ICP-MS (power: 1.25 kW) operated with argon (auxiliary and cooling gas flow rates: 1.25 and 14 L/min, respectively).

Two samples were applied: a brass sample with a Cu/Zn ratio of 63/37 and a high-alloy steel sample with the major elements Fe (36 %), Ni (29 %), Cr (25 %) and Mn (2 %). The two isotopes ^{65}Cu and ^{66}Zn, and the four isotopes ^{57}Fe, ^{62}Ni, ^{50}Cr and ^{55}Mn were measured in the brass and steel experiment, respectively.

After aerosol deposition, the tube was cut into equally long pieces (length: 20 cm). The brass deposition was chemically disintegrated by HNO_3, while the particles of the steel experiment had to be disintegrated by aqua regina. The absolute masses as well as the element ratios of the deposited aerosols were measured by ICP-MS in dependant on tube length. The element ratios were compared with the ratios obtained from aqueous solutions of the bulk material.

3. Results and discussion

Fig. 1 and 2 show the ICP-MS Cu/Zn signal ratios as measured in brass dependant on acquisition time for two different laser intensities in Ar and He, respectively. Furthermore, the ratios measured in the bulk solution are shown

as dashed lines. It can be seen that there is, within the limits of uncertainty, no dependence of the Cu/Zn ratio on laser intensity. However, there are significant differences between the dry and wet aerosols. Furthermore, the experimental ratios of the dry aerosol in Ar is always larger than than of the wet aerosol, while it is the other way around for He.
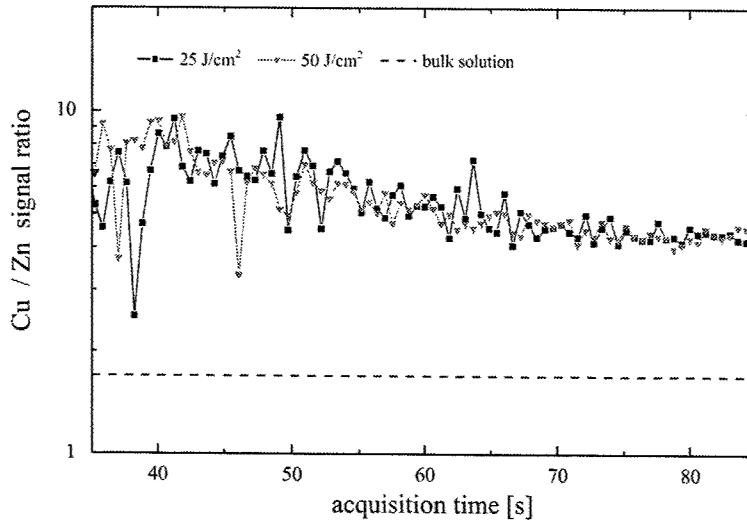

Fig. 1. Cu/Zn ratio measured on-line by LA-ICP-MS of brass in Ar at two different laser intensities. The dashed line shows the experimental result obtained with an aqueous solution of the bulk.
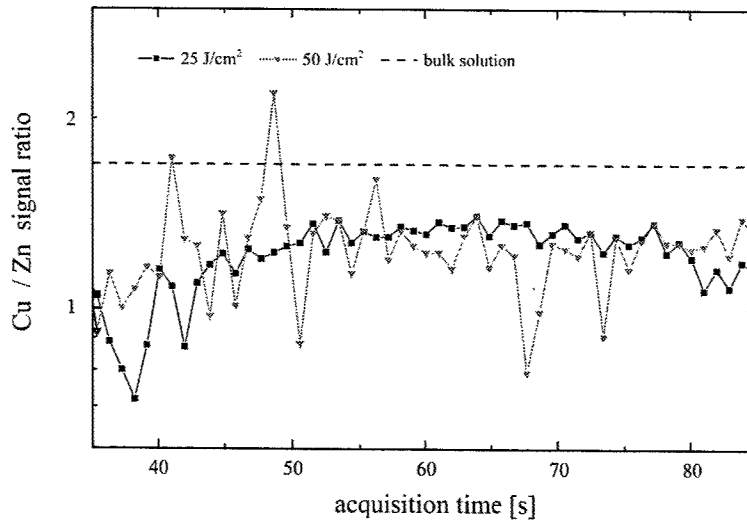
Fig. 2. Results of on-line LA-ICP-MS measurements in He. For further details: see caption of Fig. 1

The deposited mass of Cu and Zn as well as the Cu/Zn ratios dependant on the tube length are shown in Fig. 3. Helium was applied as a noble gas in the ablation cell. It can be seen that the major mass of the aerosol particles is deposited on the first part of the tube as expected. The Cu/Zn ratio in the deposited particles is smaller than the ratio

obtained with the bulk solution, in particular in the first segments of the tube. For Ar the discrepancy between the element ratios in the deposited particles and in the bulk was even larger.
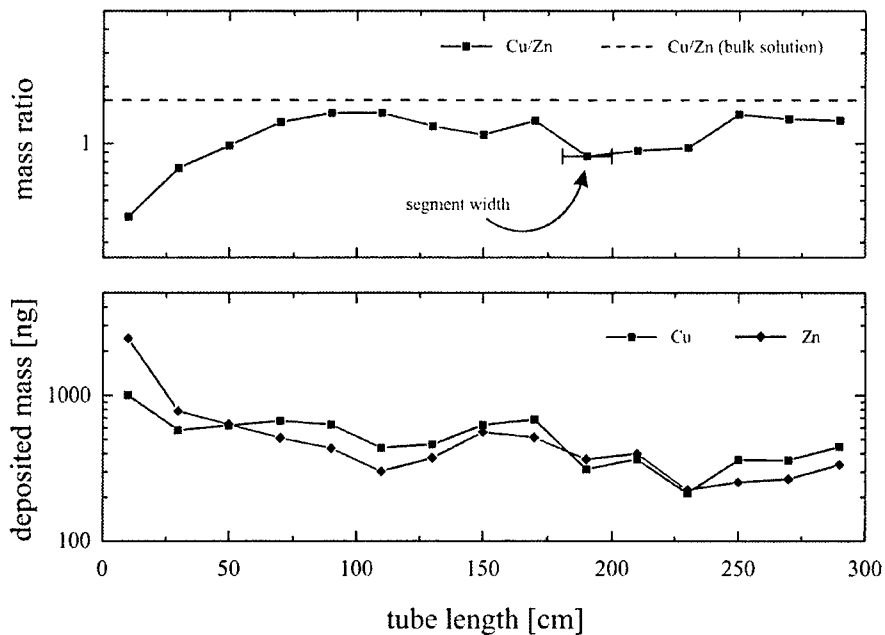
Fig. 3. The masses of Cu and Zn in aerosol particles deposited on the inner wall of the transport tube to the ICP (bottom) and their ratio (top). The Cu/Zn ratio measured in the bulk solution is shown as dashed line.

The LA measurements of steel samples in Ar and He revealed smaller fractionation effects. The differences between the element ratios measured in the dry and wet aerosol were smaller than with brass.

4. Conclusion

The present investigations have shown that LA-ICP-MS data cannot directly be calibrated with aqueous standards. Furthermore, fractionation effects can seriously effect the composition of aerosol particles transported into the ICP.

5. Reference

[1] K. Niemax, "Laser ablation – reflections on a very complex technique for solid sampling", Fresenius J. Anal. Chem. **370**, 332-340 (2001).

Diode Lasers and Applications I

Saturday, February 9, 2002

Douglas Baer, Los Gatos Res., USA
Presider

SaB
10:40am–12:20pm
Flagstaff

Analysis by diode laser absorption spectroscopy in a linear dielectric barrier discharge

K. Kunze, M. Miclea, J. Franzke, K. Niemax
Institute of Spectrochemistry and Applied Spectroscopy, Bunsen-Kirchhoff-Strasse 11, 44139 Dortmund, Germany

C. Vadla
Institute of Physics, Bijenicka 46, HR-10000 Zagreb, Croatia

Abstract: The diagnostic as well as the application of a miniaturized dielectric barrier discharge as detector for analytical spectrometry were investigated using diode laser absorption spectrometry of the excited species produced in the plasma.
©2000 Optical Society of America
OCIS codes: (300.1030) Spectroscopy, absorption; (300.6260) Spectroscopy, diode lasers

1. Introduction

Recently we reported on the detection of halogenated hydrocarbons by diode laser atomic absorption spectrometry (DLAAS) in a linear dielectric barrier discharge (DBD) at reduced pressure [1]. It was shown that introduced halogenated molecules were completely dissociated and the detection limits of the excited chlorine and fluorine atoms were similar to those obtained in a microwave discharge [2] even if the average power of the DBD is much smaller (< 1 W). In order to improve the upper results the plasma parameters of the miniaturized discharge were studied by a diagnostic method based on spatial and temporal resolved diode laser absorption measurements of excited atoms in the discharge. The determination of the gas temperature and electron density might help to understand the mechanisms which leads to a complete dissociation of the introduced molecules and to improve the detection of analytes.

2. Experimental arrangement

The linear dielectric barrier discharge consists of two parallel aluminum electrodes (50 mm length, 0.7 mm width) covered by a glass type dielectric (ε_r= 6) layer of 20 µm with an interelectrodic space of 1 mm. The discharge is operating at reduced pressure (10 - 100 mbar) in argon as well as helium with a gas flow of 10 - 1000 ml/min. The applied voltage has a rectangular shape with a frequency of 5 - 20 kHz and an amplitude of 750 Vpp. The discharge shows a transient behavior. The halfwidth of the current peak is about 10 µs and the discharge is ignited over the whole length of the electrodes.

In order to explain the analytical results obtained for the detection of halogens, we proposed a method of investigation that can give detailed information about the production of excited atoms between the electrodes. The experimental arrangement for diode laser absorption measurement with a high spatial and temporal resolution is shown in Fig.1.
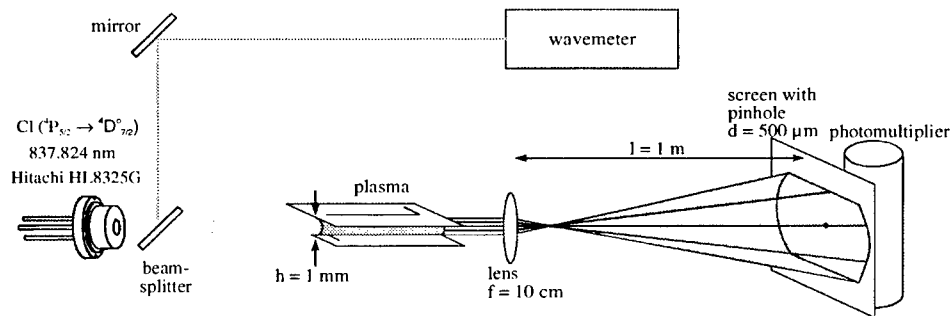

Fig. 1. Schematic view of the experimental arrangement with high spatial resolution

The collimated beam of a laser diode is passing the discharge channel and is imaged by a lens (f = 16 cm) on a screen at a distance of 1 m. A pinhole of 200 μm selects a small part of the transmitted laser beam representing a limited area in the plasma. A fast Hamamatsu photomultiplier placed very close to the pinhole is used as a detector. Moving the pinhole from the cathode to the anode side the distribution of excited species was investigated with a spatial resolution of about 50 μm. The absorption signals were measured on the whole period of the applied voltage in order to study also the temporal behavior of the excited species.

3. Results and discussion

3. 1. Absorption measurements in the buffer gas

Plasma diagnostic measurements for the determination of the excited atom density, gas temperature and electron density were performed studying the argon atoms excited on the metastable ($1s_5 \rightarrow 2p_8$, 801.699 nm) and resonance ($1s_4 \rightarrow 2p_6$, 800.836 nm) states. The highest concentration of excited argon atoms was always near the temporary cathode around 12 μs after the start of the current pulse. The absolute density of both resonance and metastable states were 2×10^{12} atoms/cm³ and 10^{13} atoms/cm³, respectively.

The gas temperature and the electron density were calculated from the absorption line profiles of the resonance transition taking into account all significant broadening mechanisms (Doppler-, pressure- [3] and Stark-broadening [4]). At the temporal maximum of the current peak the gas temperature reaches a maximum value of around 1000 K and the electron density is higher than 10^{15} /cm³ at the spatial maximum of the excited atom density, in the vicinity of the temporal cathode. During the remaining time of the discharge cycle and in other positions the gas temperature is close to room temperature and the electron density is much lower and cannot be calculated with the proposed method. There is complete dissociation in this very thin layer of high electron density.

3. 2. Measurements on halogenated hydrocarbons

Taking into account the spatial distribution of excited argon atoms it is expected to improve the detection of Cl atoms if the measurements are restricted to the volume of high atom density. The distribution of excited Cl atoms on the metastable ($^4P_{5/2}$) level was measured in Ar and He with an admixture of 150 ppm CCl_2F_2 by measurments of the 837.824 nm line.

Fig. 2 presents the spatial and temporal distribution of excited Cl atoms for one period of the applied voltage in argon and helium. The flow rate was 200 ml/min and the pressure 20 and 30 mbar, respectively.
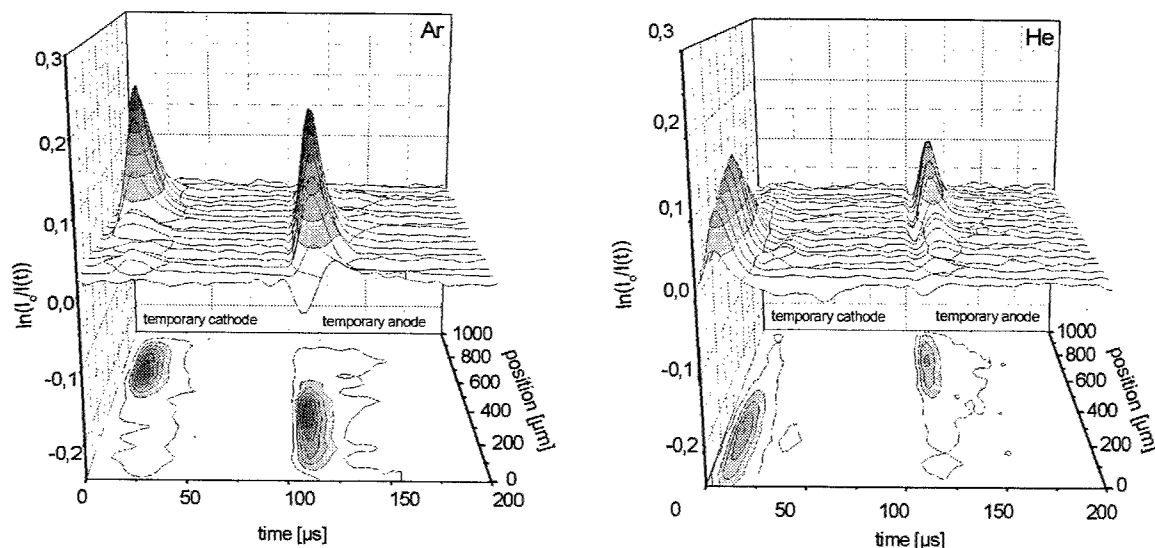

Fig. 2. Spatial distribution of excited Cl atoms in argon (left) and helium (right)

At low pressure the maximum density of excited Cl atoms in an argon discharge is close to the temporary cathode and spatially narrow, similar to the results obtained by the measurements of excited Ar atoms. In helium the distribution is broader and the highest excitation processes are taking place in between the middle of the discharge and the temporary anode. With the increase of the pressure, the maximum starts to move in the direction of the cathode. Also the relative density of excited Cl atoms is smaller in helium than in argon. This different spatial distributions of excited atoms can mainly be explained by the presence of electrons. The electron density in a He plasma is smaller than in an Ar plasma at the same operating conditions and as a consequence the probability of electron collisions in He is less. The position of the maximum density of the excited Cl atoms in these two buffer gases is determined by the mean free path of the electrons which is in argon three times smaller than in helium [5]. Electrons produced close to the cathode are moving further in helium than in an argon discharge.

Taking into account the obtained results, the absorption signal of Cl excited atoms was measured only in the plasma volume at 100 μm from the cathode in dependence on CCl_2F_2 concentration. In Fig. 3 the calibration curve of CCl_2F_2 in argon in comparison with the former calibration curve obtained measuring in the whole plasma volume is shown. The absorption was measured by a phase sensitive detection using the plasma modulation of the DBD. The signal dependence on concentration is also linear and the restriction of the absorption to the volume with the highest atom density increases the value of absorption by one order of magnitude. The detection limit calculated with the 3σ - criterion without any spatial resolution was about 5 ppb and in the new conditions this can be one order of magnitude better using a low noise detector.
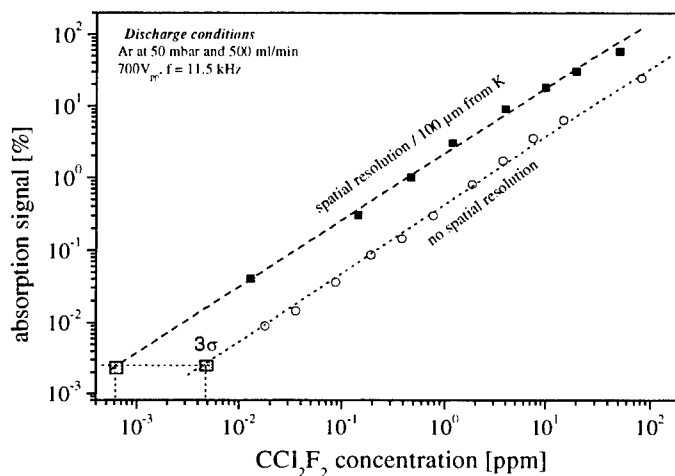
Fig. 3. Detection of CCl_2F_2 by the absorption of Cl atoms with and without spatial resolution

4. Concluding remarks

The experimental method described to study the distribution of excited atoms by diode laser spectroscopy with a high spatial resolution enable us to study the plasma parameters and to improve the detection limit of analyte by measuring only in the plasma volume containing the maximum density of excited species. The results explain the reasons for the good applicability - complete dissociation and low detection limits - of the DBD in analytical systems. Experiments applying this discharge as a selective detector for gas chromatography are under way in our laboratory.

5. References

[1] M. Miclea, K. Kunze, G. Musa, J. Franzke and K. Niemax, "The dielectric barrier discharge - a powerful microchip plasma for diode laser spectrometry", Spectrochim. Acta Part B **56**, 37-43 (2001).

[2] A. Zybin, C. Schnürer-Patschan and K. Niemax, "Wavelength modulation diode laser atomic absorption spectrometry in modulated low pressure helium plasmas for element-selective detection in gas-chromatography", J. Anal. At. Spectrometry **10**, 563-567 (1995).

[3] D.P. Aeschliman, R.A. Hill and D.L. Evans, " Collisional broadening and shift of neutral argon spectral lines", Phys. Rev. A **14**, 1421-27 (1976).

[4] H. Griem, *Plasma Spectroscopy* (McGraw-Hill, New York, 1964)

[5] A. von Engel, *Ionized gases* (Oxford University Press, 1975)

Sculpted Tone Burst Modulation Spectroscopy

Chris Hovde

Southwest Sciences Ohio Operations, 6837 Main St., Cincinnati OH 45244
tel 513-272-1323 e-mail dchovde@swsciences.com

Abstract: By manipulating the amplitude modulation waveform for tone burst spectroscopy, the response of a tunable diode laser spectrometer can be tailored to avoid the effects of many interference fringes that otherwise limit sensitivity.
©2000 Optical Society of America
OCIS codes: 300.6380 Spectroscopy, modulation; 140.3490 Lasers, distributed-feedback

1. Introduction

Various techniques have been devised to suppress source noise in tunable diode laser absorption spectroscopy (TDLAS) measurements, such that interference fringes usually limit the sensitivity of trace gas detection by tunable diode laser absorption spectroscopy. These fringes arise from weak, accidental reflections in the optical path. They result in a slowly changing, wavelength-dependent optical background from which it is difficult to distinguish the absorption feature of the target gas.

Techniques for suppressing interference fringes include mechanically dithering an optical element [1], or varying the sample pressure [2]. When using frequency or wavelength modulation spectroscopy, fringes can be reduced by careful adjustment of the modulation amplitude, adding a second modulation waveform [3,4], using non-sinusoidal modulation waveforms [5], detecting at a high harmonic of the modulation frequency [6], or modulating at a high frequency [7]. These approaches are successful for a limited number of fringes.

Tone burst spectroscopy [8,9] is a more general form of two-tone frequency modulation spectroscopy. Most applications of tone burst modulation to laser spectroscopy have involved switching a sine wave on and off. Using inexpensive digital techniques it is now possible to generate arbitrary tone burst waveforms. By adjusting the amplitude envelope of the tone burst waveform, the instrument function can be tailored to efficiently amplify only the signal components of interest. This paper describes a way of using tone burst spectroscopy to detect trace gases while suppressing optical fringes.

2. Theory

Weak stray reflections cause a sinusoidal modulation of the background. When modulation techniques are used, the sinusoidal signal that is detected depends on both the amplitude of the interfering beam and the instrument function. The instrument function is most easily defined in Fourier space. A demodulated spectrum acquired over a given wavelength interval can be Fourier transformed. The Fourier transform of such a spectrum is the product of the Fourier transform of the transmission spectrum times the Fourier transform of the instrument function. The instrument function depends on the shape [5] and amplitude of waveform, detection harmonic, etc. Wavelength modulation spectroscopy using sine wave excitation and 2nd harmonic detection yields a Bessel function [3]. The instrument
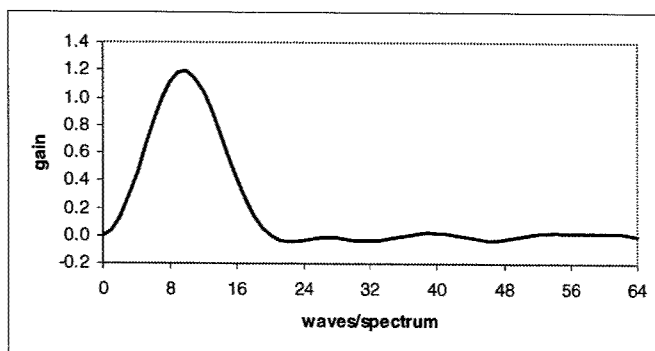

Figure 1 Instrument function for a sculpted tone burst modulation waveform, in Fourier space.

function for tone burst modulation can be found by numeric simulation (Fig. 1).

In real instruments, several weak reflections may be present, resulting in a background that is a superposition of sine waves of different period and slowly changing phase. The demodulated output may be found by multiplying each sine wave by the instrument function appropriate to that period. Thus, the instrument function serves to amplify selected Fourier periods in the transmission spectrum. Fringes of one period are efficiently detected, fringes of another period are not.

Likewise, the absorption feature can be thought of as a superposition of Fourier components of a range of periods. The demodulated signal can be found by multiplying the Fourier components by the instrument function, then back-Fourier transforming.

To optimize the detection of a trace gas signal, it seems desirable to limit the instrument function so that only those Fourier components are amplified that are present in the trace gas spectrum. Amplifying other Fourier components risks the introduction of fringes to the spectrum without adding information about the gas concentration. The instrument function for a tone burst spectrometer can be modified by adjusting the relative amplitudes of the
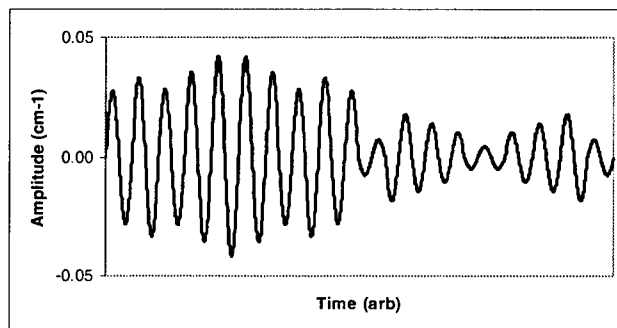
Figure 2 Scultped tone burst waveform, including both the on (left half) and "off" (right half) of the waveform.

individual sine waves that make up the tone burst waveform. It is important to allow for the possibility of weak modulation during the "off" cycle of the waveform. The waveform shown in Fig. 2 gives rise to the instrument function shown in Fig. 1. It was computed using a crude nonlinear algorithm to optimize the amplitudes of 19 sine waves that make up the waveform to produce a target instrument function similar to the final function, with some symmetry constraints to simplify the search for an optimum.

3. Experiment

As can be seen from Fig. 1, the sculpted tone burst waveform can be used to restrict the Fourier components that are efficiently detected to a range associated with the trace gas absorption signal. As a result, signals can be discerned even in the presence of strong etalons. Fig. 3 shows an experimental test. The waveform of Fig. 2 was programmed into a digital waveform synthesizer and used to modulate the current of a 1650 nm diode laser (Anritsu). The laser beam was reflected off a ring resonator to cause strong, controllable fringes, and through a methane sample. By blocking the light path through the ring resonator the fringes could be turned off without any change in optical alignment. Also in Fig 3 for comparison are the spectra obtained using conventional wavelength modulation. The laser tuning was not linear with applied current, making the cancellation of fringes somewhat more difficult. The sculpted tone burst waveform offers a clear advantage.

4. References

1. J. A. Silver and A. C. Stanton, "Optical interference fringe reduction in laser absorption experiments," Appl. Opt. 27,1914 (1988).
2. A. Fried, J. R. Drummond, B. Henry and J. Fox, "Reduction of interference fringes in small multipass absorption cells by pressure modulation," Appl. Opt. 29, 900 (1990).
3. D. T. Cassidy and J. Reid, "Harmonic detection with tunalbe diode lasers — two-tone modulation," Appl. Phys. B. 29, 279 (1982).
4. D. S. Bomse, "Dual modulation laser line-locking scheme," Appl. Opt. 30, 2922 (1991).
5. T. Iguchi, "Modulation waveforms for second -harmonic detection with tunable diode lasers," J. Opt. Soc. Am. B. 3, 419 (1986).
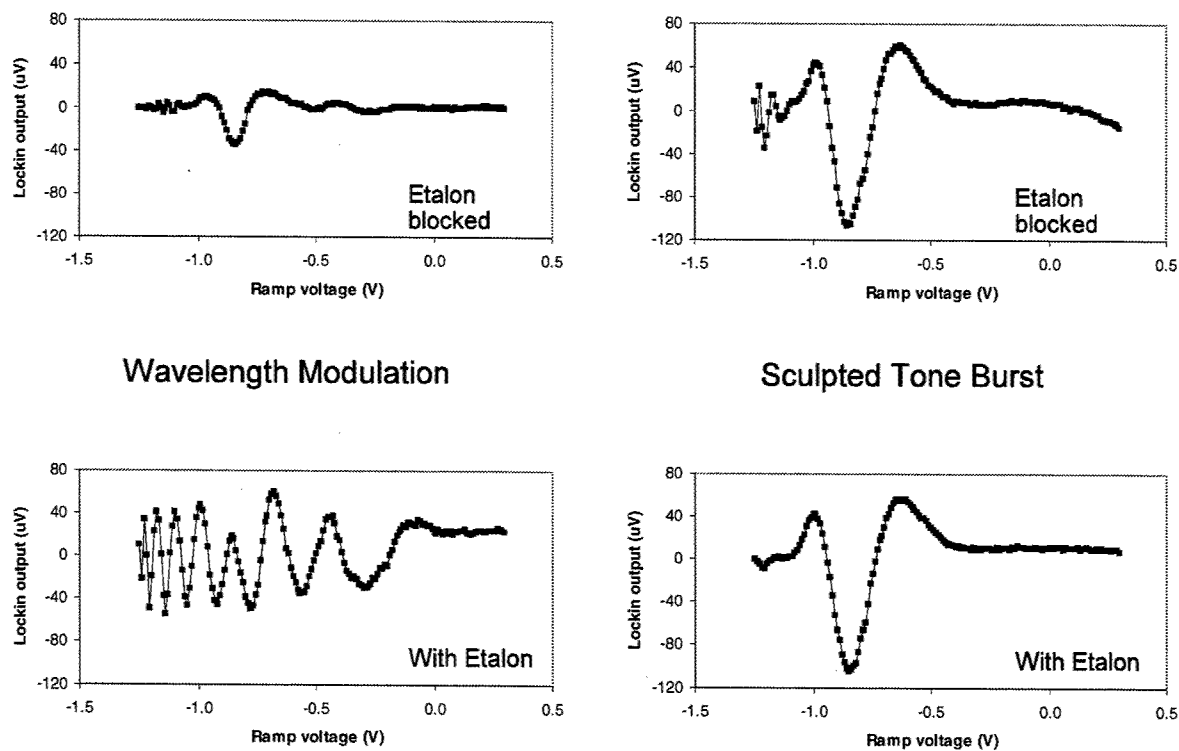
Figure 3 Experimental verification of fringe suppression using sculpted tone burst modulation (right), compared to conventional wavelength modulation(left). The ramp voltage controlled the laser current. The absorption signal arises from an 8 cm path through 33 Torr neat methane.

6. A. N. Dharamsi, P. C. Shea and A. M. Bullock, "Reduction of effects of Fabry-Perot fringing in wavelength modulation experiments," Appl. Phys. Lett. 72, 3118 (1998).

7. D. R. Hjelme, S. Neegård, and E. Vartdal, "Optical interference fringe reduction in frequency-modulation spectroscopy experiments," Opt. Lett. 20, 1731 (1995).

8. H. M. Pickett, "Determination of collisional linewidths and shifts by a convolution method," Appl. Opt. 19, 2745-2749 (1980).

9. C. S. Gudeman et al.,"Tone-burst Modulated Color-center-laser Spectroscopy," Optics Lett. Vol. 8, pp. 310-312 (1983).

Wavelength Agile External Cavity Diode Laser for Trace Gas Detection

Jeffrey S. Pilgrim
Southwest Sciences, Inc., 1570 Pacheco Street, Suite E-11, Santa Fe, NM 87505
(505) 984-1322, FAX (505) 988-9230. jpilgrim@swsciences.com

Abstract: We have developed an external cavity diode laser that is wavelength modulated with injection current. The laser has broad spectral coverage and is inexpensive. We have obtained a minimum detectable absorbance of 5E-05.

1. Introduction

Widespread application of diode laser-based trace gas sensing is inhibited by the lack of consistent diode laser availability at sufficiently numerous wavelengths. Furthermore, trace gas sensing applications typically require the most sophisticated and expensive types of diode laser architecture. Thus, devices are often not available at the required wavelength with the appropriate structure. An external cavity diode laser (ECDL) design can provide a solution to this problem. Our ECDL uses an uncoated Fabry-Perot diode as the gain element in an external resonator. The use of uncoated Fabry-Perot diodes results in devices that are both inexpensive and available at a wider variety of wavelengths than the more complicated diode architectures. In addition, use of an intracavity wavelength selective element, like a diffraction grating, in an external cavity provides for much increased available tuning ranges. The broad tuning range available to ECDLs allows for detection of multiple trace gas species with a single laser. Additionally, a diode laser that is slightly off-color can be made useful when incorporated into an ECDL.

Typical ECDL designs provide wavelength tuning and modulation by movement of a resonator optic. Thus, high sensitivity trace gas detection methods like wavelength modulation spectroscopy (WMS) are hampered by the resulting low wavelength modulation frequencies. Trace gas detection sensitivity generally decreases with decreasing modulation frequency. We have developed an ECDL at Southwest Sciences that retains the broad tuning characteristics of competing designs while simultaneously providing for wavelength modulation with injection current modulation. Injection current modulation allows for much higher modulation frequencies than mechanical movement of an optic.

2. External Cavity Diode Laser

Our ECDL is based on the well-known Littman-Metcalf design whereby the first order off a diffraction grating is fed back via a mirror to create the external cavity [1]. The zeroeth order of the grating is used as the laser output. Our design differs from the standard Littman-Metcalf design in several ways. The Fabry-Perot diode laser used as the gain element does not have an anti-reflection coating. Thus, the Fabry-Perot modes are superimposed on the ECDL frequency structure. Because the Fabry-Perot modes are tunable with diode laser temperature and injection current, the ECDL becomes tunable with diode laser temperature and injection current. The diffraction grating is used to provide low spectral dispersion in the external cavity. This allows the Fabry-Perot modes to move around within the broad pass band of the diffraction grating. Finally, the actual tuning behavior is marked by controlled mode hopping among the external cavity longitudinal modes through the interaction of the Fabry-Perot diode modes with the grating pass band.

Coarse wavelength tuning is provided, as in other ECDL designs, by rotation of the cavity feedback mirror. An example of the tuning range of our design is provided as Fig. 1 using a nominal 1550 nm Fabry-Perot diode laser as gain medium. The ECDL tunes over 30 nm in this wavelength range. The laser tunes with the feedback mirror by hopping from one Fabry-Perot mode to the next. These are the wavelengths of the data points in the figure. Fine wavelength tuning is provided by either changing the diode laser temperature or injection current, or both. Fig. 2 shows the wavelength tuning with injection current. Injection current tuning causes the laser to hop from one external cavity longitudinal mode to the next. These are the wavelengths of the data points in the figure. The external cavity retains the same tuning rate with current as the isolated diode laser. This is in contrast to other

ECDL designs where the high dispersion of the diffraction grating severely limits the ability to tune with injection current or laser temperature.
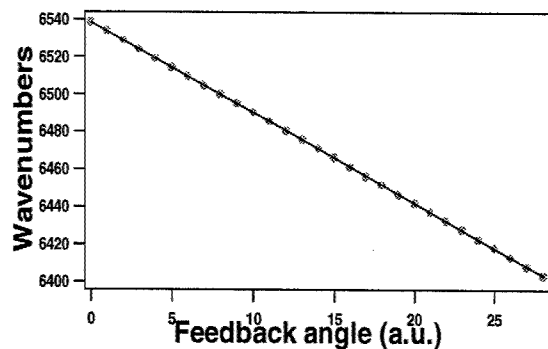

Fig. 1. Coarse wavelength tuning range of ECDL using mirror feedback angle. The laser hops diode Fabry-Perot modes.
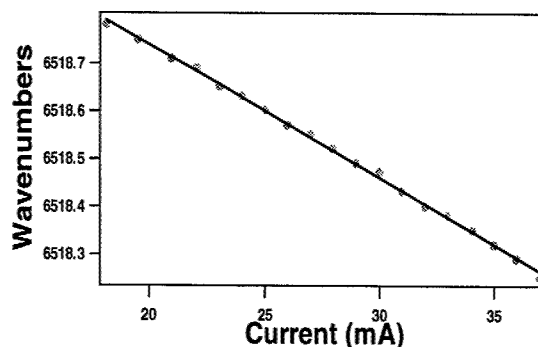

Fig. 2. Fine wavelength tuning using diode laser injection current. The laser hops longitudinal cavity modes.

The combination of the wavelength selection provided by the Fabry-Perot diode modes and the grating pass band causes the ECDL to always operate single mode within any selected Fabry-Perot mode. The laser smoothly transitions from single mode operation on one external cavity longitudinal mode to the next adjacent mode when tuned with either temperature or current. Thus, the mode hops are controlled and the overall operation is much like that of a distributed feedback (DFB) laser that is operated with a current driver using a digital modulation waveform. Indeed, in trace gas detection applications the digital nature of the ECDL laser output can be an advantage.

3. Trace Gas Detection

We have demonstrated trace gas detection with the ECDL using a 1550 nm Fabry-Perot laser as the gain element. This wavelength region is suitable for detecting both hydrogen cyanide (HCN) and acetylene (C_2H_2). We detected $H^{12}C^{14}N$ on the P(14) line of the first C-H stretch overtone at 6474.41 cm^{-1}. Fig. 3 shows an injection current scan over this absorption feature using the ECDL. The line was scanned with a triangle current ramp at 2 kHz. Note the choppy structure superimposed on the absorption feature. The structure corresponds to the longitudinal mode hops which provide the mechanism for the wavelength scan with injection current. There are over twenty mode hops across the absorption feature. A critical aspect of our ECDL design is that the laser resonator is long enough to provide sufficiently small longitudinal mode spacing to adequately sample the absorption feature of interest. The cavity length providing the data in the figure was 56 cm. We have also implemented our ECDL design with an intracavity multiple pass cell to provide the required cavity length in a compact package. Even with a cavity optical length of 56 cm, the laser need be no larger than 3" x 5".
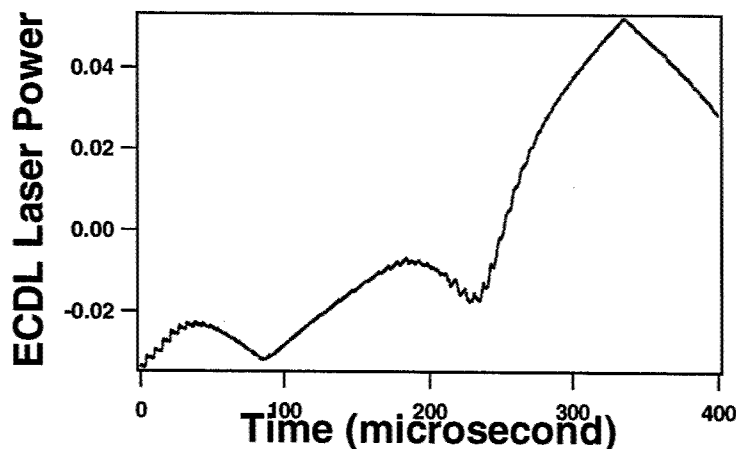
Fig. 3. Injection current spectral scan of the ECDL wavelength over an HCN absorption feature at 1544.5 nm. The fine structure is due to the longitudinal mode hop-based tuning mechanism.

The absorption line of Fig. 3 was used to demonstrate WMS detection while modulating the laser wavelength with injection current. Fig. 4 shows the demodulated signal at twice the modulation frequency ($2f$ detection) while simultaneously scanning over the absorption feature with a 10 Hz triangle current ramp. The modulation frequency was 5 kHz with a modulation depth of +/- 0.12 cm^{-1}. The achievable modulation frequency is limited only by the Fabry-Perot diode laser properties and the available equipment. We have modulated the laser at 50 kHz, which is an order-of-magnitude faster than that achieved by other ECDL designs.
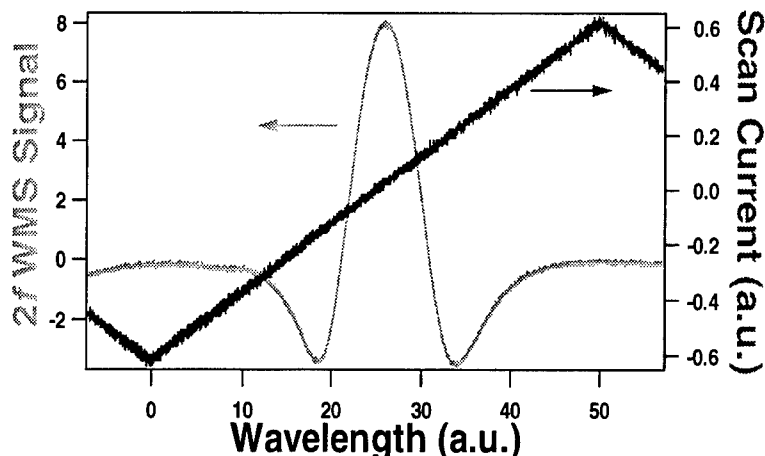
Fig. 4. Injection current modulated ECDL with phase sensitive detection at twice the modulation frequency with a simultaneous wavelength scan over the absorption feature.

We have also built an ECDL on the present design using a 1535 nm Fabry-Perot diode laser in order to detect acetylene. Acetylene is easier to handle than HCN and it is simpler to provide consistently precise concentration levels for determining absorbance sensitivity. Fig. 5 shows an acetylene concentration challenge to the ECDL trace gas sensor. The WMS signal magnitude at twice the 20 kHz modulation frequency was used as the absorbance (concentration) metric. The sensor followed the changing acetylene concentration to high precision. The standard deviations of the measurements at constant concentration average to an equivalent absorbance of 2.6E-04 in a 1 Hz bandwidth. Because it appeared that the limiting noise source in the measurement was second harmonic distortion, we combined the wavelength modulated ECDL with a New Focus Nirvana noise canceller after the design of Haller and Hobbs [2]. The noise canceller was effective in reducing the limiting noise source from second harmonic distortion to a spurious etalon. The minimum detectable absorbance was improved to 5E-05. Etalons are often the limiting noise sources in WMS experiments and, under those conditions, the ECDL performs as well as other tunable diode laser systems while providing much broader spectral coverage.
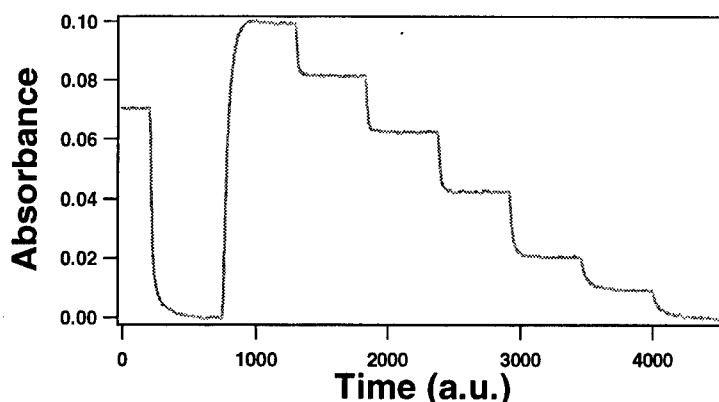

Fig. 5. Measured absorbance using $2f$ signal amplitude with changing acetylene concentration. The minimum detectable absorbance is 2.6E-04. Addition of a noise canceller improves the minimum detectable absorbance to 5E-05.

4. References

M. J. Littman and H. J. Metcalf, "Spectrally narrow pulsed dye laser without beam expander", Appl. Opt. **17**, 2224 (1978).

K. L. Haller and P. C. D. Hobbs. "Double beam laser absorption spectroscopy: shot noise-limited performance at baseband with a novel electronic noise canceller", SPIE Vol. 1435, 298 (1991).

Evanescent-field laser sensor for in-situ monitoring

of volcano gas emissions

Ulrike Willer, Irina Kostjucenko, Christian Bohling, Thomas Zentgraf, Dirk Scheel, Wolfgang Schade

Institut für Physik und Physikalische Technologien, Technische Universität Clausthal
Leibnizstrasse 4, D-38678 Clausthal-Zellerfeld, Germany
e-mail: wolfgang.schade@tu-clausthal.de

ABSTRACT

A DFB laser diode (1.57 µm) is guided through a pure core fused silica fiber. Tuning the laser frequency across molecular resonances will change the frustrated (FTR) and the attenuated total reflection (ATR). Such an evanescent-field laser sensor is used for in-situ monitoring of H_2S in volcano gases at the site "Solfatara"(Italy).

OCIS Codes: Fiber optic sensors (060.2370), diode laser spectroscopy (300.6260)

1. INTRODUCTION

Laser absorption spectroscopy is a very suitable technique for measuring gaseous environmental pollutants because of its high sensitivity and selectivity and the capabilities for online and in-situ applications. In general laser absorption spectroscopy requires an open optical path or a one- or multi-pass absorption cell that contains the gas under investigation. Further more, it requires optically thin media, scattering processes have to be negligible, and only sites with a direct optical access can be probed. This limits the possibilities of the method for most in-situ applications. However, evanescent-field spectroscopy [1-4] in the infrared (IR) or mid-infrared (MIR) provides a technique that allows to apply absorption spectroscopy for the diagnostics of molecular species in optical thick media or in media where scattering cannot be neglected.

In the present paper a concept of a compact evanescent-field laser sensor for practical in-situ and online applications is described. First results from H_2S concentration measurements in volcano fumerols are reported and discussed with respect to early diagnostics of volcano activities. In fig. 1 correlation between seismic activities and a change in the concentration of volcano gases (e.g. H_2S) is shown [5]. This indicates that a change in the concentration of H_2S may be a precursor for volcano eruptions. Measurements to affirm this assumption can be done by the evanescent-field laser sensor that is reported in the present paper.
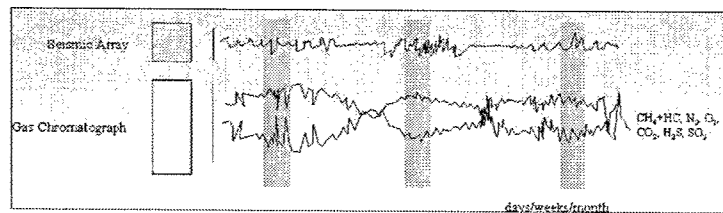

Figure 1: Schematic correlation between seismic activity and change of gas concentration in a volcano fumerole [5].

2. EXPERIMENTAL

In the case of evanescent-field spectroscopy the wavelength of the laser radiation that is transmitted through the fiber is tuned across an absorption line of a molecular species that surrounds the fiber. In the vicinity of an atomic or molecular resonance simultaneously a wavelength dispersion of the index of refraction and of the absorption coefficient is observed and results in a change of the FTR and the ATR, respectively. When measuring the laser intensity at the end of the fiber while tuning the laser wavelength across an absorption line, both effects contribute to the measured spectral line profile. Similar to the direct laser absorption spectroscopy the recorded line profiles in the case of evanescent-field spectroscopy can be used for diagnostic applications, e.g. measuring the concentrations of environmental pollutants.

In order to optimize the sensitivity the number of reflections at the interface between fiber and surrounding medium should be as large as possible. This is achieved by increasing the length z of the fiber and decreasing the radius r of the fiber. Because the numerical aperture of the fiber that is used as a sensor is given by $NA = n \sin\Theta$ there is not only one single angle Θ when a laser beam is coupled into the fiber. Therefore, the laser power P that is measured by the detector at the end of the fiber is an integral over all possible angles Θ and is proportional to the incident laser intensity I and to the reflectivity R raised to the power of m which is the number of reflections in the fiber [6]:

$$P(z,\lambda) = \int 2\pi \, I(z=0,\Theta,\lambda) \, R(\lambda,\Theta)^{m(\Theta,z)} \sin\Theta \, d\Theta \qquad (1)$$

Since the reflectivity $R(\lambda,\Theta) = [1 - \alpha(\lambda) \cdot d_{eff}(\lambda,\Theta)]$ contains the absorption coefficient $\alpha(\lambda) = \sigma_{ik} \cdot \Delta N$ the number density N_0 of molecules in the ground state can be determined by measuring $P(z,\lambda)$ with $\Delta N = N_0 - N_1$ and $N_1 << N_0$. d_{eff} gives the penetration depth of the evanescent-field into the surrounding medium and depends on the laser polarization, the index of refraction, and the wavelength λ. The number of total reflections can be calculated from $m(z,\Theta) = (z \tan\Theta)/2r$, where r is the radius of the fiber.

3. RESULTS AND DISCUSSION

Evanescent-field spectroscopy is applied to measure in-situ H_2S concentrations in volcano gas emissions by tuning a single frequency DFB diode laser at $\lambda = 1.57$ µm (SPECDILAS D, Laser Components). Evanescent-field spectroscopy is very advantageous in these experiments since scattering of the laser light by the high concentration of water vapor which is typical in volcano gas streams will dramatically limit the laser absorption method for any analytical application. Typical gas flow streams out of the volcano fumerols are 10 ms^{-1} and the temperature is about 150 °C. For these measurements a multimode fused silica fiber with a core diameter of 200 µm is used. Because of the extreme toxic environment the evanescent field fiber sensor part consists of the core material of the fiber only, no additional polymer layers for selective adsorption of selected species (e.g. H_2S) are used. In a first step the plastic cover of the fiber is removed mechanically while in a second step the cladding is removed chemically. The sensing part of the fiber is formed as a coil and is fixed in a teflon mounting. This part acts as the compact evanescent-field sensor which is placed directly into the volcano fumerole (refer to fig. 3a). The active fiber length of the evanescent-field sensor is typically 2.0 meters. The diode laser, the photodiode detector and the electronics for controlling the system and recording the data are located in a separate and sealed box to protect these devices from the toxic gases. This box is connected with the evanescent-field fiber sensor by fiber cables, typical fiber lengths are 10 meters. In fig. 2 laboratory evanescent-field spectra for H_2S at 1.57 µm are shown as the gas pressure in a cell that contains the laser sensor is changed. A broadening of the spectra with increasing H_2S pressure is obtained. A typical in-situ evanescent-field spectrum for H_2S at 1.57 µm for the conditions in a fumerole at the volcano site "Solfatara" (Italy) is shown in fig. 3b. The lower trace is measured with the sensor directly located in the fumerole. Because of the high pressure and temperature in the fumerole the H_2S absorption lines are strongly broadened (pressure- and Doppler broadening) and therefore single rotational lines cannot be resolved even though the spectral bandwidth of the DFB diode laser is in the order of several 10 MHz.
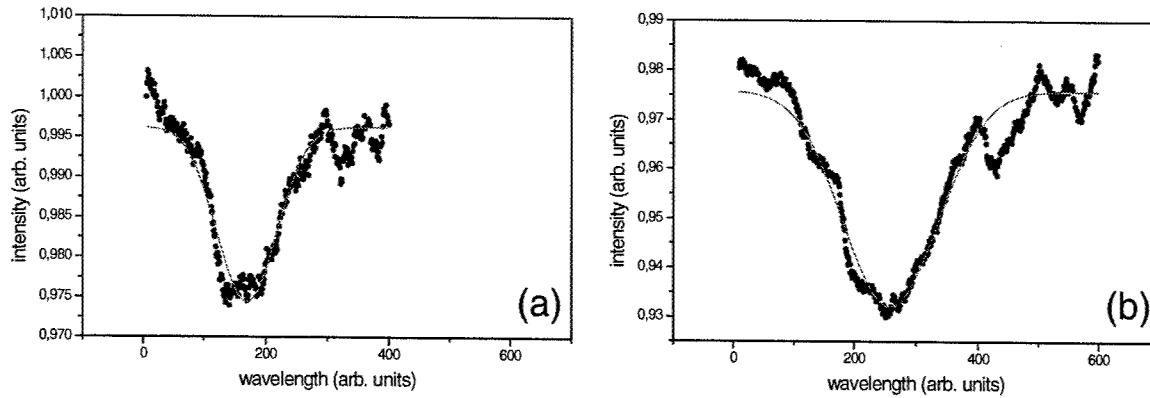
Figure 2: Laboratory evanescent-field spectra for H_2S at 1.57 μm. (a) 100 mbar H_2S pressure. (b) 400 mbar H_2S pressure.

However, the measured signal is mainly dominated by the line at 1571.304 nm because of its strong line strength. The upper trace corresponds to a scan under exactly the same experimental conditions but now the sensor is located beside the volcano fumerole. Then the H_2S concentration is much lower or even close to zero because of dilution effects and no absorption signal is detected by the evanescent-field laser sensor. Therefore these measurements can be used as a reference.
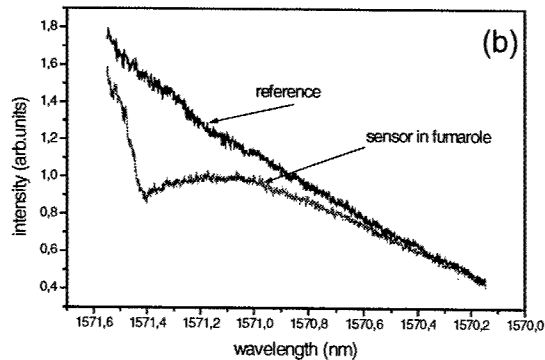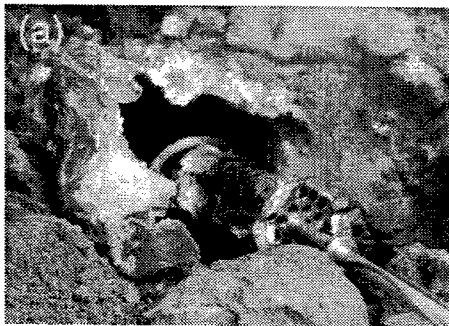
Figure 3: (a) In-situ application of the evanescent-field laser sensor at the volcano site "Solfatara" (Italy). (b) Wavelength scan for the detection of H_2S directly in the volcano fumerole.

4. References

1. D. Bunomovich et al.; Journal of Molecular Structure **292**, 125 (1993).
2. S. Simhony, E.M. Kosower, A. Katzir; Appl. Phys. Lett. **49** (5), 253 (1986).
3. I. Paiss, D. Bunimovich, A. Katzir; Appl. Opt. **32**, 5867 (1993).
4. J. P. Dunkers, K. M. Flynn, M. T. Huang, W.G. McDonough; Appl. Spectroscopy **52**, n 4, 552 (1998).
5. E. Faber, Bundesanstalt für Geowissenschaften und Rohstoffe, Hannover, private communication (2000).
6. N.J. Harrick; Internal Reflection Spectroscopy, John Wiley & Sons, New York (1967).

Spectroscopic trace gas detection with pulsed quantum cascade lasers

Anatoliy A. Kosterev and Frank K. Tittel
Rice Quantum Institute, Rice University, Houston TX 77251-1892
akoster@rice.edu

Shawn Wehe, David M. Sonnenfroh, and Mark G. Allen
Physical Sciences Inc., 20 New England Business Center, Andover, MA 01810

Rüdeger Köhler, Claire Gmachl, Federico Capasso, Deborah L. Sivco, and Alfred Y. Cho
Bell Laboratories, Lucent Technologies, 600 Mountain Avenue, Murray Hill, NJ 07974

Abstract: Pulsed quantum cascade lasers operating at wavelength of 10 and 4.6 microns were used for detection of ammonia and carbon monoxide, respectively. Variations of atmospheric CO concentration were continuously monitored with 12 ppbv precision using a 1 m optical pathlength.
©2002 Optical Society of America
OCIS codes: (280.1120) Air pollution monitoring; (280.3420) Laser sensors

Sensitive, compact devices for the quantification of trace gases are required for a number of applications that include industrial process control, environmental monitoring, and non-invasive medical diagnostics. A well-established technique for detecting molecular species in the gas phase is high-resolution infrared absorption spectroscopy. Fundamental vibrational absorption bands of molecular species are located in mid-IR region (3 to 20 μm). Quantum cascade (QC) lasers are the only kind of semiconductor lasers that enable to reach this region without the use of cryogenic cooling. When the distributed feedback (DFB) structure is embedded into such a device, it operates in a single-frequency mode, which is of particular use for spectroscopic applications [1]. However, most of the available QC-DFB lasers can operate at near-room temperature (that is, with thermoelectric cooling) only in pulsed low-duty cycle mode. This mode of operation leads to a relatively broad (>300 MHz) and asymmetric laser line [2]. These device characteristics require the development of new approaches to measurement procedures, data acquisition and analysis compared to those developed for the diode laser spectroscopy.

The QC-DFB laser based gas sensor architecture is defined by the required sensitivity to a particular gas species. We shall report two versions of the sensor. A one-channel configuration was used to detect ammonia by its absorption in the v_2 vibrational band ($\lambda \approx 10$ μm). The sensitivity of this sensor was ultimately limited by pulse-to-pulse fluctuations of the QC-DFB laser energy. A two-channel configuration removed this limitation and was used to monitor CO concentrations in ambient air at $\lambda \approx 4.6$ μm.

Configurations of the two sensors are shown in Fig. 1. The same laser housing and a 50 cm long optical gas cell were used in both experiments. The QC-DFB laser was mounted on top of a three-stage thermo-electric cooling element (Melcor 3CP) inside a vacuum-tight housing with overall dimensions of 100×160×180 mm³ (depicted in Fig. 2) assembled from commercially available vacuum and opto-mechanical components. To remove the heat generated by the operation of the Peltier cooler, the bottom of the thermo-electric assembly was soldered to a water-cooled housing base plate. A temperature controller (Wavelength Electronics LFI-3751 TE) was used to set and monitor the laser temperature. With this arrangement, the operating QC-DFB laser could be cooled to -55°C.

The laser emission was collimated using an aspheric AR coated ZnSe lens with a focal length of 3 mm and a diameter of 6 mm mounted inside the housing. The lens position could be adjusted externally. The collimated laser light emerged from the housing through a 30' wedged AR coated ZnSe window for 10 μm radiation or uncoated CaF₂ window for 4.6 μm radiation and was directed into 0.5 m long optical gas cell. This cell consisted of a glass tube fitted with Teflon valves and stainless steel window holders based on commercial 1⅓" vacuum flanges. One of the cell ends was equipped with a window, and the other one with a SiO protected flat Al mirror (both ⌀25.4 mm). This resulted in a two-pass configuration with a total optical pathlength of 1 m.

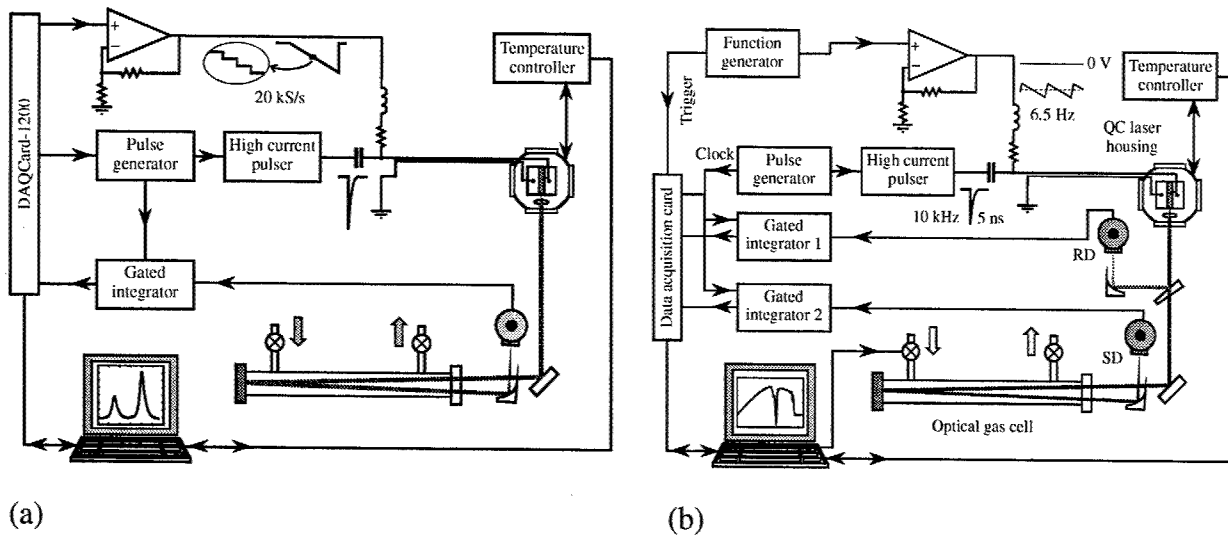(a)   (b)

Fig. 1. Schematic of the pulsed QC-DFB based gas sensors. (a) a one-channel configuration used to detect NH₃; (b) a configuration with an added reference channel, was used for atmospheric CO monitoring. SD – signal detector, RD – reference detector.

The laser current was supplied in 5 ns long, 2 to 4 A peak current pulses. The repetition rate of the laser pulses was limited to 20 kHz by the gated integrator (Stanford Research Systems, model SR250) used as an interface between the fast IR detector and data acquisition card. The concentration of the sample was found from the absorption data by finding the best fit as described by the equation

$$y_i = Bf(i - x)$$

where y_i are the acquired fractional absorption data, $f(i)$ is an absorption line envelope as measured for a known high-concentration sample at the same pressure, temperature and laser operation parameters; B is proportional to the species concentration in the test sample, and x is introduced to take into account laser frequency drift.

To detect NH₃, the absorption lines $^aR_1(2)$ at 992.4503 cm^{-1} and $^aR_0(2)$ at 992.6988 cm^{-1} (~10.1 μm) in the v_2 fundamental absorption band were selected. These lines are strong, well resolved at pressures below 200 Torr and free from interference by water and other air components absorption. The pulsed QC-DFB laser available for this work accessed this wavenumber region when operated at a temperature of –11.7°C. An example of the acquired spectrum is presented in Fig. 2a. This plot shows the averaged data obtained after 400 frequency scans, 256 laser pulses each. A sensitivity of better than 0.3 ppmv was achieved with a 1 m optical pathlength.

For detection of CO the laser frequency was scanned over a 0.41 cm^{-1} region encompassing the R(3) absorption line at 2158.300 cm^{-1}. This transition is free from interferences from atmospheric species such as H₂O. The R(3) line of CO was obtained by the 4.6 μm QC-DFB laser when its substrate temperature was maintained at –23.3°C. The subthreshold current used to scan the laser frequency [3] in these experiments was driven by the external function generator and not by the synchronized D/A converter, as in the ammonia detection experiment. This was made to avoid the limitation of 256 points per scan imposed by the available 12-bit DAQCard-1200 (National Instruments) data acquisition card. A number of laser pulses per frequency scan was increased to 1500. This result in the sensitivity gain, according to the equation [4]

$$\delta A = \sigma \sqrt{\frac{\Delta v}{\int g^2(v)dv}}$$

where δA is a standard deviation of the measured absorption line area, Δv is the frequency scan resolution (inversely proportional to the number of pulses in the scan) and $g(v)$ is the absorption spectrum normalized by the condition $\int g(v)dv = 1$.
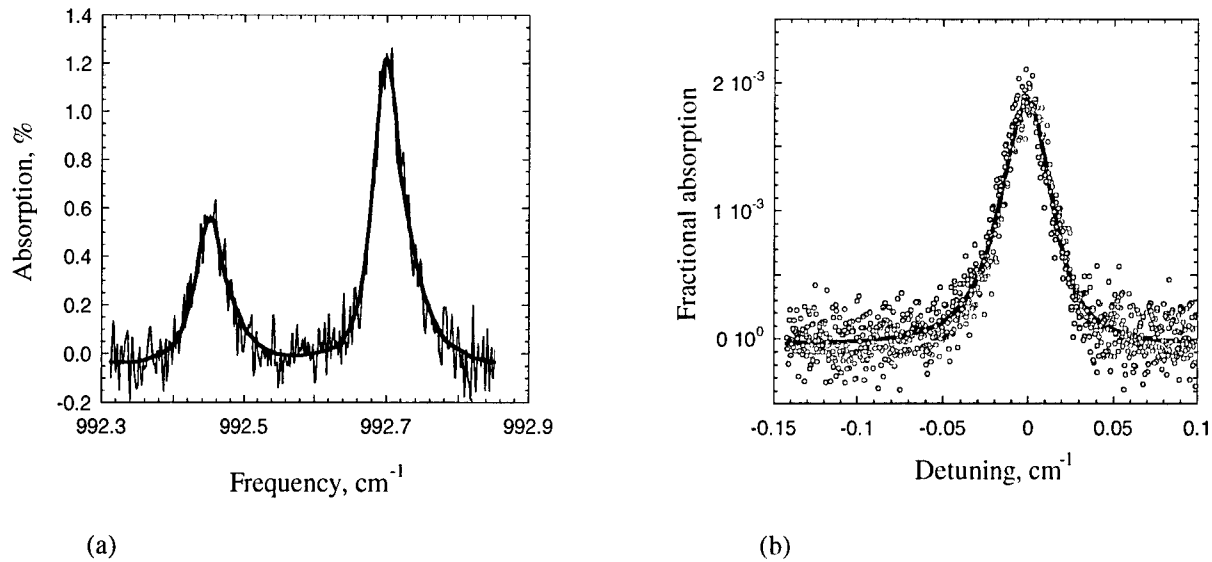
Fig. 2. Sample absorption spectra of (a) NH_3, 6.7 ppmv; (b) CO, 870 ppbv. Horizontal axis on the plot (b) shows the laser frequency detuning from the line center at 2158.300 cm^{-1}.

The detected absorption of atmospheric CO is shown in Fig. 2b. A noise-equivalent detection limit of 12 ppbv was experimentally demonstrated with the same 1m optical pathlength. This sensitivity corresponds to a standard error in the fractional absorbance of 3×10^{-5}. The CO sensor was applied to continuous monitoring of the CO concentration in the ambient laboratory air. Two characteristic maxima of CO concentration were observed during a typical day, corresponding to morning and evening rush hour traffic.

To improve the QC-DFB laser based gas sensor performance, we plan to upgrade the high amplitude pulsed current source and data acquisition electronics to enable 1 MHz current pulse and data sampling repetition rate. The data acquisition that now takes 2.5 min in our experiments would take only 1.5 s after such an upgrade. It is also possible to replace liquid nitrogen cooled detectors with the thermoelectrically cooled detectors to completely avoid the use of consumables in such gas sensors.

REFERENCES

1. C. Gmachl, F. Capasso, R. Köhler, A. Tredicucci, A. L. Hutchinson, D. L. Sivco, J. N. Baillargeon, and A. Y. Cho, "The sense-ability of semiconductor lasers", *Circuits & Devices*, May 2000, 10-18

2. A. A. Kosterev, F. K. Tittel, C. Gmachl, F. Capasso, D. L. Sivco, J. N. Baillarg   A. L. Hutchinson, and A. Y. Cho, "Trace-gas detection in ambient air with a thermoelectrically cooled, pulsed quantum-cascade distributed feedback laser", *Appl. Opt.* **39**, 6866-6872 (2000)

3. K. Namjou, S. Cai, E.A. Whittaker, J. Faist, C. Gmachl, F. Capasso, D.L. Sivco, and A.Y. Cho, "Sensitive absorption spectroscopy with a room-temperature distributed-feedback quantum-cascade laser", Opt. Lett. **23**, 219-221 (1998)

4. A. A. Kosterev, A. L. Malinovsky, F. K. Tittel, C. Gmachl, F. Capasso, D. L. Sivco, J. N. Baillargeon, A. L. Hutchinson, and A. Y. Cho, "Cavity ringdown spectroscopic detection of NO with a CW quantum cascade laser", to be published in *Applied Optics* (October 2001)

Poster Session

Saturday, February 9, 2002

SaC
7:00pm–9:00pm
Canyon

Corrections for quantitative NO concentration measurements using time-resolved picosecond laser-induced fluorescence

J. Joshua Driscoll and Volker Sick
Dept. of Mechanical Engineering, University of Michigan, Ann Arbor, MI 48109-2121
jdiv@umich.edu, vsick@umich.edu

Roger L. Farrow and Paul E. Schrader
Combustion Research Facility, Sandia National Laboratories, P.O. Box 969, Livermore, CA 94551-0969
farrow@ca.sandia.gov, peschra@sandia.gov

Abstract: The corrections necessary to obtain nitric oxide mole fractions from picosecond laser-induced fluorescence signals are outlined

The use of laser-induced fluorescence (LIF) to measure minor species concentrations in flames is well documented [1]. Recently, short pulse picosecond lasers have been used to measure minor species [2,3], and have some distinct advantages over similar nanosecond techniques. When coupled with a fast detection scheme, picosecond excitation allows the fluorescence decay rate to be measured in atmospheric-pressure flames, and the subsequent quenching corrections be applied directly to obtain concentrations. This negates the need to model the quenching rates found in a flame, which requires accurate knowledge of temperature and collider-species concentrations across a flame. The application of this technique to the measurement of nitric oxide (NO) in a non-premixed laminar flame is outlined here. Additionally, other corrections necessary to obtain species concentrations from fluorescence signals are discussed.

For nanosecond LIF, often only time-integrated fluorescence can be measured, and the relationship between integrated signal and excited population must be determined. Because electronic quenching of NO $A^2\Sigma^+$ is largely rotational-level independent [4], the fluorescence signal obeys a single-exponential decay; the time constant is given by $1/(A+Q)$ [1], where A is the spontaneous emission rate, and Q is the electronic quenching rate. Therefore, the integrated fluorescence (FS) is proportional to the upper-state population after excitation, multiplied by the decay-rate time constant (2). Thus, if this time constant can be measured or modeled, concentrations can be determined.

$$\tau = (A+Q)^{-1} \qquad (1)$$

$$FS \propto \int_0^\infty N_0 \, e^{(-t/\tau)} dt = N_0\tau \qquad (2)$$

For picosecond LIF, the fluorescence decay can be measured directly in atmospheric flames and used to correct integrated signals. Alternately, the peak of the single-exponential decay, which is directly proportional to excited population, can be determined by de-convolving the measured LIF response. The latter technique is discussed in detail below, along with experimental details and LIF corrections.

The experiments were performed at the Combustion Research Facility, Sandia National Labs. The laser used is similar to that outlined in [5], but differs in that a 110ps pump-pulse is used, which results in a shorter pulse at 226nm (~55ps) and a wider laser linewidth (1.1cm^{-1} FWHM). The beam was passed through a slit, and the slit image was re-imaged into the flame, resulting in a nearly top-hat beam profile 200 microns tall by 2mm wide. By spreading the beam energy out over a larger cross section, non-linear effects caused by saturation, rotational energy transfer and photodissociation were minimized while increasing signal due to a large probe volume. The burner used is a duplicate of the atmospheric pressure, methane/air counter-flow burner detailed in [6]; a Tsuji burner with a porous, cylindrical, temperature-regulated fuel outlet at the top and a planar air velocity profile, capable of producing a highly stable diffusion flame at a distance of 3mm from the burner surface. LIF signals were collected perpendicular to the beam propagation direction with a pair of 50mm UV-achromatic lenses (Sigma-Koki) and the resultant signals were imaged onto the entrance slit of a 150mm monochromator. The P1 (0,0) band-head was pumped, and the grating and exit slit were set to collect fluorescence from the (0,1) and (0,2) vibrational bands. This signal was measured with a fast microchannel plate photomultiplier tube (PMT) (Hamamatsu R3809U-52) and

digitized with a Tektronix SCD5000 fast transient digitizer. Beam energy was measured before and after the flame with photodiodes to quantify beam absorption by combustion gasses.

Data collection and analysis proceeds as follows, with an example from one point in the flame NO profile. First, an on-resonance signal decay is taken, here at the NO A-X P_1 (0,0) band-head, and a non-resonant decay is also taken to account for fluorescing species with broad excitation range (background fluorescence). Care must be taken to avoid other sharp spectral features, such as vibrationally-excited oxygen lines [7]. For each signal, a delayed laser pulse (from the pump laser) is passed directly to the monochromator with an optical fiber and is detected about 15ns after the signal pulse on the same scan; this 'timing peak' is used to obtain temporal registration between the signal and background decays and correct for timing jitter (Fig. 1).

The instrument response function of the laser beam, PMT and digitizer was determined by measuring Rayleigh scattering, which is instantaneous on these timescales. The FWHM of the instrument response was comparable to that of the PMT, 320ps for the overall collection and 287ps for the PMT. Now, the off-line decay is shifted in time to line up with the on-line decay using the timing peaks as references. The off-resonance signal is then subtracted from the on-line signal, and the resultant curve is the NO fluorescence decay; this NO decay needs to be de-convolved with the instrument function to obtain the step-exponential that has the information on decay time and magnitude. In practice, an iterative process is performed where an exponential is convolved with the measured instrument function, compared to the NO decay, and adjusted until a best-fit single exponential is determined (Fig. 2).

The magnitude of this single-exponential decay is proportional to the number density of the excited NO rotational levels, but must be corrected for a number of factors to obtain NO mole fraction. First, the temperature (and pressure) at the point the NO data is taken must be known to correct for gas density. For this experiment, temperature was measured with broadband coherent anti-Stokes Raman spectroscopy (CARS). With temperature known, and low laser energies, the *relative* excitation fraction at that temperature can be calculated from knowledge of laser wavelength, laser linewidth and collision linewidth. Here, laser wavelength and linewidth were determined from a model fit to an excitation scan, and the NO collision linewidth was assumed to be dominated by N_2, and therefore only a function of temperature [8]. Doppler broadening of the NO linewidth can be included in the laser linewidth (both Gaussian). This has a small effect as the linewidths add in quadrature, and the Doppler width is on the order of 0.2 cm^{-1} compared to 1.1cm^{-1} for the laser (i.e. $\sqrt{(1.1^2 + 0.2^2)} \approx 1.1$). Next, the signals must be normalized for laser-energy fluctuations and corrected for beam absorption by flame gasses, and if the signal is integrated, the signal must be corrected by dividing by the decay rate. Finally, a calibration gas consisting of a known amount of NO (in this case, 30ppm NO in N_2) is measured, corrected as above, and then used to relate NO signals to NO mole fractions.

The signal and background plots for one point in the flame are shown in figure 1, with the timing peak denoted. Figure 2 shows the NO fluorescence decay data, the instrument response function, the convolved fit and the corresponding single step-exponential. The last plot (figure 3) shows how the corrections discussed above vary throughout the methane/air diffusion flame.

References
1. A. C. Eckbreth, *Laser Diagnostics for Combustion Temperature and Species*, Gordon and Breach, 1996
2. R. Schwarzwald, P. Monkhouse, J. Wolfrum, *Chem. Phys. Lett.* **158**, 1989, pp 60-64
3. M. W. Renfro, S. D. Pack, G. B. King, and N. M. Laurendeau, *Comb. Flame* **115**, 1998, pp 443-445
4. I.S. McDermid and J.B. Laudenslager, *J. Quant. Spectrosc. Radiat. Transfer* **27**, 1982, pp 483-492
5. P. P. Yaney, D. A. V. Kliner, P. E. Schrader, R. L. Farrow, *Rev. Sci. Instrum.* **71**, 2000, pp 1296-1305
6. V. Sick et al, *Twenty-Third Symposium (International) on Combustion*, The Combustion Institute, 1990, pp 495-501
7. D. D. Thomsen, F. F. Kuligowski, N. M. Laurendeau, *Appl. Optics* **36**, 1997, pp 3244-3252
8. A. Y. Chang, M. D. DiRosa, R. K. Hanson, *J. Quant. Spectrosc. Radiat. Transfer* **47**, 1992, pp 375-390
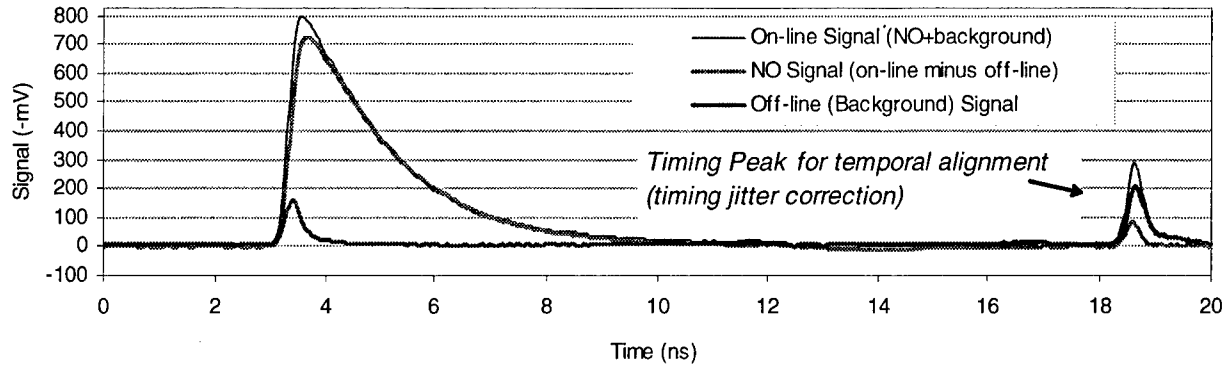
Fig. 1. On-resonance and off-resonance fluorescence decays. The timing peak is from the pump beam and coupled to the monochromator with an optical fiber.
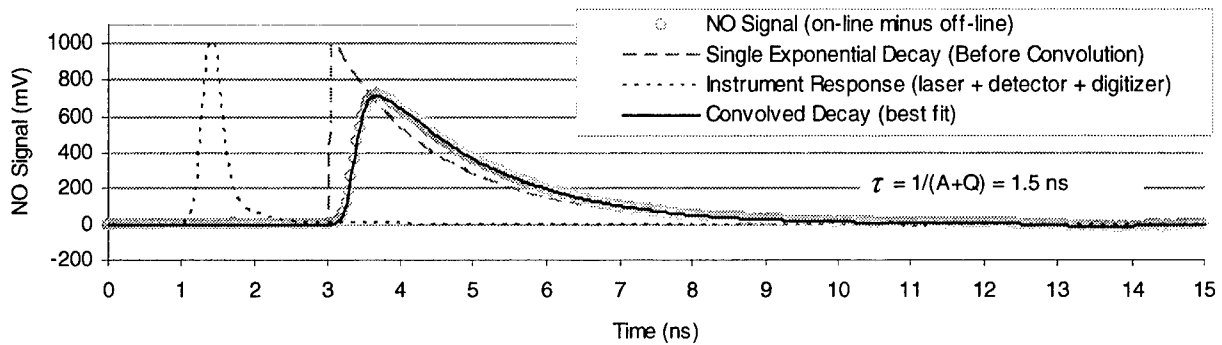

Fig. 2. Convolved step-exponential decay and fit to the measured data. The measured instrument used for convolution is shown offset in time for clarity.
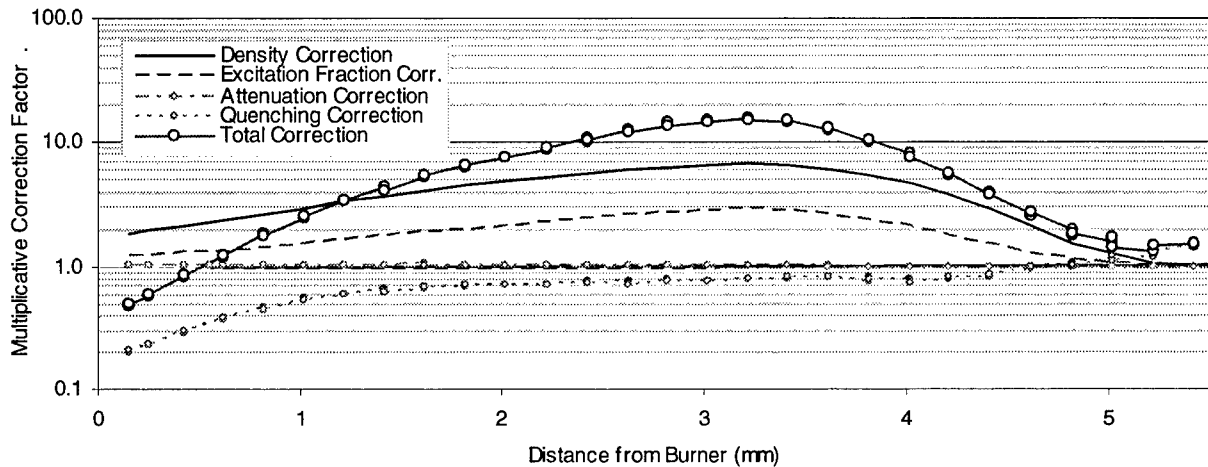

Fig. 3. Correction factors as a function of distance from burner. The fuel side corresponds to 0mm, with pure air at 6mm.

Optimization of the mode matching
in pulsed cavity ringdown spectroscopy

Dong-Hoon Lee, Youngjee Yoon, and Bongsoo Kim

Center for Electro-Optics and Department of Chemistry, Korea Advanced Institute of Science and Technology, Daejeon 305-701, Korea

Jae Yong Lee, Yong Shim Yoo, and Jae Won Hahn

Laser Metrology Group, Korea Research Institute of Standards and Science, P.O. Box 102, Yuseong, Daejeon 305-600, Korea
Tel: +82-42-868-5221, Fax: +82-42-868-5188, E-mail: jwhahn@kriss.re.kr

Abstract: A simple and reliable method is presented for optimizing the mode matching of pulsed cavity-ringdown spectroscopy (CRDS). The method is based on monitoring the non-degenerate transversal mode beating induced by beam clipping and slight cavity misalignment.
©2002 Optical Society of America
OCIS codes: (300.6360) Laser spectroscopy; (120.6200) Spectrometers and spectroscopic instrumentation

1. Motivation

Cavity ringdown spectroscopy (CRDS) is a powerful tool allowing highly sensitive absolute absorption measurements of weak transitions or rarefied species in various environments and configurations [1]. With a tunable pulsed laser source such as a dye laser or an optical parametric oscillator (OPO), CRDS is performed in the wide spectral range with a simple experimental setup. In practice, however, the sensitivity of most pulsed CRDS experiments is limited dominantly by a poor mode matching of the pulsed laser beam into the fundamental transversal (TEM_{00}) cavity mode, i.e., by the excitation of unwanted multiple transversal cavity modes [2-5]. Several methods for optimizing the mode matching have been reported, e.g. by using a charge-coupled device (CCD) camera to monitor the spatial mode pattern or by using a fast detector to monitor the transversal mode beating [5]. These methods require the availability of a high-resolution CCD camera or high-bandwidth detector, which is particularly limited in the mid-infrared range. Another simpler method for optimizing the mode matching is to monitor the deviation of the ringdown decay signal from a single-exponential decay function. But this method is not reliable as we found out experimentally that the excitation of multiple transversal modes by a slight cavity misalignment can also lead to a seemingly smooth exponential decay, but with a change in the ringdown time.

Here, we present a simple and reliable method for optimizing the mode matching of pulsed CRDS. The method is based on the minimization of the coupling of the higher-order transversal cavity modes by suppressing the non-degenerate transversal mode beating which can be observed as a slow modulation of the ringdown decay signal. No additional instrument is required but only a simple pinhole aperture to induce the beating, and the effectiveness of the method is verified experimentally by measuring the ringdown signal as a function of cavity misalignment angle, and by recording the high-sensitive spectrum easily and reproducibly.

2. Non-degenerate transversal mode beating

The electromagnetic field in a stable optical cavity as used in CRDS can be described as a superposition of the Gauss-Hermite eigenmodes, which are denoted for each longitudinal mode by TEM_{mn} with the indices (m,n) representing the node number of the transversal mode [5,6]. Each eigenmode is excited depending on the spectral and spatial overlap between the incident field and the cavity eigenmodes frequency and structure, i.e., on the mode matching. The frequency spacing between two adjacent longitudinal modes with identical set of transversal mode indices are separated by the cavity free spectral range (FSR), while the transversal mode spacing is determined by the relative values of the radius of curvature and the separation of the cavity mirrors. If more than two longitudinal cavity modes are excited by a pulsed laser, as in the standard pulsed CRDS setup, the longitudinal mode beating can be observed as a fast modulation on the ringdown signal with a frequency of the cavity FRS, e.g., 150 MHz for an 1-m long cavity. Note however that this modulation provides no useful information for the mode matching. In addition, the transversal mode beating can be observed as a modulation with the frequencies equal to the multiples of the transversal mode spacing, when the orthogonality between the transversal modes is broken, e.g. by partially blocking off the cavity transmission light incident to the detector. The value of such a transversal mode beating lies in the range of 10 MHz to 100 MHz for typical CRDS setups, and indicates whether the higher-order transversal modes are excited. To observe this beat signal, a fast detector with a bandwidth up to several tens of MHz required,

although for the detection of the ringdown signal only a detector with a bandwidth below 10 MHz is sufficient in most cases with a ringdown time of above 1 μs.

In addition to these fast beat signals, a slow modulation with a frequency of several hundreds of kHz can be observed on the ringdown signal, which originates from the non-degenerated transversal mode beating. Ideally, the frequencies of the (m+n)-order transversal eigenmodes are (m+n+1)-fold degenerate; for example, TEM_{01} and TEM_{10} modes have the same frequency. This fact relies on the symmetry of the cavity, i.e. the parameters determining the eigenmodes frequency such as beam path and mirror curvature are the same in the both Cartesian coordinate axes. If any irregularity is introduced in the cavity either by an inhomogeneity on the mirror surface or by a slight misalignment of the cavity in any particular direction, the degeneracy breaks and the transversal modes with the same index sum (m+n) will undergo splitting in frequency [7]. Since this non-degeneracy is induced by a "perturbation" that breaks the cavity symmetry, the non-degenerate transversal mode beating shows some special features. Most of all, the beat frequency depends on the degree of the perturbation, i.e. increases with the misalignment tilt angle of a cavity mirror and vanishes for the perfect alignment of the cavity. This property can be used not only to check the cavity mode matching but also to *in-situ* optimize it by monitoring the change of the beat frequency in a convenient low frequency regime below 1 MHz.
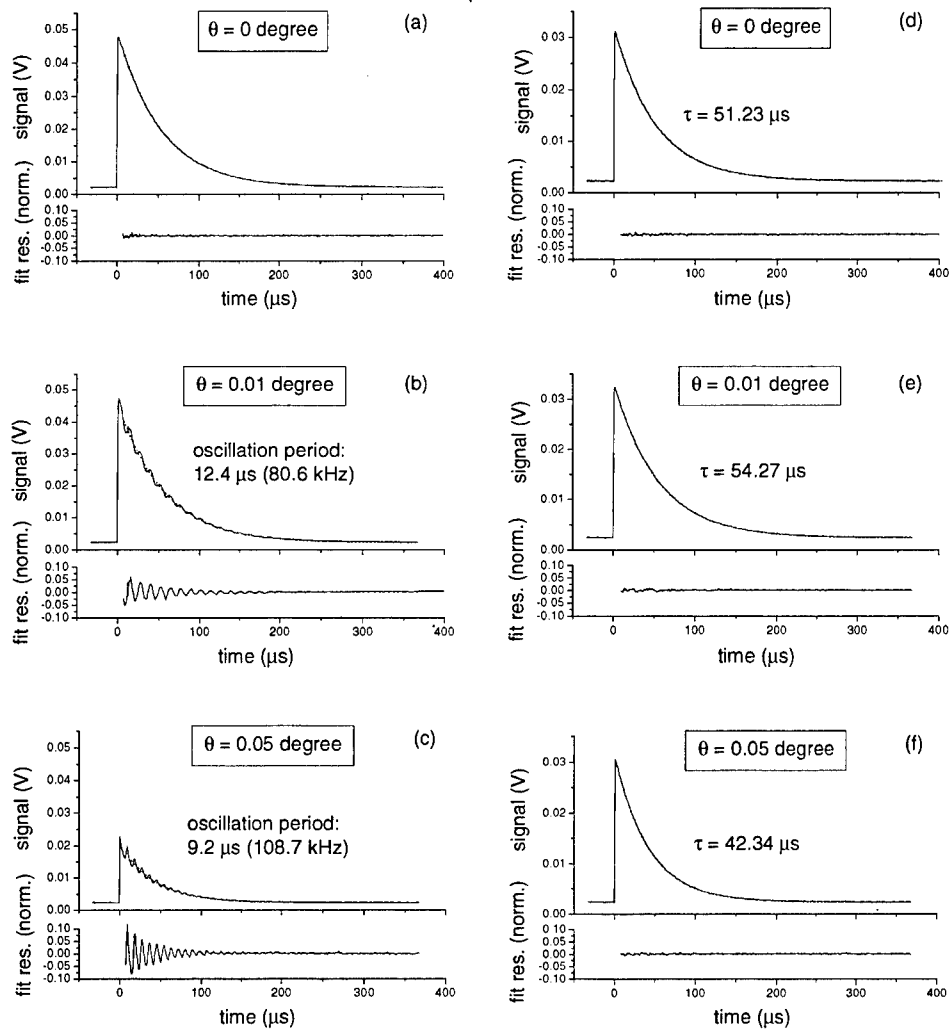
Fig. 1. The ringdown signal with different misalignment angle θ of the cavity output mirror, (a,b,c) through a pinhole aperture, (c,d,e) without a pinhole, for the θ values of 0, 0.01, and 0.05 degree, respectively. The lower insets are the normalized fit residuals from the fitted single-exponential functions (dotted lines). For θ = 0 in (a) and (d), i.e., for the good aligned cavity, the signals with and without the aperture show no difference, but the signals in (b,c) show the oscillating modulation due to the non-degenerating mode beating with a frequency depending on the misalignment

angle. In contrast, the signals in (e,f) do not reveal any systematic change with respect to the cavity misalignment though the ringdown time τ varies significantly.

3. Experimental results

To demonstrate the mode-matching optimization, we used an experimental setup of CRDS with a Nd:YAG pumped tunable OPO which provides 5-ns long pulses in 10-Hz repetition rate. The OPO output is tuned to around 570 nm and coupled after spatially filtering the beam to form a Gaussian beam into the CRDS cell with a convex lens. The cell consists of two high-reflectivity mirrors (R > 99.99 %) with 4-m radius of curvature and approximately 1-m separation and is evacuated to a pressure of approximately 2.7 kPa. The transmitted light through the cavity is detected with a photomultiplier tube and the output signal is recorded with a digital oscilloscope. The ringdown time is determined by fitting the measured ringdown signal to a single-exponential decay function.

To observe the transversal mode beating, a pinhole aperture of approximately 0.5-mm diameter is inserted on the beam axis of the transmission behind the exiting mirror. If the cavity alignment is not perfect, the non-degenerate transversal mode beating is observed as a slow modulation on the decay signal. Figures 1(a-c) show the measured ringdown signals with the mode beating for different values of the cavity misalignment angle θ. The dotted curves are the exponential fit function and the lower insets the normalized fit residual. The frequency of the oscillating modulation decreases with the decreasing misalignment angle and the modulation vanishes for the good alignment of the cavity (θ = 0), which verifies that the modulation indeed originates from the non-degenerate transversal mode beating. The beat modulation for the non-zero value of θ thus indicates the excitation of the higher-order transversal modes due to the imperfect mode matching. This demonstrates that we can optimize the mode matching by minimizing the modulation amplitude if we induce intentionally a slight misalignment of the cavity to monitor the non-degenerate mode beating. For comparison, Fig. 1(d-f) show the cavity ringdown signals measured without the pinhole aperture, i.e. without inducing the mode beating, concerning the change of the fit residuals and the ringdown time τ for the same values of θ as in Fig. 1(a-c). The ringdown signals and the fit residuals show no remarkable change with respect to the misalignment angle whereas the cavity ringdown time varies by up to 20 %. This is the clear evidence that a single smooth ringdown signal does not always mean a single-mode excitation, and that the excitation of the multiple higher-order transversal modes decreases the accuracy for the determination of τ and thus the sensitivity of the CRDS.

To demonstrate the presented method of the mode-matching optimization, we measured the ro-vibrational absorption spectrum of acetylene (C_2H_2) gas near the wavelength of 571 nm, and obtained a minimum detectable absorption coefficient of approximately 5×10^{-9} cm^{-1} by averaging 16 pulse shots. It should be emphasized that the sensitivity of this level could be achieved systematically and reproducibly with the presented optimization method by monitoring the non-degenerate transversal mode beating. We also expect that this method is of practical importance for pulsed CRDS especially in the mid-infrared range where the fast detector or high-resolution CCD camera is not easily available.

4. Summary

In summary, a simple and reliable method to optimize the mode matching of the laser pulses to the high-finesse cavity of CRDS is presented which is based on monitoring the non-degenerate transversal mode beating. The non-degeneracy of the transversal modes is brought about by splitting the eigenmodes frequencies from the induced asymmetry of the cavity through a slight misalignment. It is experimentally demonstrated that the observed beat signal can be effectively and reliably used to optimize the mode matching without an additional instrumental requirement. Also it is verified that the optimization of the mode matching is essential for achieving the ultimate sensitivity of pulsed CRDS since the procedure decreases the uncertainty of the ringdown time determination. With the present method, the pulsed CRDS absorption spectra with the sensitivity level of 10^{-9} cm^{-1} are achieved systematically and reproducibly.

References:
[1] K. W. Busch and M. A. Busch (Eds.), *Cavity-ringdown spectroscopy: an ultratrace-absorption measurement technique* (American Chemical Society, Washington DC, 1999).
[2] R. D. van Zee, J. T. Hodges, and J. P. Looney, "Pulsed, single-mode cavity ringdown spectroscopy," App. Opt. **38**, 3951-3960 (1999).
[3] P. Zalicki and R. Z. Zare, "Cavity ring-down spectroscopy for quantitative absorption measurements," J. Chem. Phys. **102**, 2708-2717 (1995).
[4] K. K. Lehmann and D. Romanini, "The superposition principle and cavity ring-down spectroscopy," J. Chem. Phys. **105**, 10263-10277 (1996).
[5] J. T. Hodges, J. P. Looney, and R. D. van Zee, "Response of a ring-down cavity to an arbitrary excitation," J. Chem. Phys. **105**, 10278-10288 (1996).
[6] A. E. Siegman, *Lasers* (University Science Books, Mills Valley, CA, 1986), chapter 19.
[7] J. P. Goldsborough, "Beat frequencies between modes of a concave-mirror optical resonator," Appl. Opt. **3**, 267-275 (1964).

Spatial-domain cavity ringdown: a potential toward broadband cavity ringdown spectroscopy

Jae Yong Lee, Yong Shim Yoo, and Jae Won Hahn

Laser Metrology Group, Korea Research Institute of Standards and Science,
P.O. Box 102, Yusong, Taejon 305-600, Korea
Phone: +82-42-868-5221, Fax: +82-42-868-5188. E-mail: jwhahn@kriss.re.kr

Abstract: We propose and demonstrate the idea of spatial-domain cavity ringdown (CRD) technique. The feasibility of the new concept toward broadband CRD implementation is supported by a firm theoretical background and a preliminary experiment.
© 2001 Optical Society of America
OCIS codes: (120.6200) Spectrometers and spectroscopic instrumentation; (999.9999) Cavity ringdown

Among the diverse spectroscopic methods capable of ultra-sensitive detection, cavity ringdown (CRD) technique [1] has become popular nowadays for the absolute absorption measurement, taking advantage of its high sensitivity and technical simplicity. The key to the success of CRD technique is the unique detection scheme on which it is based to quantify the amount of absorption; exponential decay of a transmitted probe light observable at the exit of a sample-contained cavity is recorded to yield a corresponding decay constant. The time rate of a decay, being proportional to the total cavity loss, permits a sensitive measure for the additional absorption loss introduced by a sample inside the cavity.

What we present here are a proposal to realize the CRD technique in the spatial domain, a firm theoretical underpinning, and a proof-of-principle experimental test [2]. In contrast to the conventional CRD technique associated with *temporal* CRD signals, an alternative optical arrangement using a plane-mirror Fabry-Perot (PFP) etalon will produce CRD signals in the *spatial* domain along the lateral axis at a PFP etalon exit.
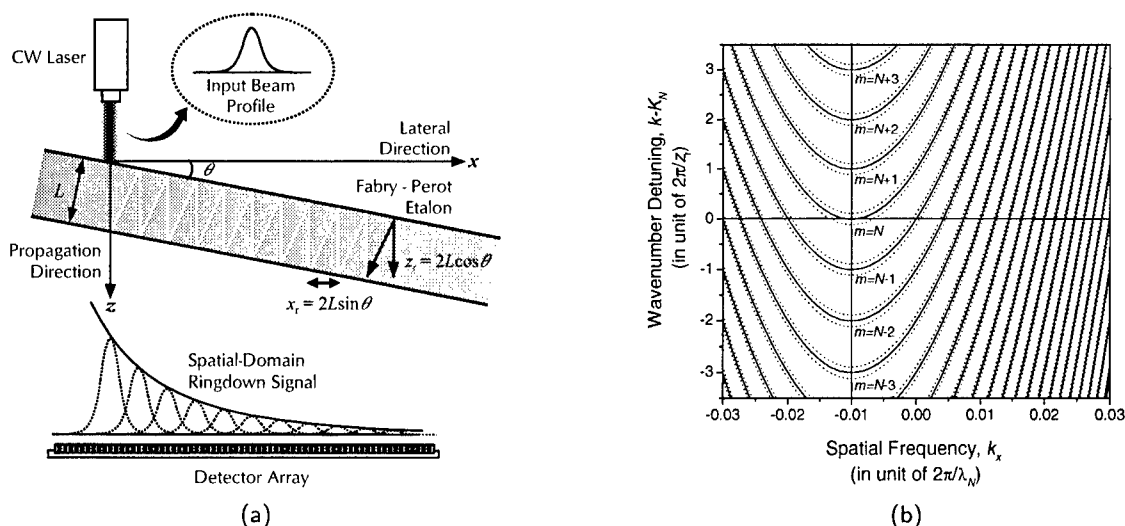
Fig. 1. Principle of spatial-domain cavity ringdown (SCRD). (a) A tilted PFP etalon in the SCRD arrangement can be treated by (b) the spatiospectral PFP transfer function, where spectral and spatial transmission resonance windows with resonance order m's around $N = 20000$ are shown for the cavity tilt angle of $\theta = 10$ mrad. Exact resonance contours are represented in solid lines along with adjacent contours of finite detunings($\Delta m = \pm 0.1$) in dotted lines.

As illustrated in Fig. 1(a), a PFP etalon with a collimated cw laser beam in oblique incidence acts in effect to produce the lateral displacement of x_r and the intensity drop by R^2 between consecutively outgoing multiple beams. This is the heart of *spatial-domain cavity ringdown* (SCRD) signal generation in a crude sense. However, more rigorous and detailed account on this SCRD signal generation is only possible in terms of a transfer function for a tilted PFP cavity given in Fig. 1(b).

It is remarkable on the spectroscopic standpoint that the SCRD implies a potential for a new principle of detecting absorption with inherited advantages from the CRD technique and several features unique to SCRD: (i) the SCRD technique can incorporate cw lasers without the need for a delicate cavity control mechanism as is the case for existing cw CRD techniques [3-5] (ii) SCRD signal persistent in time allows technical merits based on the time-averaged cw data acquisition, eliminating the limit of data repetition rate and extending the wavelength coverage over which high-speed detection is hardly available. (iii) A broadband implementation is readily compatible for many practical applications, by using a dispersive element and a two-dimensional (2-D) array detector in combination. A similar idea has been attempted previously by Scherer [6], using 2-D streak-record CRD photography. The spatial decay feature obtainable by streak recording, however, is actually the consequence of post-cavity signal transformation that cannot avoid the transient and repetitive aspects of CRD.

A rough theoretical prediction for the ringdown distance s_d can be made on the basis of geometrical optics involved; For fundamental system parameters such as the thickness of an etalon L, the mirror reflectivity R, the incidence angle of an input beam θ, and the angular frequency of incident light $\omega = ck$, the intensity I of an outgoing beam component undergone n round trips will attenuate that $I \propto I_o R^{2n} \approx I_o \exp[-2n(1-R)]$, exhibiting the spatial dependence given by $\exp[-2(1-R)x/x_r]$ for the lateral beam shift occurs by $x = nx_r$. Thus the SCRD decay constant is found to be $s_d = x_r/2(1-R) = (L\sin\theta)/(1-R)$. The primary aspect of exponential decay in the spatial domain can be offered by this crude argument.

A complete and rigorous description of SCRD, however, will need a pertinent physical treatment in the context of wave propagation theory combined with ray optics, taking into account the beam propagation and interference of multiple beams. Theoretical formulation is made for a simplified situation that a one-dimensional (1-D) input beam with its transverse profile depending on the x-coordinate propagates in the $+z$ direction toward a tilted PFP etalon. For a PFP etalon comprising two identical mirrors having reflectivity $R = |\mathcal{R}|^2$ and transmittivity $T = |\mathcal{T}|^2$, the resultant optical field at the exit mirror E_{FP} is expressible as the sum of all spatially overlapped field components:

$$E_{\text{FP}}(x;z) = \sum_{n=0}^{\infty} \mathcal{T}^2 \mathcal{R}^{2n} E(x - nx_r; z + nz_r) , \qquad (1)$$

where $x_r = 2L\sin\theta$ is the lateral beam walk-off occurring at each round trip, $z_r = 2L\cos\theta$, the path-length difference between the consecutive beams, n, the number of round trips experienced by the transmitted field, and $E(x;z)$, the incident laser field that undergoes a beam diffraction resulting in the distortion of amplitude and phase profiles. With help of angular spectrum propagation method derived from the first Rayleigh-Sommerfeld diffraction formula [7], the optical field $E(x;z)$ can be explicitly determined from the beam propagation equation in the form of $\tilde{E}(k_x;z) = \tilde{H}(k_x; z - z_0)|_k \tilde{E}(k_x;z_0)$ that is defined in the spatial frequency (k_x) domain, using the free-space transfer function $\tilde{H}(k_x;z)|_k = \exp[iz\sqrt{k^2 - k_x^2}\,]$ for a monochromatic light beam of the wavenumber $k = \omega/c = 2\pi/\lambda$. Here the Fourier transform relation, $E(x;z) = \frac{1}{2\pi}\int dk_x \tilde{E}(k_x;z)\exp[ik_x x]$, is used to directly associate the spatial field distribution $E(x;z)$ with the spatial frequency spectrum $\tilde{E}(k_x;z)$. By Fourier transforming the PFP etalon response expressed in Eq. (1), one can obtain an alternative formulation in the spatial frequency domain that relates the input and the output fields via the PFP transfer equation $\tilde{E}_{\text{FP}}(k_x;z) = \tilde{H}_{\text{FP}}(k_x; z - z_0)|_k \tilde{E}(k_x;z_0)$, where $\tilde{H}_{\text{FP}}(k_x;z)|_k$ is derived in the analytic form given by

$$\tilde{H}_{\text{FP}}(k_x;z)|_k = \frac{\mathcal{T}^2 \exp\left[iz\sqrt{k^2 - k_x^2}\right]}{1 - \mathcal{R}^2 \exp\left[i\left(z_r\sqrt{k^2 - k_x^2} - x_r k_x\right)\right]} , \qquad (2)$$

where $\mathcal{T} = \sqrt{T}\exp[i\varphi_T]$ and $\mathcal{R} = \sqrt{R}\exp[i\varphi_R]$. The PFP transfer function acts for beam filtration on both the wavenumber k and the spatial frequency k_x, as illustrated in Fig. 1(b). For a high-finesse etalon aligned in a certain tilt angle θ and above, such a filtration effect leads to a sharp Lorentzian transmission peak in the form of $|\tilde{H}_{\text{FP}}(k_x;L)|^2 \approx (T/x_r)^2/\left[\frac{1}{4}\{2(1-R)/x_r\}^2 + k_x^2\right]$, which implies a exponentially decaying transmission profile in the spatial coordinate x, by Fourier transform relation. This is what we call SCRD that is characterized with a decay constant $s_d = x_r/2(1-R)$, equal to the inverse of the FWHM linewidth $\gamma_{\text{(trm)}} = 2(1-R)/x_r$ of the Lorentzian transmission peak.

The validity of SCRD concept was confirmed also through numerical simulations based on the proposed theoretical model. Typical SCRD signal profiles are in Fig. 2(a-c). When an incident laser beam is on cavity resonance, it has been verified by the numerical fit that the SCRD signal exhibits a single exponential decay. As the input beam frequency detunes, the transient peak at the forefront of the signal develops while the signal level of an exponential decay is reduced. For the detuning beyond a certain threshold of anti-resonance, the transmitted signal contains only the transient peak without the decaying part.

Results of a proof-of-principle experiment are in an excellent accordance with the theoretical predictions, as can be seen from Fig. 2(a'-c'). The experiments also confirmed the linear dependence of the ringdown distance s_d on the incidence angle θ. In regard to the uncertainty δs_d of measuring the ringdown distance, our preliminary experiment attained the uncertainty of $\delta s_d/s_d = 0.028$, limiting the minimum detectable sample loss $\mathcal{L}_{\min} = (1 - R)\delta s_d/s_d$ at the level of 3.8×10^{-4}/pass.
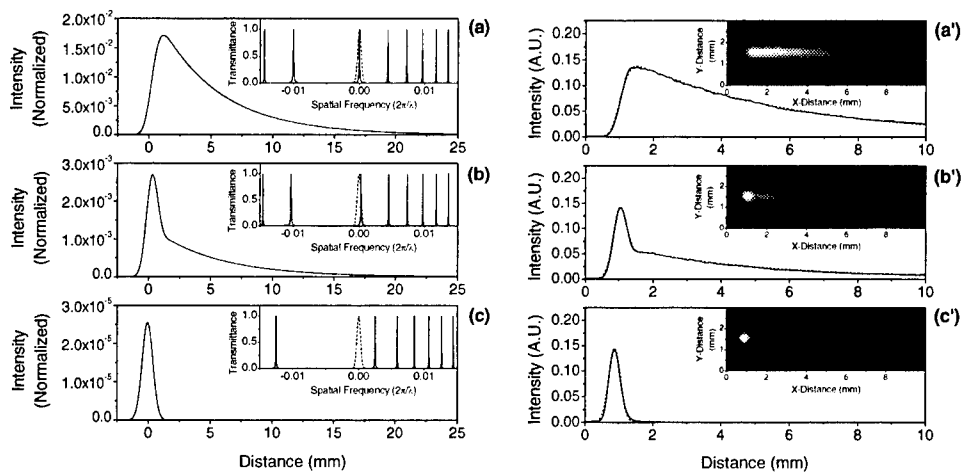
Fig. 2. SCRD signals generated by a tilted PFP etalon with Gaussian beam incidence. Numerical simulation shows the SCRD signal profiles for frequency-detuned inputs of (a) $\Omega = 0$, (b) $\Omega = 0.05$ FSR, and (c) $\Omega = 0.5$ FSR, where FSR $= 2\pi c/z_r$. Depicted in each inset are the PFP etalon transmission curve (solid) and the spatial frequency profile of an input beam (dotted). The results are for a 10-mm-long PFP etalon comprising mirrors of $R = 0.99$ with the tilt angle of $\theta = 5$ mrad which is illuminated by a Gaussian beam having the FWHM width of $D = 1.0$ mm at $\lambda = 632.8$ nm. For similar parameters, experimentally measured SCRD signals (solid) are given for the input beam detunings: (a') $\Omega = 0$, (b') $\Omega = 0.12$ FSR, and (c') $\Omega = 0.20$ FSR. The SCRD profiles (solid) extracted from the 2-D image shots are fitted to theoretical curves (dotted).

To conclude, we have proposed and demonstrated SCRD in a PFP etalon, the spatial analog of the conventional time-based CRD technique. The concept of SCRD has been supported by a firm theoretical background and tested by both numerical simulation and experiment. Further investigation has implied a potential of SCRD; the SCRD distance can be used as a measure detecting the additional loss $\mathcal{L}_{\text{sample}} = \alpha L$ of a sample filled in a PFP etalon as the decay constant would become $s_d = L\sin\theta/[(1 - R) + \alpha L]$. In addition, the feasibility of broadband implementation with SCRD would be promising for various areas of spectroscopic applications.

References

1. A. O'Keefe, and D. A. G. Deacon, "Cavity ring-down optical spectrometer for absorption measurements using pulsed laser sources," Rev. Sci. Instrum. **59**, 2544 - 2551 (1988).
2. J. Y. Lee, H.-W. Lee, and J. W. Hahn, "Spatial domain realization of the cavity ring-down technique in a plane Fabry-Perot cavity," Appl. Phys. Lett. **78**, 1481 - 1483 (2001).
3. D. Romanini, A. A. Kachanov, N. Sadeghi, and F. Stoeckel, "CW cavity ring down spectroscopy," Chem. Phys. Lett. **264**, 316 - 322 (1997).
4. B. A. Paldus, C. C. Harb, T. G. Spence. B. Wilke, J. Xie, J. S. Harris. and R. N. Zare, "Cavity-locked ring-down spectroscopy," J. Appl. Phys. **83**, 3991 - 3997 (1998).
5. J. W. Hahn, Y. S. Yoo, J. Y. Lee, J. W. Kim, and H.-W. Lee, "Cavity ring-down spectroscopy with a continuous wave laser: calculation of coupling efficiency and a new spectrometer design," Appl. Opt. **38**, 1859 - 1866 (1999).
6. J. J. Scherer, "Ringdown spectral photography," Chem. Phys. Lett. **292**, 143 - 153 (1998).
7. J. W. Goodman, *Introduction to Fourier Optics*, 2nd ed. (McGraw-Hill, New York. 1996), pp. 46-61.

Real-time ground level atmospheric nitric oxide measured by calibrated TDLAS system

Adam Mock

Department of Electrical Engineering, Columbia University, 1312 S.W. Mudd, 500 W 120th Street, New York, NY, 10027
apm30@columbia.edu

Chad Roller, Jim Jeffers, Khosrow Namjou

Ekips Technologies, Inc., 710 Asp Ave.,Suite 308, Norman, OK 73069
lasers@ekipstech.com

Patrick J. McCann, Joe Grego

Department of Electrical and Computer Engineering, University of Oklahoma, 202 W. Boyd, Norman, Oklahoma 73109
pmccann@ou.edu

Abstract: A calibrated TDLAS system was used to measure real-time ground level atmospheric NO levels near a busy suburban street. A sample atmospheric NO concentration trend diagram from midday is presented.
©2001 Optical Society of America
OCIS codes: (010.1120) Atmospheric and Ocean Optics, Air Pollution Monitoring; (300.6260) Spectroscopy, Diode Lasers

1. Introduction

The importance of atmospheric measurements of nitric oxide (NO) has been increasing as trace gas detection technology and sensitivities improve. Recent literature suggests that 68% of global atmospheric NO originates from natural sources including the burning of biomass, lightning, soils, mineral fertilizer, oxidation of NH_3, oceans and from the stratosphere [1]. The remaining NO originates primarily from the burning of fossil fuels. At ground level in populated areas, anthropogenic sources can contribute to as much as 91% of the atmospheric NO with 43% originating in passenger and commercial vehicles [1]. NO concentrations up to 485 ppb have been measured using FTIR spectroscopy in Los Angeles, CA during the summer. Results observed suggested that atmospheric NO was almost entirely consumed during the day. It was also noted that the rapid decrease of NO in the morning is typical 'smog chamber' behavior [2]. *Tobachow et. al.* report that, "NO is an important precursor to ozone (O_3) formation in the lower troposphere that can lead to undesirable air quality and detrimental effects on human health" [3]. The EPA reports that NO concentrations of 60-150 ppm cause immediate irritation of the nose and throat 6-24 hours after exposure and unconsciousness may result [4].

FTIR is a common instrument for NO atmospheric measurements; however, sensitivities and integration times are limited and lengthy. Chemiluminescence detection has also been a widely used technology for NO gas quantification, but dependence on temperature stability and water vapor interference limits its use in a variety of environments and seasons. Tunable diode laser absorption spectroscopy (TDLAS) has been described as having attributes suitable for rapid, continuous and sensitive (sub-ppb) measurements of NO, capable of assessing emissions from a moving vehicle or groups of vehicles.

This report illustrates the application of a custom fabricated TDLAS system equipped with a IV-VI semiconductor mid-IR laser for measuring NO concentrations near a roadway during various times of the day. Mean NO concentrations during late afternoon rush hour traffic were higher than mean NO concentrations in the morning and at night.

2. Experimental Apparatus and Procedure

A schematic of the TDLAS system is shown in Fig. 1 (a). A double heterostructure IV-VI tunable diode laser was mounted on a temperature controlled copper stage located inside a sealed cryostat. The operating temperature of the copper stage was chilled to cryogenic temperatures using a closed cycle refrigerator. The operating temperature was maintained at 102 K using a temperature controller and integrated heater. Injection currents between 810 mA and 850 mA were supplied using a laser diode current controller. The mid-IR beam emitted from the laser exited a ZnSe window where an OAPM directed the beam onto field mirrors, which then directed the beam into a 107-meter optical path length White Cell (16 Liters). Upon exiting the White cell, the beam was directed through a ZnSe focusing lens and window before striking a photo detector also located on the copper stage inside the cryostat.

Two function generators tuned and modulated the laser using a technique known as sweep integration coupled with frequency modulation. A saw tooth ramp (40Hz, 0.11VPP) tuned across NO and H_2O absorption features near 5.2 μm. A triangle waveform (22kHz, 0.01VPP) was superimposed onto the saw tooth waveform to tune repetitively across individual absorption features. A commercial lock-in amplifier sampled the pre-amplified photo detector output at twice the modulation frequency ($2f$). A personal computer with an analog-to-digital (A/D) converter card collected 500 data points per scan and performed a running co-average of 75 consecutive scans.
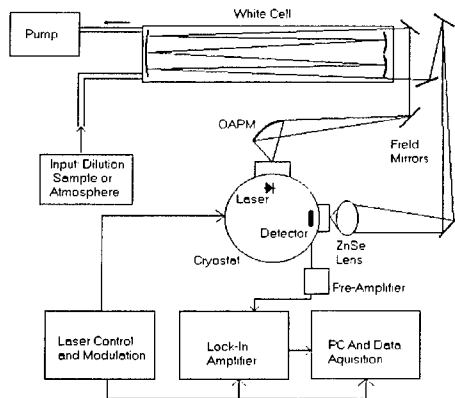
Fig. 1 (a). TDLAS system diagram.	Fig. 1 (b). NO calibration experimental design.
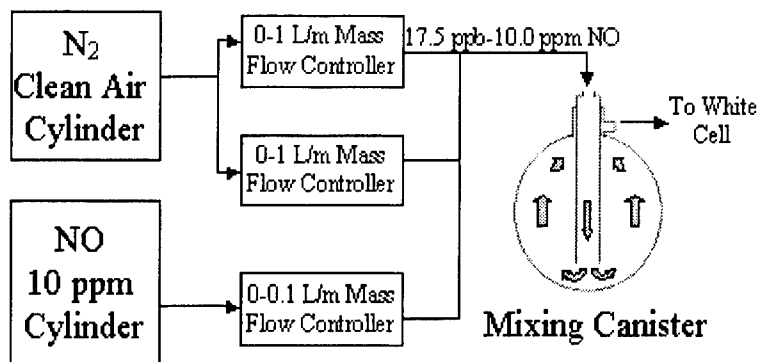
A roughing pump was used to induce flow and maintain the pressure within the White cell at 20 Torr. A schematic for the calibration apparatus with mass flow controller is shown in Fig. 1 (b). A calibrated NO gas cylinder of 10 ppm was diluted using N_2 while always keeping total flow into the White cell equal to 2.0 slm. The two gases were mixed in a canister before entering the White cell to ensure homogeneity. The concentration of the calibrated NO sample was determined using a simple proportion of the 10 ppm NO gas flow with the N_2 gas flow. The calibration procedure consisted of varying the input NO flow rate resulting in input NO concentrations ranging from 20 ppb to 125 ppb, respectively. At each step an NO concentration trend was recorded for approximately five minutes and the mean and standard variation were then determined.
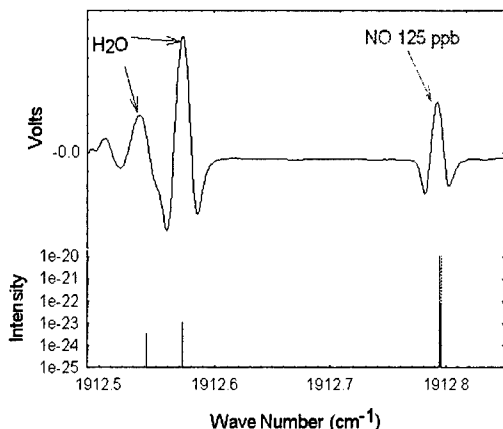
Fig. 2 (a). Absorption spectrum taken from calibrated input of 125 ppb NO with corresponding HITRAN '96 data.
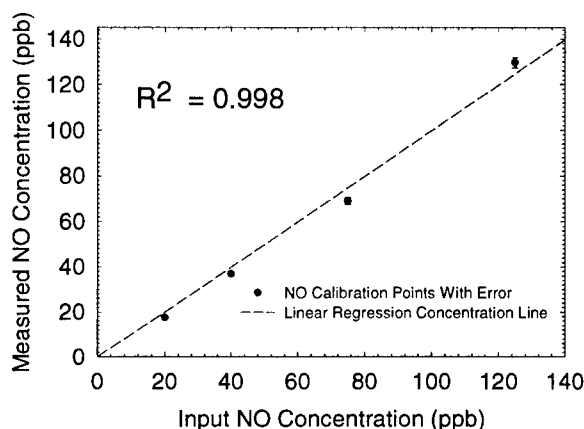
Fig. 2 (b). NO calibration curve with ranging from 20 ppb to 125 ppb

Concentration was determined by comparing a NO reference spectrum absorption feature at a known concentration to the same NO absorption feature in spectra of unknown concentrations using a linear-least squares fitting routine. During calibration, a NO absorption feature of 125 ppb at 1916.79 cm^{-1} was used to evaluate subsequent measurements of varying concentrations and is shown in Fig. 2(a) along with HITRAN 96 line intensities. A linear NO calibration curve from 20 ppb to 125 ppb is shown in Fig. 2(b). The unambiguous H_2O absorption feature at 1912.57 cm^{-1} was used as a spectral reference to align spectra before averaging, which eliminated the need for a separate reference cell and detector.

To measure atmospheric NO, 100 feet of ¼ inch tubing was attached to the input of the White cell and fed out the 4th floor laboratory window down to the sidewalk directly adjacent to a busy suburban street. The hose was secured by attaching it to a tree branch approximately 2 meters from the ground.

3. Results

Measurements of atmospheric NO near a busy street were taken continuously over extended periods of time. Measurements were performed on three separate days at varying times in the morning, afternoon, and evening. Fig. 3 shows the results of NO concentrations measured from 11:45 PM to 1:00 PM on July 26, 2001. The large NO concentrations are believed to be the results of lunch hour traffic between 12:25 PM and 12:40 PM. The plot consists of data points taken every second giving extremely detailed information on the duration of high NO concentrations.
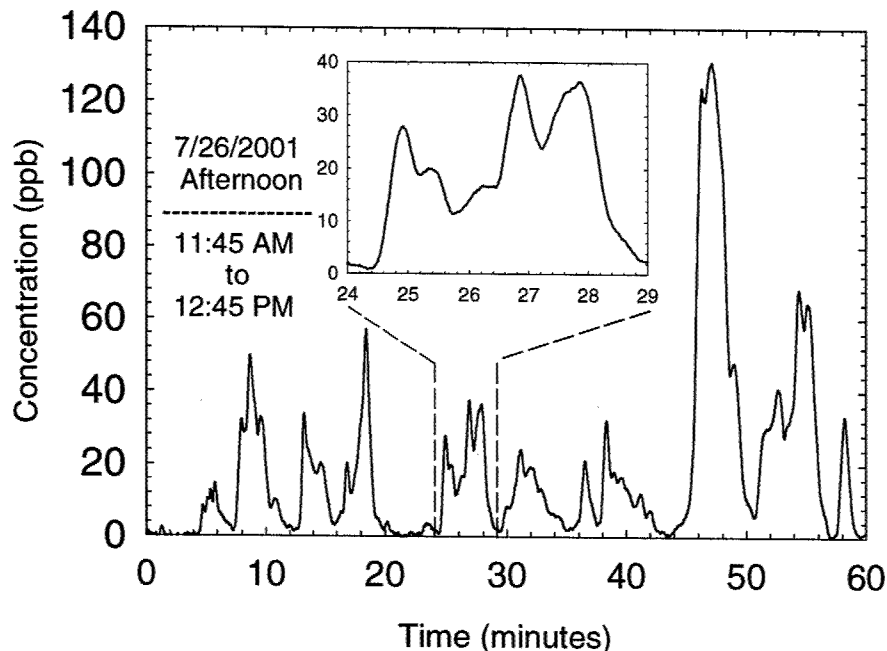
Fig. 3. Atmospheric ground level NO concentration trend on July 26, 2001.

Not surprisingly, NO concentrations exceeding concentrations of 70 ppb were most common during the late afternoon rush hour between 4:30 PM and 6:00 PM. High levels could be attributed to individual vehicles or sets of vehicles passing by. It is still unclear if the density of vehicles results in higher NO, or if one or several vehicles from a group contributed to most of the NO emissions.

4. Summary

The calibration procedure illustrates precise and accurate measurement of atmospheric NO. The possible correlation between increased traffic and high NO concentrations indicates the ability for fast, real-time measurements of NO from individual polluting vehicles. Further investigations are needed to determine the combustion reactions resulting in NO formation and its release into the atmosphere. TDLAS is well suited for such applications with the sensitivities and rapid response times required for monitoring traffic NO emissions.

5. References

[1] Horst Klingenberg, *Automobile Exhaust Emission Testing* (Springer, 1996).
[2] Philip L. Hanst, "A Long-Path Infra-Red Study Of Los Angeles Smog," Atmospheric Environment **16**, 969-981 (1982).
[3] Ross M. Tabachow, "Nitric Oxide Emissions From Fertilized And Biosolids-Amended Soil," Journal Of Environmental Engineering **127**, 517-523 (2001).
[4] Health Hazard Data, *EPA Chemical Profile*, (Environmental Protection Agency, 1987), http://www.epa.gov/swercepp/ehs/profile/10102439.txt.

Maximum-likelihood estimation of model parameters for experiments with pulsed lasers

Thomas Metz, Joachim Walewski

Division of Combustion Physics. Lund Institute of Technology. P.O. Box 118,
SE-221 00 Lund, Sweden
thomas.metz@forbrf.lth.se

Clemens F. Kaminski

Department of Chemical Engineering. University of Cambridge, Pembroke Street,
Cambridge CB2 3RA. UK

Abstract: A fitting method is presented for evaluation of non-linear spectroscopy experiments. Correct treatment of laser intensity fluctuations increases the accuracy and precision and avoids significantly wrong results. The method is compared to common fitting schemes.
© 2001 Optical Society of America
OCIS codes: 000.5490, 000.4430, 300.6360, 120.3940

1 Introduction

In many experiments unknown physical quantities (measurands) are to be estimated from experimental data. On the basis of the method of maximum likelihood (ML) [?, ?, ?] well-known fitting schemes have been derived such as different variants of least-squares (LSQ) fitting. However, the assumptions made in deriving those schemes are not generally valid. The consequence of using such schemes nevertheless, is a deterioration of the precision and the accuracy of the results. For instance, the very commonly applied simple LSQ fitting scheme assumes independence of the random variations of different observed quantities. However, this assumption is not fulfilled in many cases of laser spectroscopy, e.g. when a signal light beam is generated by interactions of matter with radiation from a pulsed laser. In many cases the observed laser and signal intensities are subject to variations, which origin from the same source, viz. laser intensity fluctuations, and are therefore correlated.
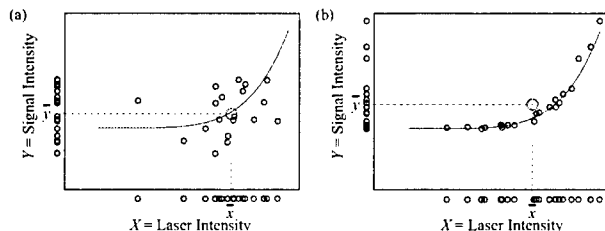
Fig. 1. (a) Without laser fluctuations, observed laser and signal intensities vary due to detector noise. A point $(\overline{x}, \overline{y})$ obtained from the mean intensities is expected to lie close to the curve. (b) Laser fluctuations contribute essentially to the variation. Although the laser intensities are distributed symmetrically, the signal intensities are not. The point $(\overline{x}, \overline{y})$ lies systematically beside (here: above) the curve, i.e. bias is introduced.

Furthermore, the source of the random variation is assumed to be related to the observed data in a linear way, e.g. a measurement error from additive detector noise. However, if the signal depends in a non-linear fashion on the laser intensity, the laser intensity fluctuations appear distorted on the signal intensities, see Figure 1. Common LSQ schemes do not account for the resulting skew distributions of the signal intensities and introduce bias into the evaluation. This problem has hardly found any attention in the physical community. Therefore, an approach is presented in this work providing estimates for unknown parameters with excellent accuracy and precision with regard to the information given by the experimental data.

2 Theory

In order to derive an appropriate fitting scheme, nothing more was done than the formulation of an adequate statistical model for the experiment and a consequent application of the method of ML with some natural

approximations such as the use of the central limit theorem or a Taylor expansion. The statistical model is illustrated in Figure 2. The output from a pulsed laser is measured on detector 1 before being passed into an interaction region. The signal generated there is registered by detector 2. The measurements are affected by additive noise, $E_{ij}^{(1)}$ and $E_{ij}^{(2)}$ for detector 1 and 2, respectively. Moreover, the laser intensity L_{ij} varies from pulse to pulse. During the experiment a number of n experimental settings are chosen. One example are power dependence measurements, where each setting corresponds to a mean intensity of the laser, changed for instance by setting filters into the laser beam.
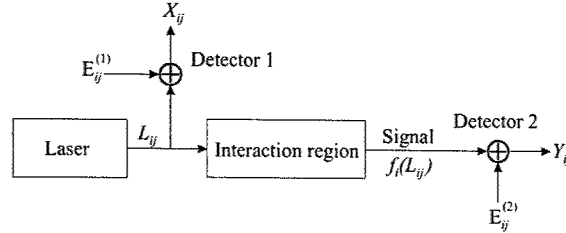
Fig. 2. Statistical model for a laser-spectroscopic experiment.

For each setting $i \in \{1, \ldots, n\}$ several measurements (replicates) are recorded resulting in clusters, each one containing m_i data points numbered by $j \in \{1, \ldots, m_i\}$. The detector noise and the laser fluctuations are assumed to be normally distributed with zero expectations for the noise and $\mathcal{E}(L_{ij}) = l_i$ for the laser intensities. The l_i are unknowns to be estimated together with the unknown parameters. The *observed* laser and signal intensities are given by $X_{ij} = L_{ij} + E_{ij}^{(1)}$ and $Y_{ij} = f_i(L_{ij}) + E_{ij}^{(2)}$. The function f_i contains known and unknown parameters, the latter of which are to be estimated. Its dependence on the setting index i does not only allow for changes in the experimental parameters, but also for totally different model functions for each setting.

The most important step of the method of ML is the formulation of the correct likelihood function $\mathcal{L}$. This function contains the unknowns as parameters, for which the method of ML chooses those values that maximize $\mathcal{L}$. Often it is instead easier minimis a function χ^2, closely related to $\mathcal{L}$. The likelihood function is basically the joint probability density function (PDF) of all observed quantities in the experimental data set. If the random variations of different data points are independent, $\mathcal{L}$ is simply the product of the PDFs of the data points. However, the coordinates X_{ij} and Y_{ij} of one point are not statistically independent and their PDF has to be described by the general, two-dimensional normal distribution including the covariance [?].

A problem in the formulation of $\mathcal{L}$ is that the distribution of the signal Y_{ij} is not normal because of the curvature of f_i, and cumbersome to describe exactly. Therefore we use the data points $(\overline{X}_i, \overline{Y}_i)$ obtained from averaging the observed intensities in each cluster. According to the central limit theorem of statistics, the means can approximately be described by a normal distribution, for which, however, the correct parameters must be used. Above all, the expectation $\mathcal{E}(\overline{Y}_i)$, is not simply $f_i[\mathcal{E}(\overline{X}_i)]$ since the data points from averaging lie systematically beside the real curve f_i (see Figure 1). An exact expression for $\mathcal{E}(\overline{Y}_i)$ is not easy to find, so we derive it from a second-order Taylor expansion of f_i. This reduces bias on the estimates of the unknowns very efficiently. In conclusion, the fitting consists of minimization of the following expression by variation of the unknown parameters and the mean laser intensities l_i:

$$\chi^2 = \sum_{i=1}^{n} \delta_i^{\mathrm{T}} \left(\frac{\hat{\mathbf{u}}_i}{m_i} \right)^{-1} \delta_i \quad \text{with} \quad \delta_i := \left(\begin{array}{c} \overline{x}_i - l_i \\ \overline{y}_i - \left[f_i(l_i) + \frac{1}{2}\mathcal{C}(X_i, Y_i) \times f_i''(l_i)/f_i'(l_i) \right] \end{array} \right) \qquad (1)$$

The empirical covariance matrix $\hat{\mathbf{u}}_i$ can be obtained from the observed clusters and the covariance $\mathcal{C}(X_i, Y_i)$ can be estimated from the corresponding element of $\hat{\mathbf{u}}_i$. The $\overline{x}_i$ and $\overline{y}_i$ are the averaged laser and signal intensities obtained from the experimental data. The additional term in the brackets is what we refer to as *bias correction* describing the approximate amount the $(\overline{x}_i, \overline{y}_i)$ are expected to lie beside the correct curve f_i (see Fig. 1). The fitting scheme presented here is referred to as *covariant WLSQ (weighted least-squares) with bias correction.*

3   Comparison of different fitting methods

In order to test the fitting scheme presented, it was compared to the following well-established ones: *Simple LSQ* where the sum of squares to be minimized contains only the residuals in the ordinate values from the curve whereas the other fitting schemes also include the residuals of the abscissa values. *Weighted least-squares (WLSQ)* weights the residuals with inverse standard deviations estimated from the clusters and *covariant WLSQ without bias correction (cov. WLSQ)* weights with the covariance matrices $\hat{u}_i$, but neglects the bias correction term in Equation 1.

Monte Carlo simulations were used to characterize the estimators provided by these fitting schemes. For this purpose, synthetic measurement sets for power dependence measurements in non-linear laser spectroscopy were generated from pre-defined parameter values chosen to mimic real measurement data in Walewski et al. [?]. The simulations were calculated thousand times and evaluated with all methods. From the large number of results obtained, the properties of the estimators could be characterized. Two model functions were tested, $f(l; a, b) = a \cdot l^b$ and $f(l; a, l_{\text{sat}}) = a \cdot l^3/(1 + l/l_{\text{sat}})^2$ (l: laser intensity), the latter of which describing polarization spectroscopy (PS) signals [?].
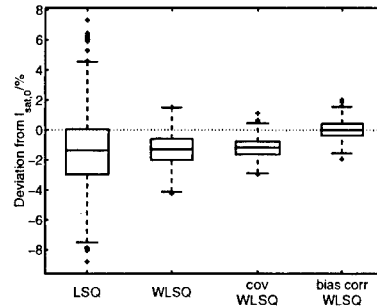
Fig. 3. Box-and-whiskers plot of estimates of the parameter l_{sat} for a rational function and the case of low detector noise. The results from different fitting schemes are shown as the relative deviation from the pre-defined model parameter $l_{\text{sat},0}$.

The results showed an increase of the precision up to three times going from simple LSQ, via WLSQ to the covariant WLSQ schemes, and bias on the parameters was observed for all methods but the one presented in this work. An example of such results is shown in Figure 3. Moreover, the variance of the estimators decreased with decreased detector noise or an increased number of replicates (points per cluster), whereas the bias was not affected. This is very important when reporting the results as *estimate ± standard deviation*, because such an interval would not cover the true value, if the standard deviation is less than the bias, leading to significantly wrong results. Finally, the bias depends on the type of model function. For instance, the exponent b in the power function showed less bias than the PS saturation intensity l_{sat} in the rational model function.

In conclusion, we showed that the method of ML is a versatile and efficient method for measurement evaluation if applied to a statistical model adequate for the considered experiment. The method can treat a variety of experiments in the fields of physics and other disciplines. For the calculations in this work MATLAB® routines were developed, freely available from the authors (http://www.forbrf.lth.se/WFIT/).

Detection of conformational changes in proteins with FRET

R. Plessow, K. Lotte and A. Brockhinke

Physikalische Chemie I, Universität Bielefeld, Universitätsstr. 25, D-33615 Bielefeld, Germany
Fax: +49-521-106-6027, e-mail: brockhinke@pc1.uni-bielefeld.de

Abstract: Förster resonance energy transfer (FRET) is detected using a combination of two techniques: picosecond time-resolved LIF and excitation-emission spectroscopy. This allows the quantitative determination of distances within and in between proteins.
©2001 Optical Society of America
OCIS codes: (300.6500) Spectroscopy, time-resolved, (170.6280); Spectroscopy, fluorescence and luminescence

1. Introduction

The study of proteins and their interaction with substrates requires a detailed knowledge of their conformation and of the distances from the active center. Förster resonance energy transfer (FRET) is a method that allows to quantitatively determine distances in proteins in the range between 10 and 100 Å under physiologic conditions [1]. The basic idea of this technique is to excite a donor fluorophor which then transfers part of its energy on an acceptor fluorophor located elsewhere in the system under investigation. The amount of energy transferred depends strongly on the distance between donor and acceptor and thus allows to determine the distance. Besides artificial dyes, intrinsic fluorophors such as the amino acids tryptophan or tyrosine can be used as donors, whereas heme are suitable acceptor molecules.

2. Experimental

Two 2D fluorescence techniques are combined in order to quantify the FRET signals: Simultaneous time- and wavelength-resolved fluorescence spectra are measured using a 80 ps laser source in conjunction with streak detection in the exit plane of an astigmatism-corrected spectrometer. This approach allows to identify different photophysical processes by their associated lifetime and spectral intensity distribution; errors due to the more common integration over a wider spectral range are avoided. Time-resolved spectra are sensitive to changes in the collisional environment (dynamic quenching) and can thus be used to monitor local conformation changes close to the respective fluorophors. A sample spectrum is reproduced in Fig. 1.

Excitation-emission spectra are two-dimensional fluorescence images with one axis corresponding to the excitation and the other to the emission wavelength. Thus, they contain all conventional excitation and fluorescence spectra of a given substance. The 2D structure facilitates the interpretation of these spectra and allows the direct identification of resonance effects, scattering and the isolation of the contribution of different fluorophors to the complete spectrum as can be seen in Fig. 3. Details of the respective experimental setups are described elsewhere [2, 3].

3. Study of FRET in neuropeptide Y

In this part of our investigation, we studied the neuropeptide Y (NPY), a molecule responsible for several regulation mechanisms in the nerve system as well as a controlling agent for blood pressure and hormones such as noradrenalin [4, 5]. NPY consists of 36 amino acids, among them five tyrosine molecules. Besides the wild type we used three different derivatives: labeled with deazaflavin in position 2 ([dFl2]NPY), flavin [6, 7] in position 34 ([Fl34]NPY) and the double labeled variant [dFl2, Fl34]NPY.

Figure 1 shows a time- and wavelength-resolved fluorescence spectrum of [dFl2, Fl34]NPY at the excitation wavelength $\lambda_{ex} = 400$ nm. Contributions of the two different fluorescence labels can be easily discerned: fluorescence from the donor deazaflavin is visible around 450 nm, whereas the acceptor molecule flavin radiates around 515 nm.

Vertical cuts through Fig. 1 yield conventional time-resolved fluorescence spectra, this is shown in Fig. 2. These spectra can be well-described by a fit to a bi-exponential model. Whereas the process with the short lifetime contains no significant information in this case, the longer lifetime of [dFl2, Fl34]NPY is significantly less than that of [dFl2]NPY (cf. Fig. 2). This drop in the lifetime of [dFl2, Fl34]NPY is due to resonance energy transfer. Quantitative evaluation of these signals along with an independent determination of the Förster radius by calibration experiments allows quantify the distance between both fluorophors.
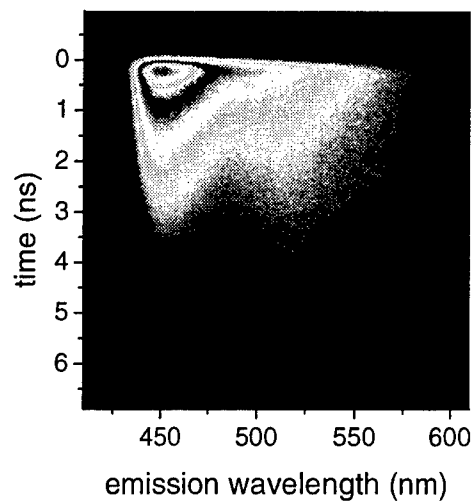
Fig. 1. Time- and wavelength-resolved fluorescence spectra for [dFl2, Fl34]NPY at λ_{ex} = 400 nm.
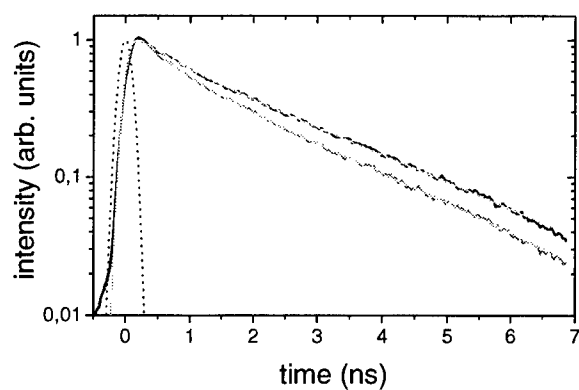

Fig. 2. Time-resolved fluorescence decay curves for [dFl2]NPY (dark) and [dFl2, Fl34]NPY (dark gray) at λ_{em} = 450 nm, laser pulse (dotted) and fits to a bi-exponential model (light gray).
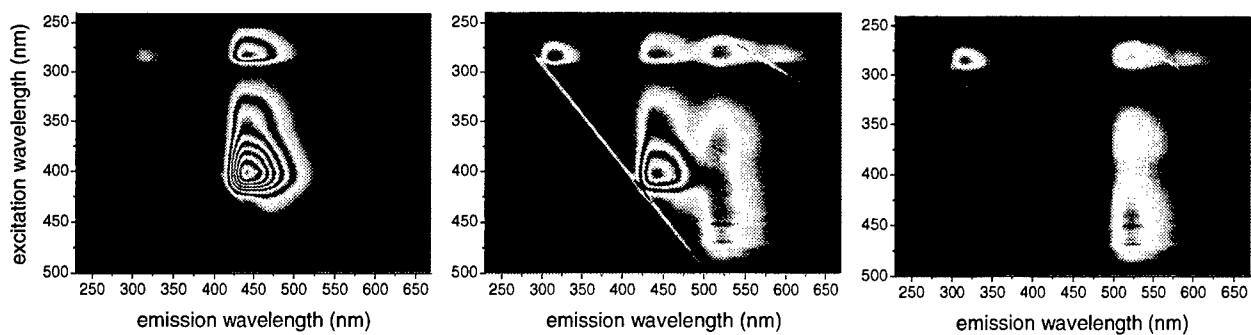

Fig. 3. Excitation-emission spectra of [dFl2]NPY (left), [dFl2, Fl34]NPY (middle) and [Fl34]NPY (right).

Figure 3 shows excitation-emission spectra (EES) of three NPY variants used in our investigation. The strong tilted line visible in all images is due to Rayleigh-scattering. Fluorescence observed at excitation wavelengths around $\lambda_{ex} = 280$ nm is due to excitation of tyrosine. Direct fluorescence is observed around $\lambda_{em} = 310$ nm; fluorescence after subsequent energy transfer to deazaflavin is observed at $\lambda_{em} = 450$ nm, after transfer to flavin at $\lambda_{em} = 525$ nm. For FRET studies, an excitation wavelength of $\lambda_{ex} = 400$ nm is advantageous. Here, strong FRET is visible in the center panel of Fig. 3 for the doubly-labeled [dFl2, Fl34]NPY. Again, this allows to quantify the FRET and to determine the distance inside of this peptide.

4. Summary

In this contribution, we described two different approaches to detect FRET signals in order to determine quantitative distances in and between proteins. Simultaneous time- and wavelength-resolved fluorescence spectra are measured using a picosecond laser source in conjunction with two-dimensional streak detection in the exit plane of an astigmatism-corrected spectrometer. Here, changes in the fluorescence lifetime are detected and used to quantify FRET. This is especially advantageous, since lifetime changes are not affected by fluctuations of the concentration and other interferences. Therefore, this approach is more robust than the direct quantification of FRET with the signal intensities alone.

Excitation-emission spectra (EES) are two-dimensional fluorescence images with one axis corresponding to the excitation and the other to the emission wavelength. They contain all conventional excitation and fluorescence spectra of a given substance and facilitates the interpretation of these spectra (identification of resonance effects, scattering and the isolation of the contribution of different fluorophors to the complete spectrum). They are ideally suited to determine good operating conditions for FRET investigations. First results are shown for the neuropeptide Y (NPY) peptide. An important advantage of this combination of time-resolved LIF and static EES is, that additional information (e.g. about the local conformation of proteins) can be acquired in addition to the FRET signal.

5. References

[1] P. Wu, L. Brand, "Resonance Energy Transfer: Methods and Applications", Anal. Biochem. **218**, 1-13 (1994).

[2] A. Brockhinke, R. Plessow, P. Dittrich, K. Kohse-Höinghaus, "Analysis of the local conformation of proteins with two-dimensional fluorescence techniques", Appl. Phys. B **71**, 755-763 (2000).

[3] R. Plessow, A. Brockhinke, W. Eimer, K. Kohse-Höinghaus, "Intrinsic time- and wavelength-resolved fluorescence of oligonucleotides: A systematic investigation using a novel picosecond laser approach", J. Phys. Chem. B **104**(15), 3695-3704 (2000).

[4] C.P. Eckard, C. Cabrele, H. A. Wieland, A.G. Beck-Sickinger, "Characterisation of neuropeptide Y receptor subtypes by synthetic NPY analogues and by anti-receptor antibodies", Molecules **6**(5), 448-467 (2001).

[5] A.G. Beck-Sickinger, H. A. Wieland, H. Wittneben, K.-D. Willim, K. Rudolf, G. Jung, "Complete L-alanine scan of neuropeptide Y reveals ligands binding to Y1 and Y2 receptors with distinguished conformations", Eur. J. Biochem. **225**, 947-958 (1994).

[6] R. Epple, T. Carell, "Flavin- and deazaflavin-containing model compounds mimic the energy transfer step in type-II DNA-photolyases", Angew. Chem. Int. Ed. **37**(7), 938-941 (1998).

[7] T. Carell, J. Butenandt, "Towards artificial DNA-repair enzymes: Incorporation of a flavin amino acid into DNA-binding oligopeptides", Angew. Chem. Int. Ed., **36**(13-14), 1461-1464 (1997).

Notes

Instrumentation II

Sunday, February 10, 2002

Richard Williams, Pacific Northwest Natl. Lab., USA
Presider

SuA
8:00am–10:00am
Flagstaff

"Miniaturized QC and TDL Laser Spectrometers for Biogenic Gases and Isotope Ratios on Mars, Titan, and Venus"

Dr. Christopher R. Webster
Jet Propulsion Laboratory (JPL)
California Institute of Technology

Address:
Jet Propulsion Laboratory
Mail Stop 183-401
4800 Oak Grove Drive,
Pasadena, CA 91109
Tel (818) 354-7478   FAX (818) 393-4485

QC lasers have been flown in Earth's stratosphere, making the first atmospheric measurements, and are now incorporated into miniature tunable laser spectrometers for biogenic gases and isotope ratios as biosignatures on Mars and other planets.

UV Laser Induced Fluorescence portable system for the detection of plastic and organic compounds in water

Vasanthi Sivaprakasam

Department of Physics, University of South Florida, 4202 E Fowler Avenue, phy 114, Tampa Fl 33620
Ph: (813)974-9930   Fx: (813)974-2635   email: vsivapra@chuma.cas.usf.edu

Dennis K. Killinger

Department of Physics, University of South Florida, 4202 E Fowler Avenue, phy 114, Tampa Fl 33620
Ph: (813)974-3995   Fx: (813)974-2635   email: killinge@chuma.cas.usf.edu

Abstract: A 266 nm Laser Induced Fluorescence system that is 1000 times more sensitive than existing in situ fluorescence sensors has been developed and tested for the detection of plastics and organics in water.
©2000 Optical Society of America
OCIS codes: (010.4450) Ocean optics; (010.7340) Water

We have developed a high-PRF, 266 nm laser based Laser Induced Fluorescence (LIF) instrument that is 1000 times more sensitive than existing in situ fluorescence sensors (SAFire) for the detection of colored dissolved organic matter (CDOM) in ocean water. The increased sensitivity is due to the use of a pulsed UV laser instead of a continuous spectral lamp for excitation, and the ability to use high-PRF boxcar integrators and sensitive optical photomultiplier tubes to detect and average the weak CDOM fluorescence signal. The system has recently been tested aboard a cruise in the Gulf of Mexico. The fluorescence signal from CDOM near 450 nm originating from clean seawater 100 miles off-shore in the Gulf of Mexico had a signal-to-noise of greater than 120.
Our portable LIF system consisted of a (4x) Nd:YAG microchip laser source (5 mW, 8 kHz) operating at 266 nm, 13 optical filter channels ranging from 239 nm to 685 nm in combination with absorption filters with cutoff at 280 nm and 295 nm, and a PMT detector and a boxcar integrator averager system. A laptop computer was used for data acquisition (via GPIB interface) and controlling the filter wheels. A software program was written in Labview to acquire, store and monitor the optical channels in real-time. The emission channels were switched every few seconds, resulting in a complete scan in about one minute. Figure 1 shows a picture of the portable LIF system. Figure 2 shows the schematic of the LIF system.
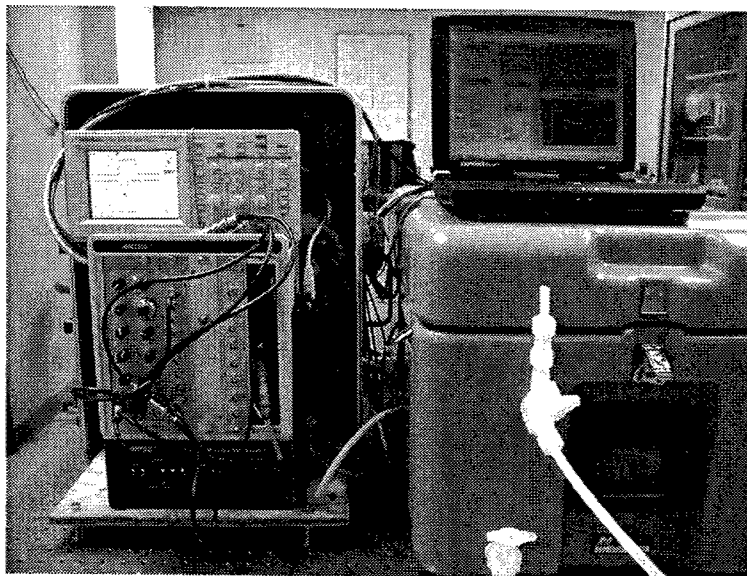
Fig. 1. Picture of the portable Laser Induced Fluorescence system showing the electronics and an enclosed case containing the optical system.
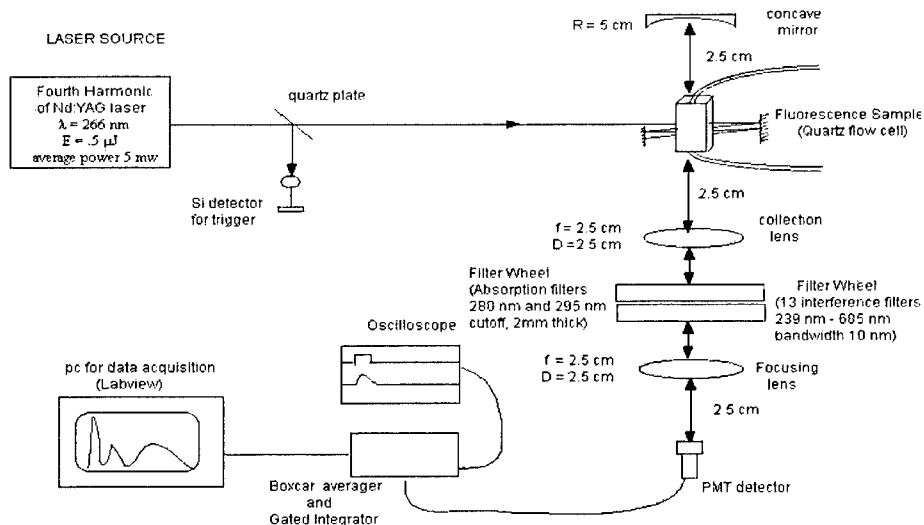
Fig. 2. Schematic of portable LIF system

To compare the detection limits of the system, quinine sulfate was used as the fluorescence standard. The detection limit of the portable LIF system was measured to be 0.001 ppb of quinine sulfate. It was determined that the sensitivity of the portable LIF system was much greater than our previous systems[1] as shown in Table 1.

Table 1. A comparison of detection limits of quinine sulfate (in 0.1 N sulfuric acid) for the different systems.

Fluorometer	*Detection Limit (quinine sulfate)*
Portable LIF system	0.001 ppb
SAFire (Wetlabs) (portable system)	1 ppb
FluoroMax (JY SPEX) (Lab system)	0.05 ppb

The portable system was tested on a 2 day cruise from the Tampa Bay to the Gulf of Mexico (approximately 100 miles offshore). Figure 3 is a plot of the LIF signal measured during the test cruise for the various optical channels as the ship approached the Tampa Bay.
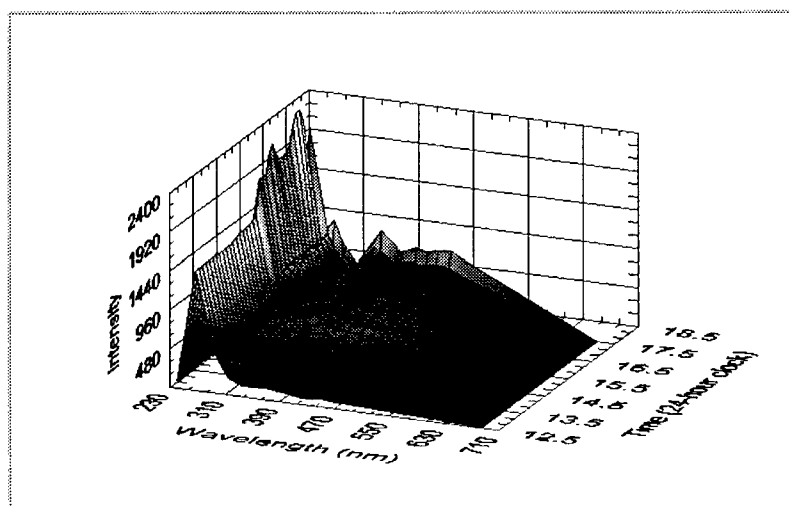
Fig. 3. LIF signal measured during the test cruise as the ship approached Tampa Bay.

Reference:

1. Boehme, J. R. and Coble, P.G. 2000. Characterization of dissolved organic matter using high energy laser fragmentation. Environmental Science and Technology, 34(15) 3283-3290.

Design of a Line-scanned Handheld Imager for Detecting Natural Gas Leaks

R. P. Bambha, T. A Reichardt, T. J. Kulp
Sandia National Laboratories, Livermore, California 94551-0969

R. L. Schmitt
Sandia National Laboratories, Albuquerque, New Mexico 87185

Abstract: An active infrared imager capable of both single- and differential-frequency detection of methane is being developed for handheld operation. The device will be capable of producing real-time video images of methane plumes.
©2000 Optical Society of America
OCIS Codes: (130.6010) Sensors, (280.1120) Air pollution monitoring, (110.3080) Infrared imaging.

1. Introduction

Active infrared imaging provides an efficient method for detecting leaks of many gases important to industrial operations and global climate. Visualization of gas plumes can greatly reduce the time required to find a leak by encompassing a three-dimensional volume in a single image. In contrast, point sensors require the operator to place the sensor at the position of a suspected leak and follow the concentration gradient to find the source.

The technique of active imaging uses laser radiation to illuminate the scene at a frequency absorbed by the gas. Solid objects behind the gas plume provide reflecting surfaces for the light returned to the imager. For single-frequency imaging, the gas plume appears as a dark cloud in an image of the background. Differential imaging can greatly enhance gas plume visibility by removing background features. Differential images are formed by alternately transmitting pulses on and off the frequency of the gas absorption feature. The ratio of intensities at the on and off frequencies is taken, and background features that have nearly the same reflectivity at the two frequencies are suppressed.

The first gas imagers used single-wavelength continuous wave CO_2 lasers operating in the 9-11µm region and single-detector raster scanning to form images[1]. Subsequently, gas imagers were developed that illuminated the full field of view (FOV) with pulsed radiation and used a two-dimensional focal plane arrays to form the image[2]. The use of periodically poled lithium niobate (PPLN) for generation of tunable radiation facilitated active gas imaging in the CH-stretch absorption region near 3.3 µm[3]. Differential gas imaging was demonstrated using bulk lithium niobate parametric devices, but the imager was not practical for routine use because of susceptibility to motion-induced errors[4].

Here, we describe the design of a handheld instrument for active imaging of methane leaks. This work was motivated by the need for routine gas line inspections performed by the Japanese gas industry. The instrument will be capable of both single- and differential-frequency imaging. The design is intended to increase immunity to motion and to satisfy constraints on size imposed by handheld operation.

2. General system requirements and design

The design goals for the imager are intended to make it useful under the conditions expected during routine leak surveys in and around homes in Japan (Table 1.). To meet the sensitivity requirement over the specified range, the frequency of operation was chosen to correspond to the CH-stretch fundamental absorption band near 3.3 µm. To allow modulation between on- and off- absorption frequencies using a telecommunications diode laser, the narrow R-branch feature at 3057.7 cm^{-1} was selected. The transmitted frequency must remain in a band of approximately 2.2 GHz width to be within 10% of the maximum absorbance of the methane R-branch. Within this frequency range, methane with a concentration of 10 ppm-m yields a round-trip absorbance of 11%, which is sufficient for visual recognition of a gas plume.

For differential imaging it is necessary maintain spatial registration between the on- and off-frequency data. Motion of the imager or the target can induce errors in the differential data, particularly where the

background surface contains high contrast edges. Thus, the on and off frequency data must be acquired rapidly to avoid errors. A pulsed-illumination scheme with the radiation concentrated in a line was chosen to satisfy the pixel registration requirements and the design goals of Table 1.

Table 1. Design goals for handheld imager

Parameter	Goal
Range	1 - 5 meters
Minimum background reflectivity	0.005 sr^{-1}
Sensitivity (path-integrated gas concentration)	10 ppm-m CH_4
Size	Handheld unit with shoulder mounted pack
Power	Battery operation for 2 hours
Video image frame rate	10 Hz differential mode 20 Hz single frequency mode

3. Laser Illuminator

The transmitter source for the handheld imager is a seeded optical parametric generator (OPG) pumped by a passively Q-switched Nd:YAG microlaser and seeded by a distributed-feedback diode laser operating near 1.577 μm. The nonlinear OPG material is PPLN. The OPG produces an idler output at the difference frequency between the pump and seed laser frequencies. The idler beam is used for methane imaging. The pump laser operates in a single longitudinal mode and the frequency is held approximately constant through temperature control. The frequency of the diode laser is dependent on its temperature and drive current. The temperature of the diode laser is held nominally constant while the current is controlled to generate the idler frequency that is either on or off the methane absorption peak. When pumped with a pulse of 75 μJ and a duration of 1.5 ns, the OPG produces an idler pulse having an energy of 7 μJ.

The pump laser consists of a 17-mm-long monolithic cavity pumped at 810 nm by a fiber-coupled diode bar. The cavity consists of three regions: (1) a Nd:YAG gain region, (2) a Cr:YAG passive Q-switch, and (3) an undoped YAG spacer. The ends are polished and coated to serve as a high reflector and a 1064 nm output coupler. During operation, the monolithic cavity is temperature controlled by a thermoelectric cooler (TEC) and exhibits single-mode operation.

A computer-based control system is used to stabilize the idler frequency at the peak of the methane absorption feature. Frequency error signals are generated by directing a portion of the idler output beam through a methane cell to an uncooled infrared detector. The detector voltage is digitized and read into computer memory. The computer calculates the frequency error and correction voltage. A digital-to-analog converter is used to control the seed laser current and hence its frequency. By modulating the seed laser frequency, the derivative of the methane transmission can be calculated. The seed laser current is adjusted to maintain zero slope corresponding to the CH_4 absorption peak. A modulation of less than 500 MHz is used to keep the OPG idler frequency within the desired 2.2 GHz range around the methane peak.

4. Focal Plane array

The focal plane array (FPA) is an InSb array hybridized to an Indigo 9809 readout circuit. The pixels are square with 30μm sides. Presently, the FPA is contained in a liquid nitrogen cooled dewar. Ultimately, the FPA will be packaged in a miniature dewar and cooled by a closed-cycle refrigerator. A 256X2 window of detectors is read out of the array, although only one of the rows is used for image formation. A 155-nm bandpass cold filter and a short integration time (~1-6 μs) are used to suppress passive background radiation. The received radiation is imaged on the array with an f/1, 25-mm-focal-length lens.

5. Image Formation

The output beam is formed into a sheet to illuminate a horizontal line that overlaps the instantaneous field-of-view (IFOV) of one line of pixels in the IR camera. To create an image of the entire target region, both the laser sheet and the camera IFOV are scanned vertically by a galvanometer-based scan mirror. Figure 1 shows the illumination approach for line-scanned imaging. The illumination pattern can be created using astigmatic optics.
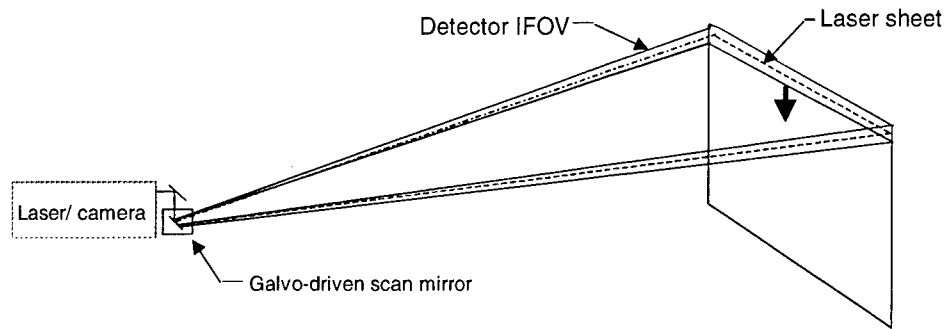
Fig. 1. Illumination approach for line scanned imaging

A computer-controlled waveform generator controls the scan mirror. In differential mode the mirror is stepped between pairs of laser pulses. In single-frequency mode the mirror is moved in a quasi-continuous motion so that consecutive laser pulses illuminate adjacent IFOVs. The data are read into the computer with a frame grabber and processed into video images. Figure 2 is a block diagram of the imaging system.
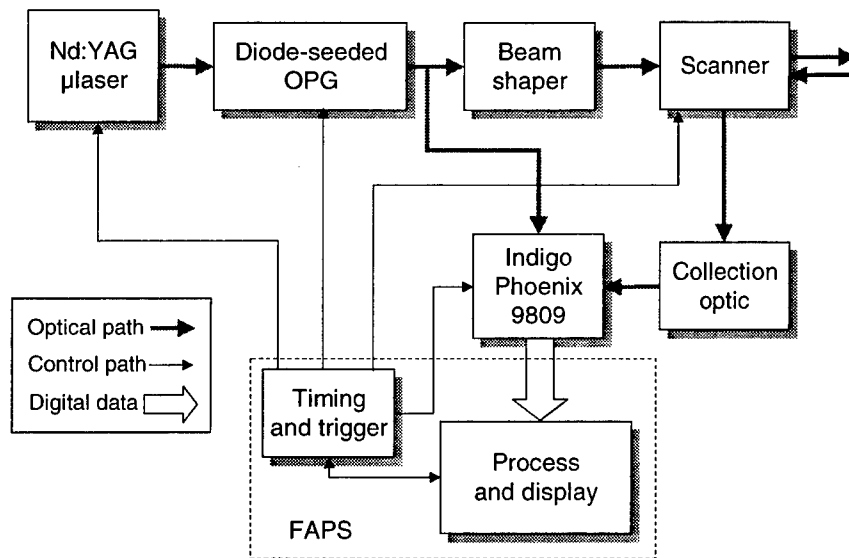

Fig. 2. Block diagram of the handheld imaging components.

4. References

1. T.G. McRae and T.J. Kulp, "Backscatter Absorption Gas Imaging — A New Technique for Gas Visualization," *Appl. Opt.* **32**, 4037-4050 (1993).
2. T.J. Kulp, P. Powers, R. Kennedy, and U.B. Goers, "Development of a pulsed backscatter-absorption gas-imaging system and its application to the visualization of natural gas leaks", Appl. Opt. **37** 3912-3922 (1998).
3. U.B. Goers, T.J. Kulp, P.E. Powers, and T.G. McRae, "A PPLN OPO based backscatter absorption gas imaging (BAGI) system and its application to the visualization of fugitive gas emissions", SPIE Proceedings **3758**, 172-180 (1999).
4. P.E. Powers, T.J. Kulp, and R. Kennedy, "Demonstration of differential backscatter absorption gas imaging", Appl. Opt. **39** 1440-1448 (2000).

Development and Evaluation of a Portable Gas Imager Using a Fiber-Amplifier-Pumped PPLN OPO Illuminator

Thomas J. Kulp, Karla M. Armstrong, Ricky Sommers, Dahv A. V. Kliner,
Uta-Barbara Goers, and Sal Birtola
Sandia National Laboratories, Livermore, CA 94551-0969
Email: tjkulp@sandia.gov

Lew Goldberg, Jeffrey P. Koplow, and Sean Moore
Naval Research Laboratory, Washington DC 20375-5672

Thomas G. McRae
Laser Imaging Systems, Punta Gorda, FL 33983

Abstract: Active imaging allows gases to be visualized in a real-time video format through their attenuation of backscattered laser radiation. Here we describe the development and testing of a battery-operated portable gas imager that employs a fiber-amplifier-pumped PPLN optical parametric oscillator as its illumination source.©2000 Optical Society of America
OCIS Codes: (130.6010) Sensors, (280.1120) Air pollution monitoring, (110.3080) Infrared imaging.

Infrared (IR) imaging is a powerful tool for detecting and locating fugitive gas emissions. Through its use, gas plumes are visualized in a real-time video format when they attenuate or emit IR radiation. Because an image instantly reveals the presence of gas clouds in a three-dimensional volume, leak location using imaging is inherently faster than that using hand-held sensors (sniffers) that measure gas concentration at a single point. Moreover, the presentation of a gas plume as a picture greatly simplifies the detection process and minimizes confusion with background gases.

In this paper, we describe the development and field evaluation of a battery-operated, operator-portable active imager for the detection of hydrocarbon leaks relevant to the petroleum processing and natural gas industries. Active imaging uses laser radiation to illuminate a scene at a wavelength that is absorbed by the gas to be detected. Gases are imaged when they attenuate laser radiation backscattered from solid surfaces in the imaged region. Because the illumination is provided by the system, there is no reliance on ambient radiation and, thus, temperature. Several types of active gas imagers have been developed in the past, using both continuous wave (cw) and pulsed laser illumination. Early imagers operated using cw CO_2 lasers in conjunction with a raster-scanned imaging camera[1]. Such devices were developed for operation at standoff ranges up to 300 m[2]. The 9-11 μm line tuning range of the CO_2 laser did not, however, allow detection of hydrocarbon effluents relevant to the natural gas or petroleum industries. This motivated the formulation of systems capable of operation in the CH-stretch absorption band region near 3.3 μm. Initially, a pulsed system[3] was pursued due to the relative ease with which pulsed light could be frequency converted using nonlinear mixing. That device exhibited an imaging range of ~70 m and was shown to be capable of differential imaging[4], where images at frequencies on and off the gas resonance (termed the on- and off-frequencies) are collected and processed to generate an absorption map of the scene. The differential image removes the clutter of objects in the scene and eases the visual recognition of the gas plume. Following the emergence of the quasi-phasematched nonlinear material PPLN (periodically-poled lithium niobate), it

became possible to efficiently convert cw light using nonlinear mixing. Initially, PPLN was employed to generate a van-mounted[5] imager that was successfully tested in natural gas distribution facilities and at a petroleum refinery. The need for a system that would provide greater mobility in the cluttered environment of a refinery subsequently motivated the development of the system described here.

The portable gas imager achieves its compact size and high electrical efficiency by using a fiber-amplifier-pumped PPLN optical parametric oscillator (OPO) as its illumination source. Figure 1 contains a schematic diagram of the laser system. The fiber amplifier consists of a double-clad, Yb-doped gain fiber that is V-groove-side-pumped using radiation from two 4-W single-stripe diode lasers operating at 975 nm. A 60-mW single-frequency seed beam from a compact Nd:YAG laser is injected into the amplifier to generate ~4W of useable output light with a spectral linewidth of <1 MHz. This radiation is fiber coupled to the OPO module which contains a singly-resonant PPLN OPO configured as a bowtie ring cavity. The PPLN crystal used allows tuning over the idler range between 3.1 and 3.6 μm with an output power of =250 mW.

Upon exiting the OPO, the idler beam is filtered to remove residual signal and pump radiation and directed into a raster-scanning IR camera. The camera contains a pair of galvanometrically-driven scan mirrors that operate in a concerted fashion to raster-scan the laser beam and the instantaneous field-of-view (IFOV) of a single element HgCdTe detector across the target at a frame rate of 23 Hz. The detector signal is digitized and electronically formatted to generate an RS-170-compatible video output image for display that is available to the operator on a video eyepiece. During operation, the video signal is also recorded using a compact Hi-8 videocassette recorder and is transmitted to a remote location using an RF video transmitter.

Figure 2 contains a photograph of the imager in operation. All optical components of the laser are contained in a shoulder-mounted camera as is the raster scanner. Electronic components are contained in a module contained in a knapsack on the operator's back. The current weight of the camera is about 30 lbs while the electronics pack weighs about 15 lbs. The weight of the latter includes the 5 lb weight of a lithium-ion battery pack. At a total power consumption of about 180-200 W, the battery pack is capable of providing about 75 minutes of operation on a single charge.

At present, most attention has been given to the use of the system as a leak surveillance tool for petroleum refineries. A typical refinery contains a wide array of process areas that contain and transport a broad range of hydrocarbon species. Environmental regulations mandate the monitoring of all potential leak points (e.g., valves, flanges, pump seals) on a quarterly basis. Because speed is an important aspect of this process, it is impractical to consider selective tuning of the imager wavelength to the absorption of particular gases. Rather, the system is operated at "generic" wavelengths that are intended to be useful for the detection of many gases. As an example, a wavelength suitable for detection of aliphatic species is a CH stretching band typically centered at about 2970 cm^{-1}.

To be successful, the system must operate to produce a reliable detection limit under a variety of environmental conditions. Performance has been evaluated in controlled tests at Sandia that measure the detection threshold under conditions of different windspeed, background surface, type of leak point, and standoff distance. To date these tests have been carried out in a wind tunnel; however, they will be followed by

controlled "roving" tests at Sandia and at a refinery during the winter of 2001. At the present time, the detection limit for propane gas is determined to be 2-3 gm/hr at low windspeeds and ranges up to 30 ft irregardless of background type and leak point type. Detection is most sensitive to windspeed with limits increasing to 20-110 gm/hr for windspeeds between 11 and 22 mph.

1. T.G. McRae and T.J. Kulp, "Backscatter Absorption Gas Imaging — A New Technique for Gas Visualization," *Appl. Opt.* **32** 4037-4050 (1993).

2. T.J. Kulp, R. Kennedy, M. Delong, D. Garvis, and J. Stahovec, "The Development and Testing of a Backscatter Absorption Gas Imaging System Capable of Imaging at a Range of 300 m", Proceedings of SPIE. Applied Laser Radar Technology, (Society of Photo-Optical Instrumental Engineers, Bellingham, WA, 1993) Orlando, FL, pp. 204-213.

3. T.J. Kulp, P. Powers, R. Kennedy, and U.B. Goers, "Development of a pulsed backscatter-absorption gas-imaging system and its application to the visualization of natural gas leaks", Appl. Opt. **37** 3912-3922 (1998).

4. P.E. Powers, T.J. Kulp, and R. Kennedy, "Demonstration of differential backscatter absorption gas imaging", Appl. Opt. **39** 1440-1448 (2000).

5. U.B. Goers, T.J. Kulp, P.E. Powers, and T.G. McRae, "A PPLN OPO based backscatter absorption gas imaging (BAGI) system and its application to the visualization of fugitive gas emissions", SPIE Proceedings, 3758, 172-180 (1999).
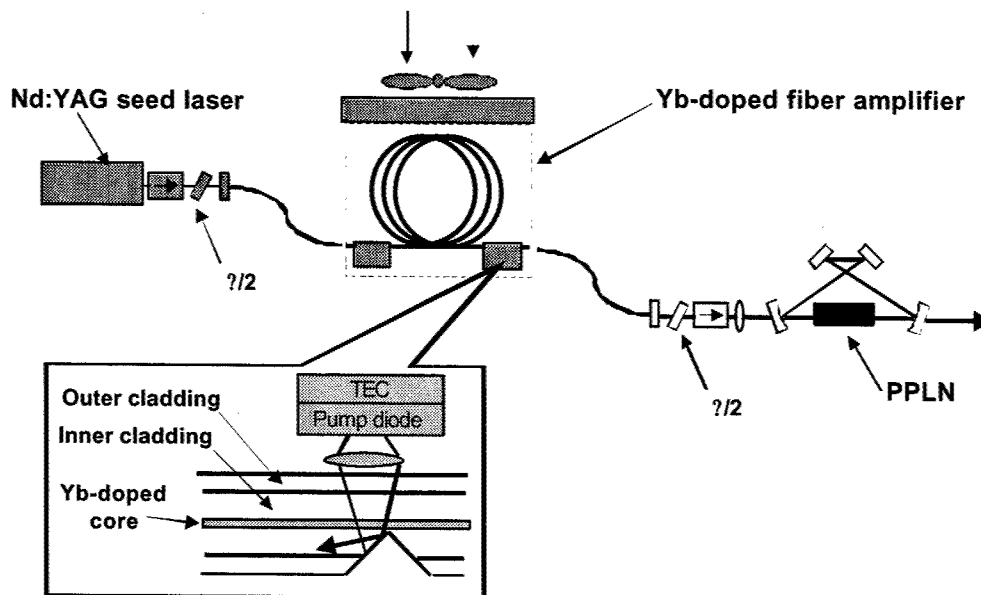
Figure 1 - Diagram of the fiber-amplifier-pumped PPLN OPO used in the portable gas imager.
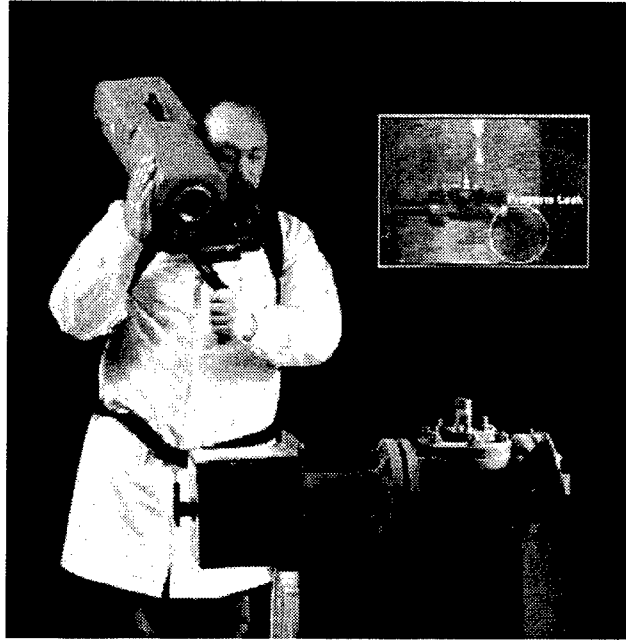
Figure 2 - Photograph of the operator portable gas imager. The picture shows the shoulder-mounted camera unit. The electronics module is worn in a knapsack on the operator's back. The inset shows an image of a propane leak.

Ultra-sensitive ammonia detection for industrial applications using photoacoustic spectroscopy

Michael E. Webber, Michael B. Pushkarsky, Ohan Baghdassarian, L. Ravi Narasimhan, C. Kumar N. Patel

Pranalytica, Inc., 1101 Colorado Ave., Santa Monica, CA 90401

T: (310) 458-2624, F: (310) 458-0171, E: webber@pranalytica.com

Abstract: An industrial trace-ammonia sensor based on photoacoustic spectroscopy and CO_2 lasers has been developed with a minimum detectivity in the parts-per-billion range. This sensor is capable of making simultaneous measurements of up to twenty gas samples with an optically multiplexed arrangement of optoacoustic cells.
©2000 Optical Society of America

OCIS codes: (120.0120) Instrumentation, measurement and metrology; (300.6430) spectroscopy, optoacoustic

1. Introduction

The field of laser-based spectroscopic sensing has enjoyed a wide array of measurement strategies and end-user applications. One laser that has a long history in the field of trace-gas detection is the CO_2 laser, whose high powers and access to strong absorption transitions for species such as ammonia, benzene, and ethylene has yielded many sensitive gas detectors since the early 1970's.[1] And, one of the older sensing techniques is photoacoustic spectroscopy, which is a particularly advantageous method for trace-gas detection because of its relative simplicity, rugged nature and sensitivity. The combination of CO_2 lasers for photoacoustic trace-gas detection has been well-established,[2] but has not been traditionally incorporated into commercially-available gas-sensing instruments because of the power requirements and size of tabletop CO_2 lasers. However, the recent commercial availability of compact, low-power (<25 W), grating-tunable CO_2 lasers enables the development of instrumentation with excellent sensitivity and compact footprints that can be readily deployed in industrial or medical settings.

The different industrial sites for trace ammonia sensors include semiconductor clean rooms, where 1 parts-per-billion (ppb) sensitivity is required; industrial facilities such as chiller plants or chemical production locations, for which a detection sensitivity of 100 ppb is necessary; and workspaces with indoor air quality monitoring needs, for which a minimum detectivity of 1 part-per-million (ppm) is suitable. We have addressed the need for sensors in these industrial settings with the development of a commercial platform using photoacoustic spectroscopy and CO_2 lasers that can offer sufficient dynamic range and sensitivity.

2. Instrumentation Details

The instrument layout is shown schematically in Figure 1, and is similar to the platform that has been demonstrated for real-time noninvasive medical breath diagnostics.[3] The system consists of a laser, optics for shaping and directing the radiation, the flow-through measurement chambers (four for this particular configuration, operated in non-resonant mode), a laser power meter, lock-in amplifiers for signal conditioning, and a computer for controlling the system and analyzing the signals to produce concentration readings in real-time. The radiation source is a sealed-off radiofrequency-excited CO_2 laser whose operating wavelength can be line switched from R40 of the 9-μm band to P50 of the 10-μm band by using an intracavity grating, yielding laser operation at 120 discrete frequencies. These transitions are separated by 1-2 cm^{-1} and the laser frequency, therefore, is not continuously tunable, however by employing appropriate pressure broadening of the absorbing species, spectral overlap with CO_2 laser frequencies can be achieved. For detecting ammonia, the optoacoustic cells are operated near atmospheric pressure, for which ammonia transitions near 9.22 μm overlap with the 9R30 laser transition.

Measurements of the target species in the sample chamber are made via the photoacoustic effect. Any light absorbed by the gases in the sample is converted into heat, thereby generating an acoustic signal that is detected by sensitive microphones. The signal size is directly proportional to the number of absorbing molecules, the absorption cross-section of that species at the operational wavelength, and the incident number of photons. Thus, by choosing wavelengths that overlap with strong absorption transitions and by using high-power lasers, detection sensitivity can be significantly enhanced. And, because the microphone signals are continuously normalized by the measured laser power, the instrument is self-calibrating. By modulating the laser power, photoacoustic pressure waves can be

generated at specific frequencies. Electronic signal conditioning units, in this case lock-in amplifiers, can then be used for discriminating photoacoustic signal from the background acoustic noise.

One advantage of the photoacoustic method is that very little of the incident laser intensity is absorbed in the sample cell, and thus sufficient power remains for making sensitive measurements in successive cells. Simultaneous measurements of up to twenty gas samples can be performed simultaneously using an optically multiplexed arrangement similar to that shown in Figure 1, thereby allowing for one central instrumentation unit to provide readings for ammonia values at many locations within an industrial facility.
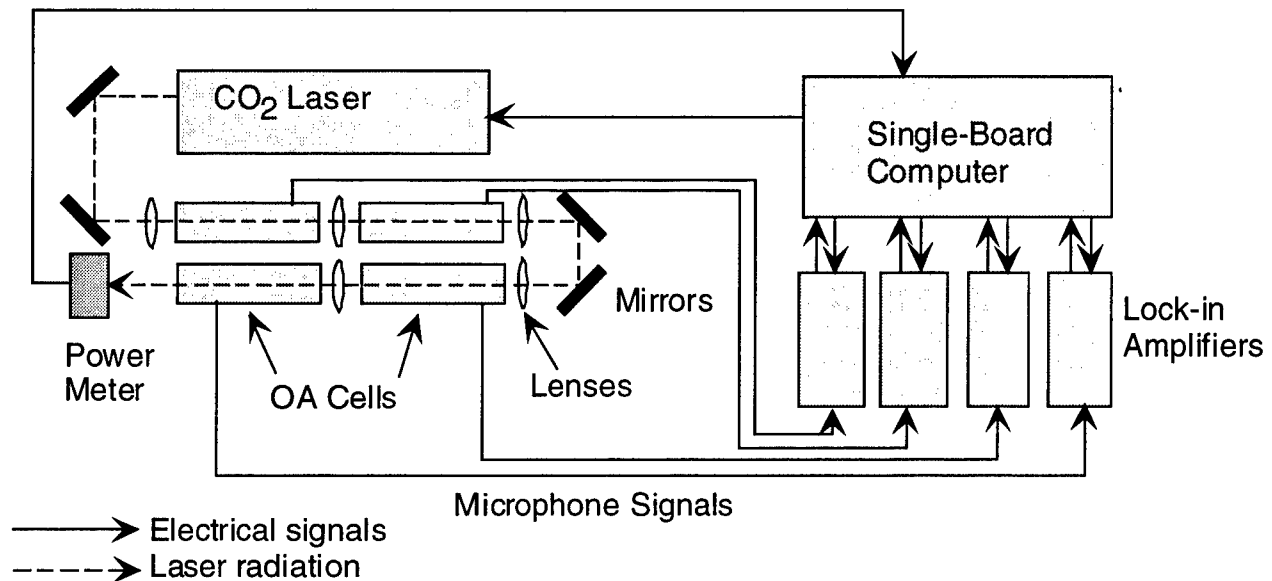
Fig. 1. Experimental schematic of the four-cell configuration, using a single radiation source, four optoacoustic cells, four lock-in amplifiers, one power meter, and one single-board computer.

For the aforementioned industrial settings, the typical interfering species will be ambient CO_2 and H_2O, with expected respective concentrations of 300-500 ppm and 1-2%. The water interference is negligible, while the background CO_2 interference corresponds to a signal size that is comparable to approximately 10 ppb of ammonia.[4] Since ambient CO_2 in industrial settings changes minimally over many hours, correcting for its contribution to the optoacoustic signal only needs to be performed a few times per day. Determining the appropriate offset adjustment can be done by switching the CO_2 laser to a transition that is non-resonant with NH_3, or by using a separate, compact, and affordable sensor, such as an electrochemical sensor, to measure the background CO_2 levels and then calculate the expected contribution.

3. Performance and Results

This platform sensing technology has demonstrated a single-digit ppb sensitivity, as determined by the signal-to-noise ratio for individual measurements, and the long-term stability of the instrument when tested with a continuous flow of a calibrated ammonia mixture. Typical integration times for the measurement are anywhere from 3 to 30 seconds, depending on the desired trade-off between sensitivity and measurement time. Another common method for improving the sensitivity includes operating the system in resonant mode, whereby the microphone data is analyzed at the resonant frequency of the optoacoustic cell instead of the frequency at which the laser is being modulated.

Figure 2 shows recent results for this sensing technology in a non-resonant mode when tested with a flow of an ammonia mixture whose concentration decreased in "staircase" fashion. Starting with a calibrated mixture of 8.8 ppm ammonia that had been diluted with two high-precision MKS Instruments flow control stages (better than +/- 1% accuracy), the following calibrated mixtures were generated: 2000, 1000, 500, 250 and 0 ppb. As these results

illustrate, the sensor tracks the varying concentrations with excellent linearity. The sensitivity of the sensor for this particular test was 10 ppb, using a 20-second integration time, non-resonant operation, and a 15% duty cycle for laser operation. Resonant operation, higher duty-cycle, and longer integration times can be used to readily achieve 1 ppb minimum detectivity.
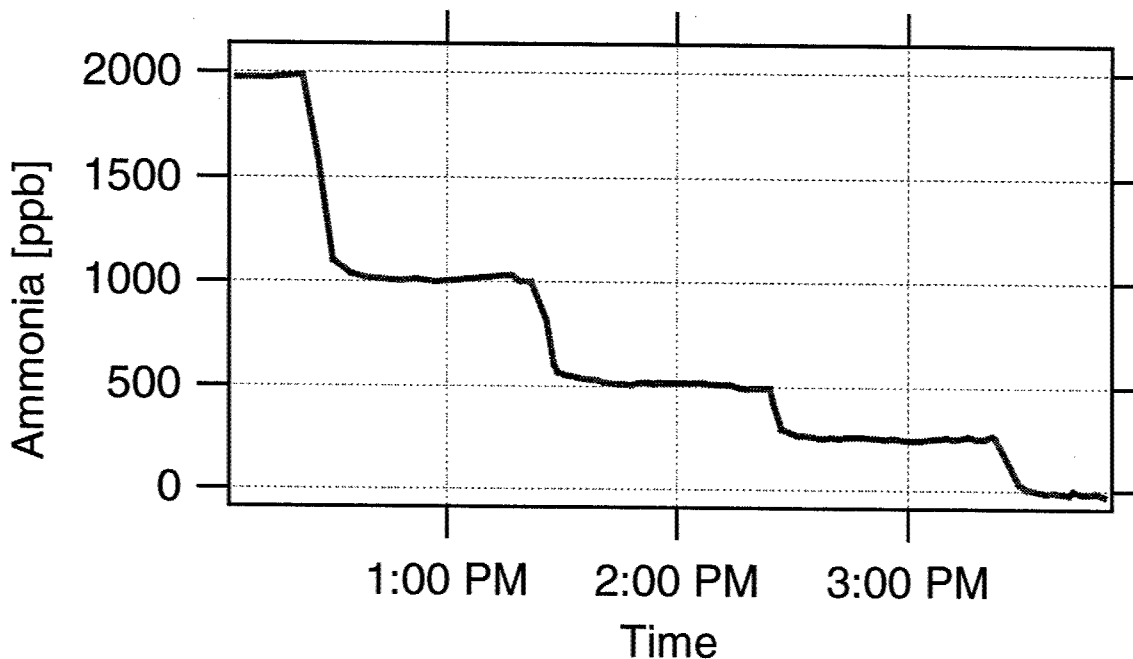
4. Conclusions

We have developed a commercial product for detecting trace concentrations of ammonia in industrial settings using CO_2 lasers and photoacoustic spectroscopy. These sensors can detect ammonia with a sensitivity in the parts-per-billion range using an integration time of approximately 15 seconds and with excellent linearity over a wide range of concentrations.

5. References

1. L.B. Kreuzer, N.D. Kenyon and C.K.N. Patel, "Air Pollution: Sensitive Detection of Ten Pollutant Gases by Carbon Monoxide and Carbon Dioxide Lasers," *Science* **177**, 347—349 (1972).
2. P. Repond and M.W. Sigrist, "Photoacoustic spectroscopy on trace gases with continuously tunable CO_2 laser," *Appl. Opt.* **35**(21), 4065—4085 (1996).
3. L.R. Narasimhan, W. Goodman and C.K.N. Patel, "Correlation of breath ammonia with blood urea nitrogen and creatinine during hemodialysis," *Poceedings of the National Academy of Sciences* **98**(8), 4617—4621 (2001).
4. L.S.Rothmann, C.P.Rinsland, A.Goldman, S.T.Massie, D.P.Edwards, J.-Y.Mandin, J.Schroeder, A.McCann, R.R.Gamache, R.B.Wattsin, K.Yoshino, K.V.Chance, K.W.Juck, L.R.Brown, V.Nemtchechin, and P.Varanasi. "The HITRAN molecular spectroscopic database and HAWKS (HITRAN atmospheric workstation):1996 edition." *J. Quant. Spectrosc. Radiat.Transfer*, **60**(665), 710 (1998).

6. Acknolwedgments

Notes

Diode Lasers and Applications II

Sunday, February 10, 2002

Juan-Carlos Rolon, Ecole Centrale Paris, France
Presider

SuB
10:40am–12:20pm
Flagstaff

Rubust external cavity diode laser (ECDL) with implemented antireflection coated "blue" laserdiodes and their performance in atom absorption spectroscopy

Lars Hildebrandt, Joachim Sacher, Richard Knispel

Sacher Lasertechnik Group, Hannah Arendt Str. 3-7, 35037 Marburg/Germany
phone:+49 6421 305290, fax: +49 6421 305299, Contact@Sacher-Laser.com

Abstract: For the first time we present antireflection coated "blue" laserdiodes and their performance in Littrow and Littman ECDL. The relevance of the achieved progress in ECDL technology for construction of ECDL-based sensor systems for in-situ analysis is discussed.
©2000 Optical Society of America
OCIS codes: (140.2020) Diode lasers, (300.0300) Spectroscopy

Summary

Wavelength tuning and spectral characteristics of commercially available standard laser diodes are far from ideal, and thus many applications in the near infrared are limited to the use of relatively expensive distributed feedback (DFB) laser diodes. External cavity diode lasers (ECDL), in which antireflection coated Fabry Perot laser diodes can be utilized, can provide a cost-effective alternative with wavelength tuning ranges of up to 100 nm (depending on the center laser wavelength), linewidths of several hundred kHz and cw-power of up to 200 mW. They are small-sized and amenable to electronic high frequency modulation which makes these light sources desirable for sensor application. A summary of existing ECDL manufactured by Sacher Lasertechnik is given in this talk.

Common ECDL designs use gratings as wavelength-selective elements with external optics either in Littrow configuration, where the laser output beam is coupled out of the resonator via the grating and the wavelength tuning is achieved by turning the grating, or in Littman configuration, in which the resonator length and thus the wavelength tuning is achieved by moving an additional reflecting element (e.g. a mirror or prism) inside the laser resonator. Wavelength regions that are currently covered by our lasers with various laser diodes include the regions 390 -430 nm, 625 - 700 nm, 730 - 1100 nm, and 1240 - 1660 nm, limited at this point by the availability of the laser diodes.

Recent improvements of room temperature diode laser technology for data storage applications have given rise to enhanced availabilty of semiconductor lasers with wavelength in the blue spectral region, which have suitable beamprofiles and reasonable lifetimes. The objective of the current work is to optimize the performance of our Littrow and Littman lasersystems by the use of these coated diodes. We compare ECDL in both Littman and Littrow konfiguration. With 10 diodes the whole spectral range from 390 nm to 430 nm is covered, while each lasersystem covers about 6 nm around its center wavelength. The linewidth is in the MHz regime with singlemode cw-power of up to 30 mW. The relevance of the achieved progress in ECDL technology for construction of ECDL-based sensor systems for in-situ analysis is discussed. An atom absorption experiment is described, which prooves the performance of the lasersystem. As these diodes were coated for the first time, we also present data of the newly coated diodes themselves.

A summary of this talk will be available as a hand-out after the talk. Some of our lasersystems can be seen at our tabletop in the exhibition hall.

References

Important references are:

C.E. Wieman, L. Hollberg, "Using diode lasers for atomic physics" Rev. Sci. Instrum. 62 (1), 1-19 (1991).

K.B. MacAdam, A. Steinbach, C. Wieman, "A narrow-band tunable diode laser system with grating feedback, and a saturated absorption spectrometer for Cs and Rb" Am. J. Phys. 60 (12), 1098-1111 (1992)

Wavelength-agile diode laser sensors for monitoring gas properties in harsh environments

Scott T. Sanders, Jay B. Jeffries, Jian Wang, and Ronald K. Hanson

High Temperature Gas Dynamics Laboratory, Department of Mechanical Engineering, Stanford University, Stanford, CA 94305
Jeffries@Navier.Stanford.edu

Abstract: Extended wavelength tuning of diode lasers enable the extension of scanned wavelength absorption techniques to transient, high pressure, hostile environments. Examples using frequency agile VCSELs and new wavelength tuning strategies are presented.

OCIS Codes: (280.3420) Laser Sensors, (300.6260) Spectroscopy, Diode Lasers

New lasers and wavelength-tuning strategies extend traditional diode-laser absorption techniques to high-pressure, transient, and generally hostile environments. We demonstrate the use of shortwave vertical cavity surface-emitting lasers (VCSELs), scanning repetitively through ~ 1 nm at up to MHz rates, to measure high pressure O_2 in a static cell as well as temperature and pressure in a Cesium-seeded pulse detonation engine (PDE). To facilitate similar measurements of high pressure H_2O near 1.4 μm, where wavelength-agile lasers are not yet commercially available, we demonstrate rapid temperature tuning of a standard distributed feedback (DFB) laser using an auxiliary 5W, 532 nm laser.

An example of recently available wavelength-agile diode lasers is illustrated in Fig. 1. The current-tuning characteristics of a typical DFB laser are surpassed both in terms of maximum tuning range (× 20) and repetition rate (× 100) by a VCSEL. For the case of O_2 absorption shown in Fig. 1, the result is an ability to rapidly probe many nearby absorption lines. This allows temperature scans across many absorption lines, which enables new strategies to infer temperature distributions along the line-of-sight[1].
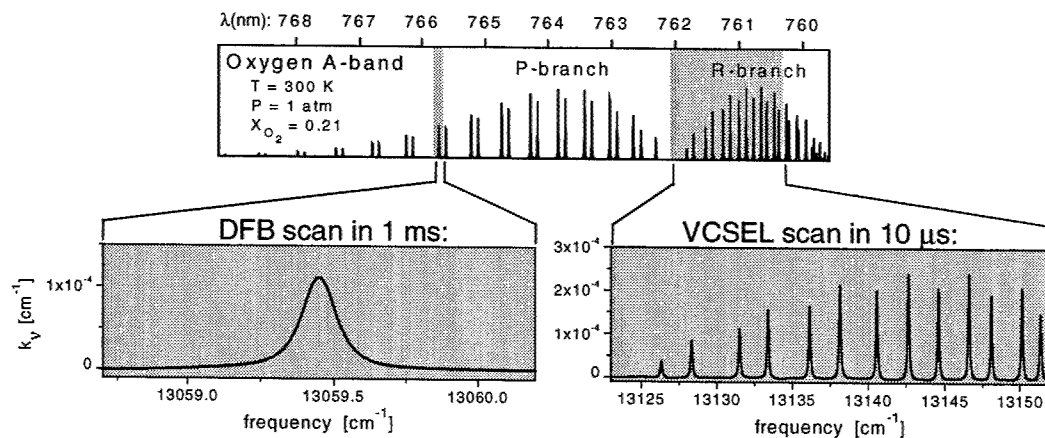
Figure 1. Illustration of the utility of increased wavelength agility.

The increased tuning range enables accurate measurements of high-pressure absorbers[2], even in blended spectra such as shown in Fig. 2 for O_2 at 10 bar. The transitions in this region are sufficiently overlapped that the region between the lines still has significant absorption. Thus, the absorbance baseline must be extracted from a spectral model. In this figure, the absolute value of the absorbance is arbitrary and therefore termed "quasi-absorbance". The spectroscopic structure is used to infer quantitative gas properties. The increased wavelength-agility also enables 2f wavelength modulation spectroscopy of high-

pressure absorbers. This capability is especially useful for detecting weak absorbers such as O_2 – or minor species – in high-pressure environments.
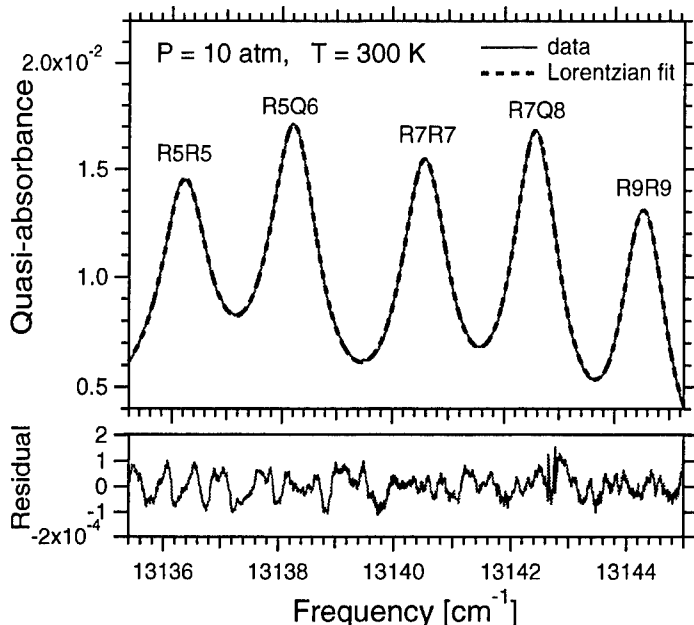
Fig. 2 five O_2 A-band absorption lines at high pressure (path length = 55 cm)

Because VCSELs provide broad scans at high repetition rates, they are ideally suited to high pressure, harsh environments. One such environment is the PDE[2], shown schematically in Fig. 3. The tube is filled with combustible gas and ignited. A detonation develops and proceeds down the tube at ~1 km/s. As the detonation passes the detector the pressure increases from 1 to nearly 40 bar and the temperature increases from 300 to 3000 K.

Temperature measurements with 10 μs time resolution are desired. We seed the PDE fill gases with Cesium oxide dust, thus, the burned gases contain trace levels of atomic Cs, which we monitor with a VCSEL laser. The VCSEL scans approximately 1 nm (~10 cm^{-1}) in 1 μs each time the laser current is pulsed on, and reverse-scans the same amount each time the laser current is pulsed off. After the detonation wave passaes, an absorption feature corresponding to the D_2 transition of atomic Cs is observed. The rapid scans track the transient gas properties, in the midst of high-frequency noise (e.g., due to beam-steering), during detonation events. The integrated absorbance areas of the features recorded by detector 1 are proportional to the population of atomic Cs in the ground electronic state; the emission intensities recorded by detector 2 are proportional to the population in the excited state. The ratio of these two populations provides the electronic temperature record. The collisional width of the Cs absorption features yields the pressure.

Because VCSELs are not yet available above 1 μm, where vibrational transitions permit measurements of
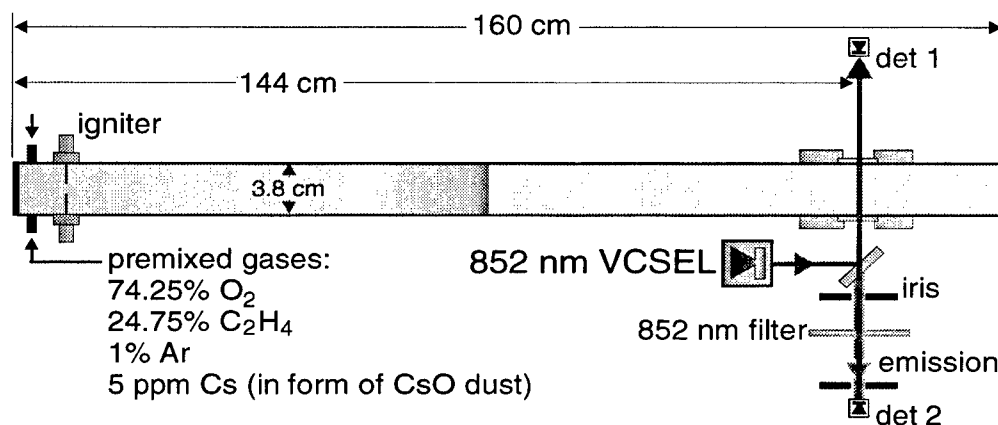
Figure 3. Schematic of VCSEL-based sensor for temperature and pressure applied to a laboratory-scale PDE

important species such as H_2O, rapid temperature-tuning[3] has been developed to extend the wavelength-agility of standard DFB lasers. A chopped 5W, 532 nm laser provides intermittent heating directly to the active region of a diode laser. When the heating laser is on, the diode laser temperature rises ~ 60 °C in 1 ms (scanning its wavelength ~ 4nm); when the heating laser is off, the diode laser returns ~ 60 °C in 1 ms by conduction to the heat sink. Such broad wavelength scans were used to measure the H_2O absorption spectra shown in Fig. 4 at 1-10 atm total pressure.

References:
1. S.T. Sanders, J. Wang, J.B. Jeffries, R.K. Hanson, *Appl. Opt.,* 2001, in press.-
2. J. Wang, S. T. Sanders, J. B. Jeffries, and R. K. Hanson, *Appl. Phys. B* **72,** (2001).
3. S. T. Sanders, M. M. Thuruchengode, D. W. Mattison, and R. K. Hanson, *23rd International Symposium on Shock Waves*: paper 5733, Fort Worth, TX, July 22-27, 2001.
4. S. T. Sanders, D. W. Mattison, J. B. Jeffries, and R. K. Hanson, *Opt. Lett.* **26,** (2001).
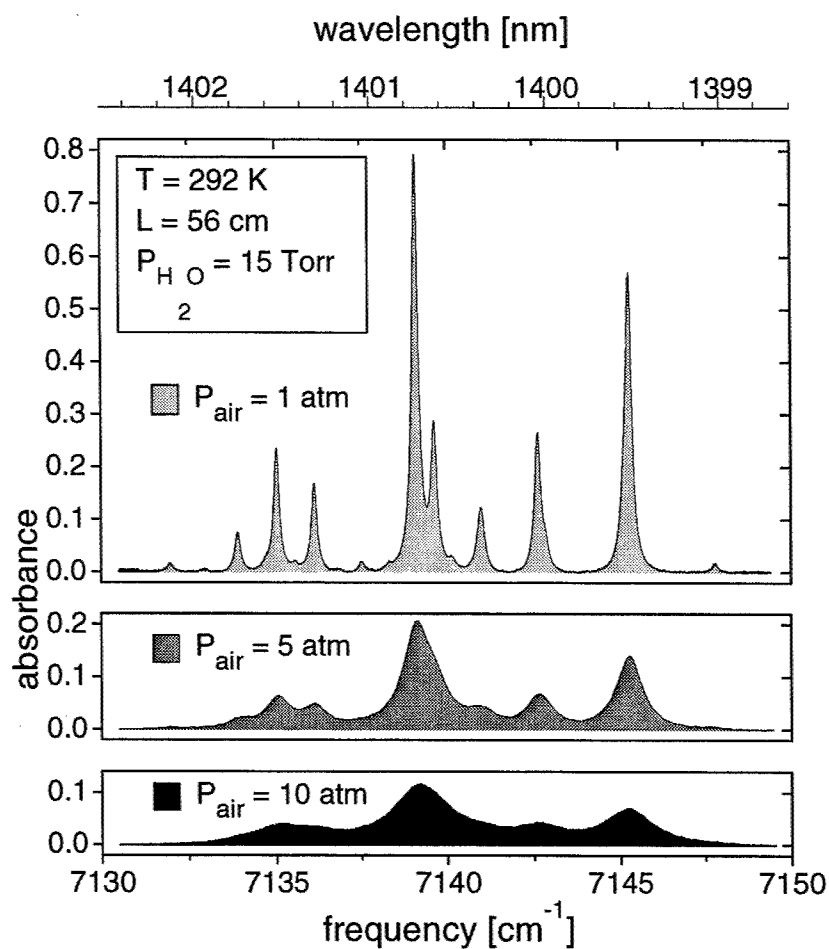
Figure 4. H_2O absorption spectra for total gas pressures of 1-10 atm, each recorded in 1 ms using the rapid temperature-tuning technique.

Low cost, low power diode laser sensing: A weather balloon hygrometer

Mark E. Paige
Southwest Sciences, Inc., 1570 Pacheco St. Suite E-11, Santa Fe, NM 87505
(505)984-1322, Fax 988-9230, mpaige@swsciences.com

Abstract: An inexpensive diode laser hygrometer is described. The engineering advances of this system greatly increase the applicability of diode laser sensors for commercial sensing applications.

OCIS codes: (300.6260) spectroscopy, diode laser, (010.3920) atmospheric and ocean optics, meteorology

The major problem in commercializing diode laser sensors is the high cost associated with them. Diode laser instruments typically retail for much greater than $10,000. This pricing is not competitive with other sensing technologies. To make diode laser sensing a viable commercial technique, the cost must be lowered dramatically. Lower cost lasers are required and further engineering of the diode laser systems is needed to make the associated electronics inexpensive, compact, and low power. The sensor described here represents a major step toward these goals.

This sensor is a diode laser based system for measuring water vapor aboard weather balloons. An accurate knowledge of water vapor content in the atmosphere is fundamental to weather modeling and is important for assessing aviation conditions. Although remote methods such as Doppler radar and satellite imaging provide useful data, the most accurate data comes from local point measurements performed on weather balloons. Thus, weather balloon measurements remain the standard method for determining the accuracy of other methods. The standard techniques used to measure water vapor on weather balloons, hygristors and capacitive sensors, have shortcomings. Problems with these methods include lack of needed sensitivity, inadequate time response at low temperatures, hysterisis, contamination and unreliable calibration. Prior work has shown that diode laser systems are among the most sensitive, rapid and reliable instruments for making water vapor measurements. Water vapor concentrations as low as 0.5 ppb have been measured with these systems. Time response well below 1 sec is possible. These systems are highly selective to water vapor and display no hysterisis. For these reasons, prototype diode laser water vapor sensors have been used to make ground and aerial meteorological measurements.

However, no diode laser system has been developed which is close to meeting the extensive engineering challenges associated with commercial weather balloon sensing. These challenges include low cost, low power consumption, light weight, and the ability to function over a severe range of atmospheric conditions (pressure and temperature as low as 40 Torr and -60°C respectively). The diode laser sensor described in this paper meets all of the engineering challenges of weather balloon sensing except cost. The component cost of the system in bulk quantity is $200. Current weather balloon sensors retail for $100. However, this system represents a dramatic reduction in the cost associated with a diode laser sensor. The key components of this system are a low cost vertical cavity laser (VCSEL) and a DSP based electronics system. The sensor measures water vapor absorption in the 940 nm band. Wavelength modulation spectroscopy and a multipass cell are employed to obtain the necessary sensitivity. The system consumes less than 0.5 W of power and weighs 8 oz (including batteries).

The single mode VCSEL used in this sensor requires only 10 mW of power and costs about $1/device at the wafer level. It has a single mode current tuning range of 40 cm^{-1} and a round beam profile with an angular divergence of 10°. The electronics system fits on a 13 x 16 cm board. The optical system is mounted directly on the electronics board. The optical mounts are made of plastic. The open air multipass cell has a basepath of 6.3 cm and provides 31 passes of the beam. This cell is configured as a folded Herriott cell with one spherical mirror and one flat mirror. The second harmonic wavelength modulation signals from two photodiodes are measured. One photodiode monitors the common mode noise from the laser. The other photodiode measures the water vapor optical absorption after the beam has been multipassed in the optical cell. Entire spectra are recorded at a 1 kHz rate. The laser is modulated at 250 kHz. The spectra are averaged for 1 second and fit using singular value decomposition. An empirically measured reference

spectrum, the common mode spectrum, and a dc offset are used as the fitting basis functions. The system CPU is a DSP chip capable of performing 100 MIPS. This chip costs $5 and consumes 150 mW of power. The powerful abilities of this chip keep the data collection duty factor at 90% while it controls system functions and performs data analysis. The water vapor concentration and ambient temperature and pressure are transmitted via a serial line once per fitting cycle. Laser modulation depth and current scan width are automatically adjusted in response to ambient conditions. The signal gain is also automatically adjusted to keep the spectrum at a constant amplitude. Thus, the only noticeable changes in the signal as concentration and ambient conditions vary are the amount of noise in the spectrum. The system is powered by two AA Li and one ½ AA Li batteries. These batteries will operate the system for several hours in the conditions encountered during a balloon flight (temperatures as low as -60°C).

Further reductions in the cost and complexity of the diode laser hygrometer should soon be possible. Recently, VCSELs in the 1.3 - 1.6 μm wavelength range have been developed. These lasers are expected to be commercially available in the near future. Water absorption bands in this wavelength region are 30 times stronger than at 940 nm. With VCSELs at appropriate wavelengths in this range, the multipass cell could be eliminated. For a mass produced sensor, elimination of the multipass cell reduces parts costs and is essential to lowering production costs associated with performing complex beam alignment

While the cost of this system described here is still too high to replace current commercial weather balloon hygrometers, the engineering advances, including the vast cost reduction and the increased portability, will lead to other commercial opportunities for performing diode laser sensing. Such opportunities include monitoring for commercial processes and environmental and combustion assessment. The sensor developed in this work demonstrates that a diode laser based sensor can retail at a price well below $10,000. At this pricing level, diode laser sensors can sucessfully compete with other commercial sensing technology.

References

1) D.C. Hovde, J.T. Hodges, G.E. Scace, and J.A. Silver, Appl. Opt. **40**, 829 (2001).
2) J.A. Silver and D.C. Hovde, J. Atmos. Oceanic Technol. **15**, 29 (1998).

A Near-IR TDL-based Sensor
for Eddy Covariance Flux Measurements of CO_2

David Sonnenfroh and Mark Allen
Physical Sciences Inc., 20 New England Business Center, Andover, MA 01810
978.689.0003 phone, 978.689.3232 fax, sonnenfroh@psicorp.com

Gerry Livingston
School of Natural Resources, University of Vermont, Burlington, VT 05405
802.656.3092 phone, 802.656.2623 fax, glivings@nature.snr.uvm.edu

Abstract: We describe some of the design considerations for a near-IR TDL-based sensor for eddy covariance flux measurements of CO_2 and H_2O. Initial data from recent field trials will be discussed.
©2000 Optical Society of America
OCIS codes: (010.1120) Air pollution monitoring, (010.1280) Atmospheric composition, (120.6200) Spectrometers and spectroscopic instruments, (300.6260) Spectroscopy, diode lasers.

1. Introduction

As the burden of CO_2 in the atmosphere increases, prediction of global climate change is predicated on a detailed understanding of the exchanges of greenhouse gases with the terrestrial ecosystem and with the hydrosphere. High quality measurements of trace gas fluxes help to quantify changes in the carbon cycle occurring in the terrestrial biosphere. These measurements are needed in studies of the biodiversity of ecosystems, their response to changing environmental parameters, and their feedbacks to the processes involved in global climate change. New sensors are needed to make these flux measurements with high precision. We are currently field-testing a prototype of this next generation sensor.

Our sensor is based on robust, near-infrared diode laser optical technology coupled with high sensitivity detection techniques. Our TDL sensor makes high precision measurements of CO_2 and H_2O fluxes via optical absorption using the eddy covariance technique. The eddy covariance technique is based on the premise that vertical flux densities between the surface and the atmosphere are proportional to the mean covariance between vertical velocity (w') and concentration (c') fluctuations [1-3]. By combining a near-IR diode laser absorption spectrometer with an *in situ*, open-air probe, our flux sensor represents an improvement over existing extractive sampling instruments and offers some new measurement capabilities. The open path air probe bypasses concerns inherent with extractive sampling including loss of high frequency eddy components, as well as wall losses. The high spectral selectivity provided by the near-IR diode laser enables monitoring isotope fractionation; for example, both $^{12}CO_2$ and $^{13}CO_2$ can be measured for source apportionment.

2. TDL Field Sensor Description

The prototype field sensor is a 3-channel instrument that simultaneously measures $^{12}CO_2$, $^{12}CO_2$, and H_2O. A separate laser is used for each species. The sensor consists of a sensor processor module (SPM) and a remote, tower-mounted sensor array, including an open path air probe for each species concentration measurement, a sonic anemometer, and a fast response barometer, as illustrated in Figure 1. The SPM houses the single board system computer, data acquisition electronics, the lasers and their control electronics, ancillary power supplies, and the detection circuitry. The SPM has a footprint of 37 x 45 x 54 cm, a weight of 25 kg, and requires < 200 W power.

The *in situ* air probe is an open path, multipass cell that provides an optical path sufficient for good precision in a physically compact footprint. The laser sensor currently uses two probes. The first cell has an optical path of nominally 1 m to measure $^{12}CO_2$ while the second has an optical path of nominally 100 m to measure $^{13}CO_2$. The cell mirrors are supported by an open frame of four rods so that air currents can pass through the cell unperturbed. The laser beam is launched into the cell using a fiber-coupled collimator. It exits via a slot in the far mirror and impinges on a large area, extended response InGaAs photodiode. This cylindrically shaped probe is oriented vertically to sample all wind directions equally. The air probe is small enough so it does not undersample high frequency flux components and does not perturb the local airflow.
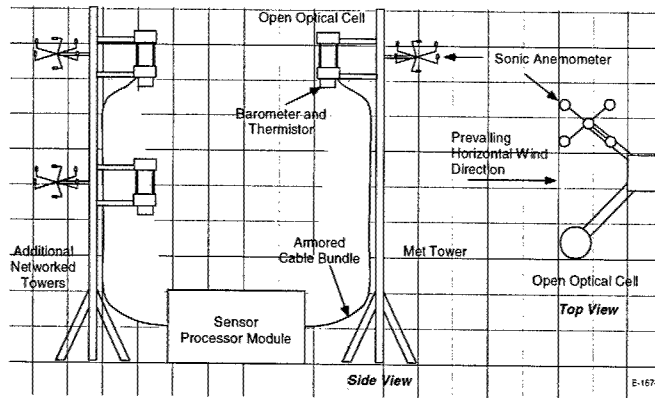
Fig. 1.   General schematic of tdl flux sensor deployment.

Wind speeds were monitored using a 3 axis sonic anemometer. This sensor provides 3 wind vector components and the calculated air temperature at 10 Hz. We also used a fast barometer for converting measured number densities to mixing ratios.

3. Initial Field Trials

For our initial work, we monitored $^{12}CO_2$ using the R32 transition of the $2v_1 + v_3$ combination band near 4999.5 cm^{-1} (2.000 μm). We monitored H_2O using the (6 6 0 – 6 6 1) transition of the $v_1 + v_3$ combination band near 7185.6 cm^{-1} (1.392 μm). $^{12}CO_2$ was monitored using the small cell set up for an optical path of 2.25 m. H_2O was monitored using the large cell with a single pass of 0.5 m. Each laser was scanned across the relevant absorption feature by modulating the laser injection current at 500 Hz. We used the balanced ratiometric detection technique to enhance our precision via its noise quieting capabilities [4]. The output of the balanced ratiometric detection was averaged over 50 scans, and the output recorded at 10 Hz. Initial characterization revealed a sensitivity of 0.3 ppmv for $^{12}CO_2$ and 20 ppmv for H_2O.

The sensor underwent its first field trials this past summer (6-17 August, 2001) at the University of Vermont Proctor Maple Research Center (PMRC) in Underhill Center, VT. These trials served to shakedown the laser sensor and intercompare it with an NDIR sensor for CO_2 as we observed forest respiration above the canopy. The site's research laboratory served as the base of operations for the trials. Our field trials were conducted at a small monitoring station located 300 ft to the NE of the lab. The station consists of a small, 5 x 10 ft instrument trailer and a 25 m tall, 4x6 ft cross section meteorological tower. The trailer provided a controlled environment for the SPM. We mounted our sensor array off the SE corner of the tower on a retractable boom, as illustrated in Figure 2. The array consisted of the two open path cells for the laser sensor, the sonic anemometer, and the sensor head for the NDIR instrument. In the extended position, the boom places the array 6 ft from the tower into the prevailing wind. The sensors are spaced by ~1 ft on a cross bar at the end of the boom. We estimate that the footprint of our sensor is on the order of 10^3 m^2; that is our fluxes are spatially integrated over this area.
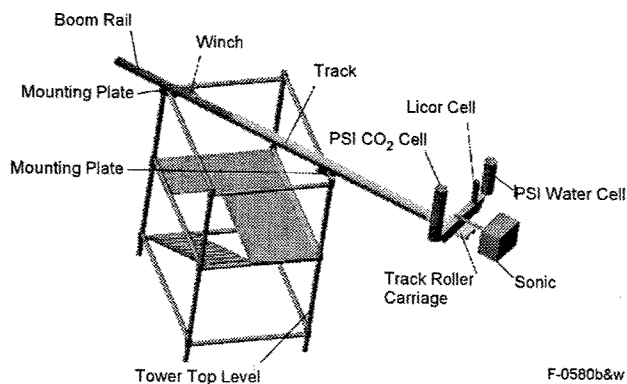
Fig. 2.   Sensor array deployed on retractable boom at PMRC tower site.

The SPM collected raw data from the sensor array and stored it for post processing. We logged 8 channels of almost continuous 10 Hz data over 8 hours for 3 days during the trials. An illustrative example of preliminary data 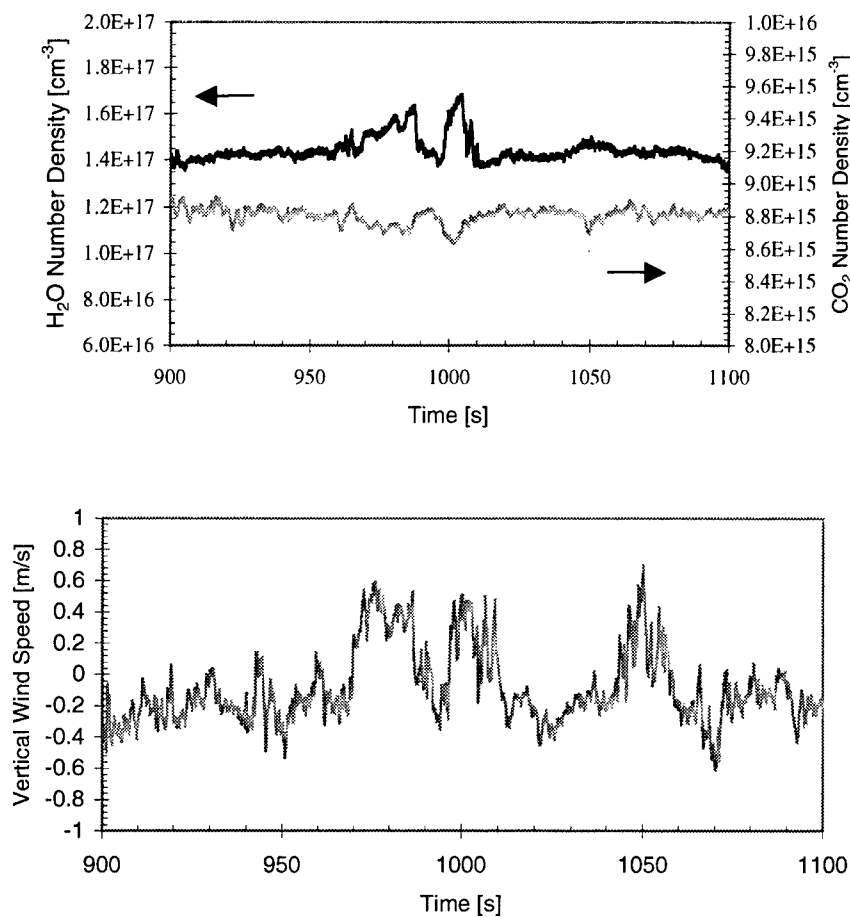taken on 15 August (start time 10:57 am local) is presented in Figure 3. The top panel shows $^{12}CO_2$ and H_2O number densities measured by the tdl laser sensor. The bottom panel shows the vertical wind component measured by the sonic anemometer. Near 1000 s, an air parcel depleted in CO_2 but enhanced in H_2O is observed moving upward past the sensor. Post processing of the raw data is ongoing and includes calculating fluxes for 4 quantities: $^{12}CO_2$ and H_2O from the laser sensor, and CO_2 and H_2O from the NDIR sensor. Thirty-minute averages for each of the 8 hour daily data sets will be calculated. We plan on continued field measurements at the site in the Spring of 2002 when we will also measure $^{13}CO_2$.

Fig. 3.   The top panel shows $^{12}CO_2$ and H_2O number densities measured by the tdl laser sensor. The bottom panel shows the vertical wind component measured by the sonic anemometer.

4. References

1.   M.L. Goulden, et al., "Measurements of carbon sequestration by long-term eddy covariance: Methods and a critical evaluation of accuracy," *Global Change Biol.*. 2, 169-182, 1996.

2.   R.T. McMillen, "An eddy correlation technique with extended applicability to non-simple terrain," *Boundary Layer Meteorol.*, 43, 231-245, 1988.

3.   D.D. Baldocchi, B.B. Hicks, and T.P. Meyers, "Measuring biosphere-atmosphere exchanges of biologically related gases with micrometeorological methods," *Ecology*, 69, 1,331-1,340, 1988.

4.   M.G. Allen, K.L. Carleton, S.J. Davis, W.J. Kessler, C.E. Otis, D.A. Palombo, and D.M. Sonnenfroh, "Ultra-sensitive dual-beam absorption and gain spectroscopy: Applications for near-ir and visible diode laser sensors," *Appl. Opt.*, 34, 3240, 1995.

External cavity diode laser
based on a transmission grating

<u>Toni Laurila</u>, Timo Joutsenoja, Rolf Hernberg, and Markku Kuittinen*

Tampere University of Technology
Institute of Physics
Optics Laboratory
P.O. 692, FIN-33101 Tampere Finland
Email: toni.laurila@tut.fi

*University of Joensuu
Department of Physics
P.O. 111, FIN-80101 Joensuu, Finland

Abstract : Design and characterization of an external cavity diode laser at 650 nm based on a transmission grating is described. The transmission grating enables compact design and removes the beam direction variation during the wavelength tuning.

In recent years strong advances have taken place in room-temperature visible and near-IR diode lasers. These lasers have been applied as light sources for telecommunication, high-speed computer networks and optical data storage, for example. A very promising area is the use of diode lasers as light sources for spectroscopic applications. The small size and high operability, as well as fiber-optic compatibility, of diode lasers is paving way for a new generation of compact, portable and relatively inexpensive sensors for temperature, velocity, pressure, mass flux and chemical species detection [1]. Therefore there is a growing interest in the development of measurement instruments based on the diode laser technology.

The properties of diode lasers are, in general, not good enough for high precision optical spectroscopy. Large linewidth, poor tunability and operation in multiple longitudinal and transverse modes restrict the use of common Fabry-Perot diode lasers in spectroscopy. There are single-mode diode lasers, e.g. distributed feedback lasers and vertical-cavity surface-emitting lasers, which have good enough properties for high resolution spectroscopy but the covered wavelength range is quite modest. The properties of Fabry-Perot diode lasers can be improved by constructing an external-cavity to provide a dispersive optical feedback for the diode laser. External cavity diode lasers (ECDL) can provide large tuning ranges, typically tens of nm, and narrow linewidths down to a few kHz.

The objective of the present work was to design and characterize an ECDL at 650 nm based on a transmission type diffraction grating that is suitable for enhanced frequency doubling. The frequency doubled output (325 nm) will be used for measurement of atomic resonance line of copper.

A schematic drawing of the ECDL is shown in Fig. 1. A single-transverse mode GaInP-AlGaInP diode laser [2] at 650 nm is used in an external cavity in which the transmission diffraction grating is used as the dispersive element [3]. The output facet of the diode laser is antireflection coated. The transmission diffraction grating is made with electron beam lithography and reactive ion etching and it is fabricated onto a SiO_2 substrate. The grating is coated with TiO_2 to enhance the reflection and the output surface is antireflection coated to minimize the unwanted reflections back to the laser. Diffraction efficiency of 15-20 % is achieved into the reflected -1 order and only a few per cent of the light power is lost into higher diffraction orders.
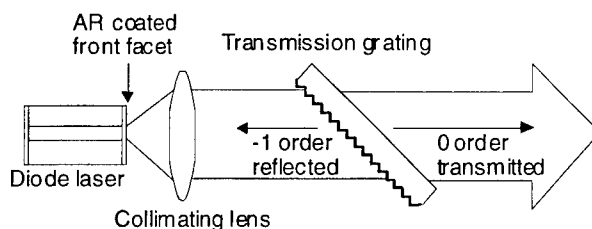
Fig.1. Schematic of the external cavity diode laser

The optical cavity length is 20 mm corresponding to a free spectral range of 7.5 GHz. The wavelength can be coarsely tuned by adjusting the grating angle mechanically with fine pitched adjustment screws. The coarse wavelength tuning range is ± 6 nm around the center wavelength 646 nm. The fine tuning is done with symmetrically aligned piezo stacks which are controlled by a personal computer and a 16-bit D/A card. The laser output is demonstrated to be mode-hop free tunable over 20 GHz (28 pm) with the grating angle tuning only. Tunable, true single-mode output power of over 20 mW is obtained at 650 nm.

The use of a transmission grating in ECDL prevents the beam direction variation as the wavelength is tuned by changing the grating angle. This is a very important property in applications where the ECDL output beam is directed into another external resonance cavity, e.g. the enhancement cavity in frequency doubling.

The emission characteristics of the diode laser prior to the external cavity configuration and of the ECDL are shown in Fig. 2. It can be seen clearly how the multi-mode structure of the Fabry-Perot diode laser is turned into a single-mode emission line of the ECDL. The side-mode suppression ratio is over 40 dB.
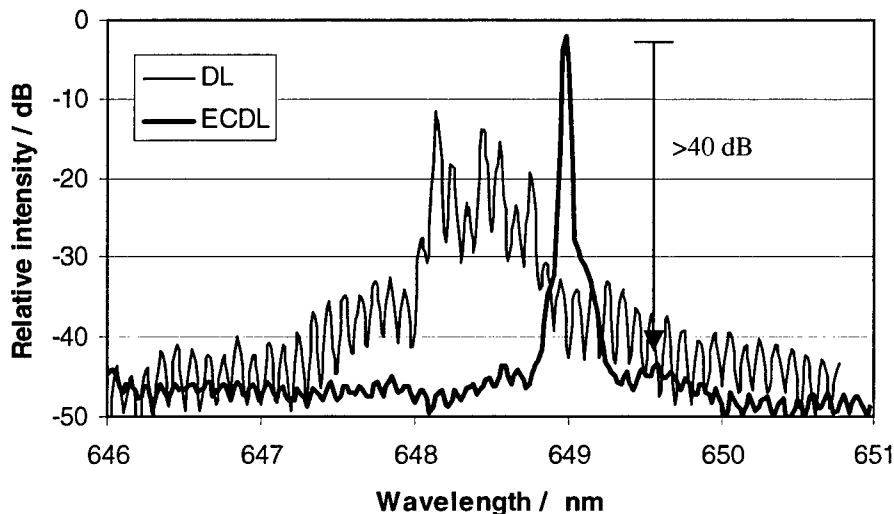
Fig. 2. Emission profiles of the original diode laser and the external cavity diode laser.

The linewidths in Fig. 2. are limited by the optical spectrum analyzer used in the measurements. Theoretical calculations based on the modified Schawlow-Townes formula give a laser linewidth of a few tens of kHz. Such a narrow linewidth has been experimentally observed in a transmission type ECDL [3].

The present ECDL design provides a compact light source for high resolution spectroscopy. The results obtained show that the transmission type grating is very competitive as compared to the reflection type gratings. The design and fabrication of a transmission grating offers many degrees of freedom that can be tailored for a specific application. The ECDL based on a transmission grating is especially well suited for applications in which the output beam must not vary as the wavelength is tuned by adjusting the grating angle.

References

[1] M. G. Allen, Meas. Sci. Technol. 9 (1998) 545-562
[2] J. Köngäs et al., IEEE Photonics Tech. Lett. 10/11 (1998) 1533-1535
[3] M. Merimaa et al., Optics Communications 174 (2000) 175-180

Key to Authors and Presiders

— A —
Allen, Mark G. — ThD, FC3, SaB5, SuB4
Anglos, D. — FA5
Armstrong, Karla M. — SuA4
Awtry, A.R. — FD1

— B —
Baer, Douglas S. — FD3, SaB
Baghdassarian, Ohan — SuA5
Bambha, R.P. — SuA3
Barnes, Michael D. — ThA, ThA3
Bartko, A. — ThA3
Bessler, Wolfgang G. — FB4, FC1
Bhargava, R. — ThA3
Birtola, Sal — SuA4
Bisson, Scott E. — ThC2
Bockhorn, H. — ThB4
Bohling, Christian — SaB4
Brockhinke, Andreas — ThC, FB2, SaC6
Bruno, Alfredo E. — SaA
Buelter, A. — FB2

— C —
Cadwell, L. — FA2
Capasso, Federico — FC3, SaB5
Chen, Shin-Juh — FB3
Cho, Alfred Y. — SaB5

— D —
Dahm, Werner J.A. — FB3
Davidson, David F. — FC2
Dickson, R.M. — ThA3
Dreyer, Christopher B. — ThB2
Driscoll, James F. — SaC1

— E —
Ebert, Volker — ThB3
Erdelyi, Miklos — ThD3

— F —
Farrow, R.L. — SaC1
Feldmann, L. — SaA5
Fernholz, Thomas — ThB3
Fetzer, Gregory J. — SaA2
Fink, Manfred — ThC4
Franzke, J. — SaB1
Fredricksen, C.J. — ThD1
Fried, Alan — ThD3

— G —
Gmachl, Claire F. — FC3, SaB5
Goers, Uta-Barbara — SuA4
Goldberg, Lew — SuA4
Grego, Joe — ThC3, SaC4
Gronki, Joachim — FC1, FC2

Gupta, Manish — FD3
Gupta, R. — ThD2

— H —
Hahn, Jae Won — FB, FC, FD2, SaC2, SaC3
Hanna, S.F. — ThD4
Hanson, Ronald K. — FB4, FC2, SuB2
Harren, Frans J.M. — ThC2
Hekkert, S. te Lintel — ThC2
Hernberg, Rolf — SuB5
Herzig, Hans Peter — SaA1
Hildebrandt, Lars — SuB1
Hofmann, Max — FC1
Hovde, Chris — SaB2
Hult, Johan — ThB1
Hunter, Amy J.R. — FA4
Hutchison, K. — FA2
Huwel, Lutz — FA2

— J —
Jakubowski, N. — SaA5
Jander, Helga — FC1
Janunts, E. — ThA4
Jeffers, Jim — ThC3, SaC4
Jeffries, Jay B. — FB4, FC2, SuB2
Joutsenoja, Timo — SuB5
Jungfleisch, B. — ThB4

— K —
Kaminski, Clemens — ThB, ThD4, SaC5
Killinger, Dennis K. — SuA2
Kim, Bongsoo — SaC2
Kliner, Dahv A.V. — SuA4
Knispel, Richard — SuB1
Koch, Jon D. — FC2, SaA5
Kohler, Rudeger — SaB5
Koplow, Jeffrey P. — SuA4
Kosterev, Anatoliy A. — SaB5
Kostjucenko, Irina — SaB4
Kubitzki, M. — FA2
Kuittinen, Markku — SuB5
Kulp, T.J. — SuA3, SuA4
Kunze, K. — SaB1

— L —
Lalayan, Asatur Alexander — ThA4
Laurila, Toni K. — SuB5
LeCaptain, Dale — ThA2
Lee, Dong-Hoon — SaC2
Lee, Jae Yong — FD2, SaC2, SaC3
Lee, Tonghun — FB4
Lehre, Thilo — ThB4
Lenhard, U. — FB2
Linne, Mark A. — ThB2, FD, FE, SaA3
Livingston, Gerry — SuB4

Optical Society of America

**Laser Applications to Chemical and
Environmental Analysis
Topical Meeting
February 7-10, 2002**

Postdeadline
Papers

**Millennium Hotel
Boulder, CO**

Laser Applications to Chemical and Environmental Analysis
POSTDEADLINE PAPERS

February 7-10, 2002
Boulder, CO

Oral Presentation
Thursday, February 07
2:00pm – 2:20pm

PD5 **Diode-laser-based ultraviolet absorption sensor for NO,** *Sherif F. Hanna, Rodolfo Barron-Jimenez, Thomas N. Anderson, Robert Lucht, Thomas Walther, Jerald A. Caton, Texas A&M Univ., USA.* A new laser sensor for absorption measurement ofNO has been developed based on sum-frequency-mixing of a 395-nm ECDL and a frequency-doubled cw Nd:YAG laser in BBO to produce tunable 226.8 nm radiation.

Poster Presentations
Saturday, February 9
7:00pm – 9:00pm

PD1 **Characterization of mechanical modification of anchored surfactants using sum-frequency generation,** *T. E. Furtak, Colorado School of Mines, USA; B. C. Chow, Corning Inc., USA.* We have used optical sum-frequency generation to reveal the structure and orientation of organic monolayers self assembled on dielectric surfaces. We studied the influence of mechanical modification, as occurs with rubbed display windows and model lubricants.

PD2 **Characterization of surfaces using reflectance and optical rotation measurement methods,** *O. Prakash, Mohan Lal, Natl. Physical Lab., India.* In order to characterize new materials being exploited for development of newer devices, in some of the cases, the materials are prepared in the form of thin films or wafers. In order to characterize thin films or wafers of the materials, a simple method has been deviced. In this method reflectance of the samples is measured at nearly normal incidence on a homemade reflectometer. Also the optical rotation of incident light beam on reflection from the sample at nearly 45° is measured on a homemade polarimeter. With the help of a graph drawn between reflectance and optical rotation, if value of reflectance of a sample can be measured, the value of its optical rotation can be approximated and vice-versa. The main advantage of the method is that the samples of diffused nature whose reflectance cannot be measured, it can be characterized with the polarimeter. The methods are non-destructive.

PD3 **Energy transfer processes in OH and CH revealed by time-resolved LIF and numerical simulations,** *A. Brockhinke, A. Bülter, U. Lenhard, U. Rahmann, K. Kohse-Höinghaus, Univ. Bielefeld, Germany.* A picosecond laser system is used

to study energy transfer process in OH and Ch in atmospheric-pressure flames. Using these measurements, a numerical code for the simulation of spectra affected by RET and VET is developed. Different methods to obtain quench-free results are suggested.

PD4 **Studies of vortex-induced flame extinction in counterflow diffusion flames using CH PLIF and PIV,** *A. Lemaire, K. Zähringer, J.C. Rolon, Ecole Centrale Paris, Paris; T.R. Meyer, Innovative Scientific Solutions, Inc., USA; J.R. Gord, Air Force Res. Lab., USA.* The interaction between a laminar non premixed flame and a vortex is examined. The CH radical layer produced by the flame is imaged, for the first time in this configuration, using planar laser induced fluorescence (PLIF). Simultaneous particle-imange velocimetry (PIV) measurements gives flowfield data. The methane-air flame is supported in a nonpremixed opposed-jet burner. In this work, the extinction processes occurred during the interaction is analyzed. Also, in the experiments, it appear that PAH fluorescence strongly perturb CH LIF measurements. To clarify this, the effects of equivalence ratio, droplet seeding and laser energies on CH vs. PAH fluorescence are studied.

PD6 **Simultaneous PLIF and stereo PIV measurements of a turbulent non-premixed flame,** *A.P. Harvey, J. Hult, Univ. of Lund, Sweden; C.F Kaminski, P. Stonestreet, Univ. of Cambridge, UK.* Stereo PIV and time sequenced PLIF were performed simultaneously on the TECFLAM turbulent, non-premixed international reference flame to investigate local flame extinction phenomena. The results show, for the first time, effects due to the out-of-plane component of the velocity.

PD7 **Application of Angle-Dependent Light Scattering and Fractal Dimension Analysis for Detection and Characterization of Biopolymers,** *J. Houston Miller, Glauco R. Souza, Carly Levin, Emily Barter, George Washington Univ., USA.* In this presentation, we demonstrate the application of angle dependent light scattering combined with fractal dimension analysis (ADLS/FD) to detect the hybridization of Au-DNA nanoparticles to oligonucleotides of complementary sequence.

Characterization of mechanical modification of anchored surfactants using sum-frequency generation

T. E. Furtak[a] and B. C. Chow[b]

[a]Physics Department, Colorado School of Mines, Golden, Colorado 80401
[b]Center for Fiber Optics Testing, Corning Incorporated, Corning, NY 14831

ABSTRACT

We have used optical sum-frequency generation to reveal the structure and orientation of organic monolayers self-assembled on dielectric surfaces. We studied the influence of mechanical modification, as occurs with rubbed display windows and model lubricants.

INTRODUCTION

Liquid crystal optoelectronic technology relies upon some mechanism to align the liquid crystal molecules parallel to the surfaces of the device.[1] In display manufacturing a thin polymer coating is mechanically buffed with a cloth to induce a preferential direction parallel to the windows of the cell. In advanced schemes, a much thinner alignment layer is desirable. Long-chain surfactants offer promise in this capacity.

The purpose of our continuing investigation of simple self-assembled monolayers is to reveal the changes, both dramatic and subtle, that can be imposed by mechanical. Our work is related not only to alignment applications but also to lubrication phenomena and durability of chemically modified surfaces. Our agenda is to directly observe the modified layer with special techniques that reveal the nature of the modification. This is in contrast to other approaches in which anchoring tendencies are explored by exposing the modified surface to liquid crystals in monolayer or bulk form. Our primary tool is vibrationally resonant optical sum frequency generation (SFG).

EXPERIMENTAL PROCEDURES

Octadecylsiloxane (ODS) molecular layers were grown by self-assembly from solution. The final product is a crosslinked buckled siloxane sheet on the surface with eighteen-unit hydrocarbon chains attached to the silicon atoms. This leads to a high density of nearly parallel chains with methyl groups at the outer surface. In our preparation method we use an octadecyltriethoxysilane (OTES) precursor, rather than the more commonly employed octadecyltrichlorosilane (OTCS) molecule. The reaction with OTCS proceeds much more rapidly and is prone to initiate while in the bulk solution. This leads to the adsorption of three-dimensional clusters on the surface and an associated poorly organized monolayer. By contrast, the OTES route is characterized by slower kinetics that can be more readily controlled.[2]

For the mechanical buffing treatment we used a microcloth (such as is used to clean a photographic lens) "slapping" machine consisting of 2-cm flaps attached to a 2-cm-diameter spinning cylinder. The flaps were allowed to gently impact with the surface. Independent testing revealed that this treatment was equivalent to a contact force of 13 mN for a distance of 250 m.

We combine two high intensity pulsed laser beams on the sample surface.[3] A small amount of the incident energy is converted to coherent outgoing light with a frequency that is the sum of those in the two incident beams. Dipole induced SFG exploits the symmetry restrictions of second order nonlinear optical phenomena. The effect is forbidden if the probed material possesses a center of inversion. This is the case for glass, as well as for any other disordered medium. At the surface, however, the symmetry is lower due to the presence of the boundary. So molecules adsorbed on a surface are preferentially detected.

By scanning the frequency of the IR beam while recording the SFG intensity one can generate a vibrational spectrum that characterizes the molecules at the surface. Finally, by careful selection of the incoming and detected optical polarizations we can sample certain combinations of the nonlinear susceptibility. This information can be used to identify the orientation of the molecular group that is giving rise to the vibrational resonance.[4]

In our SFG spectrometer light from the pulsed YAG laser is frequency doubled to 532 nm. Part of the resulting radiation is sent to a delay line, the rest of it is used to pump a dye laser. The output from the dye laser is converted
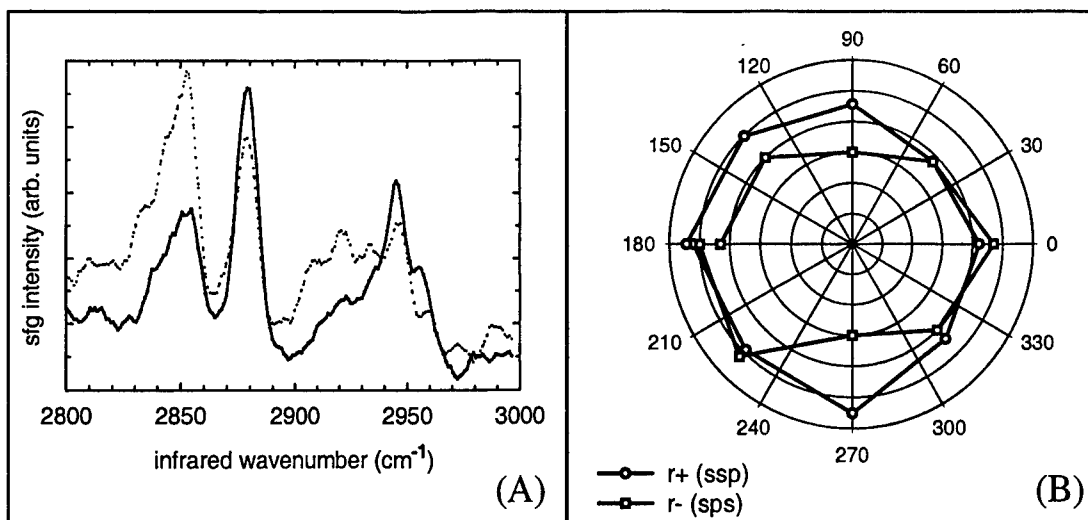
Figure 1. (A) SFG spectra from ODS on glass using the polarization combination of ssp. (dotted) as grown. (solid) after gentle buffing. (B) Polar plot displaying the result of the sample rotation experiments on buffed ODS on glass. The azimuthal angle is the orientation of the buffing direction with respect to the projection of the SFG wavevector in the sample. (circle/dotted) SFG intensity for the r^+ mode with an ssp polarization combination. (square/solid) SFG intensity for the r^- mode with an sps polarization combination.

to coherent IR by a third-order stimulated Raman effect. The tunable IR is mixed with the 532 nm visible light after the polarizations of both beams are defined with suitable optical elements. The SFG radiation is polarization filtered then spatially and spectrally selected before being sent photomultiplier detector.

RESULTS AND DISCUSSION

Figure 1(A) illustrates the main characteristics of SFG spectra from ODS monolayers. This particular monolayer was incomplete, so the effect of buffing is pronounced. The data show two narrow bands at 2880 cm^{-1} and 2945 cm^{-1}. These are both associated with the symmetric stretch vibration of the terminal methyl group, designated r^+. Additional modes are seen at 2850 cm^{-1} and 2920^{-1}. These come from methylene vibrations within the chain (d^+ and d^-, respectively). On a perfectly straight all-trans chain there is a center of inversion symmetry at the middle of each C-C bond. Under these conditions the methylene modes are SFG silent. However, if the chain is bent as occurs through gauche defects, the inversion symmetry is broken. Then the d modes show up. Less evident in Fig. 1(A) is the asymmetric stretch vibration of the methyl group (r^-), which appears as a shoulder at 2690 cm^{-1}. In other polarization combinations (sps) this feature is more easily distinguished.

In Fig. 1(A) we see the influence of buffing on a defective monolayer. In the as-grown condition we see significant intensity coming from the gauche conformations. After buffing the strength of the terminal methyl vibration increases while that associated with the methylene vibrations is reduced.

The orientation distribution of the terminal methyl group can be determined through a sample rotation experiment. This is illustrated in Fig. 1(B). At an azimuth of zero the buffing direction is in the optical plane. At 90° the buffing direction is perpendicular to the optical plane. The most prominent variation is observed in the r^- mode, which exhibits mirror symmetry with no particular preference for the direction of buffing.

To obtain more quantitative information from these results we assume that the methyl group can adopt any orientation about the terminal C-C bond and that for all molecules the direction of that bond is tilted with respect to the surface normal by the same amount. We model the distribution of the direction (ϕ) of this tilt with a simple

function that is consistent with the observed symmetry of the data, $g(\phi) = \frac{1+d_2\cos(2\phi)}{2\pi}$. We determine the r^- intensity ratio for sps and ssp polarizations with a sample orientation of zero degrees. An independent constraint is the intensity ratio under sps polarization with the sample azimuthal angle at $0°$ and $90°$. These data are consistent with a single pair of parameters in the model distribution function. The methyl tilt angle is $36.1°$ and the anisotropy factor d_2 is 0.42.

From the results of the sample rotation experiment we have learned that the symmetry axis of the terminal methyl group is inclined with respect to the surface normal by an angle that is very close to the angle between the alkane chain axis and the last C-C bond. These facts are consistent with a layer composed of closely packed, nearly vertical chains. The anisotropy factor d_2 shows that the direction of tilt of the terminal methyl groups favor the line of buffing with no preference to the buffing direction. This would be produced if the buffing reduced the fraction of the methyl groups that were perpendicular to the buffing direction. Together with the concept of chain straightening by gauche defect reduction this insight suggests the as-grown film has considerable disorder in the last few links of the hydrocarbon chain. Upon buffing, many of the chains are straightened. Those that were originally tilted orthogonal to the buffing direction are preferentially straightened. A subtle preferred direction in the molecular conformations of the surface may be sufficient to induce weak anisotropic anchoring of liquid crystal molecules in the bulk, and may explain effects of this kind that have been observed with buffed surfactants.

CONCLUSIONS

We have investigated the changes caused by mechanical treatment of well packed self-assembled monolayers of octadecylsiloxane on glass. Mechanical buffing straightens the chains so that they are mostly vertical. However the methyl ends are oriented parallel and antiparallel to the buffing direction.

ACKNOWLEDGMENTS

REFERENCES

1. B. Jerome, *Rep. Prog. Phys* **54**, 391 (1991).
2. C. R. Kessel, and S. Granick, *Langmuir* **7**, 532 (1991).
3. Y. Shen, *Appl. Phys. A* **59**, 541 (1994).
4. J. Lobau, A. Rumphorst, K. Galla, S. Seeger, and K. Wolfrum, *Thin Solid Films* **289**, 272 (1996).

Characterisation of surfaces using reflectance and optical rotation measurement methods

O.Prakash and Mohan Lal

National Physical Laboratory
Dr K.S. Krishnan Road
New Delhi-110012, India.

Abstract:

In order to characterise new materials being exploited for development of newer devices, in some of the cases, the materials are prepared in the form of thin films or wafers. In order to characterise thin films or wafers of the materials, a simple method has been deviced. In this method reflectance of the samples is measured at nearly normal incidence on a home made reflectometer. Also the optical rotation of incident light beam on reflection from the sample at nearly 45 deg. is measured on home made polarimeter. With the help of a graph drawn between reflectance and optical rotation, if value of reflectance of a sample can be measured, the value of its optical rotation can be approximated and vicei-versa. The main advantage of the method is that the samples of diffused nature whose reflectance cannot be measured, it can be characterised with the polarimeter. The methods are non-destructive.

Summary

In the present paper methods of measurement of reflectance and optical rotation on home made reflectometer and polarimeter respectively, have been described. The samples that were tried are(I) glass slide for microscope, (ii) small sized optical flat, (iii) squared shape front coated mirror, (iv) neutral density filter from M/S Ealing, U.K., (v) rectangular shaped front coated mirror, (vi) circular mirror front coated, and (vii) to (x) single crystal silicon wafers, grown, cut and polished at the Materials Division of the Laboratory.

From the curve between reflectance and optical rotation of the samples it is clear that the curve is not linear. Also, the samples having higher reflectance have the optical rotation smaller and vice-versa. This can be explained as follows. The strongly absorbing materials absorb only a small fraction of the incident light and the bigger fraction is reflected or scattered. The smaller fraction of the incident light which actually enters the material is absorbed within a short distance (thichness) below the surface. So, it is not so much effective in rotating the plane of polarisation of the incident light on reflection (optical rotation) upto a great extent, as is the case with the metal coatings. On the other hand, in weakly absorbing materials, such as inks , semiconductors, the major portion of the incident light is transmitted through the surface of the material and may be completely absorbed, if the medium is thick enough. Thus, weakly absorbing sustances effectively act to rotate the plane of polarisation of the incident light as is in the case of glass plate, glass filter etc. With the present study, it is clear that in case of those materials, whose reflectance cannot be measured, the idia of measurement of optical rotation on reflection of the incident light can give a comparative idea about the absorption properties of the samples. That is very useful for preferential treatment of the materials in developing the new devices. The optical rotation is not dependent upon the intensity of the incident beam, so, the measurement of optical rotation for the samples of diffusing nature can also be measured.

Energy transfer processes in OH and CH revealed by time-resolved LIF and numerical simulations

A. Brockhinke, A. Bülter, U. Lenhard, U. Rahmann and K. Kohse-Höinghaus

Physikalische Chemie I, Universität Bielefeld, Universitätsstr. 25, D-33615 Bielefeld, Germany
Fax: +49-521-106-6027, e-mail: brockhinke@pcl.uni-bielefeld.de

Abstract: A picosecond laser system is used to study energy transfer processes in OH and CH in atmospheric-pressure flames. Using these measurements, a numerical code for the simulation of spectra affected by RET and VET is developed. Different methods to obtain quench-free results are suggested.
©2001 Optical Society of America
OCIS codes: (280.1740) Combustion diagnostics; (300.6500) Spectroscopy, time-resolved

1. Introduction

One of the most-frequently used techniques for the detection of minor-species concentration and temperature is Laser-induced Fluorescence (LIF). However, in most cases the natural lifetime of the excited state is much longer than typical collision times (~100 ps in atmospheric pressure flames). Collisions might thus remove a part of the population ('quenching'), decreasing the total fluorescence yield. Moreover, collisions frequently induce other energy transfer processes and populate different states, further complicating the spectrum. These processes depend on the quantum numbers of the state probed, temperature, pressure and the collision partners (i.e. the chemical composition of the flame) and have to be taken into account for quantitative measurements – usually by either measurements in calibration flames or by measuring the gas composition and computing the quenching correction from literature values. Short-pulse spectroscopy offers the possibility to study these processes in detail. Moreover, if LIF is excited with a laser pulse with a duration of less than typical collision times and an appropriate detection system is used, quenching effects can be minimized. Observing the temporal decay of the signal even allows completely 'quench-free' measurements and it allows one to create a database that quantifies these effects.

2. Experimental

A laser system based on a regeneratively amplified Ti:sapphire laser which produces tunable, Fourier-limited pulses of 80 ps duration is used as light source. The output is converted to the UV by a combination of KDP crystals for frequency doubling and tripling and a Raman shifter (10 bar H_2). Pulse energies of up to 3 mJ are obtained for the third harmonic radiation with wavelengths between 250 and 300 nm. LIF signals are collected by a spherical mirror in the usual 90 degrees excitation-detection geometry. After passing a Glan-Thompson polarizer, they are spectrally dispersed by a 275 mm focal length monochromator and then detected by a streak camera. The overall temporal resolution of the complete system (including trigger jitter and broadening effects in the detection optics) is about 120 ps and thus is very well matched to the typical time between collisions in atmospheric pressure flames ($\tau_c \approx 100$ ps). This setup is described in detail elsewhere [3, 4].

3. Energy transfer measurements in OH

For these measurements, only moderate pulse energies (in the order of 100 µJ) and mild focussing of the radiation are employed to avoid saturation effects. Several rotational lines in the OH A-X (2-0) transition are probed. Entrance slits of spectrograph and streak camera are oriented perpendicular to each other. This detection geometry yields two-dimensional spectra; temporal resolution corresponds to the vertical axis and the spectral dispersion corresponds to the horizontal axis.
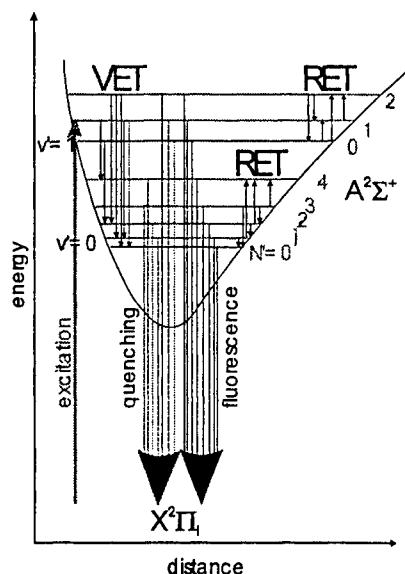
Fig. 1. Energy transfer processes competing with laser-induced fluorescence. VET: vibrational energy transfer, RET: rotational energy transfer.

Figure 1 shows the various energy transfer processes which compete with laser-induced fluorescence. In many cases, quenching is the dominant contribution. However, rotational energy transfer (RET) and vibrational energy transfer (VET) will populate additional levels and complicate the observed fluorescence spectrum. With the simultaneous temporal and spectral resolution of the system used in our investigations, it was possible to study the temporal development of LIF signals. At the time of the exciting laser pulse, LIF signals are dominated by fluorescence from the directly populated level; at later times, the major part of the signal stems from levels populated by RET and VET. This can clearly be seen in Fig 2, which shows a time-integrated fluorescence spectrum after excitation of the OH $Q_1(7)$ line in the A-X (1-0) band. Further analysis allows to determine the time-averaged population after excitation in the OH A (v'=1, J'=13) level. It can be seen, that more than 87% of the total fluorescence originates from levels populated by RET and VET.

4. Summary

Energy transfer processes for OH and CH are studied for several excitation lines using a regeneratively amplified Ti:sapphire laser (80 ps duration, pulse energies of up to 3 mJ in the UV). Signals have been spectrally dispersed by a spectrograph and detected by a streak camera. Comparison of the obtained results with model simulations (LASKIN) show, that typically 80-90% of the time-integrated fluorescence yield stems from levels populated be either rotational or vibrational energy transfer.

5. References

[1] K. Kohse-Höinghaus, "Laser techniques for the quantitative detection of reactive intermediates in combustion systems", Prog. Energy Combust. Sci., **20**, 203-279, (1994)
[2] Proceedings of the Combustion Institute, vol. **28**, (2001)
[3] A. Brockhinke, A. Bülter, J.C. Rolon, K. Kohse-Höinghaus, "ps-LIF measurements of minor species concentration in a counterflow diffusion flame interacting with a vortex", Appl. Phys. B **72**, 491-496, (2001)
[4] A. Brockhinke, W. Kreutner, U. Rahmann, K. Kohse-Höinghaus, T.B. Settersten, M.A. Linne, "Time-, wavelength-, and polarization-resolved measurements of OH ($A^2\Sigma^+$) picosecond laser-induced fluorescence in atmospheric-pressure flames", Appl. Phys. B **69**, 477-485 (1999)
[5] U. Rahmann, W. Kreutner, K. Kohse-Höinghaus, "Rate-equation modeling of single- and multiple-quantum vibrational energy transfer of OH ($A^2\Sigma^+$, v'=0 to 3)," Appl. Phys. B **69**, 61-70 (1999)
[6] A. Brockhinke, K. Kohse-Höinghaus, "Energy transfer in combustion diagnostics: experiment and modeling", Proc. Royal Soc. (Faraday Discussion 119), in press, 2001
[7] R. Kienle, M. P. Lee, K. Kohse-Höinghaus, "A detailed rate equation model for the simulation of energy transfer in OH laser-induced fluorescence," Appl. Phys. B **62**, 583-599 (1996)

Fig 2: Time-integrated fluorescence spectrum after excitation of the OH $Q_1(7)$ line in the A-X (1-0) band. It is evident, that the major part of the visible lines stems from levels populated by RET and VET.
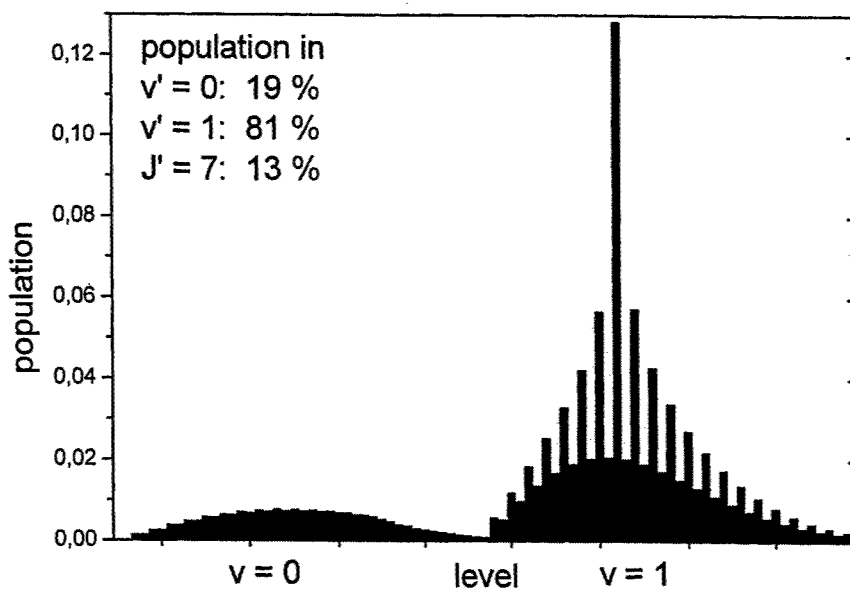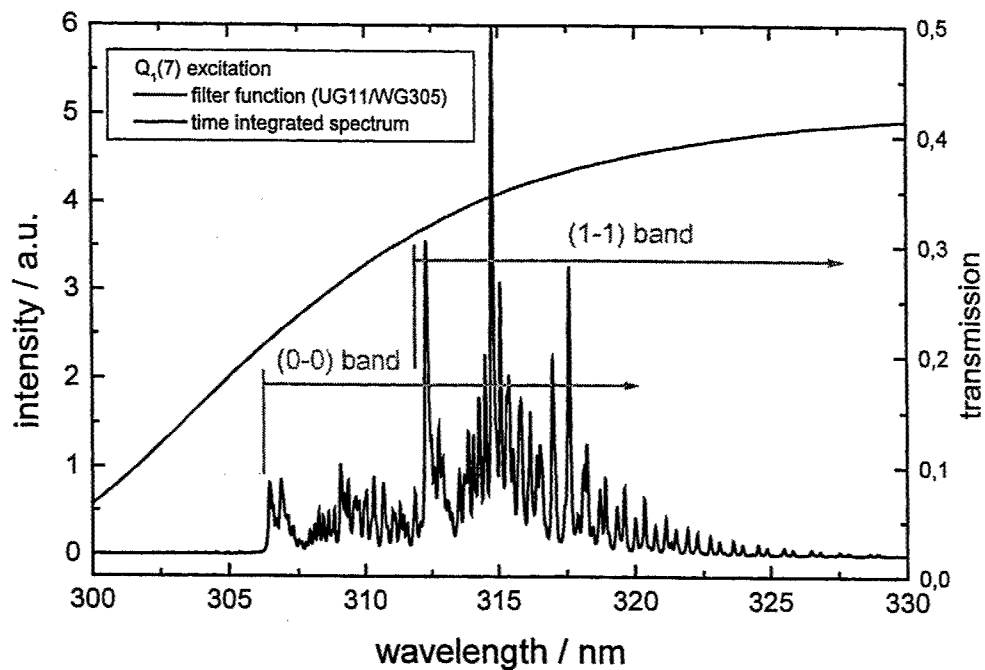

Fig 3: Time-averaged population after excitation in the OH A (v'=1, J'=13) level. This distribution leads to the fluorescence spectrum in Fig. 2. More than 87% of the total fluorescence originates from levels populated by RET and VET.

Studies of Vortex-Induced Flame Extinction
in Couterflow Diffusion Flames Using CH PLIF and PIV

A. Lemaire[1], T. R. Meyer[2,*], K. Zähringer[1], J. R. Gord[3] and J. C. Rolon[1]

[1]École Centrale Paris, Laboratoire d'EM2C
Grande Voie des Vignes, 92295 Chatenay-Malabry Cedex, France

[2]Innovative Scientific Solutions, Inc.
2766 Indian Ripple Road, Dayton, OH 45440, USA

[3]Air Force Research Laboratory, Propulsion Directorate
Wright-Patterson Air Force Base, OH 45433-7103, USA

Abstract

The interaction between a laminar non premixed flame and a vortex is examined. The CH radical layer produced by the flame is imaged, for the first time in this configuration, using planar laser induced fluorescence (PLIF). Simultaneous partcle-imange velocimetry (PIV) measurements gives flowfield data. The methane-air flame is supported in a nonpremixed opposed-jet burner. In this work, the extinction processes occurred during the interaction is analyzed. Also, in the experiments, it appear that PAH fluorescence strongly perturb CH LIF measurements. To clarify this, the effects of equivalence ratio, droplet seeding and laser energies on CH vs. PAH fluorescence are studied.

2 Introduction

The interaction between a vortex and a flat laminar diffusion flame is generally used to simulate a number of features that are common in turbulent combustion, such as dynamic strain, stretch, and curvature[1]. Using well-controlled experiments to verify numerical simulations, phenomena such as flame extinction and micro-vortex-flame behavior have been studied using gaseous fuels [2-4]. These previous studies have shown that the dynamic interaction between a laminar flame and a vortex may be examined by laser induced fluorescence of the hydroxyl (OH) layer produced by the flame. The CH radical is also a good candidate for these dynamic studies, since the concentration distribution constitutes a narrow layer in the flame region. Nevertheless, this concentration of this radical is low, and difficult the fluorescence detection. This may be one of the reasons why the use of CH laser induced fluorescence in the non-premixed vortex flame interaction is not mentioned in the literature. The second difficulties in the detection of CH fluorescence, arise from the short CH fluorescence lifetimes. In a recent work, Renfro et al reported CH-LIF concentration measurements in atmospheric hydrocarbon flames, by using a picosecond laser [5-6]. In particular, they reported CH fluorescence lifetimes of the order of 2-5ns. Finally, the presence of PAH (polycyclid-polyharomatic-hydrocarbon), which fluoresce under the same UV (390 nm) excitation diffucult also the interpretation of CH fluorescence signals. The formation of PAH is typically observed in the rich fuel side of diffusion flames. In this work we show that the fluorescence signals from CH and PAH are separated, and despite these difficulties, they may be correctly analyzed.

The goal of this investigation is to study vortex-flame interactions using a number of laser diagnostic approaches, including particle image velocity (PIV), planar laser-induced fluorescence (PLIF), and planar Mie scattering.

3 Experimental Apparatus and Procedure

The experimental set-up consists of a counterflow burner with air in the upper stream and fuel in the lower stream (Fig. 1). The fuel is composed of methane diluted with nitrogen and seeded with a monodisperse spray of ethanol droplets. The PLIF technique uses CH as the tracer molecule. The laser system is composed of a Nd:YAG laser which second harmonic pump a tunable dye laser (Rhodamine 640). The dye laser beam is frequency-mixed with the Nd:YAG fundamental in order to obtain a wavelength corresponding to the $Q_1(5)$ excitation band of the $B^2\Sigma^+ \Rightarrow X^2\Pi(0,0)$ transition at 389.6 nm. The laser system gives pulses of about 7 ns duration, with a energy mean value of approximately 20 mJ. The sheet forming optics provides a laser sheet of 13.5 mm height and 0.2 mm thickness. This laser sheet was much larger than the expected CH profile width, and to capture the vortex structure. Detecting the $A^2\Delta - X^2\Pi$ (0,0) and (1,1) bands at 90° to the direction of the laser beam by an intensified CCD camera with the combination of a 410 nm high-pass and a 450 nm low-pass filter in front of the 105 mm objective, the images were saved on a PC. PIV is accomplished using ethanol droplets, with a diameter distribution mean value centered at 5μm , a 1008x1018 pixel dual frame digital camera, and a double-pulse second harmonic Nd:YAG laser. The PIV (Dantec) laser sheet generated by the forming optics is directed in the same plane as the CH laser sheet. Mie scattering is accomplished on the ethanol droplets as well as silicon oil to mark temperature isocontours.
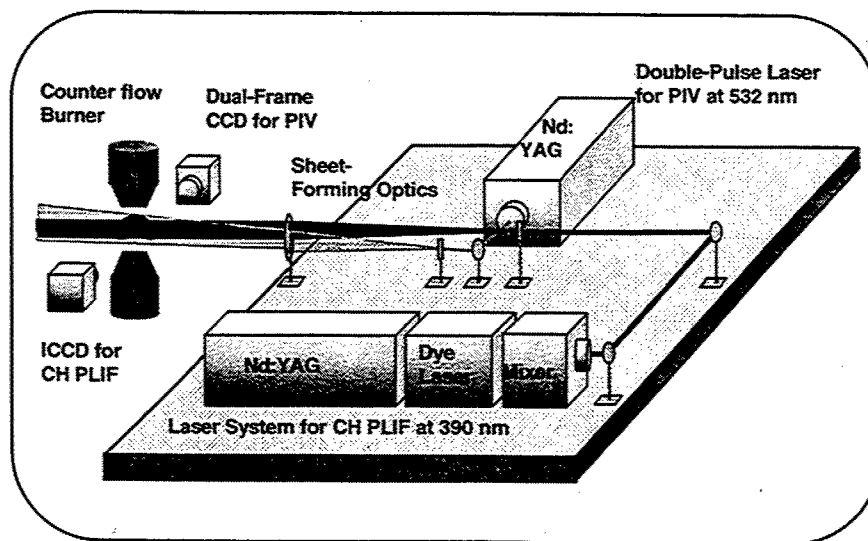
Figure 1. Lasers and Optics for CH PLIF and PIV

4 Results

Figures 2 show single shot and average of 20 images of PLIF measurements, during extinction around the axis of the counterflow flame interacting with the vortex. The CH profile in both cases are respectively of 4.5 pixels(0.2mm) and 6 pixels (0.25 mm), that shows the repeatability of the measurements.
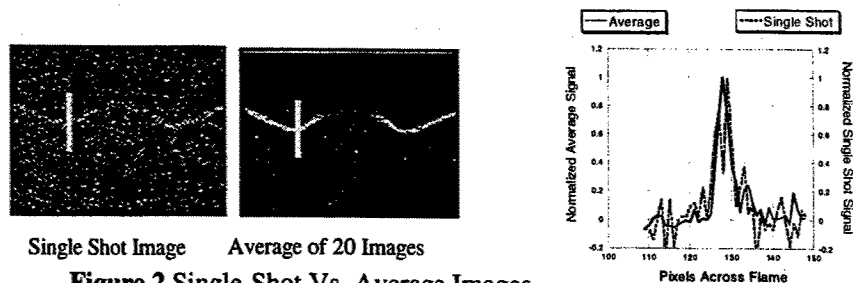

Single Shot Image   Average of 20 Images

Figure 2 Single-Shot Vs. Average Images

a Mie Scattering from
Ethanol Droplets

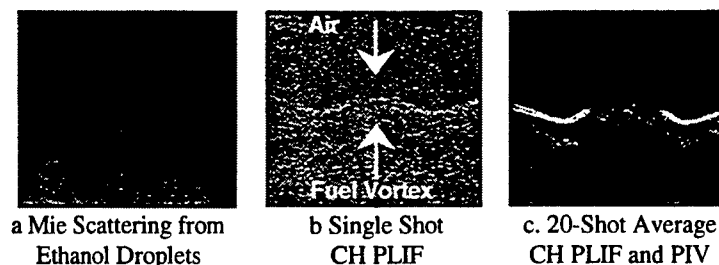b Single Shot
CH PLIF

c. 20-Shot Average
CH PLIF and PIV

Fig gure 3. Mie Scattering on Ethanol Droplets and CH PLIF / PIV During Flame Extinction. Phi =4, CH Laser E =1.2 mJ.

Figure 3a shows a Mie scattering image of ethanol droplets seeded in methane/nitrogen during a vortex flame interaction. Due to the strong vortex injection speed (4.5 m/s) and droplet momentum, the flame is quenched and allows the ethanol droplets to pass without evaporation. Figure 3c shows simultaneous CH PLIF and PIV velocity vector field of droplets during a two-phase vortex-flame interaction. Figure 4 shows the effect of laser energy on relative CH-PAH PLIF at equivalence ratio Phi=5. The line plots on Figure 5 indicate that their are separated. If decrease the laser energy and the equivalence ratio, the effects of PAH on measurements is diminished.

1.2 mJ   4 mJ   18 mJ
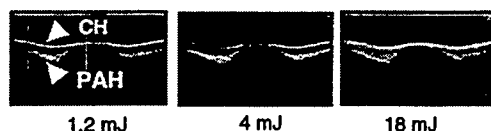
Figure 4. Effect of Laser Energy on Relative CH-PAH PLIF
and Scattering at Phi = 5
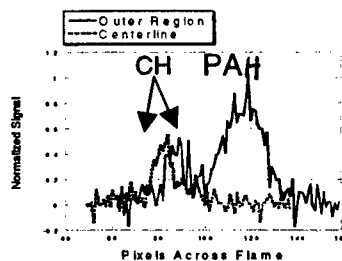
Figure 5. Line Plots of CH PLIF and PAH Fluorescence
at phi = 5 and 1.2 mJ

4. Conclusions

The results of the current investigation show that the droplets strongly affect the quenching behavior of the laminar diffusion flame. It is possible to avoid effects of PAH acting on the laser ebergy and the equivalence ratio of fuel. Future work will involve the post-processing of a large data-set of PIV and Mie scattering images. In addition PLIF of OH and CH will be performed for a more accurate depiction of the flame surface and regions of extinction.

Acknowledgments

This work is supported by U.S. Air Force Contract F33615-00-C-2068 and DGA/ONERA PEA-number 982703-TITAN in a U.S.-French collaborative program. These experiments were carried out at E.M2.C. Laboratory Ecole Centrale Paris.

* Actually in a sabatical stay at Ecole Centrale Paris as Assistant Professor.

References
1. Renard, P. H., Thevenin, D., Rolon, J. C. and Candel, S. (2000), "Dynamics of flame/vortex interactions," *Progress in Energy and Combustion Science*, Vol. 26, pp. 225-282.
2. Rolon, J. C., Aguerre, F. and Candel, S. (1995), *Combustion and Flame*, Vol. 100, pp. 422-429.
3. Fiechtner, G. J., Renard, P. H., Carter, C. D., Gord, J. R. and Rolon, J. C. (2000), "Injection of Single and Multiple Vortices in an Opposed-Jet Burner," *Journal of Visualization*, Vol. 2, pp. 331-341.
4. Renard P. H., Rolon, J. C., Thevenin, D., and Candel, S. ('1999), "Investigations of heat release, extinction, and time evolution of the flame surface for a non-premixed flame interacting with a vortex," *Combustion and Flame*, Vol. 117, pp. 189-205.
5. Renfro, M. W., Chaturvedy, A. and Laurendeau, N. M., (2001) Comb. Sci. and Tech. in press.
6. Renfro, M. W., King, G. B. and Laurendeau, N. M., (2000) Combust. And Flame 122:139-150.

Diode-Laser-Based Ultraviolet Absorption Sensor for NO

Sherif F. Hanna,* Rodolfo Barron-Jimenez,* Thomas N. Anderson,* Robert P. Lucht,*† Thomas Walther,** and Jerald A. Caton*

*Department of Mechanical Engineering (3123 TAMU)
**Department of Physics (4242 TAMU)
Texas A&M University
College Station, TX 77845

We have developed a new diode-laser-based sensor system for ultraviolet absorption measurements of the NO molecule. The laser system is illustrated schematically in Fig. 1. This system is based on sum-frequency-mixing (SFM) of a tunable, 395-nm external-cavity diode laser (ECDL) from Toptica Lasers with a frequency-doubled, diode-pumped Nd:YAG laser (CrystaLaser) in a beta barium borate (BBO) crystal. Because of the strength of the ultraviolet $A^2\Sigma^+$ - $X^2\Pi$ electronic transition of NO, the detection limit of the system is approximately 0.1 ppm of NO per meter of path length. In addition, the simplicity, generality, and relatively low cost of the SFM-based sensor strategy discussed in this paper will enable the development of absorption sensors throughout the entire ultraviolet spectrum, opening up a wide range of new possibilities for sensing and control of chemically reacting flow processes.

The wavelength of both the ECDL and the frequency-doubled Nd:YAG system were measured with a Burleigh WA-1000 cw wavemeter. The vacuum wavelength of the frequency-doubled Nd:YAG system was determined to be 532.299 nm. The frequency spectrum of the frequency-doubled Nd:YAG system was measured with a spectrum analyzer and it was confirmed that the output was single-mode. The vacuum wavelength of the ECDL system was tuned to 395.24 nm for the initial measurements, so that the 226.820 nm (vac) SFM output of the sensor system was in resonance with the overlapped $P_2(10)$ and $^PQ_{12}(10)$ transitions in the (v'=0, v"=0) band of the $A^2\Sigma^+$–$X^2\Pi$ electronic transition (Luque and Crosley, 1999), as shown in Fig. 2. The frequency spectrum of the ECDL was monitored with a Burleigh SA Plus spectrum analyzer as the ECDL wavelength was tuned over a mode-hop-free tuning range of 25 GHz. The etalon fringes are shown at the bottom of Fig. 2. The power of the ECDL was approximately 10 mW, the CrystaLaser 532-nm power was 115 mW, and the SFM process produced approximately 50 nW of 226-nm radiation.

The ultraviolet laser radiation was divided into a reference beam and a signal beam using a 50-50 beamsplitter. The simultaneous detection of the reference and signal beams allows the subtraction of common mode noise and etalon effects and significantly enhances the detection efficiency. The reference beam was directed to a solar-blind photomultiplier (PMT). The signal beam was transmitted through a room-temperature gas cell filled with a mixture of 100 ppm NO (nominal concentration) in N_2. Bandpass filters centered at 226 nm were placed in front of each PMT. Two absorption traces are actually shown in Fig. 2. One of these was acquired while the ECDL frequency was tuned up, and the other while the frequency was tuned down. The data shown were averaged over 32 traces on the digital oscilloscope. The ECDL was tuned over the mode-hop-free tuning range at a frequency of approximately 5 Hz, so the spectrum shown was acquired in approximately 6 seconds.

†Author to whom correspondence should be addressed. Phone: 979-862-2623, Fax: 979-862-2418, Email: rlucht@tamu.edu.
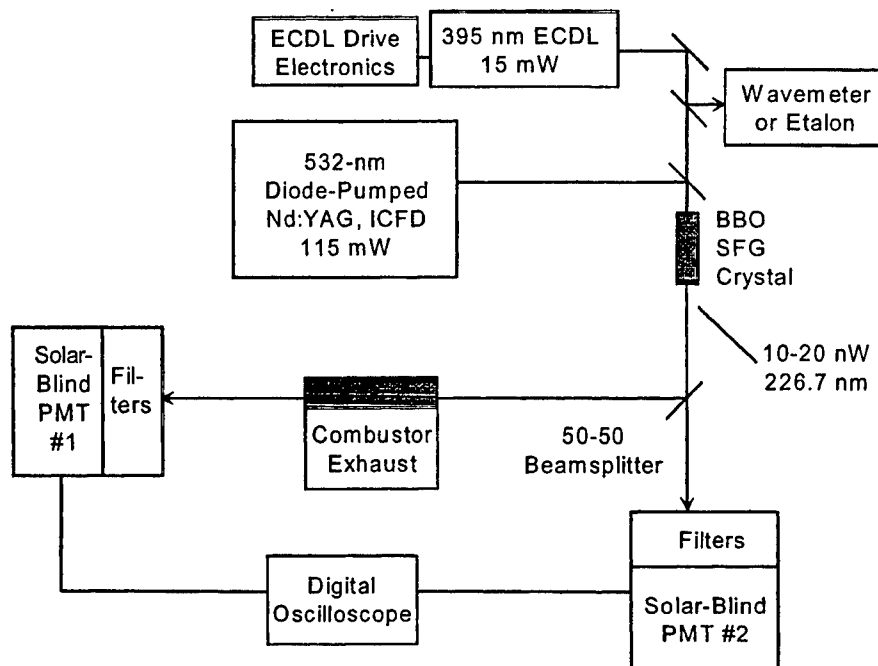
Fig. 1. Schematic drawing of the diode-laser-based NO sensor.

Our initial set of measurements was performed using a gas mixture of 100 ppm NO in nitrogen. A computer code for the analysis of the absorption spectra is under development and has been used to analyze this initial set of data. The theoretical spectrum shown in Fig. 2 is calculated assuming a Voigt profile with a Doppler width (FWHM) of 2.97 GHz. The collisional width (FWHM) that gives the best fit for the various NO lines that we have analyzed is 0.18 GHz/kPa, with most of the broadening due to the nitrogen. This is in excellent agreement with broadening parameters measured by Chang et al. (1992) for collisions of NO with N_2. The spectrum in Fig. 2 was recorded at a pressure of 13.1 Pa, and the collisional width of the theoretical line is 2.32 GHz. As evident from Fig. 2, the theoretical spectral line shape is in excellent agreement with the experimental line shape. The NO concentration is also a parameter in the theoretical calculation, and the concentration that gives the best fit to the experimental spectrum is 94 ppm. This is in good agreement with the quoted value of 100±10 ppm for the NO-N_2 gas mixture from Matheson.

The sensitivity of the NO sensor system in its present configuration is limited by the noise level in our detection channel. We are limited currently to detecting an absorption level of 0.1%, determined by lowering the pressure in our gas cell to below 1 Torr and monitoring the resulting absorption. Our estimated sensitivity for the current system is thus approximately 0.3 ppm for a meter of path length in 1000 K combustion exhaust. This is sufficient sensitivity for monitoring the exhaust of any practical combustion device, but that sensitivity can be improved by at least an order of magnitude using wavelength modulation spectroscopy (WMS) or frequency modulation spectroscopy (FMS). For cw absorption systems, absorption levels of 10^{-5} or lower can be measured either by wavelength modulation techniques and phase sensitive detection (Silver, 1992) or by balanced radiometric detection (Allen et al., 1995). We can modulate the frequency of our ECDL by modulating the current at frequencies f up to 100 MHz by using a bias-T connector and detecting the 2f absorption signal using a lock-in amplifier. We have not yet

implemented these WMS, FMS, or balanced radiometric techniques, but Peterson and Oh (1999) demonstrated recently a minimum detectable absorbance of about 2×10^{-5} using a similar detection system and estimated that with further effort to reduce etalon effects that the minimum detectable absorbance could be lowered to 10^{-6}.

ACKNOWLEDGEMENTS

REFERENCES

M. G. Allen, K. L. Carleton, S. J. Davis, W. J. Kessler, C. E. Otis, D. A. Palombo, and D. M. Sonnenfroh (1995), "Ultrasensitive Dual-Beam Absorption and Gain Spectroscopy: Applications for Near-Infrared and Visible Diode Laser Sensors," Appl. Opt. **34**, 3240.

A. Y. Chang, M. D. DiRosa, and R. K. Hanson (1992), "Temperature Dependence of Collision Broadening and Shift in the NO A-X (0,0) Band in the Presence of Argon and Nitrogen," JQSRT **47**, 375-390.

J. Luque and D. R. Crosley (1999), "LIFBASE: Database and Spectral Simulation Program (Version 1.5)," SRI International Report MP 99-009.

K. A. Peterson and D. B. Oh (1999), "High-Sensitivity Detection of CH Radicals in Flames by use of a Diode-Laser-Based Near-Ultraviolet Light Source," Opt. Lett. **24**, 667.

J. A. Silver (1992), "Frequency-Modulation Spectroscopy for Trace Species Detection: Theory and Comparison Among Experimental Methods," Appl. Opt. **31**, 707.
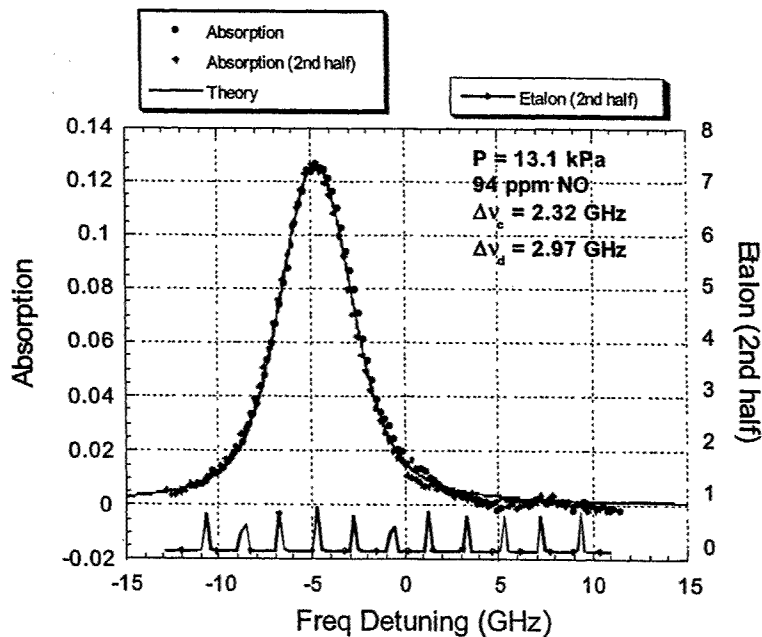
Fig. 2. NO absorption spectrum of the $P_2(10)$ and $^PQ_{12}(10)$ overlapped absorption lines.

Simultaneous PLIF and Stereo PIV measurements of a Turbulent Non-Premixed Flame

A.P. Harvey**, J. Hult*, C.F. Kaminski, P. Stonestreet

Department of Chemical Engineering, University of Cambridge, UK.
*Department of Combustion Physics, University of Lund, Sweden.
**To whom correspondence should be addressed

Abstract

Stereo PIV and time sequenced PLIF were performed simultaneously on the TECFLAM turbulent, non-premixed international reference flame to investigate local flame extinction phenomena. The results show, for the first time, effects due to the out-of-plane component of the velocity.

Introduction

The international standard TECFLAM flame (Bergmann *et al* (1998)) consists of an axial flow of a mix of 44.7 vol. % nitrogen, 22.1 vol. % methane and 33.2 vol. % hydrogen, surrounded by a co-flow of air at approximately 3 m/s. The fuel supply tube has an inner diameter of 8 mm, while the outer nozzle has a diameter of 140 mm [see Figure 1 below]. The flame front was tracked by the PLIF method, following the concentration of OH radicals. Simultaneous measurement of this and the flow field allowed correlations between the two to be observed, and correlated with extinction events. The stereo PIV allowed the 3-dimensional nature of the turbulent eddies, and other flow effects, to be observed for the first time for this flame, and correlated to flame front phenomena.
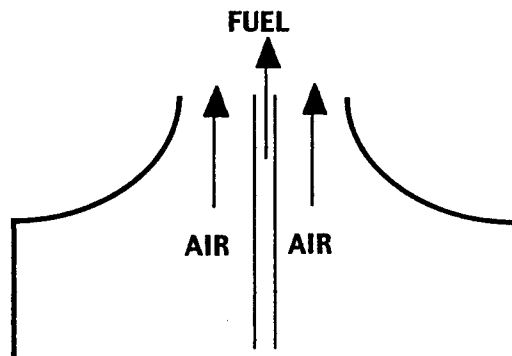
Figure 1: The TECFLAM Standard Flame

The flame has been studied by OH - PLIF/PIV methods previously (Hult *et al*, 2001), but this was by standard 2D PIV means. A number of other flames have also been studies by simultaneous 2D PIV and PLIF methods (Su *et al* (2000), Mueller *et al* (1995) and Frank *et al* (1999)). SPIV (stereo PIV) methods have been used to study flames previously (Stella *et al*, 2001), but this was for premixed flames. Hence, this is the first SPIV/PLIF study of a non-premixed flame, and the first time-sequenced data in combination with overall flow field visualization. The 3rd component of the velocity should give a much clearer picture of the vortices that cause the local extinctions, as the 2D data merely gives an XY projection of the real vortex, whereas the SPIV data will allow the out-of-plane velocity of these vortices to be calculated for the first time.

PIV Equipment

The stereo PIV equipment consisted of a pair of 'Big Sky' 40mJ, Nd:YAG pulsed lasers, two 12-bit CCD cameras (PCO Sensicam) at 60° to the object plane and an ILA synchroniser unit. The 'VidPIV 4.0e' software (OFS) controlled the operation and was used for most of the post processing of the data. The seeding material used was titanium dioxide.

PLIF Equipment

The high-speed planar LIF system consisted of a cluster of 6 Nd:YAG lasers with beam combination optics and a high speed framing camera with image intensifier. The system was capable of recording PLIF images with time resolution as low as 10 ns. This equipment is described in more detail in Kaminski *et al* (1999).
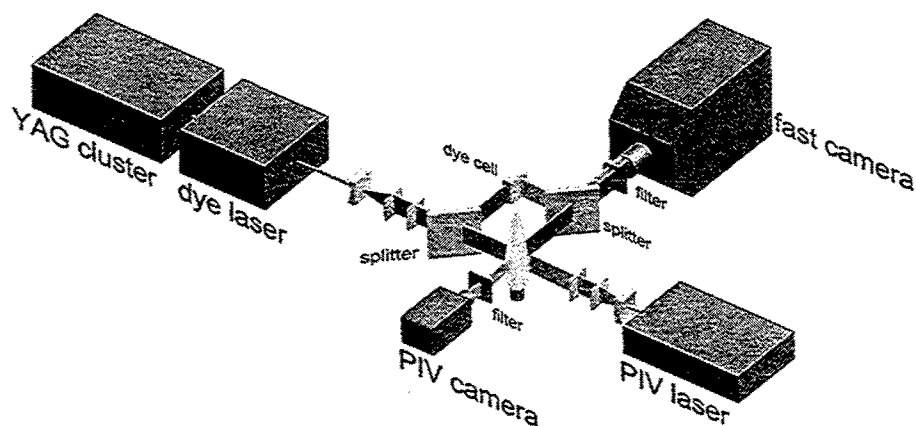

Figure 2: OH-PLIF Set-up

PIV Data processing

The acceptability criterion for the data was that less than 20 % of the vectors are interpolated. After the initial cross correlation the vectors were globally filtered, i.e., any vectors outside a certain range were discounted, and then locally filtered using a local median. The interrogation area used was 32 pixels, with a vector separation of 0.05 cm, such that adjacent interrogation areas overlapped.by 0.025 cm.

Results

In figure 3a below the third PLIF image of a 6-image sequence can be seen. The PIV image pair was taken at 5 μs either side of this image. A number of extinction events are clearly in progress. In figure 3b the 3-component velocity magnitude is shown.
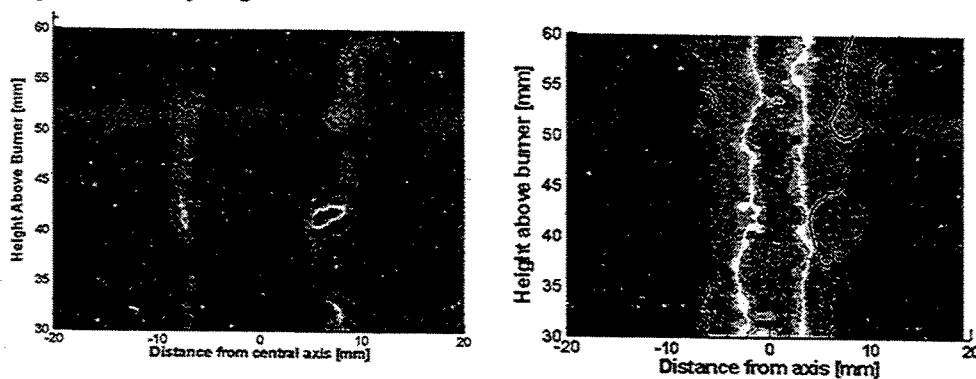
Figure 3a) OH PLIF Image b) Velocity Magnitudes

Figures 4a) and 4b) on the following page show the x and z velocities of the complete flow. There are clearly patches of high x- and z-velocity that correspond to flame extinctions (x and z velocities are often indicative of vortex formation).
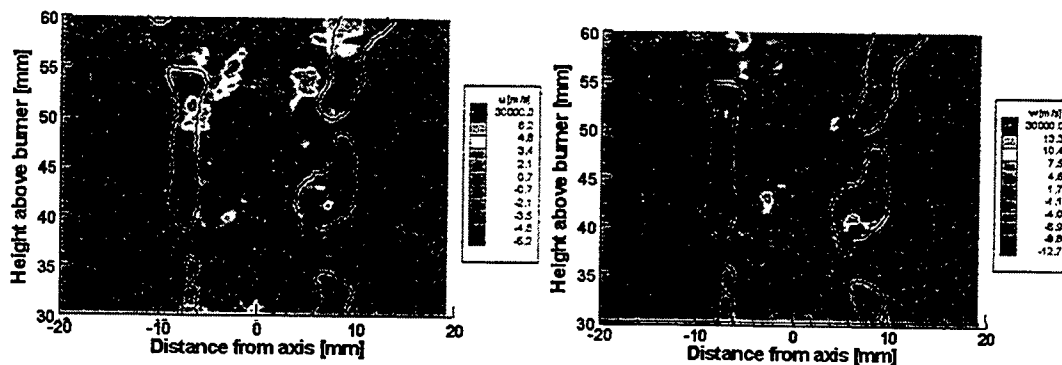
Figure 4a) X velocity map b) Z velocity map

Figure a) below focuses on one flame extinction. The vectors have had a reference y-velocity of 5m/s removed, so that the vortex can be clearly seen. Figure b) shows the variation of the z-velocity in this area, illustrating the 3D nature of the vortex.
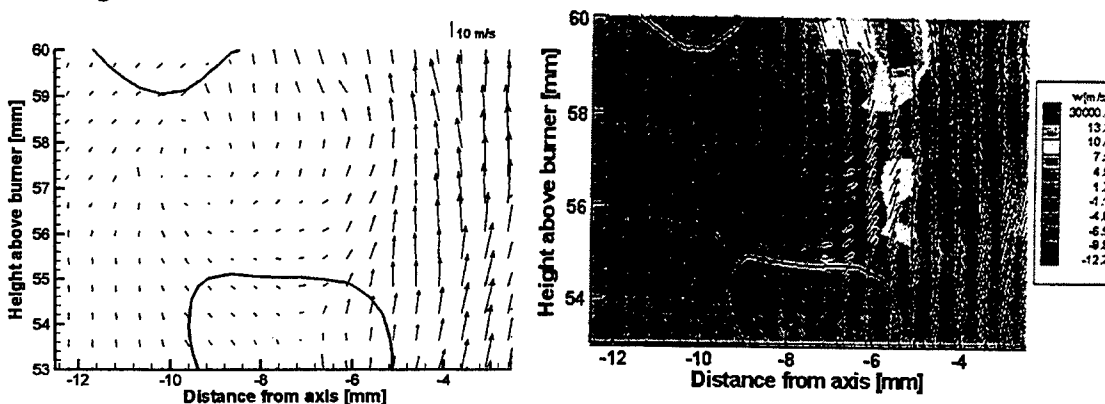

Figure 5 a) PLIF & XY vectors, b) W-velocity colour map & XY vectors

Conclusions
In the correct circumstances, turbulent vortices can move through the flame front, straining it such that the flame is locally extinguished. The out-of-plane component of the velocity of the vortices can clearly be seen in the figures above. Previous 2D PIV work has not shown the 'full picture', as the data can only give a 2D projection of the real 3D vortices responsible for the flame extinction phenomena.

References
1. Bergmann, V., Meier, W., Wolff, D. and Stricker, W. *"Application of spontaneous Raman and Rayleigh scattering and 2D LIF for the characterization of a turbulent CH4/H2/N2 jet diffusion flame"*, Appl. Phys. B, 66, 489-502 (1998).
2. J. Hult, G. Josefsson, M. Aldén, and C.F. Kaminski, *"Flame front tracking and simultaneous flow field visualization in turbulent combustion"*, Proceedings of the 10th International Symposium on Application of Laser Techniques to Fluid Mechanics, Lisbon (2000).
3. Su L.K., Han D.H. and Mungal M.G., *"Measurements of velocity and fuel concentration in the stabilization region of lifted jet diffusion flames"*, Proc. Comb. Inst., 28, 327 – 334, part1 (2000).
4. Mueller C.J., Driscoll J.F., Sutkus D.J, Roberts W.L., Drake M.C. and Smooke M.D., *"Effect of unsteady Stretch Rate on OH Chemistry During a Flame Vortex interaction – to assess Flamelet Models"*, Combustion and Flame, 100 (1-2), 323 – 331 (1995).
5. Frank J.H., Kalt P.A.M. and Bilger R.W., *"Measurements of Conditional Velocities in Turbulent Premixed Flames by simultaneous OH PLIF and PTV"*, Combustion and Flame, 116 (1-2), 220–232 (1999).
6. Stella A, Guj G.L., Kompenhans J., Richard H and Raffel M, *"Three-components Particle Image Velocimetry measurements in premixed flames"*, Aerospace science and Technology, 5(5), 357–364 (2001).
7. Kaminski, C.F., Hult, J. and Aldén, M., *"High repetition rate planar laser-induced fluorescence of OH in a turbulent non-premixed flame"*, Appl. Phys. B, 68, 757-760 (1999).

Application of Angle-Dependent Light Scattering and Fractal Dimension Analysis for Detection and Characterization of Biopolymers

J. Houston Miller, Glauco R. Souza, Carly Levin and Emily Barter

Department of Chemistry
The George Washington University
Washington, DC

Project Summary

Over the past year we have performed both theoretical calculations and light scattering measurements utilizing simplified model systems in which we demonstrate the feasibility of combining ADLS/FD and Au-DNA nanopariticles of different sizes for detecting specific sequences of DNA and characterizing Au-DNA fractal aggregates. The ADLS apparatus used in this work was constructed from off-the shelf optical components (Souza and Miller, 2001).

Our results demonstrate that the ADLS/FD signal is sensitive to both concentration and length of an oligonucleotide-target, and is sensitive to the fractal structure of an Au-DNA aggregate. The hybridization strategy used in this work is based on the principle first shown by Mirkin (Mirkin, et al 1996). In their work, it was demonstrated that thiol-modified oligonucleotides covalently attached to gold nanoparticles (Au-DNA probe) hybridize to a target single-strand oligonucleotide of complementary sequence (oligonucleotide-target) in a liquid sample, forming a network of DNA and Au nanoparticles (Scheme 1). In Mirkin's work, UV-Vis absorption of Au nanoparticles was used to detect DNA hybridization.

The ADLS instrumentation utilized in this work used a 4 mW Fabry-Perot diode laser with an output wavelength of 660 nm as light source. The incident laser light was perpendicularly polarized and modulated by a mechanical chopper (1 KHz) which triggered a lock-in amplifier for phase sensitive detection. The polarized beam was focused into the center of a 1 cm diameter quartz scattering cell. All light collection components sit on a rotation stage. The scattered light passes through a polarizer which isolates perpendicularly polarized scattered light, and then it is focused onto a photodiode detector. The light collection geometry provided a 5° angular resolution. The ADLS signal was detected at angles between 15° and 50° in increments of 5°. This instrumentation does not nearly provide the measurement speed, angular resolution, detection limit, dynamic range and time dependent measurement capability of the proposed instrumentation. The characteristics of the proposed instrumentation will be outlined in the instrumental description section.

The angle dependence of the scattering signal can be used to determine both radius of gyration (R_g) and fractal dimension (D_f) and thus unveil details of the Au-DNA aggregate morphology. Both the radius of gyration and the fractal dimension are found to be sensitive to target concentration. However, the latter shows a much greater sensitivity.

The increase in aggregate density (as shown by the increase in Df with oligo-target concentration) is likely the outcome of increased intra-particle cross-linking at higher oligo-target concentration.

Our concentration data suggest that the morphology of the aggregates can be measurably altered by target DNA concentration. The fractal dimension is also dependent on the length of the oligonucleotide-target, effectively increasing the spacing between the primary particles. To demonstrate this sensitivity, we compared the fractal dimension values for two systems with different oligo-target lengths: one in which the Au-DNA probe hybridizes to a 21 base long oligo-target, and the other in which the Au-DNA probe hybridizes to a 30 base long oligo-target. Each concentration of target showed lower Df values for the system containing the 30 base long oligo-target, in comparison to the one containing 21 base long oligo-target, indicative of more swollen and better solvated clusters for the former. Further, the increase in fractal dimension with concentration for both lengths of oligo-target further suggests a transition from string like aggregates (when Df is near unity) to denser, more compact structures at higher fractal dimension.

References cited

C.A. Mirkin, R.L. Letsinger, R.C. Mucic, and J.J. Storhoff, *Nature* 382, 607-611 (1996).
G.R. Souza and J. H. Miller, *J. Am Chem. Soc.*,123, 6734-6735 (2001).

KEY TO AUTHORS

Anderson, Thomas • PD5
Barron-Jimenez, Rodolfo • PD5
Barter, Emily • PD7
Brockhinke, A. • PD3
Bütler, A. • PD3
Caton, Jerald • PD5
Chow, B. C. • PD1
Furtak, T. E. • PD1
Gord, J. R. • PD4
Hanna, Sherif • PD5
Harvey, A. P. • PD6
Hult, J. • PD6
Kaminski, C. F. • PD6
Kohse-Höinghaus • PD3
Lal, Mohan • PD2
Lemaire, A. • PD4
Lenhard, U. • PD3
Levin, Carly • PD7
Lucht, Robert • PD5
Meyer, T. R. • PD4
Miller, J. Houston • PD7
Prakash, O. • PD2
Rahmann, U. • PD3
Rolon, J. C. • PD4
Souza, Glauco R. • PD7
Stonestreet, P. • PD6
Walther, Thomas • PD5
Zähringer, K. • PD4

Addendum

The paper FA1/Recent Progress in the Science and Technology of LIBS was submitted late and therefore could not be included in the Laser Applications to Chemical and Environmental Analysis Conference edition.

Recent progress in the science and technology of LIBS

Andrzej W. Miziolek, Kevin L. McNesby, and Russell S. Harmon[a]
US Army Research Laboratory
AMSRL-WM-BD
Aberdeen Proving Ground, MD 21005-5069 USA
410-306-0861/1909 Tel/FAX
miziolek@arl.army.mil
[a]ARL/Army Research Office
Research Triangle Park, NC 27709-2211

Abstract: Laser Induced Breakdown Spectroscopy (LIBS) is an emerging, minimally-destructive sensor technology for in-situ real-time chemical and biological species identification and analysis. This laser-based analytical technology is undergoing very rapid growth in both instrumentation advances and in the number and variety of applications in both the military and civilian sectors.
©2000 Optical Society of America
OCIS codes: (300.0300) Spectroscopy, (300.6210) Spectroscopy, Atomic, (040.0040) Detectors, (040.1880) Detection

1. Introduction

In the 1970s a few research groups published papers that reported astounding success in chemical analysis-one atom detection. In each case they used lasers as their primary tool for the analysis. Both laser ionization and fluorescence were demonstrated in the laboratory to show such sensitivity. These early successes generated considerable expectation with regards to the potential of laser spectroscopy to make major advances in chemical and biological analysis. In 1987 the first Laser Applications to Chemical Analysis (LACA I) was organized to bring together the community working in this promising area. The meeting was held in Lake Tahoe and featured a panel discussion concerning the future of practical applications. Even then it was recognized that in spite of the early laboratory successes the previous decade, actual progress in the development of commercial instrumentation based on laser spectroscopy was quite slow. Many reasons were provided for the apparent lack of progress. These included (1) the fact that lasers are expensive and difficult to work with (not turn key), (2) lasers were also not very amenable for field use, and (3) there are many different types of lasers (e.g. cw, pulsed, visible, uv, etc.) and no single one had wide applicability in laser-based chemical analysis. Yet another issue was the difficulty of tuning vis-uv radiation which was a requirement for most techniques based on spectroscopy.

In the early 1980s a technique called Laser Induced Breakdown Spectroscopy (LIBS) was originated and subsequently developed at Los Alamos National Laboratory which showed considerable promise as a new type of tool for chemical analysis. The bulk of the early work performed using LIBS was aimed towards the detection of a single element (usually a metal) and thus frequently a single elemental emission line was monitored during the analysis. LIBS, which is basically a simple spark spectrochemical technique which uses a Q-switch pulsed laser to create the spark, has many attributes that makes it an attractive tool for chemical analysis. Such attributes include (1) LIBS is relatively simple and straightforward, (2) no sample preparation required, (3) only engages a very small sample (pg-ng) of matter in each laser microplasma event, and (4) all components of the instrument can be made small and rugged for field use.

2. Highlights and Examples of Recent Exciting Developments in LIBS

Over the 20+ years of LIBS development, there has been great progress in (1) the understanding of the LIBS phenomenon, (2) advances in instrumentation, and (3) in data analysis. A growing number of researchers were drawn to the LIBS field, particularly due to the practicality of working with LIBS. A major event in the field of LIBS occurred in October 2000 when the LIBS 2000 1st International Conference on Laser Induced Plasma Spectroscopy and Applications was held in Tirrenia, Italy. This meeting consisted of 130 presentations from the world-wide LIBS community and subsequent to the meeting a special issue (ref. 1) was published which contained 39 papers that cover a very wide range of topics. These include (1) environmental analyses (soils, particulate matter), (2) materials (metals, plastics), (3) biomedical (teeth, bones), (4) security (chemical agents), (5) art .

(pigments, precious/ancient metals), (6) hyphenated techniques, (7) underwater detection, (8) analysis in nuclear reactors, and (9) femtosecond LIBS, amongst others.

Very recently there has been a major advance in LIBS instrumentation with the development of a broadband detector which is based on 7 spectrometers. This detector, which was developed by Ocean Optics, Inc. in collaboration with the Army Research Laboratory at APG, MD, has salient features of (1) spectral coverage of 200-940 nm, (2) spectral resolution of 0.1 nm, and (3) instantaneous response time. Figure 1 shows a picture of the instrument in the laboratory.
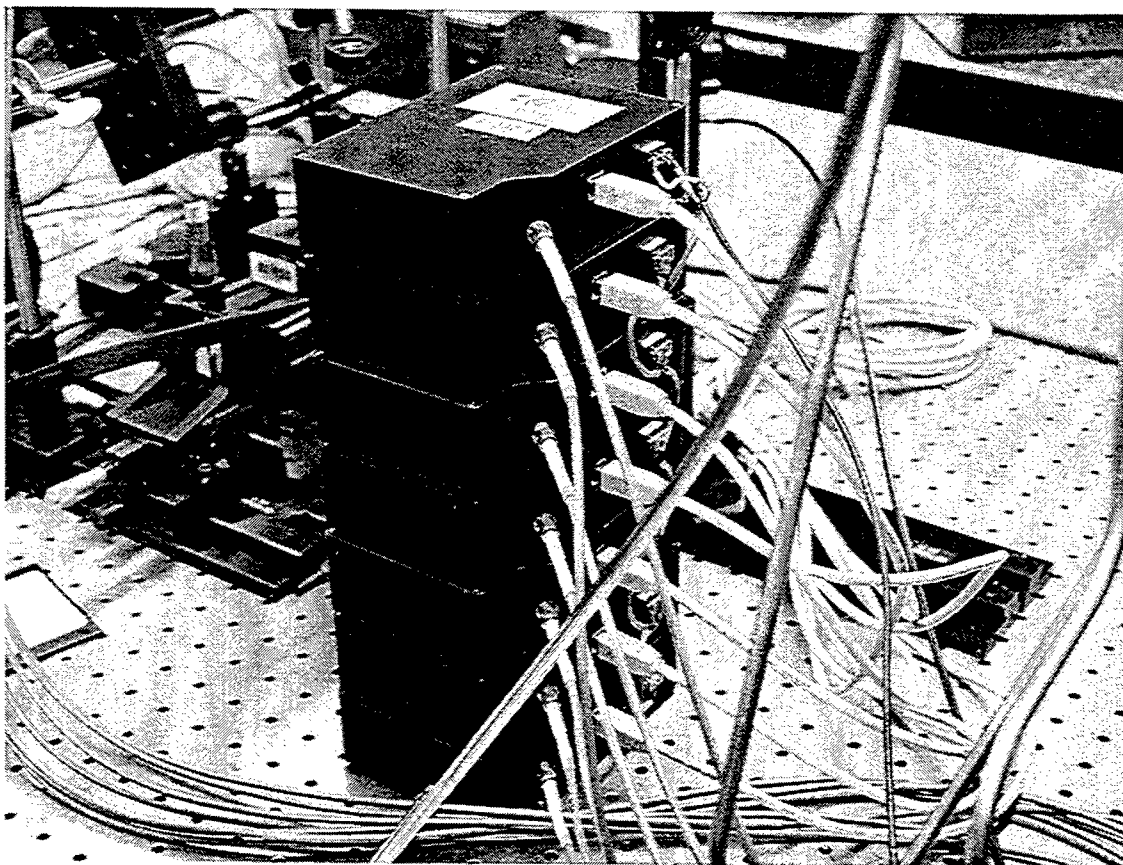
Figure 1. Broadband LIBS Detector (7 spectrometers)

3. Military Applications of LIBS

LIBS has certain important characteristics that make it a very attractive sensor technology for military use. These include: (1) real-time response, (2) the sensor can be made man-portable, (3) it can be used for both point sensing and in a standoff mode, and (4) the sensor responds to all forms of unknowns, both chemical and biological. Table 1 provides a list of examples of specific military applications. Figure 2 shows two recent and preliminary spectra of energetic materials. It should be noted that these are single-shot spectra and the analysis is done real-time. Also, LIBS readily can detect illicit and dangerous materials such as black powder, which is important given that black powder evades detection by standard explosives sensor technologies. The typical explosives sensors are aimed at detecting organo-nitro compounds. The nitrate salts that are ingredients in typical black powder formulations escape detection by these standard methods. The two spectra are quite different one from the other which is expected given that C4 is composed of approximately 91% RDX (an organo-nitro compound), and the rest of various organic compounds including motor oil.

Table 1. Examples of Military Applications of LIBS

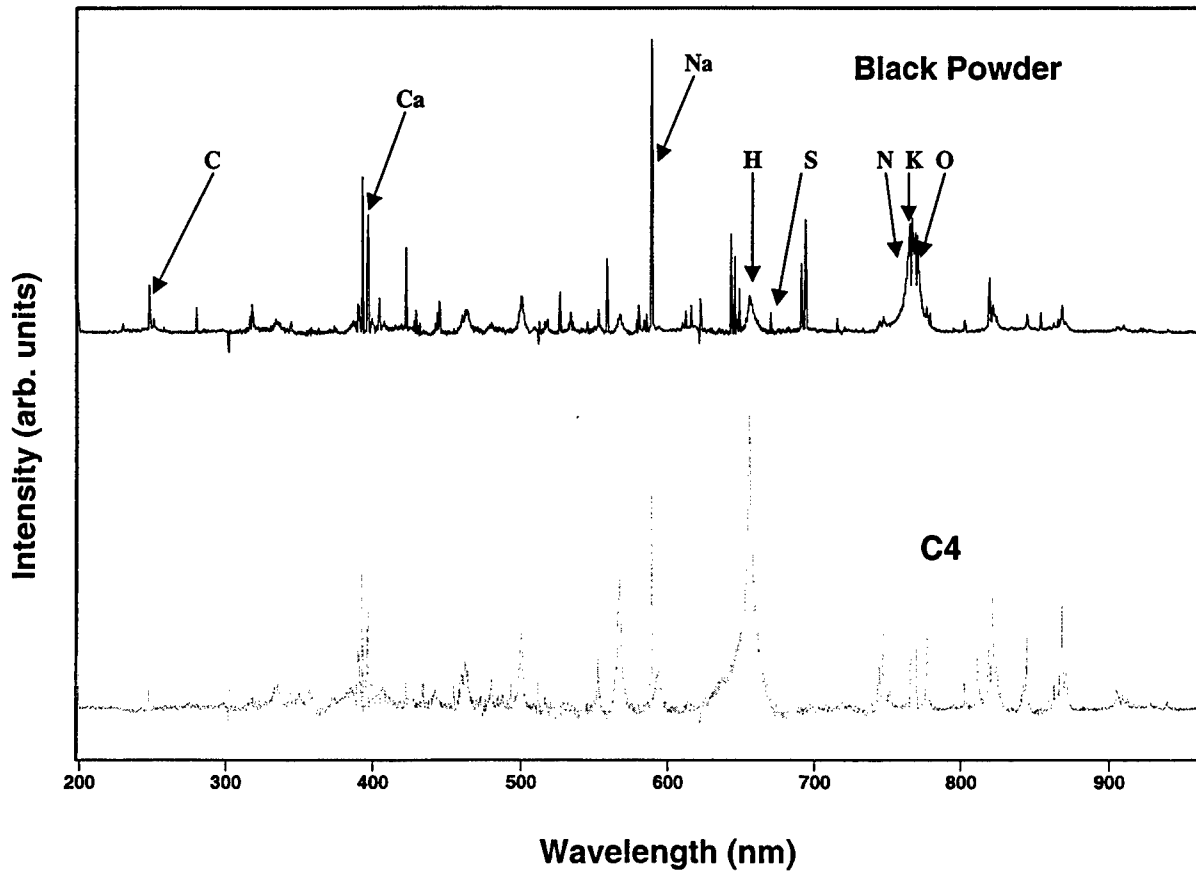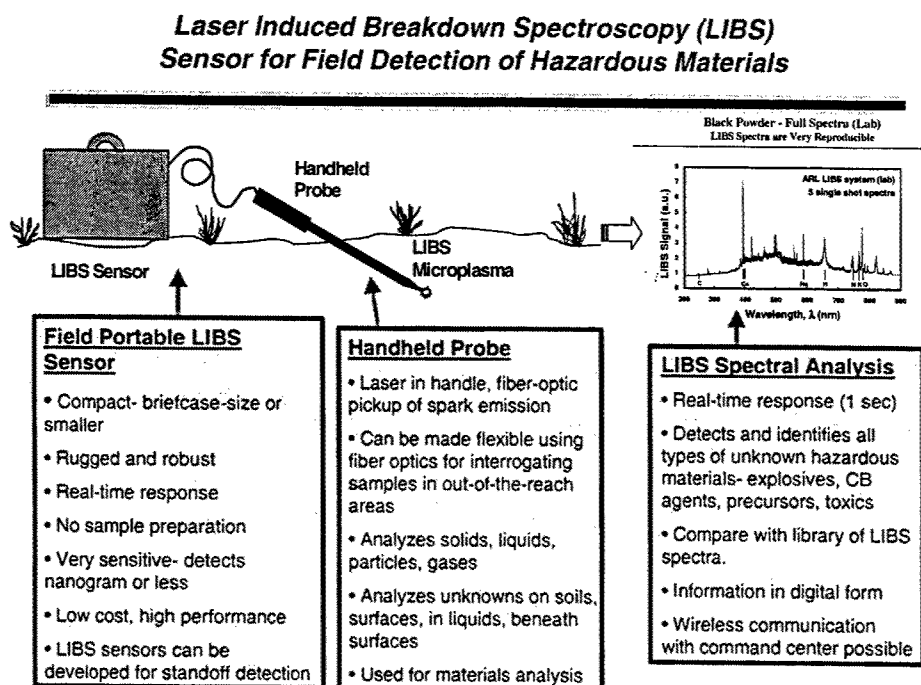| Robotics- chem-bio agents, explosives, others |
|---|
| Unexploded Ordnance (UXO) |
| Standoff detection |
| Hazardous vapors (e.g. halon replacements) |
| RCRA toxic metals in soils and waters |
| Pb in paint |
| Depleted Uranium (DU) |
| Field analysis of unknown matter |
| Contaminated buildings/debris |
| Excessive engine wear |
| Process monitoring of production |

Figure 2. Single-Shot LIBS Spectra of Energetic Materials

4. Peeking Into the Future

Looking into the future, a major area of LIBS sensor development is in field instrumentation. A number of concepts exist of making hand-portable devices (suitcase size) with a hand-held probe where the LIBS spark is generated at the tip of the probe. In this configuration analyses can be made readily by touching the object that one is interested in identifying. Another variant of this approach would be the development of a flexible probe where the light is delivered and collected by means of optical fibers. In order to maintain maximum flexibility, an advanced version of this concept includes the use of a diode laser to pump a micro Nd:YAG laser at the tip of the probe to make an energy efficient and robust field sensor. Such a sensor could be used to make analyses in out-of-the-reach locations where direct line-of-sight is not possible. Figure 3 shows a concept of a field-portable LIBS sensor.

Figure 3.

Laser Induced Breakdown Spectroscopy (LIBS) Sensor for Field Detection of Hazardous Materials

Field Portable LIBS Sensor

- Compact- briefcase-size or smaller
- Rugged and robust
- Real-time response
- No sample preparation
- Very sensitive- detects nanogram or less
- Low cost, high performance
- LIBS sensors can be developed for standoff detection

Handheld Probe

- Laser in handle, fiber-optic pickup of spark emission
- Can be made flexible using fiber optics for interrogating samples in out-of-the-reach areas
- Analyzes solids, liquids, particles, gases
- Analyzes unknowns on soils, surfaces, in liquids, beneath surfaces
- Used for materials analysis

LIBS Spectral Analysis

- Real-time response (1 sec)
- Detects and identifies all types of unknown hazardous materials- explosives, CB agents, precursors, toxics
- Compare with library of LIBS spectra.
- Information in digital form
- Wireless communication with command center possible

5. Acknowledgements

6. References

1. Special Issue: LIBS 2000 1st International Conference on Laser Induced Plasma Spectroscopy and Applications, *Spectrochimica Acta, Part B: Atomic Spectroscopy*, Vol. 56, June 2001.

Laser Applications to Chemical and Environmental Analysis Technical Program Committee

Trends in Optics and Photonics Series

Alexander A. Sawchuk, Series Editor

*Denotes Technical Digest Postconference Edition volumes.

For more information on TOPS volumes, please refer to www.osa.org or call the Optical Society of America at 202-416-1907.

TOPS Vol. 69, Laser Apps to
Chemical & Environ 2002
List Price: $92.00
Mtg./Member Price: $60.00